

**SMOOTHED PARTICLE HYDRODYNAMICS (SPH)
MODELLING OF NEARSHORE BREAKING WAVES**

Ayesha Mahomedy

Submitted in fulfillment of the requirements for the degree of
Master of Science in Engineering
in the
College of Agriculture, Engineering and Science,
University of KwaZulu-Natal
Durban
December 2021

Supervisors: Professor D. D. Stretch and Doctor J. J. Pringle

COLLEGE OF AGRICULTURE, ENGINEERING AND SCIENCE

DECLARATION - PLAGIARISM

I, Ayesha Mahomedy, declare that

1. The research reported in this thesis, except where otherwise indicated, is my original research.
2. This thesis has not been submitted for any degree or examination at any other university.
3. This thesis does not contain other persons' data, pictures, graphs or other information, unless specifically acknowledged as being sourced from other persons.
4. This thesis does not contain other persons' writing, unless specifically acknowledged as being sourced from other researchers. Where other written sources have been quoted, then:
 - a. Their words have been re-written but the general information attributed to them has been referenced
 - b. Where their exact words have been used, then their writing has been placed in italics and inside quotation marks, and referenced.
5. This thesis does not contain text, graphics or tables copied and pasted from the Internet, unless specifically acknowledged, and the source being detailed in the thesis and in the References sections.

Signed

.....
Ayesha Mahomedy

22/03/2022.....
Date

As the candidate's Supervisor I agree/do not agree to the submission of this thesis

Signed

.....
Derek. D. Stretch

22/03/2022.....
Date

.....
Justin. J. Pringle

22/03/2022.....
Date

ACKNOWLEDGEMENTS

First and foremost, I would like to praise and thank God, the most kind and merciful, for helping me accomplish this dissertation. I would further like to acknowledge and express my gratitude to those who have given me a great deal of support and assistance:

Thank you to my supervisors, Professor Derek D. Stretch and Doctor Justin J. Pringle, whose expertise and invaluable advice guided me to complete this dissertation. I will always be grateful for the opportunity to be a part of their Environmental Fluid Mechanics Laboratory (EFML) team at UKZN and to share in their enthusiasm for learning.

I would also like to thank my parents, Nazira I. Motala and Mahomed S. Mahomed, for their unconditional love and support for me in all my endeavours. I am also thankful to my family and friends who have always believed in me and encouraged me.

Finally, I could not have completed this dissertation without the companionship and tutelage of my favourite PhD candidates, Calvin P. Wells and Atish Deoraj. I will always have a deep regard for our bottomless coffees and the conversations that accompanied them.

ABSTRACT

Breaking waves drive sediment transport in the nearshore zone of coastal regions and directly govern beach transformation. Accurate coastal modelling of breaking waves is essential to predict sediment transport accurately. Efficient and sustainable management of natural coastal systems and urban coastal developments relies on accurate sediment transport predictions. This study proposes a mesh-free, Lagrangian, smoothed particle hydrodynamics (SPH) model to simulate nearshore breaking waves in two-dimensions. This study emphasises using SPH to evaluate the wave field parameters (local velocities, vorticities, and shear stresses) that can be used to predict coastal phenomena, namely sediment transport in nearshore, wave-driven environments. This study showed that a two-dimensional SPH model could replicate the free surface of nearshore breaking waves and accurately predict the flow characteristics beneath breaking waves. However, the accuracy of the results can vary depending on the position of the breaking wave in the surf zone. Furthermore, SPH applications must choose between accuracy and computational efficiency.

The key SPH calibration parameters identified were the artificial viscosity coefficient (α), the dimensionless smoothing length ratio (h_{SPH}/dp), and the particle resolution (H/dp). Extensive comparative analysis was performed between simulated results and measured data to obtain suitable parameter values for a plunging solitary wave. A suitable choice of $\alpha=0.1$, $h_{SPH}/dp=3$, and $H/dp=90$ were selected based on the results. Furthermore, the results suggested that a suitable choice of model parameters depends on the viscosity treatment method (artificial/sub-particle scale viscosity approach) and the type of wave breaking simulated (plunging/spilling). Thus, $\alpha=0.1$, $h_{SPH}/dp=3$, and $H/dp=90$ were only deemed suitable when the standard SPH artificial viscosity approach is used to simulate breaking plunging and spilling waves on beach slopes milder than 1/10.

The model sensitivity to α , h_{SPH}/dp , and H/dp was also investigated based on the numerical wave energy dissipation and simulated wave surface of a plunging solitary wave in the space and time domain. When α was above or below the ideal value of 0.1 for a given h_{SPH}/dp and H/dp , the numerical wave energy dissipation and wave height at breaking did not match the measured data. The choice of α was strongly related to H/dp , and a reduced α became more appropriate for a lower H/dp . The results also showed that the model was less sensitive to h_{SPH} than the choice of α and H/dp in terms of the model performance. However, when h_{SPH}/dp was less than 1, for any given α and H/dp ,

the numerical wave energy dissipation and wave height at breaking were under-predicted. The choice of H/dp was of principal importance and influenced the choice of the other model parameters. When H/dp was below the ideal value of 90, for any given α and h_{SPH}/dp , the numerical wave energy dissipation and wave height at breaking did not match the measured data. Additionally, the breaking wave shape was poorly simulated. However, $H/dp=90$ becomes computationally expensive when simulating breaking waves in large numerical domains or with relative wave heights significantly less than 0.6. Hence, the available computing power limits the choice of H/dp .

The performance of a two-dimensional SPH model was assessed by analysing the simulated flow field under several breaking waves. The local velocities, vorticities, and bed shear stresses were evaluated beneath two plunging solitary waves and a spilling solitary wave. Generally, the characteristics of the simulated flow field were fairly accurate during wave shoaling and wave breaking, less accurate during wave run-up, and inaccurate during wave run-down. The results also hinted at obliquely descending eddies occurring under the breaking plunging waves. However, the three-dimensional eddy structure beneath the breaking waves could not be investigated due to the limited two-dimensional nature of the model setup used in this study.

A well-calibrated SPH wave and hydrodynamic model is an important coastal engineering tool. Thus, this study can serve as a physically based framework for using a two-dimensional SPH model to investigate coastal engineering problems that include wave-structure interactions, wave-run up on beach slopes and sediment transport in the surf zone over a wide range of scales and wave conditions.

CONTENTS

LIST OF FIGURES.....	ix
LIST OF TABLES.....	xix
CHAPTER 1.....	23
1 INTRODUCTION.....	23
1.1 Motivation.....	24
1.2 Research Question	26
1.3 Aims.....	26
1.4 Objectives	26
1.5 Dissertation Outline.....	27
CHAPTER 2.....	29
2 LITERATURE REVIEW.....	29
2.1 Wind-generated waves.....	29
2.2 Wave theory.....	30
2.2.1 Airy waves	30
2.2.2 Stokes waves.....	32
2.2.3 Cnoidal waves.....	32
2.2.4 Solitary waves.....	33
2.3 The wave boundary layer	34
2.4 Wave transformations	35
2.4.1 Wave shoaling	35
2.4.2 Wave breaking.....	37
2.4.3 Links to sediment transport	43
2.5 Wave modelling techniques.....	46
2.5.1 Physical wave models.....	46
2.5.2 Numerical wave models	50
CHAPTER 3.....	53
3 SMOOTHED PARTICLE HYDRODYNAMICS (SPH)	53
3.1 Kernel approximation	53
3.1.1 Smoothing function	54
3.2 Momentum equation and viscous dissipation	56
3.2.1 Artificial viscosity scheme.....	56
3.2.2 Laminar viscosity and sub particle scale (SPS) turbulence scheme	57
3.3 Continuity equation	59
3.4 Equation of state	59
3.5 Density diffusion term.....	60
3.6 Time stepping algorithm	60

3.7	Boundary condition	62
3.7.1	Dynamic boundary condition (DBC)	62
3.8	Important calibration parameters	63
3.8.1	The artificial viscosity coefficient (α)	64
3.8.2	The dimensionless smoothing length ratio (h_{SPH}/dp).....	64
3.8.3	The particle resolution (H/dp)	65
CHAPTER 4	67
4	METHODOLOGY.....	67
4.1	Physical wave model.....	67
4.1.1	Mechanical wave generation	67
4.1.2	Data acquisition	68
4.1.3	Image post-processing.....	69
4.2	Smoothed particle hydrodynamics (SPH) model	70
4.2.1	Model calibration and sensitivity analysis	72
4.2.2	Model performance	74
4.3	Limitations and shortcomings	74
CHAPTER 5	76
5	PHYSICAL MODEL: RESULTS AND DISCUSSION	76
5.1	The physical wave height decay and wave energy dissipation	76
5.2	Spatially varying wave profile	77
5.2.1	Phase one: offshore wave profile	77
5.2.2	Phase two: shoaling wave profile	79
5.2.3	Phase three: breaking wave profile	81
5.2.4	Phase four: breaking wave profile	83
5.2.5	Final wave profiles	85
5.3	Temporal evolution of the wave surface	87
CHAPTER 6	90
6	SPH MODEL: RESULTS AND DISCUSSION	90
6.1	Model calibration and sensitivity analysis	91
6.1.1	Calibrated model parameters	91
6.1.2	Case dependency of calibrated parameters	96
6.1.3	Influence of the artificial viscosity coefficient (α)	108
6.1.4	Influence of the dimensionless smoothing length ratio (h_{SPH}/dp).....	111
6.1.5	Influence of the particle resolution (H/dp)	114
6.2	Model performance	119
6.2.1	Case one: plunging solitary wave ($S_0=0.118$)	119
6.2.2	Case two: plunging solitary wave ($S_0=0.078$).....	138

6.2.3	Case three: spilling solitary wave ($S_0=0.019$).....	149
CHAPTER 7		156
7	CONCLUSION	156
7.1	Suitable model parameters	156
7.1.1	Case dependency of calibrated parameters	157
7.1.2	Influence of the artificial viscosity coefficient (α)	159
7.1.3	Influence of the dimensionless smoothing length ratio (h_{SPH}/dp).....	159
7.1.4	Influence of the particle resolution (H/dp)	159
7.2	Model performance	160
7.2.1	Case one: a plunging solitary wave.....	160
7.2.2	Case two: a plunging solitary wave	161
7.2.3	Case three: a spilling solitary wave	161
7.3	Engineering implications	161
7.4	Recommendations for further research	163
REFERENCES.....		164
8	REFERENCES.....	164
A.	APPENDIX B	172
B.	APPENDIX B	180
C.	APPENDIX C	184

LIST OF FIGURES

Figure 1-1: Schematic of the wave action zones that form the nearshore zone and the transformation of waves advancing into shallow water (after Komar, 1998).....	23
Figure 2-1: The a) spatially varying wave profile measured over the direction of wave propagation at a single moment in time, and the b) time varying wave profile measured over a specific time period at a single location. (after Bosboom and Stive, 2012).....	30
Figure 2-2: The typical wave profile of an (a) Airy wave, a (b) Stokes wave, a (c) cnoidal wave, and a (d) solitary wave (after Le Méhauté, 1976).	30
Figure 2-3: A simulated spatially varying wave profile at an instant in time using a) a sinusoidal wavemaker and b) a sinusoidal wavemaker with an added second-order wavemaker motion to eliminate the second-order free waves (after Dong and Huang, 2004).	32
Figure 2-4: Schematic of the characteristic horizontal velocity profiles for a) a pre-passing solitary wave (before the wave crest passes the measuring section), and b) a post-passing solitary wave (after the wave crest passes the measuring section), propagating over a horizontal bed (after Lin et al., 2010).....	34
Figure 2-5 The transformation of a nearly sinusoidal wave profile in deep water to positively skewed and asymmetric prior to breaking (after Rocha et al., 2014).	36
Figure 2-6: The wave profile of different breaker types on a smooth, impermeable slope (adapted Bosboom and Stive, 2012).	38
Figure 2-7: Schematic of some of the possible modes of splash-up after the plunge point of a plunging wave hits the water surface (after Peregrine et al., 1983). The shaded area denotes the falling jet	38
Figure 2-8: Schematic representation of the two-dimensional transverse vortices with horizontal axes (horizontal eddies) and the three-dimensional vortices (obliquely descending eddies) beneath breaking waves (after Nadaoka, 1986).....	43
Figure 3-1 The SPH particle approximations in a two-dimensional numerical domain (after Liu and Liu, 2010). The smoothing function W interpolates the physical quantities at a particle i using averaged summations over particles j within the support domain. The two-dimensional domain has a surface S and a cut-off distance of $\kappa(h_{SPH})_i$	54
Figure 3-2 The SPH kernel functions (W) available in DualSPHysics only consider neighbouring particles within a maximum radius of $2h_{SPH}$ (Adapted Alonso et al., 2020).....	55

Figure 4-1: Schematic side view of the laboratory wave tank and camera positioning (FOV 1 and FOV 2) used to record physical wave data of a plunging solitary wave.67

Figure 4-2: Location of the simulated free surface. The SPH model computes the numerical mass of water particles at different vertical positions using the mass values of neighbouring water particles, and the surface is defined at the vertical (z) point coordinate for which the mass of a water particle is half of a reference mass (adapted Alonso et al., 2020).72

Figure 5-1: The average wave height (H) and wave energy dissipation (D) over the horizontal wave tank section for ten runs of a plunging solitary wave ($S_0=0.118$) in a laboratory wave tank. The x-axis is the horizontal distance from the wave paddle.76

Figure 5-2: The spatially varying wave profile of a plunging solitary wave ($S_0=0.118$) when the wave crest is 5 m from the wave paddle in a laboratory wave tank. The image shows a) one of ten instantaneous waves recorded in the laboratory wave tank with the digitised wave profile overlaid, b) the digitised wave profile of ten instantaneous waves recorded in a laboratory wave tank, and c) the average wave profile of ten instantaneous waves recorded in a laboratory wave tank with the standard deviation. The x-axis is the horizontal distance from the wave paddle.78

Figure 5-3: The average spatially varying wave profile of a plunging solitary wave ($S_0=0.118$) compared to the instantaneous spatially varying wave profiles with the a) highest and b) lowest correlation to the average, when the wave crest is 5 m from the wave paddle in a laboratory wave tank. The x-axis is the horizontal distance from the wave paddle.79

Figure 5-4: The spatially varying wave profile of a plunging solitary wave ($S_0=0.118$) at 0.16 s before wave impingement on a plane beach slope in a laboratory wave tank. The image shows a) one of ten instantaneous waves recorded in the laboratory wave tank with the digitised wave profile overlaid, b) the digitised wave profile of ten instantaneous waves recorded in a laboratory wave tank, and c) the average wave profile of ten instantaneous waves recorded in a laboratory wave tank with the standard deviation. The x-axis is the horizontal distance from the wave paddle. ..80

Figure 5-5: The average spatially varying wave profile of a plunging solitary wave ($S_0=0.118$) compared to the instantaneous spatially varying wave profiles with the a) highest and b) lowest correlation to the average profile, at 0.16 s before wave impingement on a beach slope in a laboratory wave tank. The x-axis is the horizontal distance from the wave paddle.81

- Figure 5-6: The spatially varying wave profile of a plunging solitary wave ($S_0=0.118$) at 0.08 s before wave impingement on a plane beach slope in a laboratory wave tank. The image shows a) one of ten instantaneous waves recorded in the laboratory wave tank with the digitised wave profile overlaid, b) the digitised wave profile of ten instantaneous waves recorded in a laboratory wave tank, and c) the average wave profile of ten instantaneous waves recorded in a laboratory wave tank with the standard deviation. The x-axis is the horizontal distance from the wave paddle. ...82
- Figure 5-7: The average spatially varying wave profile of a plunging solitary wave ($S_0=0.118$) compared to the instantaneous spatially varying wave profiles with the a) highest and b) lowest correlation to the average profile, at 0.08 s before wave impingement on a beach slope in a laboratory wave tank. The x-axis is the horizontal distance from the wave paddle.83
- Figure 5-8: The spatially varying wave profile of a plunging solitary wave ($S_0=0.118$) at 0.04 s before wave impingement on a plane beach slope in a laboratory wave tank. The image shows a) one of ten instantaneous waves recorded in the laboratory wave tank with the digitised wave profile overlaid, b) the digitised wave profile of ten instantaneous waves recorded in a laboratory wave tank, and c) the average wave profile of ten instantaneous waves recorded in a laboratory wave tank with the standard deviation. The x-axis is the horizontal distance from the wave paddle. ...84
- Figure 5-9: The average spatially varying wave profile of a plunging solitary wave ($S_0=0.118$) compared to the instantaneous spatially varying wave profiles with the a) highest and b) lowest correlation to the average profile, at 0.04 s before wave impingement on a beach slope in a laboratory wave tank. The x-axis is the horizontal distance from the wave paddle.85
- Figure 5-10: The spatially varying wave profile of a plunging solitary wave ($S_0=0.118$) in a laboratory wave tank at a) the instant the wave crest is 5 m from the wave paddle, b) 0.16 s before wave impingement on the beach slope, c) 0.08 s before wave impingement on the beach slope, and d) 0.04 s before wave impingement on the beach slope. The x-axis is the horizontal distance from the wave paddle.86
- Figure 5-11: The time varying wave elevation (η) profile of a plunging solitary wave ($S_0=0.118$), at 1.238 m from the toe of the beach slope in a laboratory wave tank. The image shows a) the digitised wave profile of ten instantaneous waves recorded in a laboratory wave tank and b) the average wave profile of ten instantaneous waves recorded in a laboratory wave tank with the standard deviation., The x-axis is the time since the paddle motion stops, and the wave leaves the paddle.88
- Figure 5-12: The average time varying wave profile of a plunging solitary wave ($S_0=0.118$) compared to the instantaneous time varying wave profiles with the a) highest and b)

lowest correlation to the average wave profile, at 1.238 m from the toe of the beach slope in a laboratory wave tank. The x-axis is the time since the paddle motion stops, and the wave leaves the paddle.89

Figure 6-1: The numerical wave energy dissipation (D) of a plunging solitary wave ($S_0=0.118$), using the combinations of α , h_{SPH}/dp , and H/dp in Table 6-1, in comparison to measured data, over the horizontal wave tank section.92

Figure 6-2: The simulated time varying wave surface elevation (η/h_0) profile of a plunging solitary wave ($S_0=0.118$), using the combinations of α , h_{SPH}/dp , and H/dp in Table 6-2, compared to measured data, at $X=8.25$ on the beach slope. The measured profile is annotated at times $T=6$, $T=7$, $T=8$, $T=10$, and $T=12$93

Figure 6-3 The simulated spatially varying wave (z/h_0) profile of a plunging solitary wave ($S_0=0.118$), using the combinations of α , h_{SPH}/dp , and H/dp in Table 6-3, compared to measured data, at the fourth defined phase of evolution, one timestep before wave impingement on the beach slope.95

Figure 6-4: The simulated spatially varying wave (z) profile of a plunging solitary wave ($S_0=0.118$), using the standard artificial viscosity approach, compared to measured data, at four phases of wave evolution in a wave tank.97

Figure 6-5 The simulated spatially varying wave (z) profile of a plunging solitary wave ($S_0=0.118$), using the laminar viscosity and sub particle turbulence (SPS) scheme, compared to measured data, at four defined phases of evolution in a wave tank. 98

Figure 6-6: The simulated time varying wave elevation (η/h_0) profile, using the standard artificial viscosity scheme and the laminar viscosity and SPS turbulence scheme, compared to measured data, at $X=8.25$ on the beach slope. The measured wave profile is annotated at $T=6$, $T=7$, $T=8$, $T=10$, and $T=12$99

Figure 6-7: The simulated wave profile of a solitary wave with a relative wave height (H/h_0) of 0.8 and slope parameter (S_0) of 0.136, propagating over a 1/10 beach slope (test 1 in Table 6-5) in space and time. 102

Figure 6-8: The simulated wave profile of a solitary wave with a relative wave height (H/h_0) of 0.4 and slope parameter (S_0) of 0.078, propagating over a 1/10 beach slope (test 2 in Table 6-5) in space and time. 103

Figure 6-9: The simulated wave profile of a solitary wave with a relative wave height (H/h_0) of 0.6 and slope parameter (S_0) of 0.192, propagating over a 1/5 beach slope (test 3 in Table 6-5) in space and time. 104

Figure 6-10: The simulated wave profile of a solitary wave with a relative wave height (H/h_0) of 0.6 and slope parameter (S_0) of 0.048, propagating over a 1/20 beach slope (test 4 in Table 6-5) in space and time. 105

Figure 6-11: The simulated wave profile of a solitary wave with a relative wave height (H/h_0) of 0.6 and slope parameter (S_0) of 0.024, propagating over a 1/40 beach slope (test 5 in Table 6-5) in space and time..... 106

Figure 6-12: The simulated wave profile of a solitary wave with a relative wave height (H/h_0) of 0.6 and slope parameter (S_0) of 0.019, propagating over a 1/50 beach slope (test 6 in Table 6-5) in space and time..... 107

Figure 6-13: Simulated results of a plunging solitary wave ($S_0=0.118$), using various α , compared to measured data. The image compares the (a) numerical and measured wave energy dissipation (D) over the horizontal wave tank section, the b) simulated and measured spatially varying wave (z/h_0) profiles, at a defined phase of evolution, one timestep before wave impingement on the beach slope, and the c) simulated and measured time varying wave elevation (η/h_0) profiles, at $X=8.25$ on the beach slope. 109

Figure 6-14: The simulated wave surface (z) of a plunging solitary wave ($S_0=0.118$) using various α , compared to measured data in space and time, as well as the simulated water particles in the numerical domain, using various α . The parameters $h_{SPH}/dp=3$ and $H/dp=90$ are constant. 110

Figure 6-15: The influence of various α (in combination with a range of h_{SPH}/dp and H/dp) on the correlation coefficient ($p_{x\eta}$) between the simulated and measured time varying wave elevation (η/h_0) profiles, at $X=8.25$ on the beach slope. 111

Figure 6-16: Simulated results of a plunging solitary wave ($S_0=0.118$), using various h_{SPH}/dp , compared to measured data. The image compares the (a) numerical and measured wave energy dissipation (D) over the horizontal wave tank section, the b) simulated and measured spatially varying wave (z/h_0) profiles, at a defined phase of evolution, one timestep before wave impingement on the beach slope, and the c) simulated and measured time varying wave elevation (η/h_0) profiles, at $X=8.25$ on the beach slope..... 112

Figure 6-17: The simulated wave surface (z) of a plunging solitary wave ($S_0=0.118$) using various h_{SPH}/dp , compared to measured data in space and time, as well as the simulated water particles in the numerical domain, using various h_{SPH}/dp . The parameters $\alpha=0.1$ and $H/dp=90$ are constant..... 113

Figure 6-18: The influence of various h_{SPH}/dp (in combination with a range of α and H/dp) on the correlation coefficient ($p_{x\eta}$) between the simulated and measured time varying wave elevation (η/h_0) profiles, at $X=8.25$ on the beach slope. 114

Figure 6-19: Simulated results of a plunging solitary wave ($S_0=0.118$), using various H/dp , compared to measured data. The image compares the (a) numerical and measured wave energy dissipation (D) over the horizontal wave tank section, the b) simulated

and measured spatially varying wave (z/h_0) profiles, at a defined phase of evolution, one timestep before wave impingement on the beach slope, and the c) simulated and measured time varying wave elevation (η/h_0) profiles, at $X=8.25$ on the beach slope. 115

Figure 6-20: The simulated wave surface (z) of a plunging solitary wave ($S_0=0.118$) using various H/dp , compared to measured data in space and time, as well as the simulated water particles in the numerical domain, using various H/dp . The parameters $\alpha=0.1$ and $h_{SPH}/dp=3$ are constant. 117

Figure 6-21: The influence of various H/dp (in combination with a range of α and h_{SPH}/dp) on the correlation coefficient (p_{η}) between the simulated and measured time varying wave elevation (η/h_0) profiles, at $X=8.25$ on the beach slope. 118

Figure 6-22: The simulated spatially varying velocity magnitude beneath a plunging solitary wave ($S_0=0.118$), propagating over a 1/10 beach slope, during the interval $T=5.67$ to $T=6.33$. The velocity vectors are overlaid as a quiver plot. 120

Figure 6-23: The simulated spatially varying vorticity beneath a plunging solitary wave ($S_0=0.118$), propagating over a 1/10 beach slope, during the interval $T=5.67$ to $T=6.33$. The velocity vectors are overlaid as a quiver plot. 121

Figure 6-24: The simulated spatially varying velocity magnitude beneath a plunging solitary wave ($S_0=0.118$), propagating over a 1/10 beach slope, during the interval $T=6.33$ to $T=7.33$. The velocity vectors are overlaid as a quiver plot. 124

Figure 6-25: The simulated spatially varying vorticity beneath a plunging solitary wave ($S_0=0.118$), propagating over a 1/10 beach slope, during the interval $T=6.33$ to $T=7.33$. The velocity vectors are overlaid as a quiver plot. 125

Figure 6-26: The simulated spatially varying velocity vectors and vorticity, near the bed, beneath a plunging solitary wave ($S_0=0.118$), propagating over a 1/10 beach slope, during the interval $T=6$ to $T=12$ 127

Figure 6-27: The simulated spatially varying velocity magnitude beneath a plunging solitary wave ($S_0=0.118$), propagating over a 1/10 beach slope, during the interval $T=14$ to $T=20$. The velocity vectors are overlaid as a quiver plot. 128

Figure 6-28: The simulated spatially varying vorticity beneath a plunging solitary wave ($S_0=0.118$), propagating over a 1/10 beach slope, during the interval $T=14$ to $T=20$. The velocity vectors are overlaid as a quiver plot. 129

Figure 6-29: The simulated spatially varying velocity vectors and vorticity, near the bed, beneath a plunging solitary wave ($S_0=0.118$), propagating over a 1/10 beach slope, during the interval $T=14$ to $T=20$ 131

Figure 6-30: The simulated spatially varying velocity magnitude beneath a plunging solitary wave ($S_0=0.118$), propagating over a 1/10 beach slope, during the interval $T=30$ to $T=34$. The velocity vectors are overlaid as a quiver plot.	133
Figure 6-31: The simulated spatially varying vorticity beneath a plunging solitary wave ($S_0=0.118$), propagating over a 1/10 beach slope, during the interval $T=30$ to $T=34$. The velocity vectors are overlaid as a quiver plot.	134
Figure 6-32 The simulated spatially varying velocity vectors and vorticity, near the bed, beneath a plunging solitary wave ($S_0=0.118$), propagating over a 1/10 beach slope, during the interval $T=24$ to $T=28$ and $T=38$ to $T=40$	136
Figure 6-33: The a) spatially varying peak bed shear stress ($\tau_{b(\text{peak})}$), and the b) time varying bed shear stress (τ_b) at $X=10.1$ on the beach slope, as a plunging solitary wave ($S_0=0.118$), propagates over a 1/10 beach slope, during the interval $T=0$ to $T=40$	137
Figure 6-34: The simulated spatially varying wave (z) profile of a plunging solitary wave ($S_0=0.078$), propagating over a 1/10 beach slope, at $T=7.5$, using $\alpha=0$, $h_{\text{SPH}}/dp=3$ and $H/dp=50$	138
Figure 6-35: The simulated time varying wave elevation (η/h_0) profile of a plunging solitary wave ($S_0=0.078$), propagating over a 1/10 beach slope, using $\alpha=0$, $h_{\text{SPH}}/dp=3$, and $H/dp=50$	139
Figure 6-36: The simulated spatially varying velocity magnitude beneath a plunging solitary ($S_0=0.078$), propagating over a 1/10 beach slope, during the interval $T=7.5$ to $T=9$. The velocity vectors are overlaid as a quiver plot.	140
Figure 6-37: The simulated spatially varying vorticity beneath a plunging solitary wave ($S_0=0.078$), propagating over a 1/10 beach slope, during the interval $T=7.5$ to $T=9$. The velocity vectors are overlaid as a quiver plot.	141
Figure 6-38: The simulated spatially varying vorticity and velocity vectors, near the bed, beneath a plunging solitary wave ($S_0=0.078$), propagating over a 1/10 beach slope, during the interval $T=6$ to $T=12$	143
Figure 6-39: The simulated spatially varying velocity magnitude of a plunging solitary ($S_0=0.078$), propagating over a 1/10 beach slope, at $T=15$. The velocity vectors are overlaid as a quiver plot.	144
Figure 6-40: The simulated spatially varying vorticity of a plunging solitary ($S_0=0.078$), propagating over a 1/10 beach slope, at $T=15$. The velocity vectors are overlaid as a quiver plot.	144
Figure 6-41 The simulated spatially varying vorticity and velocity vectors, near the bed, beneath a plunging solitary wave ($S_0=0.078$), propagating over a 1/10 beach slope, during the interval $T=14$ to $T=20$	145

Figure 6-42: The simulated spatially varying velocity magnitude beneath a plunging solitary ($S_0=0.078$), propagating over a 1/10 beach slope, at $T=38$. The velocity vectors are overlaid as a quiver plot.	146
Figure 6-43: The simulated spatially varying vorticity beneath a plunging solitary ($S_0=0.078$), propagating over a 1/10 beach slope, at $T=38$. The velocity vectors are overlaid as a quiver plot.	146
Figure 6-44 The simulated spatially varying vorticity and velocity vectors, near the bed, beneath a plunging solitary wave ($S_0=0.078$), propagating over a 1/10 beach slope during the intervals $T=24$ to $T=28$ and $T=38$ to $T=40$	147
Figure 6-45: The a) spatially varying peak bed shear stress ($\tau_{b(\text{peak})}$) and the b) time varying bed shear stress (τ_b) at $X=10.5$ on the beach slope, as a plunging solitary wave ($S_0=0.078$), propagates over a 1/10 beach slope, during the interval $T=0$ to $T=40$	148
Figure 6-46 The simulated spatially varying velocity magnitude beneath a spilling solitary wave ($S_0=0.019$), propagating over a 1/50 beach slope, during the interval $T=24.33$ to $T=28$. The velocity vectors are overlaid as a quiver plot.	151
Figure 6-47 The simulated spatially varying vorticity beneath a spilling solitary wave ($S_0=0.019$), propagating over a 1/50 beach slope, during the interval $T=24.33$ to $T=28$. The velocity vectors are overlaid as a quiver plot.	152
Figure 6-48: The a) spatially varying peak bed shear stress ($\tau_{b(\text{peak})}$), and the b) time varying bed shear stress (τ_b) at $X=28.9$ on the beach slope, as a spilling solitary wave ($S_0=0.019$), propagates over a 1/50 beach slope, during the interval $T=0$ to $T=40$	154
Figure A-1: The numerical wave energy dissipation (D) of a plunging solitary wave ($S_0=0.118$), using various combinations of α , h_{SPH}/dp , and H/dp , compared to measured data, over the horizontal wave tank section.	172
Figure A-2 The simulated spatially varying wave (z/h_0) profile of a plunging solitary wave ($S_0=0.118$), using various combinations of α , h_{SPH}/dp , and H/dp , compared to measured data, at the first defined phase of evolution, when the solitary wave crest is at $x/h_0=33.3$ from the wave paddle.	173
Figure A-3: The simulated spatially varying wave (z/h_0) profile of a plunging solitary wave ($S_0=0.118$), using various combinations of α , h_{SPH}/dp , and H/dp , compared to measured data, at the third defined phase of evolution, four timesteps before wave impingement on the beach slope.	174
Figure A-4: The simulated spatially varying wave (z/h_0) profile of a plunging solitary wave ($S_0=0.118$), using various combinations of α , h_{SPH}/dp , and H/dp , compared to	

measured data, at the third defined phase of evolution, two timesteps before wave impingement on the beach slope.....	175
Figure A-5: The simulated spatially varying wave (z/h_0) profile of a plunging solitary wave ($S_0=0.118$), using various combinations of α , h_{SPH}/dp , and H/dp , compared to measured data, at the fourth defined phase of evolution, one timestep before wave impingement on the beach slope.....	176
Figure A-6: The simulated time varying wave surface elevation (η/h_0) profile of a plunging solitary wave ($S_0=0.118$), using various combinations of h_{SPH}/dp and H/dp , compared to measured data, at $X=8.25$ on the beach slope. The measured profile is annotated at times $T=6$, $T=7$, $T=8$, $T=10$, and $T=12$	177
Figure A-7: The simulated time varying wave surface elevation (η/h_0) profile of a plunging solitary wave ($S_0=0.118$), using various combinations of α and H/dp , compared to measured data, at $X=8.25$ on the beach slope. The measured profile is annotated at times $T=6$, $T=7$, $T=8$, $T=10$, and $T=12$	178
Figure A-8: The simulated time varying wave surface elevation (η/h_0) profile of a plunging solitary wave ($S_0=0.118$), using various combinations of α and h_{SPH}/dp , compared to measured data, at $X=8.25$ on the beach slope. The measured profile is annotated at times $T=6$, $T=7$, $T=8$, $T=10$, and $T=12$	179
Figure B-1: The measured spatially varying velocity vectors, near the bed, under a plunging solitary wave ($S_0=0.078$), propagating over a 1/10 beach slope, during the interval $T=6$ to $T=12$ (after Lin et al., 2015).....	180
Figure B-2: The measured spatially varying velocity vectors near the bed, under a plunging solitary wave ($S_0=0.078$), propagating over a 1/10 beach slope, during the interval $T=14$ to $T=20$. (after Lin et al., 2015).....	181
Figure B-3: The measured spatially varying velocity vectors near the bed, under a plunging solitary wave ($S_0=0.078$), propagating over a 1/10 beach slope during the intervals $T=24$ to $T=28$ and $T=38$ to $T=40$ (after Lin et al., 2015).	182
Figure B-4: A version of Shields diagram showing the grain diameter versus the shear velocity (u_*) required to initiate the movement of quartz density material ($\rho_s=2.65$ g/cm ³) in water at 20° C (adapted Miller and Komar, 1977).	183
Figure C-1 The measured spatially varying wave (z) profile of a plunging solitary wave ($S_0=0.078$), propagating over a 1/10 beach slope (after Lin et al., 2015). Images (a–d) show four runs for the spatial evolution of free surface elevation before breaking, and (e) compares the free surface elevations among the four runs.	184
Figure C-2: The measured time varying wave elevation (η/h_0) profile of a plunging solitary wave ($S_0=0.078$), propagating over a 1/10 beach slope, at $X=8.25$ (after Lin et al., 2015).....	185

Figure C-3: A non-dimensional timeline showing the complete evolution of a plunging solitary wave ($S_0=0.078$), propagating over a 1/10 beach slope (after Lin et al., 2015).
..... 185

LIST OF TABLES

Table 2-1: The Iribarren number (ζ_0) range associated with different breaker types.....	40
Table 2-2: The values of the wave breaking criterion S_0 associated with each breaker types	40
Table 4-1: Wave characteristics of a solitary wave generated in a laboratory wave tank.	68
Table 4-2: Camera settings used to record physical wave data of a plunging solitary wave in a laboratory wave tank.	69
Table 4-3: The selected SPH parameters and calibrated SPH parameters for a two-dimensional SPH model using DualSPHysics (Crespo et al., 2015a).	71
Table 4-4: The values considered for each SPH calibration parameter.	72
Table 4-5: Different cases of breaking waves used to test the performance of the SPH model. The relative wave height (H/h_0), beach slope ($\tan(\beta)$), slope parameter (S_0), and associated type of wave breaking are shown for the various cases.	73
Table 5-1: The peak wave elevation (η_{peak}) of a plunging solitary wave above the still water depth (h_0) and the location of this peak value (x_{peak}) at the four phases of evolution in a laboratory wave tank shown in Figure 5-10 (a-d).	86
Table 6-1: Trialled combinations of α , h_{SPH}/dp , and H/dp that yielded a numerical wave energy dissipation (D) within 5% of the measured value ($D \approx 44\%$) of a plunging solitary wave ($S_0=0.118$) at $x/h_0=60$ from the wave paddle.....	91
Table 6-2: Trialled combinations of α , h_{SPH}/dp , and H/dp that yielded a simulated time varying wave elevation (η/h_0) profile similar ($p_{x\eta} \geq 0.98$) to measured data of a plunging solitary wave ($S_0=0.118$), at $X=8.25$ on the beach slope.....	92
Table 6-3: Trialled combinations of α , h_{SPH}/dp , and H/dp that yielded a simulated spatially varying wave profile similar ($p_{x\eta} \geq 0.98$) to measured data of a plunging solitary wave ($S_0=0.118$), at four phases of evolution in the wave tank. The correlation coefficient ($p_{x\eta}$) denotes the similarity between the simulated and measured wave profiles at the fourth phase of evolution, one model time step before wave impingement on the beach slope.....	94
Table 6-4: A quantitative comparison between the simulated and measured spatially varying plunging wave profiles in Figure 6-4(d) and Figure 6-5(d). The correlation coefficient ($p_{x\eta}$) between the simulated and measured spatially varying wave profiles, the peak wave elevation (η_{peak}) above the still water depth (h_0), and the location of the peak wave elevation in the wave tank (x_{peak}) are shown.	99

Table 6-5: The relative wave height (H/h_0), beach slope ($\tan(\beta)$), slope parameter (S_0), and associated breaker type, for various simulated solitary waves, including the original plunging solitary wave ($S_0=0.118$), used to calibrate the SPH model parameters. The number of simulated water particles (N) in the numerical domain, and computation runtime for a 15 s simulation, are also shown for each case.	101
Table 6-6: The maximum simulated velocity and vorticity under a plunging solitary wave ($S_0=0.118$), propagating over a 1/10 beach slope, during the interval $T=5.33$ to $T=7.33$	126
Table 6-7: The maximum simulated velocity and vorticity under a plunging solitary wave ($S_0=0.118$), propagating over a 1/10 beach slope, during the interval $T=15$ to $T=20$	130
Table 6-8: The maximum simulated velocity and vorticity under a plunging solitary wave ($S_0=0.118$), propagating over a 1/10 beach slope, during the interval $T=30$ to $T=34$	135
Table 6-9: The maximum onshore and offshore directed bed shear stresses ($\tau_{b(max)}$) and shear velocities ($u^*_{(max)}$), the time they occur, and their position on the beach slope, as a plunging solitary wave ($S_0=0.118$), propagates over a 1/10 beach slope, during the interval $T=0$ to $T=40$	137
Table 6-10: The maximum simulated velocity and vorticity under a plunging solitary wave ($S_0=0.078$), propagating over a 1/10 beach slope, during the interval $T=7.5$ to $T=9$	142
Table 6-11: The maximum onshore and offshore directed bed shear stresses ($\tau_{b(max)}$) and shear velocities ($u^*_{(max)}$), the time they occur, and their position on the beach slope, as a plunging solitary wave ($S_0=0.078$), propagates over a 1/10 beach slope, during the interval $T=0$ to $T=40$	148
Table 6-13: The maximum velocity and vorticity under a spilling solitary wave ($S_0=0.019$), propagating over a 1/50 beach slope, during the interval $T=24.33$ to $T=28$	153
Table 6-14: The maximum onshore and offshore directed bed shear stresses ($\tau_{b(max)}$) and shear velocities ($u^*_{(max)}$), the time they occur, and their position on the beach slope, as a spilling solitary wave ($S_0=0.019$), propagates over a 1/50 beach slope, during the interval $T=0$ to $T=60$	154

LIST OF SYMBOLS

$a =$	Artificial viscosity coefficient
$\beta =$	Seafloor angle, Acceleration skewness coefficient
$\delta =$	Wave boundary layer thickness [m]
$\zeta =$	Wave paddle position [m]
$\eta =$	Wave elevation above the still water depth [m]
$\Pi_{ab} =$	Artificial viscosity term
$\xi =$	Offshore Iribarren Number
$\nu_0 =$	Kinematic viscosity [$\text{m}^2 \text{s}^{-1}$]
$\mu =$	Dynamic viscosity [$\text{Pa}\cdot\text{s}$]
σ	Standard deviation
$\vec{\tau}$	SPS stress tensor [N/m^2]
$\tau_b =$	Bed shear stress [N/m^2]
$\tau_{b(\text{peak})} =$	Peak bed shear stress [N/m^2]
$\tau_{b(\text{max})} =$	Maximum bed shear stress [N/m^2]
$c =$	Wave celerity [m/s], speed of sound [m/s]
$D =$	Wave energy dissipation [%]
$dp =$	Interparticle spacing [m]
$E =$	Wave energy [J]
$Fr =$	Froude number
$g =$	Gravitational acceleration [m/s^2]
$H =$	Wave height [m]
$H_0 =$	Offshore wave height [m]
$h =$	Water depth [m]
$h_0 =$	Still water depth [m]
$h_{\text{SPH}} =$	Dimensionless smoothing length ratio
$k =$	Wave number
$L =$	Wave length [m]
$L_0 =$	Offshore wave length [m]
$m =$	Mass [kg]

$P =$	Pressure [Pa]
$\rho =$	Density [kg/m^3]
$p_{x\eta} =$	Correlation coefficient
$R =$	Velocity skewness coefficient
$\mathbf{r} =$	Position vector [m]
$S =$	Wave paddle stroke [m]
$S_0 =$	Offshore slope parameter
$T =$	Non-dimensional time coordinate
$T_p =$	The wave period [s]
$t =$	Time [s]
$Ur =$	Ursell number
$u =$	Horizontal velocity [m/s^2]
$u_* =$	Shear velocity [cm/s^2]
$u_{*(\text{peak})} =$	Peak shear velocity [m/s^2]
$u_{*(\text{max})} =$	Maximum shear velocity [m/s^2]
$u_\infty =$	Free stream velocity [m/s^2]
$\mathbf{v} =$	Velocity vector [m/s^2]
$W =$	Interpolation or smoothing function
$w =$	Angular frequency [rad s^{-1}], vorticity [s^{-1}]
$X =$	Non-dimensional distance coordinate
$x =$	Horizontal distance coordinate [m]
$z =$	Vertical distance coordinate [m]

CHAPTER 1

INTRODUCTION

Wave breaking drives complex flows that transport sediment either offshore or onshore. Therefore, understanding the structure of the nearshore flow field is fundamental to the development and application of sediment transport models and many other aspects of coastal engineering (Doering and Bowen, 1995). However, the highly non-linear nature and large surface deformations associated with breaking waves lead to complexities in simulating breaking wave-induced flows. Many efforts are actively being made to improve wave theory, numerical modelling methods, and integrated modelling systems. This study explores the capability of a Lagrangian smoothed particle hydrodynamics (SPH) model for accurately simulating the free surface of breaking waves and the flow field under breaking waves in the nearshore zone. Figure 1-1 shows the nearshore zone of a beach and the three smaller zones of wave action comprising the nearshore zone, the breaker zone, the surf zone, and the swash zone.

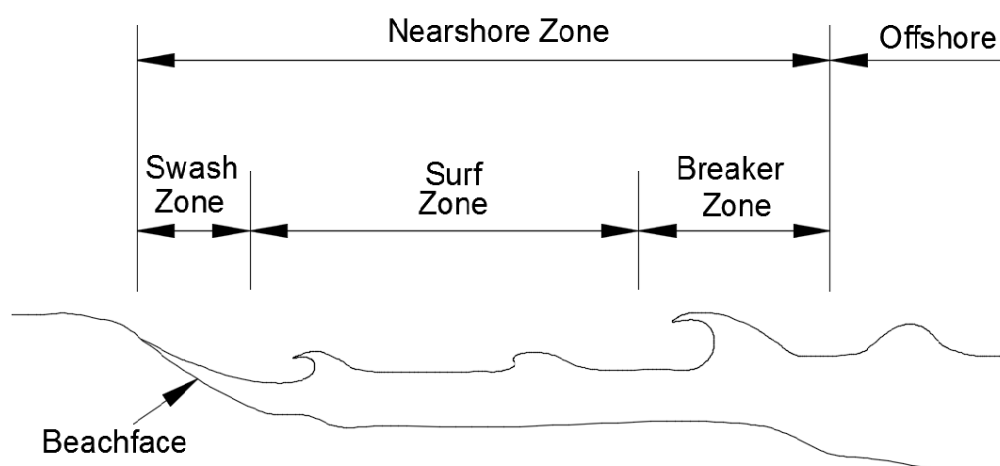


Figure 1-1: Schematic of the wave action zones that form the nearshore zone and the transformation of waves advancing into shallow water (after Komar, 1998).

Wind-generated waves form offshore and propagate into the breaker zone (Figure 1-1), where the water depth decreases. As a result, waves start to shoal, steepen, become unstable, and eventually break, giving rise to the surf zone (Sou and Yeh, 2011).

The surf zone (Figure 1-1) is characterised by incident wind-generated waves irreversibly transforming into motions of different scales and types (Sou and Yeh, 2011). Broken waves in the surf zone continue advancing towards the shore as swash, a thin layer of water that runs up the beach slope until the point of maximum run-up and then runs down again (Battjes, 1974).

The swash zone (Figure 1-1) is traditionally defined as the inner part of the surf zone wherein wave run-up occurs periodically (Sou and Yeh, 2011).

Wave breaking is responsible for the majority of the sediment suspension in the surf zone driven by shear stresses along the bottom and eddies associated with breaking waves (Miller, 1976; Zhang and Sunamura, 1990). However, the hydrodynamics in the surf and swash zones are complex and still not fully understood, despite significantly impacting coastal regions (Sou et al., 2010).

1.1 Motivation

Breaking waves drive sediment transport in the surf zone and, therefore, directly govern beach transformation (Baldock et al., 2010; LeClaire and Ting, 2017). The driving forces and fluid motions of breaking waves are complex and can lead to the erosion and sometimes destruction of coastlines and coastal structures. Therefore, there is a need to understand, predict, and model the breaking wave-induced flow field structure to improve sediment transport forecasting.

Many studies on sediment transport in the surf zone show strong evidence that breaking wave-induced turbulence reaches the sea bed and drives sediment suspension (e.g., Nielson, 1984; Sato et al., 1990; Zhang and Sunamura, 1995; Beach and Sternberg, 1996; Voulgaris and Collins, 2000; Okayasu et al., 2004; Scott et al. 2009; Aagaard and Hughes, 2010; Yoon and Cox 2012). The breaking wave-induced turbulence is associated with irregular, fluctuating, and unpredictable motions comprising small eddies that propagate in the flow (Mukaro et al., 2010).

Previous studies emphasise that the shape and position of breaking waves in the surf zone influence the amount of sediment in suspension during wave breaking (e.g., Brenninkmeyer, 1974, 1976; Kana 1977, 1978; Inman et al., 1980; Shibayama and Horikawa, 1982; Beach and Sternberg, 1996). However, despite these significant advances in research, the role of wave breaking on surf and swash zone hydrodynamics remains unclear and predicting sediment transport remains a formidable challenge (Kimmoun and Branger, 2007, Sou et al., 2010; LeClaire and Ting, 2017).

Wave breaking is non-linear and challenging to model due to strong turbulence and complex boundary conditions, including a dynamic free surface, multi-phased flows, and a mobile bed (Mukaro et al., 2010; Sou et al., 2010). Most models parameterise wave breaking using empirical relations that must be calibrated and do not incorporate the spatial variation of turbulence characteristics within the surf zone (Voulgaris and Collins,

2000. Kimmoun and Branger, 2007; Ting, 2013). Typically, experimental data is used to calibrate the effect of wave breaking on beaches. However, it is difficult to measure the velocity field beneath breaking waves even in well-controlled laboratory environments due to chaotic, thin and multiphase flows. (Kimmoun and Branger, 2007). Additionally, it is inefficient or sometimes unfeasible to measure the evolution of the velocity field over the whole surf zone in the space and time domain (Ting, 2013).

The relatively new Lagrangian SPH method is well suited for simulating multiphase flow problems involving highly non-linear and potentially violent free surface flows such as those associated with breaking waves (De Padova et al., 2014; Wang et al., 2016). SPH was developed for simulating problems in astrophysics and uses a set of arbitrarily distributed particles compared to conventional methods that utilise a grid (Gingold and Monaghan 1977; Lucy 1977). The SPH method allows for more adaptability and versatility than conventional grid-based methods (Gomez-Gesteira et al., 2010). Hence, SPH can precisely capture the water surface during highly non-linear free surface motions, which is often a limitation in standard grid-based methods (Lin, 2008; De Padova et al., 2014). Furthermore, two-dimensional and three-dimensional test cases have shown that SPH is at a mature developmental stage that allows for quantitative comparison with experimental measurements with an accuracy level close to that observed for more conventional grid-based methods (Gomez-Gesteira et al., 2010).

SPH is a powerful method capable of comprehensively describing the complete transformation of breaking waves (De Padova et al., 2009). However, critical analysis of the SPH method for replicating breaking waves is still essential to progress the method to a point where it is viable for accurately modelling a wide range of breaking wave conditions and scenarios. This study adds to the understanding and analysis of the SPH method to resolve better the physical processes controlling breaking waves and sediment transport in the surf zone. This was done by providing a physically based framework for SPH in terms of selecting appropriate parameters for wave breaking applications and the advantages and disadvantages of using SPH to provide information (e.g., velocity, vorticity, and bed shear stress) that cannot easily be obtained from direct experimental observation in the surf zone. This study complements previous studies on SPH (e.g., Dalrymple and Rogers, 2006; Altomare et al., 2015;2017; Crespo et al., 2015a).

1.2 Research Question

Can an SPH model replicate the free surface of nearshore breaking waves and accurately predict the flow field beneath nearshore breaking waves? This overarching research question was investigated by addressing the following:

- What is a suitable choice of SPH parameters for simulating nearshore wave breaking, and are these parameters case sensitive to the type of viscosity treatment used and the type of wave breaking simulated?
- How well does the simulated wave surface of a breaking wave compare to measured data in a laboratory wave tank in the space and time domain?
- How well do the simulated flow field characteristics beneath breaking waves compare to previously measured data?

1.3 Aims

The overarching aim of this study is to show the capability of the mesh-free, Lagrangian SPH method for simulating the free surface of nearshore breaking waves and accurately predicting the flow beneath nearshore breaking waves. Specific aims of the project were established as follows:

- Analyse the role of various SPH parameters in simulating nearshore wave breaking.
- Present a framework for selecting suitable SPH parameters for wave breaking applications to reduce the time needed to find appropriate values in future studies.
- Evaluate the performance of a two-dimensional SPH model for breaking plunging and spilling waves on a plane beach slope with emphasis on the parameters (velocity, vorticity, and local shear stresses) of the wave field that can be used to predict coastal phenomena, namely sediment transport in the surf and swash zones.

1.4 Objectives

The objectives of the project were established as follows:

- Conduct a literature survey to identify flow characteristics of breaking plunging and spilling waves.

- Conduct a laboratory experiment to obtain measured wave profile data of a physical plunging wave breaking wave on a plane beach slope.
- Conduct a literature survey to identify SPH parameters that need to be tuned for wave breaking applications.
- Set up a two-dimensional SPH model following the conditions and breaking wave characteristics of a physical model.
- Systematically calibrate a two-dimensional SPH model using the standard SPH viscous formulation, the artificial viscosity scheme.
- Test the case dependency of calibrated SPH parameters based on the SPH viscous formulation.
- Test the case dependency of calibrated SPH parameters on the type of wave breaking (plunging and spilling waves).
- Perform a sensitivity analysis of a two-dimensional SPH model to various parameters that need to be tuned for wave breaking applications.
- Apply SPH with a suitable choice of parameters to evaluate the flow field beneath breaking plunging and spilling waves on a plane beach and compare the simulated results to experimental data in the space-time domain.

1.5 Dissertation Outline

Chapter 2 presents a literature review that establishes and analyses different wave theories, hydrodynamic concepts, published results, and investigation techniques relevant to this study.

Chapter 3 presents an overview of the SPH method used in this study. An overview of the DualSPHysics formulation is provided, and important calibration parameters regarding wave breaking problems are identified and discussed.

Chapter 4 presents the methodology applied in this study in two parts. The first part of the methodology describes the experimental procedure used to obtain accurate physical data of a plunging wave in a laboratory wave tank. The wave tank set-up, wave characteristics, data acquisition and post-processing steps are outlined. The second part of the methodology presents the steps taken to systematically calibrate, test the sensitivity, and test the performance of a two-dimensional SPH wave breaking model

Chapter 5 presents and discusses the physical model results of a plunging solitary wave in a laboratory wave tank. The results are presented as digital summaries of the physical wave energy dissipation and physical wave profile in the space and time domain.

Chapter 6 presents and discusses the results of a two-dimensional SPH model used to simulate the flow field beneath breaking waves. First, the model calibration and sensitivity to various parameters are presented. Then the model performance is analysed for multiple breaking waves. The SPH model performance is also briefly compared for the two viscosity schemes available in DualSPHysics (Crespo et al., 2015b).

Chapter 7 presents the conclusions drawn from this study. The main findings and practical implications of this study are summarised. Recommendations are also included for further research.

CHAPTER 2

LITERATURE REVIEW

This chapter presents a literature review that establishes and analyses different wave theories, hydrodynamic concepts, published results, and investigation techniques relevant to this study. The first section briefly describes wind-generated waves in the ocean. The following section reviews the classical wave theories used to approximate a wave field. Section 2.3 discusses the wave boundary layer through which the influence of propagating waves is transmitted to the seabed. Section 2.4 examines the wave transformations that occur in the nearshore zone, specifically wave shoaling and wave breaking and the implications for sediment transport in the surf zone. Finally, section 2.5 discusses the application and limitations of common physical and numerical wave modelling techniques.

2.1 Wind-generated waves

Wind blowing on the water surface gives rise to wind-generated waves in the ocean. The speed, direction, duration, and fetch of the wind field determine the wave characteristics. The water depth (h) over the wave generation area also influences the wave characteristics (Bosboom and Stive, 2012). Statistical wave characteristics include the wave height (H), wave period (T_p), and propagation direction.

Sea and swell waves supply the most energy to coastal systems (Bosboom and Stive, 2012). Local wind fields generate irregular sea waves (relatively short and random oscillations of the water surface) (Bosboom and Stive, 2012). However, sea waves that travel long distances away from their area of generation transform into swell waves, which are longer, faster, and more regular than sea waves. Figure 2-1 shows two ways of observing a regular propagating wave. Figure 2-1(a) shows the spatially varying wave profile measured at a single instant in time, and Figure 2-1(b) shows the time varying wave profile measured at a single location. In the figure, η is the wave elevation, L is the wavelength, and c is the wave celerity.

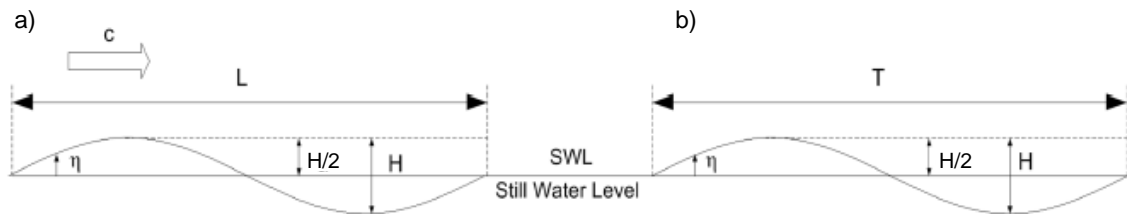


Figure 2-1: The a) spatially varying wave profile measured over the direction of wave propagation at a single moment in time, and the b) time varying wave profile measured over a specific time period at a single location. (after Bosboom and Stive, 2012).

2.2 Wave theory

Wave theory is used to approximate a wave field as a series of regular waves (Figure 2-1). Classical wave theories include Airy (1845), Stokes (1847), cnoidal (e.g., Korteweg and De Vries, 1895), and solitary (e.g., Boussinesq, 1871) wave theories. Existing wave theories assume that the flow is irrotational and the sea bottom is flat and are therefore invalid when rapid changes in the bottom geometry cause change to the wave form and when the wave amplitude is so large that the wave front breaks (Lin, 2008). Figure 2-2 compares the typical wave profiles of a theoretical Airy, Stokes, cnoidal, and solitary wave, which are distinguished by linear or non-linear wave motion.

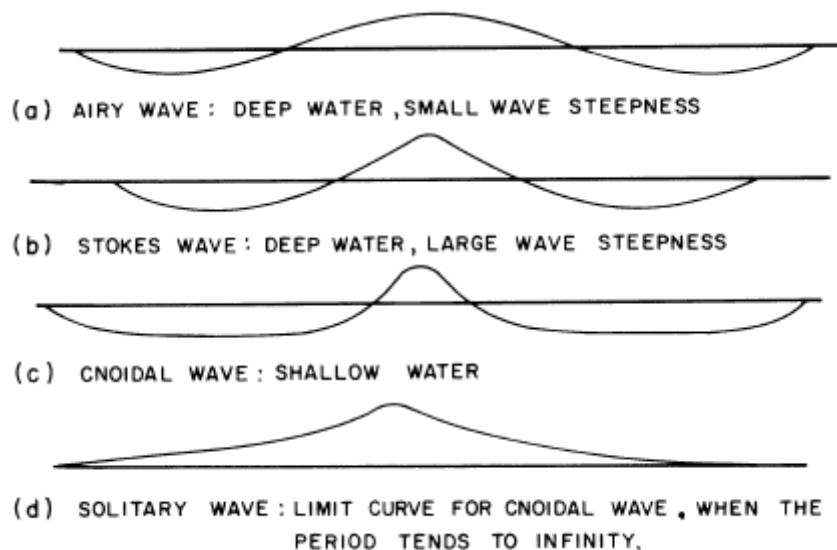


Figure 2-2: The typical wave profile of an (a) Airy wave, a (b) Stokes wave, a (c) cnoidal wave, and a (d) solitary wave (after Le Méhauté, 1976).

2.2.1 Airy waves

Airy (1845) wave theory is the simplest way to describe the displacement of the water surface due to orbital or oscillatory water motions (Young, 2017). The theory assumes that the water particle accelerations are negligibly small when compared to gravity. This implies that the hydrostatic pressure is the only pressure acting on any particle below

the water surface (Airy, 1845). The free surface of a propagating Airy wave is sinusoidal (Figure 2 3a). The sine wave is a solution to the linearised equations describing the water motion and is defined as,

$$\eta(x, t) = \frac{H}{2} \sin(kx - \omega t) \quad (2-1)$$

where η is the wave elevation, H is the wave height, $k=2\pi/L$ is the wave number, x is position, ω is the angular wave frequency, and t is time.

Airy (1845) wave theory is valid for small-amplitude waves and is invalid in shallow water, where the water motions are highly non-linear (Lin, 2008). The Ursell number (Ursell, 1953) measures the non-linearity of a water surface by combining the wave steepness with the relative water depth as,

$$Ur = \frac{\text{steepness}}{(\text{relative depth})^3} = \frac{(H/L)}{(h/L)^3} = \frac{HL^2}{h^3} \quad (2-2)$$

where Ur is the Ursell number. Airy (1845) wave theory is only valid when $Ur \ll 32\pi^2/3 \approx 100$ (Ursell, 1953). Furthermore, Goda (1967) showed that sinusoidal waves generated in a wave flume are contaminated by one or more free second harmonic or second-order Stokes waves. According to Goda (1967), the primary wave's period matches the wavemaker's period. However, the second-order Stokes wave has half of the primary wave's period (Goda, 1967). As a result, the second-order free waves propagate slower than the primary wave and slowly disperse from the primary wave's crest, which causes spatial and temporal variations in the wave profile. The second-order free waves become more pronounced with increasing wave steepness (H/L) and decreasing relative depth (h/L) (Dong and Huang, 2004). Thus, if there is no force feedback mechanism to "kill" the second-order free waves, experiments that require uniform waves may be compromised and experience severe wave distortion. Figure 2-3 shows a simulated spatially varying wave profile at an instant in time using a sinusoidal wavemaker (Figure 2-3a) and using a sinusoidal wavemaker with an added second-order wavemaker motion that eliminates the second-order free waves (Figure 2-3b).

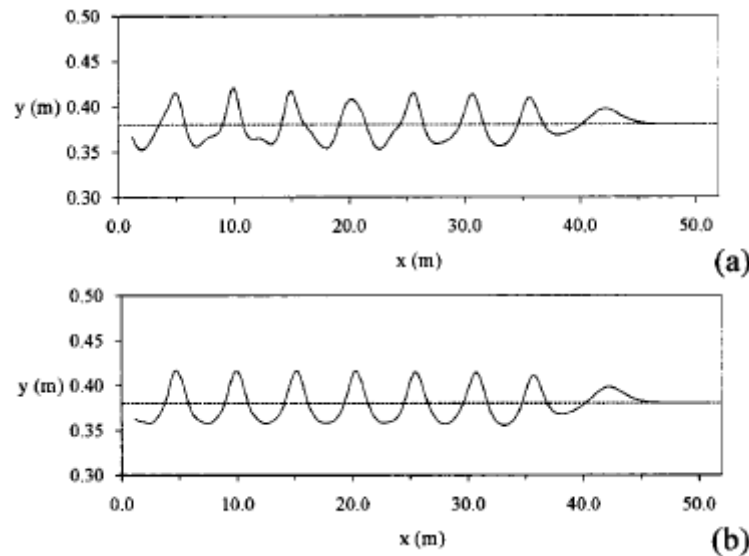


Figure 2-3: A simulated spatially varying wave profile at an instant in time using a) a sinusoidal wavemaker and b) a sinusoidal wavemaker with an added second-order wavemaker motion to eliminate the second-order free waves (after Dong and Huang, 2004).

2.2.2 Stokes waves

Stokes (1947) wave theory is a non-linear expansion of the Airy (1845) wave theory. Stokes (1947) established the first-order approximation of the neglected non-linear terms in Airy (1845) wave theory and developed a second-order correction to the first (linear) approximation. Stokes (1947) second-order correction can be used to find a third-order correction and so forth. A Stokes (1947) series describing Stokes waves (Figure 2 3b) and is defined as,

$$\eta = \hat{\eta}_1 \cos(kx - wt) + \hat{\eta}_2 \cos 2(kx - wt) + \hat{\eta}_3 \cos 3(kx - wt) + \dots \quad (2-3)$$

where η is the wave elevation and the first term is the linear solution. Stokes wave theory applies to large-amplitude waves in deep waters (Lin, 2008). Stokes (1947) series diverges if the Ursell number (Equation 2-2) is too large and in shallow water, which is usually the case for long waves ($L > 7h$) of appreciable height (Bosboom and Stive, 2012). Thus, cnoidal and solitary wave theories are more appropriate to use as the wavelength (L) increases, and the water depth (h) decreases (Bosboom and Stive, 2012).

2.2.3 Cnoidal waves

Cnoidal wave theory comprises several irrotational theories that represent cnoidal waves as a truncated series (Le Méhauté, 2013). According to Le Méhauté (2013), the primary cnoidal wave theory is the theory established by Korteweg and De Vries (1895). Korteweg and de Vries (1895) derived a non-linear partial differential equation, known as the KdV equation, to model the surface elevation of shallow water (Munk, 2006). In the simplified form, the Korteweg-de Vries equation reads,

$$\frac{\partial \eta}{\partial t} - 6\eta \frac{\partial \eta}{\partial x} + \frac{\partial^3 \eta}{\partial x^3} = 0 \quad (2-4)$$

where η is the wave elevation, x is position, and t is time. A cnoidal wave (Figure 2 3c) has a slow and gentle return flow under long flat troughs between the wave crests.

2.2.4 Solitary waves

Solitary wave theory describes long shallow water waves with a single crest of infinite length (Munk, 2006). Boussinesq (1871) was the first to establish a well-founded theory of solitary waves. The Boussinesq (1871) solitary wave solution describes the free surface displacement of the solitary wave (Figure 2 3d) as,

$$\eta = H \operatorname{sech}(k(x - ct))^2 \quad (2-5)$$

where η is the wave elevation, $c = \sqrt{g(H + h)}$ is the wave celerity with g being the acceleration due to gravity, and $k = \sqrt{3H/4h^3}$ is the wave number. The solitary wave height (H) equals the maximum amplitude (a) above the water surface. Hence, solitary waves can be described as a limited case of the cnoidal wave when the wave period tends to infinity (Le Méhauté, 2013). The volume and energy of a solitary wave is focussed within a narrow band about the wave crest (Munk, 2006).

Solitary wave theory assumes that the wave is infinitely long and unbounded in the direction that the wave propagates (Munk, 2006). Therefore, applying solitary wave theory to nearshore problems departs from the type of phenomenon for which the theory was intended (storm surges, tsunamis, and other long free surface waves) because the assumptions are not fulfilled for ocean waves travelling into shallow water where a beach imposes an additional boundary that establishes a return flow system (Munk, 2006). However, there is a likeness between the theoretical solitary wave profile (Figure 2-2d) and the observed wave profile just offshore of the breaker zone (Figure 1-1) which suggests the use of solitary wave theory for nearshore problems (Munk, 2006). Additionally, solitary waves are simple to generate, control and reproduce in a shallow wave tank without second-order free waves (Goring, 1978; Pedersen et al., 2013). Solitary waves are also advantageous for testing computationally demanding numerical models (Ting, 2013). Solitary waves can be simulated at a lower computational cost than periodic wave conditions because of relatively simple boundary conditions (Ting, 2013). These simple boundary conditions allow for wave flume experiments and numerical simulations that can be matched and compared precisely.

For the reasons stated above, solitary wave theory was used in the present study to physically and numerically model wave breaking on a plane beach slope. Previous

nearshore studies have applied solitary wave theory to problems regarding the humping of waves just before breaking, wave refraction, prediction of breaker height and depth of breaking, and the prediction of longshore currents (Munk, 2006). Boussinesq's (1871) first approximation is adequate for most applications (Munk, 2006) and was used in this study.

2.3 The wave boundary layer

Surface waves transmit energy to the sea bottom through the wave boundary layer (Sana and Tanaka, 2007). The wave boundary layer is a thin transition layer that forms a small distance above the bed due to intermolecular force interactions at the fluid-solid interface (Bosboom and Stive, 2012). Figure 2-4 shows a sketch of the wave boundary layer and the characteristic nature of the horizontal velocity profile for a solitary wave propagating over a horizontal bed. Figure 2-4(a) shows the velocity distribution in the wave boundary layer for a pre-passing solitary wave (before the wave crest passes the measuring section). Figure 2-4(b) shows the velocity distribution in the wave boundary layer for a post-passing solitary wave (after the wave crest passes the measuring section). In the figure, $\delta \approx 0.99u_\infty$ is the thickness of the wave boundary layer, u_∞ is the free stream velocity, b_m is the height of the maximum negative velocity, b_h is the half-velocity-deficit where $u = (u_\infty - u_m)/2$, and b_0 is the maximum thickness of reverse flow. The free stream velocity (u_∞) is defined as the time varying velocity immediately above the wave boundary layer (Malarkey and Davies, 2012).

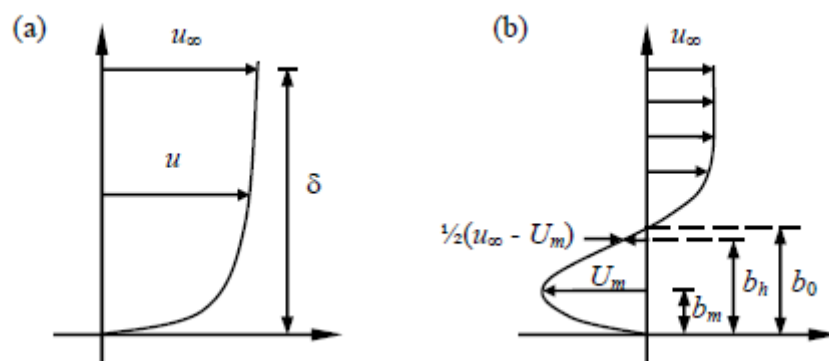


Figure 2-4: Schematic of the characteristic horizontal velocity profiles for a) a pre-passing solitary wave (before the wave crest passes the measuring section), and b) a post-passing solitary wave (after the wave crest passes the measuring section), propagating over a horizontal bed (after Lin et al., 2010).

The no-slip condition at the fluid-solid boundary interface (Figure 2-4) assumes that the fluid directly interacting with the solid boundary will have zero velocity relative to the solid boundary (Day, 1990). As a result, the flow sticks to the solid boundary and exerts a shear stress on the bed, resulting in bottom friction as the water propagates over the bed

(Bosboom and Stive, 2012). The instantaneous shear stress at a solid boundary is defined as,

$$\tau_b(z) = \mu \frac{\Delta u}{\Delta z} \quad (2-6)$$

where τ_b is the shear stress at the solid boundary or bed, μ is the dynamic viscosity of the flow (typically 8.90×10^{-4} Pa·s for water), and z is the height above the solid boundary. Significant shear stresses create more bottom friction in the wave boundary layer, resulting in higher wave energy dissipation (Bosboom and Stive, 2012). Additionally, wave-induced bed shear stresses have a significant role in the physical processes in the surf zone, such as sediment resuspension events and sediment transport (Cox and Kobayashi 2000; Trowbridge and Elgar 2001; Vittori and Blondeaux, 2009). Wave-induced shear stresses can initiate sediment particle motion and mobilise sediment particles along the bed, and entrain sediment particles into the water column. Wave-induced flows and currents can then transport the suspended sediment. (Dean, 1973). Therefore, the shear stress at the bed is a fundamental hydraulic parameter used to predict sediment transport (Johnson and Cowen, 2017). The thickness of the wave boundary layer governs a significant amount of the suspended sediment transported (Van Rijn, 1989). Thinner wave boundary layers induce larger velocity gradients perpendicular to the bed and, therefore, more significant stresses in the wave boundary layer (Bosboom and Stive, 2012).

2.4 Wave transformations

As waves propagate from deep water to shallow water, they transform through the effects of refraction, diffraction, and shoaling (Robertson et al., 2013). When propagating waves reach a critical height, they become unstable, overturn, and break (Robertson et al., 2013). Subsequently, waves run up shoreward on a sloping beach until reaching a maximum run-up height (Lin et al., 2018). Thereafter, waves run down seaward on a sloping beach due to the action of gravity (Lin et al., 2018). This study presents a two-dimensional analysis of breaking solitary waves in the nearshore zone. Therefore, the effects of reflection, refraction and diffraction are not within the scope of the present study.

2.4.1 Wave shoaling

Wave shoaling occurs as waves propagate over a sloping beach and undergo continuous deformations due to a decreasing water depth (Malarkey and Davies, 2012). Wave shoaling transforms the wave height and wavelength in response to the changing

free surface and increases wave non-linearity (Robertson, 2013). Shoaling waves steepen exhibiting skewness and asymmetry which govern the wave shape during breaking (Isobe and Horikawa, 1982; Drake and Calantoni, 2001; Nielsen, 2002; Hoefel and Elgar 2003; Gonzalez-Rodriguez and Madsen, 2007; van Rijn et al., 2011; Malarkey and Davies, 2012).

2.4.1.1 Skewness and asymmetry

The free-stream velocity changes as the wave height and steepness changes due to shoaling. This subsequently affects the wave skewness and asymmetry (Malarkey and Davies, 2012). The maximum horizontal velocity occurs below the wave crest and increases as the wave crest height increases due to shoaling (Lin et al., 2015). Therefore, skewness increases along the horizontal axis during shoaling. This results in larger orbital velocities below the wave crest and smaller orbital velocities below the wave trough (Malarkey and Davies, 2012; Ruessink et al., 2012). However, asymmetry increases along the vertical axis during shoaling. This results in the accelerations between trough and crest being larger than the accelerations between crest and trough (Malarkey and Davies, 2012; Ruessink et al., 2012). Hence, the wave profile becomes increasingly pitched forward with a steep front face and a gentle rear face before breaking (Ruessink et al., 2012). Figure 2-5 shows the transformation of a nearly sinusoidal wave profile from deep water into the swash zone showing the wave skewness and asymmetry as the wave propagates shoreward.

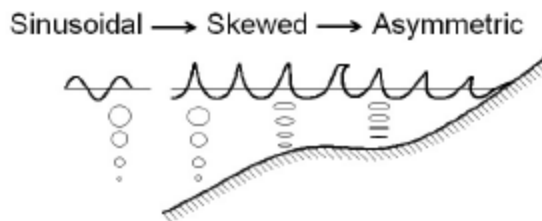


Figure 2-5 The transformation of a nearly sinusoidal wave profile in deep water to positively skewed and asymmetric prior to breaking (after Rocha et al., 2014).

Currently, there are various methods to quantify the velocity skewness and asymmetry beneath a wave (Malarkey and Davies, 2012). Different measures of skewness and asymmetry are applied based on context. The measures adopted by Silva et al. (2011) and Drake and Calantoni (2001) can be used to characterise sediment transport. The definition applied by Silva et al. (2011) considers skewness and asymmetry in terms of maximum and minimum values in a wave cycle. According to Silva et al. (2011), skewness is defined as,

$$R = \frac{u_{max}}{u_{max} - u_{min}} \quad (2-7)$$

where R is the velocity skewness coefficient, u_{max} is the peak velocity beneath the wave crest, and u_{min} is the peak velocity under the wave trough. The velocity skewness coefficient (R) reaches a maximum value near the breaker line, and $R=1/2$ corresponds to no skewness (Malarkey and Davies, 2012). According to Silva et al. (2011) the asymmetry is defined as,

$$\beta = \frac{a_{max}}{a_{max} - a_{min}} \quad (2-8)$$

Where β is the acceleration skewness coefficient, a_{max} is the peak acceleration beneath the wave crest, and a_{min} is the peak deceleration beneath the wave crest. The acceleration skewness coefficient (β) corresponds to no asymmetry when $\beta=1/2$ (Malarkey and Davies, 2012). Alternative measures of the skewness and asymmetry are given in literature (e.g., Drake and Calantoni, 2001; Hoefel and Elgar, 2003; Ruessink et al., 2009). The present study analyses the changing free surface and corresponding flow field of shoaling solitary waves. Therefore, the shoaling waves only exhibit asymmetry.

2.4.2 Wave breaking

Waves break at the instant a wave reaches its maximum stability (Robertson et al., 2013). The precise definition of the breaking point still varies among different authors (e.g., Miche, 1944; Iverson, 1952; Fenton, 1972; Kraus and Larson, 1988). However, the most widely applied definition of the breaking point is the instant that the wave front becomes vertical (Iverson, 1952; Seyama and Kimura, 1988; Bonmarin, 1989; Smith and Kraus, 1991; Grilli et al., 1997; Blenkinsopp and Chaplin, 2008). The breaking wave characteristics describe how the water surface and flow field evolves (Ting, 2013). The breaking wave characteristics depend on the breaker type.

2.4.2.1 Breaker types

Breaking waves on beaches are broadly classified into spilling, plunging, collapsing, and surging breakers (Galvin, 1968, 1972; Battjes, 1974; Grilli et al., 1997). Figure 2-6 shows the typical wave profile associated with spilling, plunging, collapsing and surging breakers.

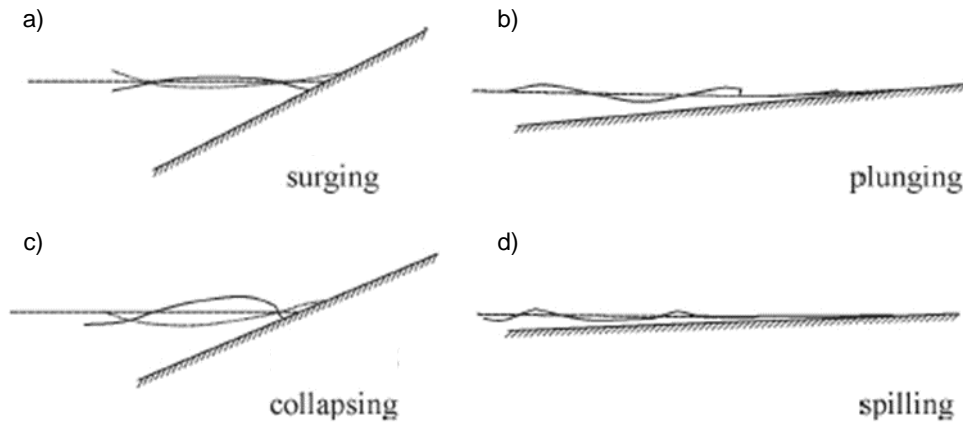


Figure 2-6: The wave profile of different breaker types on a smooth and impermeable slope (adapted Bosboom and Stive, 2012).

Spilling breakers (Figure 2-6d) are distinguished by the appearance of white/aerated water near the wave surface when breaking occurs. The aerated water subsequently cascades or spreads/spills down over the face of the wave front (Battjes, 1974), sometimes preceded by the projection of a small jet (Peregrine, 1983).

Plunging breakers (Figure 2-6b) are characterised by a steepening and overturning wave crest that curls over to form an overturning jet (Battjes, 1974; Peregrine, 1983; Ting, 2013). The overturning jet hits the water at the plunge point and causes a splash (Peregrine, 1983). The rebounding jet depicted in Figure 2-7(a) commonly occurs for weak and moderate plunging waves on gentle slopes. For strong plunging waves on a steep beach, the plunging jet is more likely to penetrate the surface, pushing up a jet of previously undisturbed fluid, as shown in Figure 2-7(b). A possible intermediate case is shown in Figure 2-7(c).

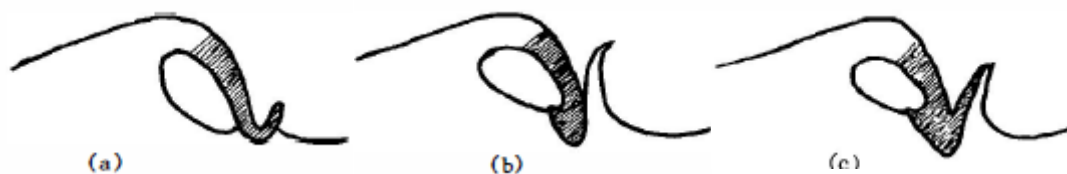


Figure 2-7: Schematic of some of the possible modes of splash-up after the plunge point of a plunging wave hits the water surface (after Peregrine et al., 1983). The shaded area denotes the falling jet

Collapsing breakers (Figure 2-6c) are distinguished by the lower portion of the wave front, which steepens and behaves like a truncated plunging breaker (Peregrine, 1983). The wave crest remains unbroken. Hence, collapsing breakers denote a transition from plunging to surging breakers and, therefore, a transition from breaking to non-breaking waves (Bosboom and Stive, 2012).

Surging breakers (Figure 2 6a) exhibit a smooth wave profile with no significant disturbance except near the moving shoreline (Peregrine, 1983).

The breaker type influences the flow structure during wave breaking, which has important links to generating and maintaining sediment suspensions (Svendsen, 1987; Beach and Sternberg, 1995; Ting and Kirby, 1994;1995;1996; Kobayashi and Tega, 2002; Ting, 2002; Aagaard and Hughes, 2010). According to Grilli (1997), spilling and plunging waves propagate for 1 to $3h_0$ past the breaking point before their breaker jet hits the water surface. However, the impact pressure of breaking waves on the water surface decreases when the breaker type transitions from plunging to spilling and from plunging to surging (Pedrozo-Acuña et al., 2008; Ting, 2013). Hence, the turbulence in plunging breakers has a prominent shoreward motion and is concentrated in the roller when compared with the turbulence that is more distributed for spilling breakers (Stansby and Feng, 2005). According to Battjes (1974), the breaker type also significantly affects the degree of wave reflection and other periodic wave processes that occur on a slope, like wave set-up, wave run-up, and wave rundown.

2.4.2.2 Breaking criteria

There are many published criteria that predict and approximate the breaking wave characteristics (e.g., McCowan, 1894; Miche, 1944; Iribarren and Nogales, 1949; Galvin, 1968; Battjes, 1974). However, a single, easily implementable relationship covering all wave breaking phenomena remains elusive (Robertson et al., 2013). Early studies dealt only with the breaking water depth and wave height (e.g., McCowan, 1894; Tanaka et al., 1987). Other studies accounted for the incoming wave characteristics and bathymetric slopes to improve the consistency and accuracy in breaking wave predictions over a broader range of allowable conditions (e.g., Iribarren and Nogales, 1949; Galvin, 1968; Battjes, 1974; Madsen, 1976; Svendsen, 1987).

The Iribarren number or surf similarity parameter (Iribarren and Nogales, 1949) is a non-dimensional characterisation term that encompasses all shallow water wave breaking types that are governed by the seafloor slope and wave characteristics and is defined as,

$$\xi_0 = \frac{\tan(\beta)}{\sqrt{H_0/L_0}} \quad (2-9)$$

where ξ_0 is the offshore Iribarren number, β is the seafloor angle, H_0 is the offshore wave height, and L_0 is the offshore wavelength. Table 2-1 shows the Iribarren number range associated with spilling, plunging, collapsing and surging breakers.

Table 2-1: The Iribarren number (ξ_0) range associated with different breaker types.

Spilling	$\xi_0 < 0.5$
Plunging	$0.5 < \xi_0 < 3.3$
Collapsing	$3.3 < \xi_0 < 5$
Surging	$\xi_0 > 5$

The Iribarren number (ξ_0) is widely applied in empirical formulae associated with the design of coastal processes and structures. However, the Iribarren number assumes waves are periodic, long-crested, and are propagating through an incompressible fluid. The Iribarren number also assumes that the beach slope is rigid, plane, impermeable and extends from deep water to the water surface at a constant angle (Robertson et al., 2013). Therefore, numerous studies have shown that Equation (2-9) does not accurately differentiate between the breaker types in cases involving complex bathymetry, which features bars, platforms and steps (e.g., Smith and Kraus, 1991; Mead and Black, 2001; Scarfe et al., 2003; Blenkinsopp and Chaplin, 2008).

The Iribarren number (Iribarren and Nogales, 1949) is generally the standard method of categorising breaking wave studies according to the breaker type (Robertson, 2013). However, Grilli et al. (1997) noted that Equation (2-9) could not be calculated for solitary waves which have a theoretically infinite wavelength and wave period (refer to section 2.2.4). To predict the breaker type of solitary waves, Grilli et al. (1997) recommended using a non-dimensional criterion defined as,

$$S_0 = 1.521 \tan \beta \sqrt{\frac{H_0}{h_0}} \quad (2-10)$$

where S_0 is the slope parameter, β is the angle of the beach slope, H_0 is the offshore wave height, and h_0 is the offshore still water depth. Table 2-2 shows the slope parameter (S_0) range associated with spilling waves, plunging, collapsing, and surging breakers. The present study identified breaker types for shoaling solitary waves using the slope parameter (equation 2-10).

Table 2-2: The values of the wave breaking criterion S_0 associated with each breaker types

Spilling	$S_0 < 0.025$
Plunging	$0.025 < S_0 < 0.3$
Collapsing/surging	$0.3 < S_0 < 0.37$

Grilli et al. (1997) emphasised that the effect of the beach slope is more significant than the wave height to still water depth ratio (relative wave height) in determining the shape of breaking waves and that breaker shapes are generally similar on a given slope. Waves break at smaller water depths on steep beach slopes than gentle beach slopes (Bosboom and Stive, 2012), and the size of plunging jets for spilling and plunging breakers increases significantly with the slope due to shallower water depths in front of the breakers (Grilli et al., 1997; Arntsen et al. 2000). Therefore, several studies suggest that the interaction between the breaking wave-induced turbulence and the bed is significantly intense for plunging waves on steep slopes where the wave overturning occurs in a very shallow region. (e.g., Arntsen et al., 2000; Pedrozo-Acuña et al., 2008; Ting, 2013; Zhou et al., 2014). Milder slopes, typical of sandy beaches, have a larger water depth in front of breaking waves which dampens the impact of plunging jets and reduces their impact pressure (Ting, 2013).

2.4.2.3 Flow characteristics beneath breaking waves

There have been numerous experimental measurements of wave profiles, and velocity distributions as waves begin to break (e.g., Hansen and Svendsen, 1979; Flick et al., 1981; Peregrine et al. 1980; Hedges and Kirkgoz, 1981; Chang and Liu, 1998; 1999). There has also been considerable research on the flow field generated by a plunging jet impact on the water surface shoreward of the wave crest (e.g. Stive, 1980; Nadaoka and Kondoh, 1982; Jansen, 1986; Battjes, 1988; Ting and Kirby, 1994, 1995, 1996; Chang and Liu 1998, 1999; Nadaoka et al., 1988, 1989; Cox and Anderson, 2001; Okayasu et al., 2004; Ting, 2006, 2008, 2013; Kimmoun and Branger, 2007; Huang et al., 2010; Ting and Nelson, 2011).

The initial overturning motion of the wave crest is a prominent stage of the breaking wave flow field (Peregrine et al., 1980). In a detailed study, Peregrine et al. (1980) showed that breaking waves exhibit three distinct characteristics prior to the wave front becoming vertical. The water particle velocities exceed the wave velocity, the water accelerations exceed the acceleration due to gravity in a thin region in front of the wave, and the water accelerations are low in an extensive region on and beneath the back slope of the wave.

Chang and Liu (1998; 1999) used Particle Image Velocimetry (PIV) to measure the fluid particle velocity and acceleration at the tip of the overturning jet in a plunging breaker. Chang and Liu (1998) found the breaking jet to have a maximum fluid particle velocity of $1.68c$, where c is the wave celerity, and maximum fluid particle acceleration of $1.1g$ angled at 88° downward, where g is the acceleration due to gravity. Chang and Liu (1999) found the breaking jet to have a maximum fluid particle velocity of $1.5c$.

Pioneers in the field, Nadaoka and Kondoh (1982), discovered, through extensive experimental research, the coexistence of large-scale turbulence in the surf zone from the breaking wave and small-scale bed-generated turbulence. Later, Battjes (1988) found that the overturning jet in a plunging breaker generates topologically induced vorticity when the jet hits the water surface, and Chen et al. (1999) found that much of the vorticity was generated during jet impact, splash-up and air entrainment. More recently, Ting (2013) showed that a plunger vortex is generated at incipient breaking. This vortex interacts with the sea bed when the wave-induced velocity is at its maximum and causes large apparent shear stresses in front and behind the plunger vortex. Furthermore, Sou and Yeh (2011) showed that a strong induction of the clockwise vorticity occurs in the surf zone due to the collision of the run-up and run-down flows, which leads to the formation of a thin layer of counter-clockwise vorticity on top of clockwise vorticity on the water surface and flow separation at the bore front.

Numerous studies (Jansen, 1986; Peregrine, 1983; Battjes, 1988; Nadaoka, 1986; Nadaoka et al., 1988; 1989) suggest that the fluid motions are organised during the initial stages of wave breaking despite the appearance that the breaking process degenerates rapidly into a chaotic motion of air and water. Nadaoka (1986) and Nadaoka et al. (1988, 1989) observed two families of large-scale, organised flow structures beneath breaking waves, shown in Figure 2-8. The first family were coherent transverse vortices with horizontal axes (horizontal eddies), and the second family were coherent three-dimensional vortices termed obliquely descending eddies (ODEs). The ODEs appeared for a short time and thereafter rapidly broke up into chaotic, three-dimensional turbulence. Many laboratory studies have since been performed to quantify the dynamics of wave-breaking induced turbulent coherent structures, which show clear evidence of ODEs interacting with the bed (e.g., Cox and Anderson, 2001; Ting, 2006;2008;2013; Kimmoun and Branger, 2007; Huang et al.,2010. Ting and Nelson, 2011). Okayasu et al. (2004) calculated the instant of eddy touchdown on the bed and the corresponding local velocity. They found that large three-dimensional velocity fluctuations near the bottom occur due to ODEs. Ting (2006, 2008, 2013) and Ting and Nelsen (2011) showed that ODEs comprise of two counter-rotating eddies with strong downward velocity fluctuations. The size of ODEs was in the order of the local water depth, resulting in a strong spanwise variability in the instantaneous flow field.

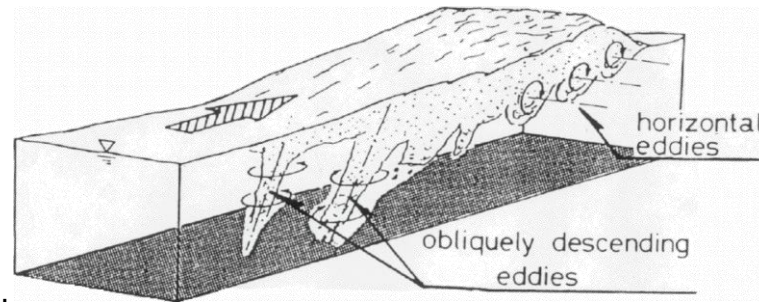


Figure 2-8: Schematic representation of the two-dimensional transverse vortices with horizontal axes (horizontal eddies) and the three-dimensional vortices (obliquely descending eddies) beneath breaking waves (after Nadaoka, 1986).

Studies also show that a plunging breaker may produce distinct cycles of plunge and splash-up that entrain air resulting in strong horizontal vortices (Figure 2-8) (e.g. Miller, 1976; Nadaoka et al., 1989; Zhang and Sunamura, 1990; Kimmoun and Branger, 2007). Jansen (1986) found that the particle trajectories inside the plunge and splash-up motions are smooth and repeatable when considering a series of waves. Nadaoka et al. (1989) found that similar coherent vortices repeatedly occur in successive breakers, but the size and location of the vortices may vary from structure to structure. Kimmoun and Branger (2007) found that four horizontal vortices, with varying vorticity and positions with time, are generated in the jet-splash sequence during breaking. According to Ting (2013), the plunging jet impact angle and water depth may be responsible for the variations in the flow patterns produced by the impingement of the primary and successive breakers on the bed.

Lin et al. (2015) investigated the shoaling of a plunging solitary wave, focusing on the near bottom and boundary layer flows. Their results showed that the boundary layer flow is laminar in the pre-breaking zone during wave shoaling and in the post-breaking zone during wave run-up and wave run-down. However, soon after wave breaking and prior to wave run-up, the laminar boundary layer had disappeared. The laminar boundary layer also disappeared during the later stage of the run-down motion.

2.4.3 Links to sediment transport

Wave breaking enhances the bottom shear stress significantly (Kimmoun and Branger, 2007), and many studies on surf zone sediment transport provide strong evidence that breaking wave-induced shear stresses and turbulence can reach the seabed and initiate sediment particle motion causing large sediment suspension (e.g., Dean, 1973; Nielson, 1984; Sato et al., 1990; Jaffe and Sallenger, 1993; Zhang and Sunamura, 1995; Ogston and Sternberg, 1995; Beach and Sternberg, 1996; Voulgaris and Collins, 2000; Okayasu

et al., 2004; Scott et al. 2009; Aagaard and Hughes, 2010; Yoon and Cox 2012, Grasso et al., 2012, LeClaire and Ting, 2017).

According to many studies, the height above the bed, breaker type, and distance from the breaking point or position in the surf zone govern the sediment concentration in the surf zone. (e.g., Brenninkmeyer, 1974, 1976; Kana 1977, 1978; (e.g., Inman et al., 1980; Sato, 1990; Shibayama and Horikawa, 1982; Sato, 1990; Beach and Sternberg, 1996, Yang et. al. 2017). Intermittent eddies generated by wave breaking are considered the primary cause of sediment pick up and cloud formation (Okayasu et al., 2004). Okayasu et al. (2004) showed that the length scale of the sediment clouds was in the order of the water depth and as the wave steepness increases and the water depth decreases and, more sediment is entrained during the wave breaking process.

Experimental results suggest that specifically plunging waves cause high suspended sediment concentrations (e.g., Nielsen, 1984; Kana, 1978, 1979; Inman et al., 1980; Beach and Sternberg, 1996 Voulgaris and Collins, 2000; Okayasu et al., 2004; Ting, 2013; LeClaire and Ting, 2017). Plunging waves in the surf zone almost instantaneously distribute turbulence throughout the water column suspending sediment (Voulgaris and Collins 2000). Nielsen (1984) explained that strong plunging jets penetrate through the water column to the bed, introducing turbulence external to the wave boundary layer (refer to section 2.3 and entraining air within the wave boundary layer. As a result, large upwards localised velocities are generated that are hundreds of times greater than the sediment settling velocity. De Serio and Mossa (2006) showed that the maximum turbulence intensity values occur near the bottom for plunging breakers and near the surface for spilling breakers.

Sediment transport only occurs beneath spilling breakers when the scale and intensity of the turbulence generated are large enough to agitate a significant amount of sediment into suspension (Sato, 1990). Sato (1990) observed that the area and amount of sediment in suspension were smaller due to spilling breakers than a typical plunging breaker of the same height. However, sediment suspension due to wave breaking is an intermittent process, with the sediment suspension beneath spilling breakers being much more intermittent and three-dimensional than beneath plunging breakers (Sato, 1990). Therefore, the amount of suspended sediment is much smaller beneath spilling breakers than beneath plunging breakers (Sato, 1990).

LeClaire and Ting (2017) showed that the impact of breaking wave-induced vortices on the bed creates a velocity distribution that significantly affects the net sediment transport over one wave cycle. During wave impingement, the breaking wave-induced vortices

produced strong onshore directed turbulence velocities through the surf zone resulting in significant onshore sediment transport events. Furthermore, breaking plunging waves were more efficient in transporting sediment shoreward than breaking spilling waves. According to LeClaire and Ting (2017), several wave characteristics combine to enhance onshore sediment transport beneath plunging breakers. These characteristics included an asymmetrical velocity pattern (generated by the impingement of obliquely descending eddies (Figure 2-8)), high turbulence velocities associated with the impinging jet, and high turbulent kinetic energy and shear stress near the plunging wave crest. However, LeClaire and Ting (2017) also reported that significant offshore sediment transport events occur after wave run-down. LeClaire and Ting (2017) showed that many sediment particles could remain in suspension due to counter-rotating vortices that trap sediment particles until the breaking wave-induced turbulence has dissipated. Thereafter, these sediment particles were transported offshore due to offshore flow velocities.

Studies by Scott et al. (2009) and Aagaard and Hughes (2010) also showed that vortices due to wave breaking would enhance onshore or offshore sediment transport depending on the relative timing between sediment suspension and the wave velocity phase beneath a breaking wave. Generally, wave skewness increases the rate of the net onshore transport, wave asymmetry produces a net sediment transport in the direction of the highest acceleration, and increasing the bed slope causes increased offshore sediment transport (Silva et al., 2011). LeClaire and Ting (2017) found that in most cases, enhancement of offshore sediment transport was net the effect of the breaking wave-induced vortices due to advection by primarily offshore flow velocities. van der Werf (2007) and Yang et al. (2017) achieved similar results. They showed that two mechanisms were responsible for producing a net offshore sediment transport beneath plunging breakers. These mechanisms were an offshore stream beneath strong breaking wave induced-vortices and a skewed oscillatory onshore-offshore current that occurred quasi-periodically in a surf zone due to wave run-up and run-down on a beach slope. The onshore current was stronger and occurred over a shorter time period than the offshore current (van der Werf et al., 2007).

To evaluate the sediment transport due to wave breaking, it is essential to study the breaking wave height, the velocity field, the near-bottom velocity and shear stress at the breaking point, the settling velocity of sediment particles, and the amount of suspended sediment in the vicinity of the wave breaking point (Sato et al. 1990, LeClaire and Ting, 2017). Aagaard and Hughes (2010) measured fluid velocities and suspended sediment concentrations in the field and found that peak sediment concentrations in the plunging breakers coincide with the maximum onshore velocity. Furthermore, LeClaire and Ting

(2017) showed that during impingement of breaking wave-induced vortices on the bed and entrapment of sediment in counterrotating vortices, the suspended sediment concentrations correlate well with the vorticity magnitude. LeClaire and Ting (2017) also showed that shear stress parameters are a more reliable indication of sediment suspension events than the turbulent kinetic energy. They reasoned that high suspended sediment concentrations do not always occur when the turbulence intensity is high, except when the primary source of turbulent kinetic energy in the flow field is counter-rotating vortices (LeClaire and Ting, 2017). According to LeClaire and Ting (2017), the three-dimensional flow requirements for sediment suspension can be better represented by shear stress distributions because the shear stress parameters combine the effects of horizontal and vertical fluid velocities.

2.5 Wave modelling techniques

Predicting the hydrodynamic processes in nearshore, wave-driven environments requires realistic modelling of the breaking wave mechanisms. The classical wave theories (refer to section 2.2) do not describe shoaling and breaking waves (Lin, 2008). Thus, breaking wave characteristics are mainly determined through small-scale physical models built in the laboratory of a prototype wave system in nature (Lin, 2008). However, physical model studies become expensive and time-consuming when the physical model cannot satisfy all the critical scaling laws involved in designing and constructing a complex physical system. Increasing knowledge of the wave breaking process and rapid developments in computational power has led to the development of several numerical models to describe the motions associated with wave breaking (Dong and Huang, 2004). These numerical models can simulate and describe the breaking wave flow field in detail which is useful for solving coastal problems in a reliable, cost-effective and time-saving manner (Lin 2008). However, each numerical technique has capabilities and limitations when simulating wave breaking (Altomare et al., 2017).

2.5.1 Physical wave models

Physical wave models allow for well-controlled conditions that allow for a systematic study. Hence, most quantitative investigations of wave breaking have been achieved through laboratory experiments in wave tanks. The quality and control attained through laboratory experiments are unmatched despite significant advances in field experiments and numerical models (Melville, 2002). Most field measurements cannot capture the complete evolution of the velocity field during shoaling and breaking (Melville, 2002). Furthermore, small-scale laboratory experiments generally allow visual feedback and

easier data collection at a lower cost than prototype testing and field experiments (Hughes, 1993). However, physical wave models are limited by scale. Readers are referred to Hughes (1993) for a more detailed description of the physical models in coastal engineering.

2.5.1.1 Mechanical wave generation

Mechanical wave generation in laboratory wave tanks is a widely researched field on its own. Piston or flap-type wave paddles are the most common generators built in wave tanks. Generally, it is simpler to generate shallow water waves using the piston-type paddle because the piston motion more closely resembles the water particle trajectories (Dean and Dalrymple, 1984). However, the flap type is more efficient in deep water (Dean and Dalrymple, 1984). Biesel and Suquet (1954) provides a list of wavemaker principles for both piston and flap-type wave paddles. Goring's (1978) wavemaker theory was used in the present study to generate a plunging solitary wave in a wave tank.

Goring's (1978) theory predicts the wave paddle trajectory for generating a solitary wave using a piston-type wave paddle. The wavemaker theory assumes that the average water particle horizontal velocity adjacent to the wave paddle is equal to the velocity of the wave paddle as follows,

$$\frac{d\zeta}{dt} = \frac{c\eta|_{x=\zeta}}{h + \eta|_{x=\zeta}} \quad (2-11)$$

where ζ is the position of the piston at the elapsed time, t , since the start of the wave generation, c is the wave celerity, η is the wave elevation, and h is the water depth. The piston stroke is calculated as,

$$S = \frac{2H}{kh} \quad (2-13)$$

where S is the piston stroke, H is the solitary wave height, $k = \sqrt{3H/4h^3}$ is the wave number. The duration of paddle motion is described by,

$$\tau = \frac{2}{kc} \left(3.8 + \frac{H}{h} \right) \quad (2-12)$$

where τ is the duration of paddle motion. Goring's (1978) wavemaker theory generates acceptable solitary wave profiles without second-order free waves (refer to section 2.2). According to Svendsen (1985), including the motion of the wave paddle in the formulation of the solitary wavemaker theory eliminates one source of the second-order waves.

2.5.1.2 Flow measuring methods

Many researchers in the past have used laser-Doppler velocimetry (LDV) to measure the time varying velocities beneath breaking waves (e.g., Nadaoka et al., 1989; Ting and Kirby 1994, 1995, 1996; Cox and Kobayashi 2000; Petti and Longo 2001; De Serio and Mossa 2006). LDV allows for high-frequency data acquisition rate measurements within a small measurement volume. However, measurements are taken locally at one point. Hence, LDV cannot obtain the instantaneous spatial description of the physical phenomena in the flow (Kimmoun and Branger, 2007). Furthermore, two-component velocity measurements are needed to calculate the time-averaged and ensemble-averaged wave and turbulence quantities. Hence, LDV becomes highly inefficient and challenging when investigating the structure of large eddies from single-point LDV measurements because hundreds of measurements are required to obtain a reasonable description of the average spatial distribution of the velocity field (Chang, 1999; Ting, 2013). Difficulty also ensues from interpreting the data from single point measurements due to the relative positions of the eddies and sensors as well as the temporal resolution and spatial distribution of the sensors (Ting, 2013).

Hot-film anemometry is another measurement technique that researchers have applied to investigate the processes of sediment suspension beneath nearshore breaking waves (Hattori and Aono 1985; Conley and Inman 1992; George et al., 1994). Hot-film anemometry, like LDV, also has the advantages of a high-frequency data acquisition rate (Chang, 1999). However, the technique is fragile and intrusive. Hence the equipment is prone to damage beneath breaking waves. A drag plate can also be used to directly measure the bed shear stress over the area of the plate and hence sediment transport (Johnson and Cowen, 2017). However, this method is inefficient for large-scale implementation in the field (Johnson and Cowen, 2017).

In the past two decades, researchers have extensively applied the particle image velocimetry (PIV) to obtain instantaneous spatial velocity measurements of the flow beneath breaking waves (e.g., Chang and Liu 1999; Cox and Anderson, 2001; Kimmoun and Branger, 2007; Huang et al., 2010; Sou et al., 2010; Sou and Yeh, 2011; Ting and Nelson, 2011; Ting, 2013; Lin et al., 2015; LeClaire and Ting, 2017). A distinct advantage of PIV over LDV and hot-film anemometry is that PIV is nonintrusive and yields spatiotemporal data sets (Sou and Yeh, 2011). Hence, PIV provides the spatial distribution of an instantaneous velocity field at a time step and can be used in unsteady or high-speed flows or in boundary layers close to the wall, where probes would otherwise cause disturbances in the flow. Thus, PIV is an effective method for investigating breaking waves. However, the technique does not provide accurate velocity

measurements in the aerated regions beneath breaking waves because of the entrained air bubbles (Chang et al., 1999). Furthermore, the resolution of the captured flow field depends on the CCD camera and light intensity being used.

2.5.1.3 Scale effects

It is impossible to model all the relevant forces in the model due to the limitations of laboratory facilities and scale effects arising due to differences between the physical model and the prototype being modelled. Scale effects can significantly affect the results of small-scale experiments (Hughes, 1993). Therefore, scaled laboratory results should be carefully interpreted due to the limitations of scaling certain characteristics.

Most wave models apply the Froude scaling criterion to geometrically scale wave parameters and beach/coastal structure dimensions due to the gravitational motion of waves (Hughes, 1993). The Froude number is defined as,

$$Fr = \frac{u}{\sqrt{gl}} \quad (2-14)$$

where u is a characteristic velocity, g is the gravitational acceleration, and l is a characteristic length. To scale a model up to a prototype without distortion, the Froude numbers should be made equal. However, the shear stresses that develop in the laminar boundary layers cannot be scaled accurately using the Froude number (Hughes, 1993). Hence, surface tension and surface roughness become significant contributors to hydraulic processes in small-scale physical wave models (Hughes, 1993).

The effects of surface tension and roughness can have considerable influence in a physical model and a negligible influence in the prototype (Hughes, 1993). Air and surface tension combined in drops and bubbles causes the rate at which the breaking wave motion becomes more disorganised and turbulent to increase. Moreover, the typical size of bubbles is very different in salt and fresh water, which is particularly important regarding laboratory experiments used to model ocean conditions (Peregrine, 1983). Generally, moderate viscosity and surface tension effects are expected in small-scale wave tank experiments performed with depths of 10 cm to 50 cm (Shuto, 1977; Miles, 1980, Pederson, 2013). However, scale effects may be more significant in the very thin flows during wave run-up on sloping beds in a laboratory swash zone (Pedersen, 2013). When the objective is to study wave sediment transport, the laboratory model should have the same flow and transport regimes as in the prototype (Henriquez et al., 2008).

2.5.2 Numerical wave models

Numerical wave models are mathematical representations of physical wave concepts governed by relevant equations and solved through computation (Hughes, 1993). The model performance depends on how accurately the physical phenomena is parameterised into the numerical schemes to predict the wave parameters (Lin, 2008). A high-performance numerical method is stable and compatible with analytical equations and yields computational results that converge to the right solution (Di Lisio et al., 1998). Numerical wave models are generally incorporated with sediment dynamics problems as constituents in a compound model to study and understand nearshore wave-induced flows and sediment transport in more detail (Battjes, 1988).

2.5.2.1 Governing equations

The Navier-Stokes equations govern general fluid flows, including water waves, and are derived from the general principle of mass and momentum conservation (Lin 2008). For most water wave problems, the fluid is assumed to be incompressible, which leads to the incompressible Navier-Stokes equations,

$$\frac{D\mathbf{v}}{Dt} = -\frac{1}{\rho}\nabla P + \nu_0\nabla^2\mathbf{v} + \mathbf{g}$$

$$\frac{D\rho}{Dt} = -\rho\nabla\cdot\mathbf{v} = 0$$
(2-15)

where \mathbf{v} is velocity, ρ is density, P is pressure, ν_0 is the kinematic viscosity, \mathbf{g} is the acceleration due to gravity.

Several computational models based on Navier-Stokes equations have been developed in the last decade. These models can simulate flows in complex geometries and enable a detailed description of the physical flow properties (e.g., velocity, pressure and turbulence) beneath breaking waves. These models all require approximating the continuous time and space in a physical problem by the discrete time and space in numerical computations and can be classified as grid-based Eulerian models or meshless Lagrangian models (Lin, 2008).

The expensive computational effort is the main barrier preventing the broad application of Navier-Stokes based numerical models. Navier-Stokes based numerical models require more computational power than all the previously introduced wave models, such as the limited flow representations of Boussinesq and non-linear shallow water wave models (Altomare et al., 2017). Hence, the application of Navier-Stokes based numerical models in engineering computation is still restricted to the simulation of local wave phenomena near the location of interest, such as the surf zone when the breaking wave

and/or sediment transport is considered and flows around a coastal and offshore structure when the wave-structure interaction is considered (Lin, 2008).

2.5.2.2 Eulerian models

Eulerian Navier-Stokes based models consider the fluid as a continuum discretised in control volumes and require a predetermined grid or mesh system for discretising the computational domain (Lin, 2008; Altomare et al., 2017). The grid or mesh configuration quality is important to the numerical accuracy and stability, especially near an irregular boundary or when the flow is violent (Lin, 2008). While Eulerian Navier-Stokes based models apply to a wide range of engineering problems involving coastal structures and the generation of regular and random waves, difficulty arises when applying these models in a domain with complex boundary geometry. The free-surface motion of Eulerian Navier-Stokes based models requires special treatment using techniques such as direct numerical simulation (DNS) of the Navier-Stokes equations, the volume of fluid (VOF), and large eddy simulation (LES). Hence, applying Eulerian Navier-Stokes based models becomes increasingly challenging when air entrainment and splashing become important.

2.5.2.3 Lagrangian models

Lagrangian Navier-Stokes based models have been developed to resolve the complex surface geometry that Eulerian methods cannot readily handle. Lagrangian Navier-Stokes based models use material points or particles without explicit connectivity to discretise the computational domain (Lin, 2008). The particles can be regularly or randomly distributed, moving or stationary (Lin, 2008). The domain of influence for a particle of interest is determined, and the collective behaviour of many neighbouring particles is used to approximate the fluid properties of each particle (Lin, 2008). Thus, Lagrangian methods tend to be less cumbersome in the arrangement of particles used to discretise the computational domain and operate on the distribution of scattered particles, unlike Eulerian methods, where specific gridlines must be used to connect neighbouring nodes.

Accurate free surface tracking is of paramount importance for water wave models, and Lagrangian methods can determine the exact free surface location within a computational cell, whereas Eulerian methods provide the bulk fluid property (e.g., mean density) in a computational cell from which the free surface can be reconstructed only approximately (Lin, 2008). However, similar to the Eulerian methods where a certain mesh resolution is needed, Lagrangian methods require a certain number of particles to represent a physical phenomenon adequately. Hence, Lagrangian Navier-Stokes based

models can be more computationally expensive than conventional grid-based methods but can improve flexibility and accuracy near irregular boundaries. Although, Lagrangian Navier-Stokes based models are still being developed and refined (Lin, 2008).

Presently, most Lagrangian Navier-Stokes based models use the smoothed particle hydrodynamics (SPH) method to resolve the flow. SPH has successfully been applied in water wave modelling for the study of breaking waves and interaction with coastal structures in two dimensions (Gomez-Gesteira et al., 2005; Dalrymple and Rogers, 2006; Shao and Ji, 2006; Crespo et al., 2007a; Crespo et al. 2015a) and three dimensions (Gomez-Gesteira and Dalrymple, 2004; Dalrymple and Rogers, 2006; Crespo et al. 2007; Crespo et al., 2008; Farahni and Dalrymple, 2014).

The robustness and simple form of the conservation of mass, momentum and total energy makes the SPH method uniquely advantageous compared to other techniques. However, many authors agree that the primary limitation of the SPH method is the high computational cost that arises from needing large numbers of particles and tiny time steps to obtain physical results with reasonable accuracy (Dalrymple and Knio, 2001, Dalrymple and Rogers, 2006, Gomez-Gesteira et al., 2010; De Padova et al., 2014). Furthermore, optimal values for the model parameters can be case dependent, and the inconsistency and the errors associated with particle disorder is a generic problem in SPH (Zhu et al., 2015; Roselli et al., 2018). The present study further demonstrates the capability of SPH for comprehensively describing the complete physical processes associated with wave breaking and proposes a physically based framework for using SPH to simulate breaking waves accurately. The open-source GPU SPH solver, DualSPHysics (Crespo et al., 2015b), was used for all numerical computations.

CHAPTER 3

SMOOTHED PARTICLE HYDRODYNAMICS (SPH) OVERVIEW

Smoothed particle hydrodynamics (SPH) is a Lagrangian meshless modelling method that applies continuum fluid dynamics to estimate the equations of motion and particle properties (Crespo et al., 2015b). SPH is the earliest established Lagrangian method for computational physics and was initially developed for applications to astrophysics (Gingold and Monaghan, 1977; Lucy, 1977). SPH has since been modified and applied to numerous areas within the field of engineering, such as wave run-up and wave run-down on beaches (Monaghan and Kos, 1999), wave breaking (Dalrymple and Rogers, 2006; De Padova et al., 2009), and dam break flows (Crespo et al. 2008; Khayyer and Gotoh 2010). This chapter presents an overview of the SPH formulation used in the DualSPHysics (Crespo et al., 2015b) model and establishes important model calibration parameters regarding wave breaking problems.

3.1 Kernel approximation

The classical SPH formulation discretises the Navier-Stokes equations of motion from their partial differential form into a non-continuous, discrete particle form, treating the fluid as weakly compressible (Altomare et al., 2015; Crespo et al., 2015b). The Navier-Stokes equations are discretised and locally evaluated at each particle location by considering the physical quantities (e.g., position, velocity, density, pressure) of neighbouring particles (Crespo et al., 2015b).

An interpolation function, referred to as the smoothing kernel, is used to yield an estimate of the physical quantities at a specific location. A distance-based function with an associated smoothing length determines the set of neighbouring particles used for the interpolation. At each timestep, updated physical quantities are evaluated at each particle location, and each particle then moves according to the new physical quantities (Crespo et al., 2015b). The integral approximation represents a function,

$$F(\mathbf{r}) = \int F(\mathbf{r}')W(\mathbf{r}' - \mathbf{r}, h_{\text{SPH}})d\mathbf{r}' \quad (3-1)$$

where $F(\mathbf{r})$ is a function defined in \mathbf{r}' by the integral approximation of any scalar or tensor quantity, W is the interpolation function or smoothing function, h_{SPH} is the smoothing length which governs the size of the area around particle a in which neighbouring

particles are considered, and $d\mathbf{r}'$ is a volume element. The discretisation of the integral approximation in a non-continuous discrete form results in the particle approximation,

$$F(\mathbf{r}_a) \approx \sum_b F(\mathbf{r}_b) \frac{m_b}{\rho_b} W(\mathbf{r}_a - \mathbf{r}_b, h_{\text{SPH}}) \quad (3-2)$$

where the function F is interpolated at a particle (a) by summation over all the particles that fall within the smoothing kernel, defined by the smoothing length h_{SPH} . The subscripts a and b denote different individual particles, \mathbf{r} is the difference in position of any two given particles (a and b), and m_b and ρ_b are the mass and density of a neighbouring particle (b), respectively. Figure 3-1 shows the SPH particle approximations in a two-dimensional numerical domain.

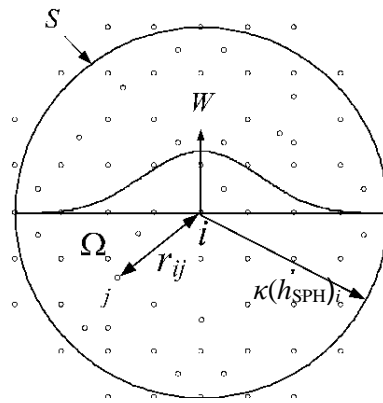


Figure 3-1 The SPH particle approximations in a two-dimensional numerical domain (after Liu and Liu, 2010). The smoothing function W interpolates the physical quantities at a particle i using averaged summations over particles j within the support domain. The two-dimensional domain has a surface S and a cut-off distance of $\kappa(h_{\text{SPH}})_i$.

3.1.1 Smoothing function

The smoothing function (W) can take different forms, and the choice of the smoothing function strongly influences the performance of an SPH model (Crespo et al., 2015b). The smoothing function must have compact support over the smoothing region so that summation over particles is only taken from neighbouring particles, must be positive inside a defined zone of interaction (Figure 3-1), must have normalisation over the support domain, and must have a monotonically decreasing value with distance and differentiability (Monaghan, 1992; Dalrymple and Rogers, 2006). According to De Padova et al. (2014), the influence of the smoothing function choice is reduced when the basic smoothing function requirements are met and where the smoothing length (h_{SPH}) and inter-particle spacing (dp) become small. Research by Fulk and Quinn (1995), Vila (1999), Quinlan et al. (2005) shows the efficiency and accuracy of all existing smoothing functions.

Within DualSPHysics, the user can choose either the cubic spline (Monaghan and Lattanzio, 1985) function or the Wendland quintic (Wendland, 1995) function. Both the cubic spline and quintic spline functions are commonly applied forms of the smoothing kernel (W). The cubic spline function is defined as,

$$W(r, h_{SPH}) = \alpha_D \begin{cases} 1 - \frac{3}{2}q^2 + \frac{3}{4}q^3 & \text{for } 0 \leq q \leq 1 \\ \frac{1}{4}(2 - q)^3 & \text{for } 1 \leq q \leq 2 \\ 0 & \text{for } q \geq 2 \end{cases} \quad (3-3)$$

where α_D is the normalisation constant, and q is the non-dimensional distance r/h_{SPH} between any two given particles (a and b). In two dimensions $\alpha_D=10/(7\pi h_{SPH}^2)$ and in three dimensions $\alpha_D=1/(\pi h_{SPH}^3)$. The Wendland quintic spline function (Wendland, 1995) is defined as,

$$W(r, h_{SPH}) = \alpha_D \left(1 - \frac{q}{2}\right)^4 (2q + 1) \text{ for } 0 \leq q \leq 2 \quad (3-4)$$

where α_D is the normalisation constant, and q is the non-dimensional distance r/h_{SPH} between any two given particles (a and b). In two dimensions $\alpha_D=7/(4\pi h_{SPH}^2)$ and in three dimensions $\alpha_D=21/(16\pi h_{SPH}^3)$. In DualSPHysics (Crespo et al., 2015b), both the Cubic spline (Monaghan and Lattanzio, 1985) and Wendland Quintic (Wendland, 1995) functions only consider particles within a maximum radius of $2h_{SPH}$ as shown in Figure 3-2

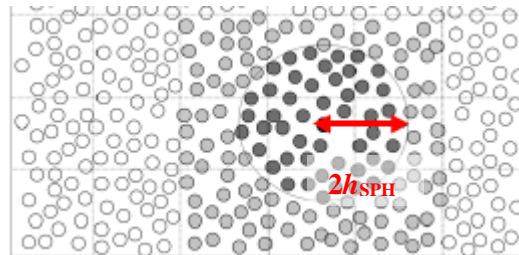


Figure 3-2 The SPH kernel functions (W) available in DualSPHysics only consider neighbouring particles within a maximum radius of $2h_{SPH}$ (Adapted Alonso et al., 2020).

The cubic-spline function (Monaghan and Lattanzio, 1985) yields a higher resolution when defined on a sphere of diameter $2h_{SPH}$ than higher-order kernels using the same number of particles (De Padova et al., 2014). The cubic spline function is also proven to be effective when the gradients of the flow quantities are not strong, and no violent impacts occur (Farahani et al., 2014). However, the second derivative of the cubic-spline function results in a linear piecewise function. Hence, the cubic spline function suffers a loss of accuracy and is less effective than the quintic kernel in interpolating the second-

order derivatives and can be less stable (Liu and Liu, 2010). Higher degree quintic spline functions are computationally superior and allow for a large number of neighbouring particles, and hence better numerical convergence compared to higher-order B-splines and are therefore better suited to SPH smoothing kernels (Dehnen and Aly, 2012). The present study used the Wendland quintic spline function (Wendland, 1995) for all SPH computations.

3.2 Momentum equation and viscous dissipation

DualSPHysics (Crespo et al., 2015b) follows the classical SPH formulation and solves the governing conservation of momentum and mass equations in Lagrangian form, treating the fluid as weakly compressible. The momentum conservation equation in a continuum is defined as,

$$\frac{d\mathbf{v}}{dt} = -\frac{1}{\rho}\nabla P + \mathbf{g} + \mathbf{\Gamma} \quad (3-5)$$

where \mathbf{v} is velocity, P is pressure, \mathbf{g} is the acceleration due to gravity, and $\mathbf{\Gamma}$ refers to dissipative terms. Numerous formulations have been derived for including the effects of dissipation. Without a suitable viscosity formulation, the SPH simulation is subject to instabilities such as “boiling”, where each particle begins to move chaotically (De Padova et al., 2014).

DualSPHysics offers a standard artificial viscosity approach (Monaghan, 1992) and a combined laminar viscosity (Lo and Shao, 2002) and sub-particle scale (SPS) turbulence approach (Dalrymple and Rogers, 2006). Gómez-Gesteira et al. (2010) found comparable accuracy among both methods. This study applied the standard artificial viscosity approach to calibrate a weakly compressible two-dimensional SPH model. However, the sensitivity of the calibrated SPH model to the type of viscosity formulation was briefly analysed.

3.2.1 Artificial viscosity scheme

Artificial viscosity schemes are the standard approach for describing viscosity in SPH simulations due to their simplicity (Altomare et al., 2015; Crespo et al., 2015b). The artificial viscosity scheme (Monaghan, 1992) discretises the momentum equation (Equation 3-5) to determine the acceleration of a particle (particle a) as a result of the particle interaction with its neighbour particles (particles b), and is written in SPH notation as,

$$\frac{d\mathbf{v}_a}{dt} = -\sum_b m_b \left(\frac{P_b}{\rho_b^2} + \frac{P_a}{\rho_a^2} + \Pi_{ab} \right) \nabla_a W_{ab} + \mathbf{g} \quad (3-6)$$

where Π_{ab} is the viscosity term defined as,

$$\Pi_{ab} = \begin{cases} \frac{-\alpha \overline{c_{ab}} \mu_{ab}}{\rho_{ab}} & \text{for } \mathbf{v}_{ab} \cdot \mathbf{r}_{ab} < 0 \\ 0 & \text{for } \mathbf{v}_{ab} \cdot \mathbf{r}_{ab} > 0 \end{cases} \quad (3-7)$$

where α is the artificial viscosity coefficient, $\mathbf{r}_{ab} = \mathbf{r}_a - \mathbf{r}_b$ is the particle position, $\mathbf{v}_{ab} = \mathbf{v}_a - \mathbf{v}_b$, is the particle velocity, $\overline{c_{ab}} = 0.5(c_a + c_b)$ is the mean speed of sound, $\mu_{ab} = h_{SPH} \mathbf{v}_{ab} \cdot \mathbf{r}_{ab} / (\mathbf{r}_{ab}^2 + \eta^2)$ with $\eta^2 = 0.01 h_{SPH}^2$. The artificial viscosity coefficient α is tuned to implement the proper dissipation in SPH simulations.

Using an artificial viscosity scheme has advantages and disadvantages. The original purpose of the viscosity term (Π_{ab}) was used to represent viscosity and prevent particles from interpenetrating because the artificial force repels approaching particles (Dalrymple and Rogers, 2006). Furthermore, Π_{ab} is a Galilean invariant, conserves linear and angular momentum, and disappears for rigid body rotations (De Padova et al., 2014). For free surface flows, Π_{ab} also keeps the SPH simulation numerically stable by dampening noise variations in the pressure field that result from a weakly compressible SPH formulation (Dalrymple and Rogers, 2006). However, Π_{ab} is a scalar viscosity and cannot account for flow directionality (De Padova et al., 2014). Furthermore, Π_{ab} is purely phenomenological, depending only on the artificial viscosity coefficient (α) that must be externally tuned to introduce the proper dissipation in the momentum equation (Altomare et al., 2015). As a result, SPH simulations can be over diffusive if α is not carefully chosen (De Padova et al., 2014; Altomare et al., 2015). Moreover, in many cases, Π_{ab} is excessively dissipative, which affects the shear in the fluid and, therefore, the accuracy of SPH when trying to capture coherent turbulent structures (Dalrymple and Rogers, 2006).

3.2.2 Laminar viscosity and sub particle scale (SPS) turbulence scheme

The laminar viscosity (Lo and Shao, 2002) and sub-particle scale (SPS) turbulence scheme (Dalrymple and Rogers, 2006) is the second viscosity formulation offered in DualSPHysics (Crespo et al., 2015b). For this scheme, the momentum conservation equation is defined as,

$$\frac{d\mathbf{v}}{dt} = -\frac{1}{\rho} \nabla P + \mathbf{g} + \nu_0 \nabla^2 \mathbf{2v} + \frac{1}{\rho} \nabla \cdot \vec{\tau} \quad (3-8)$$

where ν_0 is the kinematic viscosity (typically 10^{-6} m/s for water) and $\vec{\tau}$ is the SPS stress tensor. The momentum equation including the laminar viscous stresses can be expressed in SPH notation as,

$$\frac{d\mathbf{v}_a}{dt} = - \sum_b m_b \left(\frac{P_b + P_a}{\rho_b \cdot \rho_a} \right) \nabla_a W_{ab} + \mathbf{g} + \sum_b m_b \left(\frac{4v_0 \mathbf{r}_{ab} \cdot \nabla_a W_b}{(\rho_a + \rho_b)(r_{ab}^2 + \eta^2)} \right) \mathbf{v}_{ab} \quad (3-9)$$

Dalrymple and Rogers (2006) implemented SPS into weakly compressible SPH simulation using an approach similar to the large eddy simulation (LES) approach used in incompressible flows to represent the effects of turbulence at sub-particle scales (Meneveau and Katz, 2000; Gomez-Gesteira et al., 2010). The method involves spatially averaging the governing equations over a length scale comparable to the computation elements (Dalrymple and Rogers, 2006). The averaged equations are adequate to solve large-scale eddies resolved by the interparticle spacing. However, a closure scheme resolves the effects of turbulent eddies smaller than the interparticle spacing. Dalrymple and Rogers (2006) used a unique Favre averaging technique to account for compressibility in a weakly compressible SPH simulation. Favre averaging uses the eddy viscosity assumption to model the SPS stress tensor ($\vec{\tau}$) with Einstein notation for the shear stress component in coordinate directions i and j as,

$$\frac{\vec{\tau}_{ij}}{\rho} = v_t \left(2S_{ij} - \frac{2}{3} k \delta_{ij} \right) - \frac{2}{3} C_I \Delta^2 \delta_{ij} |S_{ij}|^2 \quad (3-10)$$

Where, $\vec{\tau}_{ij}$ is the sub-particle stress tensor, $v_t = [(C_s \Delta l)]^2 |S|$ is the turbulent eddy viscosity with C_s being the Smagorinsky constant, Δl the interparticle spacing, and $|S| = 0.5(2S_{ij}S_{ij})$, k is the SPS turbulent kinetic energy, $C_I = 0.0066$, and S_{ij} is an element of the SPS strain tensor. The momentum equation, including the laminar viscous stresses and SPS turbulence, can be expressed in SPH notation as,

$$\begin{aligned} \frac{d\mathbf{v}_a}{dt} = & - \sum_b m_b \left(\frac{P_b + P_a}{\rho_b \cdot \rho_a} \right) \nabla_a W_{ab} + \mathbf{g} \\ & + \sum_b m_b \left(\frac{4v_0 \mathbf{r}_{ab} \cdot \nabla_a W_b}{(\rho_a + \rho_b)(r_{ab}^2 + \eta^2)} \right) \mathbf{v}_{ab} \\ & + \sum_b m_b \left(\frac{\vec{\tau}_{ij}^b}{\rho_b^2} + \frac{\vec{\tau}_{ij}^a}{\rho_a^2} \right) \nabla_a W_{ab} \end{aligned} \quad (3-11)$$

The SPS approach is similar to the sub-grid scale used in Eulerian models (Shao and Ji, 2006). However, DualSPHysics uses a set Smagorinsky constant (C_s) of 0.12, which the user cannot tune.

3.3 Continuity equation

In a weakly compressible SPH simulation, the mass of each particle remains constant. Only the density associated with each particle fluctuates (Crespo et al., 2015b). To compute the density changes, the conservation of mass or continuity equation is solved in SPH form as,

$$\frac{d\rho_a}{dt} \sum_b m_b \mathbf{v}_{ab} \cdot \nabla_a W_{ab} \quad (3-12)$$

3.4 Equation of state

The weakly compressible SPH method uses an equation of state to calculate the fluid particle pressures explicitly based on particle density (Monaghan 1994; Dalrymple and Roger 2006). The pressure is related to the density following the work of Monaghan et al. (1999) and Batchelor (1974) and is expressed as,

$$P = B \left[\left(\frac{\rho}{\rho_0} \right)^\gamma - 1 \right] \quad (3-13)$$

where, P is the pressure of the fluid, $B = c_0^2 \rho_0 / \gamma$ with ρ_0 being the reference density of the fluid (typically 1000 kg/m³ for water), $\gamma = 7$, and $c_0 = c(\rho_0) = \sqrt{(\partial P / \partial \rho)}|_{\rho_0}$ is the speed of sound at the reference density.

The alternative incompressible SPH approach developed by Lo and Shao (2002) solves a Poisson pressure equation (De Padova et al., 2014). However, using an equation of state is less time consuming since a partial differential equation for pressure does not need to be solved (De Padova et al., 2014). Although, a problem can arise in the weakly compressible approach when the high speed of sound and sound wave reflection at the boundaries results in a crippling Courant-Friedrichs-Lewy (CFL) time step constraint (Cummins and Rudman 1999, Shao et al. 2006).

There is a rigorous discussion in literature on the advantages and disadvantages of the weakly compressible SPH approach and the incompressible SPH approach. Shipilova et al. (2009) and Lee et al. (2008) presented detailed comparisons of both SPH approaches. In DualSPHysics (Crespo et al., 2015b), adjustments made to the compressibility are restricted so that the speed of sound is always at least ten times greater than the maximum fluid velocity in the system. This limits the density fluctuations in the weakly compressible SPH simulation to less than 1%, preventing significant deviations from an incompressible SPH method (Monaghan, 1992).

3.5 Density diffusion term

The SPH method produces an unstable and erratic pressure field due to low amplitude, high-frequency oscillations throughout the density scalar field. The high-frequency oscillations result from the equation of state used to describe a stiff density field and from the natural disordering of the particles (Crespo et al., 2015b). Therefore, DualSPHysics (Crespo et al., 2015b) adds a diffusive term in the continuity equation to reduce the density fluctuations in SPH simulations and stabilise the pressure field. A delta-SPH formulation (Molteni and Colagrossi, 2009) is used to implement the diffusive term and is defined,

$$\frac{d\rho_a}{dt} \sum_b m_b \mathbf{v}_{ab} \cdot \nabla_a W_{ab} + 2\delta_{SPH} h_{SPH} \sum_b m_b \overline{c_{ab}} \times \left(\frac{\rho_a}{\rho_b} - 1 \right) \frac{1}{r_{ab}^2 + \eta^2} \cdot \nabla_a W_{ab} \quad (3-14)$$

where, $\overline{c_{ab}}=0.5(c_a+c_b)$ and $\eta^2=0.01h_{SPH}^2$ and δ_{SPH} is the delta-SPH coefficient, a free parameter given a suitable value. The recommended value for most applications is $\delta_{SPH}=0.1$ (Crespo et al., 2015).

While solving for the conservation of mass of each particle, the density diffusion term filters large wave numbers from the density field, thereby reducing the noise throughout the weakly compressible SPH simulation (Crespo et al., 2015b). However, near open boundaries such as a free surface, where an incomplete interpolation kernel occurs, the behaviour of the diffusive term changes and a net force occurs that acts on the particles (Crespo et al., 2015b). Thus, the density diffusion term should not be used for applications that require hydrostatic equilibrium (Crespo et al., 2015b). For non-hydrostatic situations where the force is many orders of magnitude smaller than the pressure and viscous terms, the effect of the net force is not considered relevant (Crespo et al., 2015b). Fourtakas et al. (2019) introduced a correction for the density diffusion term, which improves pressure behaviour near the wall boundaries by substituting the dynamic density with the total one

3.6 Time stepping algorithm

The SPH method integrates the equations for momentum, density, and position, in time. The governing equations are defined

$$\frac{d\mathbf{v}_a}{dt} = F_a; \quad \frac{d\rho_a}{dt} = D_a; \quad \frac{d\mathbf{r}_a}{dt} = \mathbf{v}_a \quad (3-15)$$

where the momentum, density, and position terms are defined, respectively. A stable time-stepping algorithm is used to reduce the partial differential equations to sets of ordinary differential equations. For numerical stability, the time steps must not exceed the travel time of the speed of sound in the fluid across a smoothing length (h_{SPH}) (Monaghan, 1992).

A variable time step (Monaghan et al., 1999) is calculated according to a Courant-Friedrichs-Lewy (CFL) condition, the force terms and the viscous diffusion term (Roselli et al., 2018) as,

$$\begin{aligned} \Delta t &= C_{CFL} \cdot \min(\Delta t_f, \Delta t_{cv}) \\ \Delta t_f &= \min_a \left(\frac{h_{SPH}}{\sqrt{|f_a|}} \right) \\ \Delta t_{cv} &= \min_a \frac{h}{c_s + \max_b \frac{|h\mathbf{v}_a \cdot \mathbf{r}_a|}{r_{ab}^2 + \eta^2}} \end{aligned} \quad (3-16)$$

where Δt is the variable time step, Δt_f is based on the force per unit mass $|f_a|$, and Δt_{cv} combines the Courant and the viscous time step controls (Crespo et al., 2015b). The Courant condition used to determine the time step at any one moment is based on the currently calculated speed of sound for all particles (Crespo et al., 2015b). The CFL number C_{CFL} is a correcting factor for minimum criteria derived by the forcing and viscous diffusion terms (Roselli et al., 2018). Generally, $C_{CFL}=0.1$ or $C_{CFL}=0.2$ is used to keep the mean water level stable (Roselli et al., 2018).

DualSPHysics offers two explicit time integrations schemes used with a variable time step, the Verlet scheme (Verlet, 1967) and the Symplectic position Verlet time integrator scheme (Leimkuhler and Matthews, 2016). The Symplectic based scheme is a more numerically stable method than the Verlet based scheme and was therefore used for all SPH computations in the present study. However, the Symplectic based scheme is also more computationally intensive than the Verlet based scheme (Crespo et al., 2015b).

The Symplectic position Verlet time integrator scheme (Leimkuhler and Matthews, 2016) is a two-stage method that uses a predictor and corrector stage. The predictor stage estimates accelerations and density halfway through the time step as,

$$\begin{aligned} \mathbf{r}_a^{n+\frac{1}{2}} &= \mathbf{r}_a^n + \frac{\Delta t}{2} \mathbf{v}_a^n \\ \rho_a^{n+\frac{1}{2}} &= \rho_a^n + \frac{\Delta t}{2} D_a^n \end{aligned} \quad (3-17)$$

where the superscript n is the time step and $t=n\Delta t$. The corrector stage uses $\frac{dv_a^{n+1/2}}{dt}$ to calculate the corrected velocity and position according to,

$$\begin{aligned} \mathbf{v}_a^{n+1} &= \mathbf{v}_a^n + \frac{\Delta t}{2} \mathbf{F}_a^{n+\frac{1}{2}} \\ \mathbf{r}_a^{n+1} &= \mathbf{r}_a^{n+\frac{1}{2}} + \frac{\Delta t}{2} \mathbf{v}_a^{n+1} \end{aligned} \quad (3-18)$$

Finally, \mathbf{v}_a^{n+1} and \mathbf{r}_a^{n+1} are used to calculate the corrected density (Monaghan, 2005) value,

$$\frac{d\rho_a^{n+1}}{dt} = D_a^{n+1} \quad (3-19)$$

The Symplectic based scheme is second-order accurate in time. Furthermore, in the absence of diffusive terms, the scheme is also time reversible and symmetric, thereby preserving the geometric features of the flow and making it ideal for Lagrangian applications.

Model time steps are small, generally of $O(10^{-5})$ s and are determined by the interparticle spacing and the numerical speed of sound (Monaghan, 1992; Dalrymple and Rogers, 2006). The speed of sound is far greater than the particle speeds in the fluid, which results in small time steps. Hence, the compressibility is adjusted to allow the speed of sound to be artificially lowered to maintain a reasonable size time step and thus computation time. However, the time step also becomes smaller and increases the computation time when smaller interparticle spacings are used due to the smoothing length increasing with an increasing number of simulated particles (Monaghan, 1992).

3.7 Boundary condition

The formulation of realistic boundary conditions in SPH is still an open subject. Gomez-Gesteira et al. (2010) and Domínguez et al. (2015) compare and test various types of boundary particles and conditions. The dynamic boundary condition (DBC) is the standard boundary approach used in DualSPHysics (Crespo et al., 2015b) and was used for all computational boundaries in this study.

3.7.1 Dynamic boundary condition (DBC)

The DBC method describes boundaries using dynamic particles that follow the same equations as fluid particles. However, the boundary particles do not move according to the forces exerted on them and are considered separate from the fluid particles (Gómez-Gesteira et al., 2010). The boundary particles can remain as fixed boundaries or move

according to an externally imposed function as moving objects in the case of wavemakers (Gómez-Gesteira et al., 2009).

There is no need to make an a priori assumption about the nature of the force exerted by the boundaries when using the DBC. A repulsive force is exerted by boundary particles when the distance between them and fluid particles falls below twice the smoothing length. The repulsive force occurs due to an increase in the density of the boundary particles, which increases the pressure when fluid particles approach the boundary (Crespo et al., 2007). For stability, the DBC relies on a sufficiently small time step to cope with the maximum present velocity of any fluid particles interacting with boundary particles (Crespo et al., 2007).

A primary issue with the DBC is that as particles begin moving and separate from the boundary walls, the local density decreases resulting in a pressure decrease and a “pseudo-viscosity”, which forces small groups of particles to stick to the walls (Gómez-Gesteira et al., 2009). As a result, a larger than physical boundary layer occurs in order of the smoothing length (Gómez-Gesteira et al., 2009). The DBC also does not ensure no unphysical behaviour regarding the fluid particles penetrating through the boundary. This problem does not occur when applying the other boundary methods (Gómez-Gesteira et al., 2009). However, despite these issues, the DBC has been successfully applied in studies of the interaction between waves and coastal structures (Gómez-Gesteira and Dalrymple 2004, Gómez-Gesteira et al. 2005, Crespo et al. 2007, Crespo et al. 2008).

3.8 Important calibration parameters

Sensitivity analyses on the main SPH parameters have primarily been carried out manually and for a limited range of values despite advances in SPH for engineering purposes (Roselli et al., 2018). Furthermore, choosing optimal values for the model parameters can be case dependent and accompanied by higher or lower degrees of accuracy (Roselli et al., 2018). Several attempts are usually required to select appropriate parameters depending on the user’s expertise on the SPH method and the simulated phenomenon (Roselli et al., 2018).

Roselli et al. (2018) attempted to automate the calibration process for five parameters, including the interparticle spacing (dp), the artificial viscosity coefficient (α), the coefficient for the speed of sound, the smoothing length (h_{SPH}) and the Courant-Friedrichs-Lewy (CFL) number. However, their results only had a fairly general validity for wave propagation using the DualSPHysics model. Thus, the present study proposes a

physically based framework for calibrating an SPH model and minimising the time spent tuning individual SPH parameters until convergence to the most suitable set for a specific problem is achieved. The framework focuses on the artificial viscosity coefficient (α), dimensionless smoothing length ratio (h_{SPH}/dp) and particle resolution (H/dp) due to their crucial role in the performance and efficiency of SPH simulations (De Padova et al., 2014).

3.8.1 The artificial viscosity coefficient (α)

Generally, α should be tuned for every specific problem because a wrong choice of α can lead to numerical instabilities or strong dissipation in SPH simulations, specifically in cases involving complex shearing flows (Ellero et al. 2002; Dalrymple and Rogers, 2006; De Padova et al., 2014; Altomare et al., 2015).

Excessively high values of α lead to high dissipation and wave height under-prediction (De Padova et al., 2014). However, if α is below a minimum threshold, the SPH computation becomes unstable, and the particles start moving chaotically (De Padova et al., 2014). According to Altomare et al. (2015), an $\alpha=0.01$ is the minimum value that prevents instability and high frequency noise in SPH simulations and yields the best results for applications regarding wave propagation and wave loadings exerted onto coastal structures. However, Crespo et al. (2015b) suggested an $\alpha>0.01$ is required for dam-break problems. Studies also emphasise that the optimal α depends on the smoothing length (h_{SPH}), interparticle spacing (dp) and the type of wave breaking (De Padova et al., 2009; De Padova et al., 2014; Crespo et al., 2015b; Roselli et al., 2018). De Padova et al. (2014) showed that the optimal α depends only on the type of wave breaking when the best values of h_{SPH} and dp have been defined. De Padova et al. (2014) showed that the best value of α can be considered as a linear function of the Iribarren number (ξ_0) as,

$$\alpha = 0.073\xi_0 + 0.015 \quad (3-20)$$

De Padova et al. (2014) found that an α of 0.085 and 0.055 were optimal for plunging breakers with an Iribarren number (ξ) of 0.959 and 0.548, respectively. The present study analysed the effect of α on SPH simulations of breaking waves using an α of 0, 0.01, 0.1, and 1.

3.8.2 The dimensionless smoothing length ratio (h_{SPH}/dp)

The smoothing length of the SPH kernel is computed in DualSPHysics in two dimensions using,

$$h_{SPH} = coefh\sqrt{2dp^2} = coefh \cdot dp\sqrt{2} \quad (3-21)$$

where h_{SPH} is the smoothing length, $coefh$ is an empirical coefficient, and dp is the interparticle spacing. The value of either $coefh$ or the dimensionless smoothing length ratio h_{SPH}/dp is selected in the DualSPHysics (Crespo et al., 2015b) model. The choice of $coefh$ or h_{SPH}/dp is usually case dependent on the type of application and the desired computational accuracy and efficiency (De Padova et al., 2014).

SPH applications in engineering have used an h_{SPH}/dp , ranging from around 0.7 to 1 (De Padova et al., 2014). De Padova et al. (2014) suggested that h_{SPH}/dp should be greater than or equal to 1.4 for cases of regular wave breaking on a plane slope. Although, Roselli et al. (2018) suggested, based on experience, that an h_{SPH}/dp of 1.7 up to 2.5 yields more accurate results with low wave decay when using SPH to simulate wave propagation in large numerical domains. Roselli et al. (2018) also suggested that the choice of smoothing length (h_{SPH}) might be more significant than the diffusive schemes for reliable wave propagation using SPH. The present study analysed the effect of h_{SPH}/dp on SPH simulations of breaking waves using an h_{SPH}/dp of 1, 2, and 3.

3.8.3 The particle resolution (H/dp)

The interparticle spacing dp at time $t=0$ is the grid size used to locate the particles inside the domain. After the simulation commences, the particles in the domain are free to move, and dp determines the total amount of fluid and boundary particles in the domain and hence the number of particles per the simulated wave height or particle resolution (H/dp).

Convergence studies are generally applied to analyse the influence of H/dp on SPH simulations. De Padova et al. (2014) and Altomare et al. (2015) showed that increasing the spatial resolution by applying smaller values of dp improves the accuracy of SPH simulations. According to De Padova et al. (2014), the numerical dissipation effects become smaller and smaller as H/dp increases. However, the optimal H/dp is case dependent because using SPH as a numerically convergent method requires a computational cost that increases sublinearly with the increasing number of particles (Zhu et al., 2015).

De Padova et al. (2014) found that the optimal H/dp ranged from 2 to 5 for six cases of regular breaking waves, using a constant $h_{SPH}/dp=1.4$ and $\alpha=0.055$. Altomare et al. (2015) used a H/dp ranging from 17 to 24 to simulate the impact of waves on vertical structures and storm return walls in two dimensions using an $\alpha=0.01$. They achieved a good correspondence between the simulated results and measured data. However, the simulated results did not perfectly match the measured data. The minimum recommended H/dp is 10 for wave propagation applications based on experience (Roselli

et al., 2018). The present study analysed the effect of H/d_p on SPH simulations of breaking waves using an H/d_p of 10, 15, 30, and 90.

CHAPTER 4

METHODOLOGY

This chapter presents the method used to obtain physical wave data and then employ a weakly compressible two-dimensional smoothed particle hydrodynamics (SPH) model to simulate wave breaking. The first section describes the physical model set-up, data acquisition, and data post-processing. The following section describes the SPH model set-up, calibration, sensitivity analysis, and performance tests. Thereafter, the study limitations and shortcomings are listed.

4.1 Physical wave model

A physical wave model was set up in a wave tank situated in the Environmental Fluids Mechanics Laboratory at the University of KwaZulu-Natal. The wave tank is 15 m long, 0.2 m wide, and 0.3 m high, with transparent plexiglass walls. The laboratory wave tank constrained the hydrodynamics to two dimensions. A beach was created at the shoreward end of the wave tank using a 1/10 plexiglass slope. The toe of the beach slope was positioned at 9.3 m from a piston-type wave paddle. Figure 4-1 shows a schematic of the wave tank where x is the horizontal distance from the wave paddle, z is the vertical distance from the tank bottom, η is the wave elevation above h_0 , the still water depth, and FOV 1 and FOV 2 are two field of views used to measure the physical wave profile. The first field of view (FOV 1) considers the non-shoaling wave profile over the horizontal wave tank section. The second field of view (FOV 2) considers the shoaling and breaking wave profile on the beach slope.

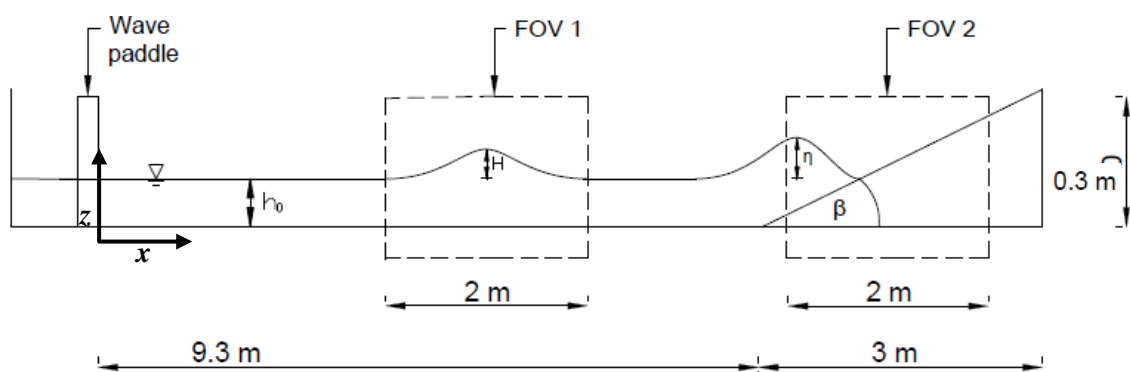


Figure 4-1: Schematic side view of the laboratory wave tank and camera positioning (FOV 1 and FOV 2) used to record physical wave data of a plunging solitary wave.

4.1.1 Mechanical wave generation

Goring's (1978) wavemaker theory (refer to section 2.5.1.1) was applied to a piston-type wave paddle to generate a solitary wave from a resting/still state in a laboratory wave

tank. This was repeated ten times. The wave height (H) was 0.09 m, the still water depth (h_0) was 0.15 m, and the slope parameter (S_0) was 0.118, which falls within the range ($0.025 < S_0 < 0.3$) associated with plunging breakers (refer section 2.4.2.2). Table 4 1 summarises the wave characteristics of the solitary wave generated in a laboratory wave tank.

Table 4-1: Wave characteristics of a solitary wave generated in a laboratory wave tank.

Wave height, H [m]	0.09
Still water depth, h_0 [m]	0.15
Beach slope, $\tan(\beta)$	1/10
Slope parameter, S_0	0.118

This study used a solitary wave to prevent any reflection and any trailing second-order free waves in the wave tank due to the limiting 0.3 m tank depth (refer to section 2.2.4). Moreover, there is a resemblance between the theoretically derived solitary wave profile and the observed wave profile outside the breaker zone (Munk, 2006). Furthermore, the chosen wave characteristics were generic in purpose and not site-specific to any prototype beach. Hence, no scaling criterion was applied. However, the measurements can be scaled to use as indications of wave breaking in real cases or for benchmarking theoretical models of wave breaking on sloping beaches. This study used the measured data to calibrate a weakly compressible two-dimensional SPH wave model.

4.1.2 Data acquisition

A Nikon D7000 CMOS single-lens reflex digital camera was used to record physical wave data. Table 4-2 shows the camera settings used to record ten runs of a physical plunging solitary wave in the laboratory wave tank. The physical wave was captured at 1 m intervals over the horizontal wave tank section, and the physical wave profile was captured over 2 m in two field of views (FOV) shown in Figure 4-1. To illuminate the free surface, LED lights were placed on top of the wave tank.

Table 4-2: Camera settings used to record physical wave data of a plunging solitary wave in a laboratory wave tank.

Focal length [mm]	50
Aperture	f/5.6
Shutter speed [s]	1/640
Exposure time [ms]	1.56
Frame rate [fps]	24
Resolution [pixels]	1920 x 1080
FOV [m]	2

4.1.3 Image post-processing

The WebPlotDigitizer (Rocha et al., 2014) software was used for digitising the physical wave surface, in terms of horizontal (x) and vertical (z) point coordinates, from raw images of the plunging solitary wave.

4.1.3.1 Wave energy dissipation

The physical wave height (H) was measured at 1 m intervals over the horizontal wave tank section. The measured data was used to calculate the physical wave energy (E) over the horizontal wave tank section. The wave energy of the solitary wave was calculated using the expression derived by Boussinesq (1871),

$$E = \frac{8}{3} \rho g h_0^3 \frac{H}{h_0} \sqrt{\frac{H}{3h_0}} \quad \text{between } -\infty \leq \frac{x}{h_0} \leq \infty \quad (4-1)$$

where E is the total wave energy of a solitary wave above the still water depth, ρ is the water density, g is the acceleration due to gravity, H is the solitary wave height, and h_0 is the still water depth. The wave energy dissipation (D) was calculated over the horizontal wave tank section as a percentage of the initial wave energy at 1 m from the wave paddle.

4.1.3.2 Wave profile

The spatially varying wave profile was measured at four phases of wave evolution in the wave tank. The first phase was captured in FOV 1 (refer to Figure 4-1) at the instant the solitary wave crest was 5 m from the wave paddle. The second, third, and fourth phases were captured in FOV 2 (refer to Figure 4-1) at 0.16, 0.08, and 0.04 [s] prior to wave impingement on the beach slope, respectively. The time varying wave profile was also measured at 1.238 m from the toe of the beach slope, during the interval 7.92 to 8.88 s after wave generation in the laboratory wave tank.

4.1.3.3 Wave repeatability

The wave repeatability was investigated for ten runs of a plunging solitary wave in a laboratory wave tank by averaging the measured wave data over the ten runs and computing the standard deviation as,

$$\sigma = \sqrt{\frac{\sum(x_i - \mu)^2}{N}} \quad (4-2)$$

where σ is the standard deviation, x_i is a data point, μ is the mean of all the data points, and N is the number of data points. A standard deviation close to zero indicated that the physical data points were close to the mean. In contrast, a high or low standard deviation showed that the data points were above or below the mean, respectively.

The similarity between the average and instantaneous wave profiles of ten plunging solitary waves in the laboratory wave tank was measured by cross-correlating the average profile to each instantaneous profile using,

$$p_{x\eta} = \frac{\overline{\bar{\eta}(x, t_i) \cdot \eta(x, t_i)} - \mu_{\bar{\eta}}\mu_{\eta}}{\sigma_{\bar{\eta}}\sigma_{\eta}} \quad (4-3)$$

where $p_{x\eta}$ is the correlation coefficient ranging from -1 to 1, $\mu_{\bar{\eta} \cdot \eta}$ is the mean of the dot product between the average wave elevation $\bar{\eta}$ and instantaneous wave elevation η at a point in time t_i , x is the position vector, $\mu_{\bar{\eta}}$ and μ_{η} are the means of the average wave elevation and instantaneous wave elevation, respectively, and $\sigma_{\bar{\eta}}$ and σ_{η} are their standard deviations. A $p_{x\eta} < 0.35$ represented a low or weak correlation (Taylor, 1990). A $p_{x\eta}$ ranging from 0.36 to 0.67 represented a moderate correlation. A $p_{x\eta}$ ranging from 0.68 to 0.90 depicted a strong correlation, and a $p_{x\eta} > 0.90$ showed that the correlation was very high with a strong positive relationship between the two cross-correlated variables (Taylor, 1990). Hence, a $p_{x\eta} > 0.90$ indicated that the measured wave data in this study was highly reproducible/repeatable. However, the cross-correlation could only be performed on the monotonically increasing section of the spatially varying breaking wave profiles. Hence, the similarity between average and instantaneous breaking wave profiles was not measured with complete accuracy.

4.2 Smoothed particle hydrodynamics (SPH) model

A weakly compressible two-dimensional SPH model was set up following the conditions and wave characteristics of the physical wave model. The numerical wave tank and wave paddle were created using the dynamic boundary condition (refer to section 3.7.1) and

boundary particles comprising three layers of stationary water particles. The piston motion of the wave paddle from the experiment was imposed as a moving-wall boundary condition per Goring's (1978) solitary wave theory (refer to section 2.5.1.1). Table 4-3 shows the selected SPH parameters and SPH calibration parameters. All SPH computations were performed using the GPU implementation of the open-source code, DualSPHysics (Crespo et al., 2015b) with an Nvidia GeForce RTX 2080 GPU.

Table 4-3: The selected SPH parameters and calibrated SPH parameters for a two-dimensional SPH model using DualSPHysics (Crespo et al., 2015b).

Kernel function	Wendland quintic
Time step algorithm	Symplectic
Viscosity scheme	Artificial viscosity
Coefficient of sound	20
CFL number	0.2
Delta-SPH, $\delta\phi$	0.1
Simulation runtime [s]	15
Data output rate [fps]	24
Boundary condition	No-slip, dynamic boundary condition (DBC)
Artificial viscosity coefficient (α)	Calibrated
Dimensionless smoothing length ratio (h_{SPH}/dp)	Calibrated
Particle resolution (H/dp) based on the number of particles per the simulated wave height.	Calibrated

SPH discretises and locally integrates the Navier-Stokes equations at each particle location by considering the physical quantities of neighbouring particles (refer to chapter 3). Hence, for a given location, the numerical mass and velocity were computed using the velocity values of neighbouring water particles. SPH located the wave elevation (η) at the vertical (z) point coordinate where the mass of a water particle is half of a reference mass, as shown in Figure 4-2 below.

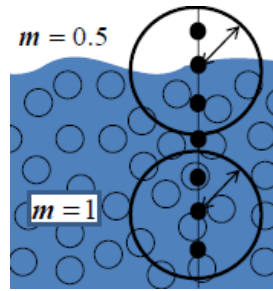


Figure 4-2: Location of the simulated free surface. The SPH model computes the numerical mass of water particles at different vertical positions using the mass values of neighbouring water particles, and the surface is defined at the vertical (z) point coordinate for which the mass of a water particle is half of a reference mass (adapted Alonso et al., 2020).

The vorticity of each particle is the curl of velocity and is defined in SPH notation as (Monaghan, 1992),

$$w_a = \sum_b m_b (\mathbf{v}_a - \mathbf{v}_b) \times \nabla_a W_{ab}$$

where w is vorticity interpolated at a particle (a), \mathbf{v} is the velocity, and W is the smoothing function. The subscripts a and b denote different individual particles.

Based on the simulated velocities, the instantaneous bed shear stress (τ_b) was calculated at $z/h_0=0.03$ above the beach slope in the surf zone using Equation (2-6) (refer to Chapter 2 section 2.3).

4.2.1 Model calibration and sensitivity analysis

Various combinations of α , h_{SPH}/dp , and H/dp were considered for the SPH model, using the values shown in Table 4-4 for each parameter, respectively. For each combination of α , h_{SPH}/dp , and H/dp , the numerical wave energy dissipation and simulated wave surface were analysed and compared to measured data in a laboratory wave tank. Suitable values of α , h_{SPH}/dp , and H/dp were chosen based on the results. Thereafter the case dependency of the calibrated SPH parameters was analysed with regards to the viscosity treatment method used in the SPH model and the type of wave breaking simulated.

Table 4-4: The values considered for each SPH calibration parameter.

Artificial viscosity coefficient (α)	0, 0.01, 0.1, 1
Dimensionless smoothing length ratio (h_{SPH}/dp)	1, 2, 3
Particle resolution (H/dp)	10, 15, 30, 90

The calibrated h_{SPH}/dp and H/dp were used with the laminar viscosity and SPS turbulence scheme (refer to section 3.2.2) to simulate a plunging solitary wave. The simulated wave surface was compared to measured data in a laboratory wave tank and the simulated wave surface using the standard artificial viscosity approach (refer to section 3.2.1). Thereafter, the calibrated α , h_{SPH}/dp , and H/dp were used to simulate various breaking plunging and spilling waves to test their case dependency based on the type of wave breaking. The relative wave height (H/h_0) and beach slope ($\tan(\beta)$) in the SPH model were varied, respectively, to simulate solitary waves with varying slope parameters (S_0). Table 4-5 shows the relative wave height (H/h_0), beach slope, slope parameter (S_0), and associated type of wave breaking for the simulated solitary waves. The simulated wave profile, number of particles in the numerical domain, and computation time were analysed for the cases listed in Table 4-5, and the type of wave breaking (spilling/plunging) associated with the various slope parameters (S_0) was used to gauge the simulation performance in each case.

Table 4-5: Different cases of breaking waves used to test the performance of the SPH model. The relative wave height (H/h_0), beach slope ($\tan(\beta)$), slope parameter (S_0), and associated type of wave breaking are shown for the various cases.

Case	Relative wave height (H/h_0)	Beach slope ($\tan(\beta)$)	Slope parameter (S_0)	Breaker type
Original/physical wave	0.6	1/10	0.118	Plunging
Test 1	0.8	1/10	0.136	Plunging
Test 2	0.4	1/10	0.118	Plunging
Test 3	0.6	1/5	0.19	Plunging
Test 4	0.6	1/20	0.05	Plunging
Test 5	0.6	1/40	0.024	Spilling
Test 6	0.6	1/50	0.019	Spilling

Finally, the individual effect of α , h_{SPH}/dp , and H/dp on the SPH simulation was analysed using the values shown in Table 4-4 for each parameter, respectively. Each parameter was individually varied while keeping the other two parameters constant, and the numerical wave energy dissipation and simulated wave surface were analysed relative to measured data in a laboratory wave tank.

4.2.2 Model performance

The performance of a two-dimensional SPH model was analysed based on the simulated flow field beneath breaking waves. The first breaking wave case followed the same wave conditions produced in a laboratory wave tank, a plunging solitary wave with a relative wave height (H/h_0) of 0.6 and slope parameter (S_0) of 0.118. Due to experimental limitations, the simulated flow field could not be validated using laboratory measurements for the same wave characteristics. Hence, the simulated velocity, vorticity, and instantaneous bed shear stress (τ_b) during wave breaking were analysed relative to previous experimental results for plunging waves (e.g., Ting, 2013; Lin. et al., 2015; LeClaire and Ting, 2017).

The second breaking wave case was a plunging solitary wave with a relative wave height (H/h_0) of 0.262 and slope parameter (S_0) of 0.078. The wave characteristics and tank set up followed the experimental conditions by Lin et al. (2015). Hence, the simulated wave profile and flow field were compared to their measured wave data. The simulated results were also compared to the first simulated case of a plunging solitary wave.

The last breaking wave case was a spilling solitary wave with a relative wave height (H/h_0) of 0.6 and slope parameter (S_0) of 0.019. The simulated velocity, vorticity, and instantaneous bed shear stress (τ_b) during wave breaking were analysed relative to previous experimental results for spilling waves (e.g., Sato et al. 1990; Yu et al., 1993; Dabiri and Gharib, 1997; Ting, 2013; LeClaire and Ting, 2017). The simulated results and model performance were also compared to the simulated cases of plunging solitary waves.

4.3 Limitations and shortcomings

The limitations and shortcomings of this study include:

- Scale effects in the laboratory experiment will occur if the physical wave model is scaled up to a prototype beach due to limitations of scaling certain characteristics such as surface tension and surface roughness. Surface tension and surface roughness can have considerable influence in the model and a negligible influence in the prototype (Hughes, 1993). The scale effects may be more significant in the very thin flow during run-up on sloping beds in the laboratory swash zone (Pedersen, 2013).
- The hydrodynamics were constrained to two-dimensions in the laboratory experiment and SPH model. Hence, the angle of attack of the wave was unaccounted for, and

the three-dimensional nature and coherent structures associated with the breaking wave flow field could not be analysed.

- Wave transformation was analysed on a plane, rigid, and impermeable slope that extended from deeper water to the water surface at a constant angle. Hence, the results may vary in cases involving complex bathymetry.
- The results are limited to solitary waves, which do not exhibit wave skewness (see section 2.4.1.1). Hence, wave skewness was unaccounted for in this study. However, in shallow, wave-dominated conditions, both wave skewness and wave asymmetry, near the bed, have important implications for sediment transport (Isobe and Horikawa, 1982; Gonzalez-Rodriguez and Madsen, 2007; Nielsen, 2002; van Rijn et al., 2011; Malarkey and Davies, 2012).
- Due to experimental limitations, only physical wave elevation/profile data was used to calibrate the SPH model.

CHAPTER 5

PHYSICAL WAVE MODEL: RESULTS AND DISCUSSION

This chapter presents the physical wave model results of a plunging solitary wave in a laboratory wave tank. The results are presented as digital summaries of the physical wave height decay and corresponding wave energy dissipation, and the physical wave profile in the space and time domain.

5.1 The physical wave height decay and wave energy dissipation

Figure 5-1 shows the average wave height (H) and wave energy dissipation (D) over the horizontal wave tank section for ten runs of a plunging solitary wave ($S_0=0.118$) in a laboratory wave tank. The standard deviation of the average values is also shown. The average physical wave height (H) at 1 m from the wave paddle was 0.09 m. The average physical wave height at 9 m from the wave paddle was 0.058 m. Hence, the average physical wave height decay over a horizontal 8 m distance was 0.032 m and corresponded to a physical wave energy dissipation of approximately 44 % over the 8 m distance. The wave energy dissipation was a result of bottom friction during wave propagation.

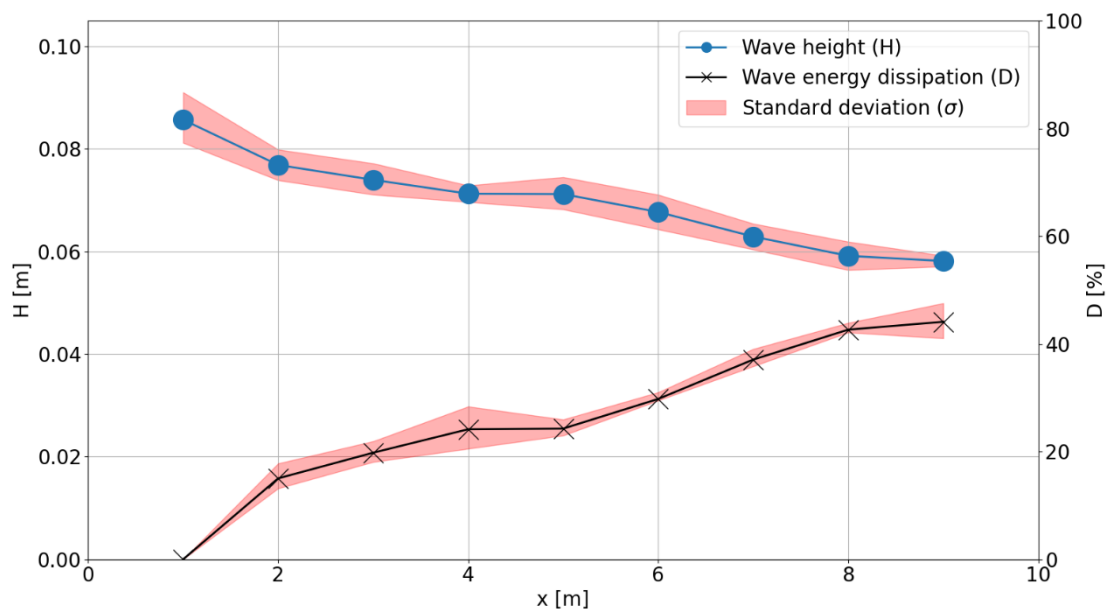


Figure 5-1: The average wave height (H) and wave energy dissipation (D) over the horizontal wave tank section for ten runs of a plunging solitary wave ($S_0=0.118$) in a laboratory wave tank. The x-axis is the horizontal distance from the wave paddle.

5.2 Spatially varying wave profile

The spatially varying wave profile was extracted at four defined phases of evolution and phase averaged for ten runs of a plunging solitary wave ($S_0=0.118$) in a laboratory wave tank. The first phase considered the offshore wave profile when the wave crest is 5 m from the wave paddle. The second phase considered the shoaling wave profile at 0.12 s before wave impingement on the beach slope. The third and fourth phases considered the breaking wave profile at 0.08 s and 0.04 s before wave impingement on the beach slope, respectively.

5.2.1 Phase one: offshore wave profile

Figure 5-2 shows the spatially varying wave profile of a plunging solitary wave ($S_0=0.118$) when the wave crest is 5 m from the wave paddle in a laboratory wave tank. Figure 5-2(a) shows an example of one of ten instantaneous waves recorded in a laboratory wave tank with the corresponding digitised wave profile overlaid. Figure 5-2(b) shows the digitised wave profile of ten instantaneous waves recorded in a laboratory wave tank. Figure 5-2(c) shows the average wave profile of ten waves recorded in a laboratory wave tank with the standard deviation. The average physical wave profile (Figure 5-2c) is qualitatively comparable to the ten instantaneous wave profiles (Figure 5-2b). Furthermore, the standard deviation of the average wave profile is low, which suggests that the physical plunging solitary wave is highly repeatable offshore in the laboratory wave tank.

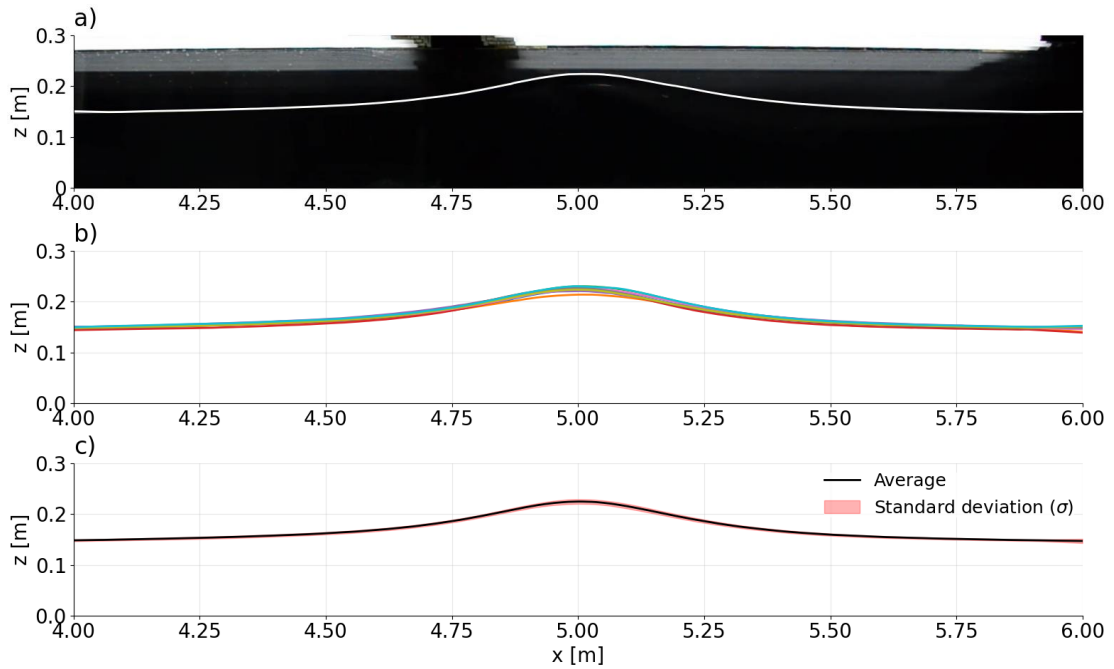


Figure 5-2: The spatially varying wave profile of a plunging solitary wave ($S_0=0.118$) when the wave crest is 5 m from the wave paddle in a laboratory wave tank. The image shows a) one of ten instantaneous waves recorded in the laboratory wave tank with the digitised wave profile overlaid, b) the digitised wave profile of ten instantaneous waves recorded in a laboratory wave tank, and c) the average wave profile of ten instantaneous waves recorded in a laboratory wave tank with the standard deviation. The x-axis is the horizontal distance from the wave paddle.

Figure 5-3 shows the average spatially varying wave profile of a plunging solitary wave ($S_0=0.118$) compared to the instantaneous spatially varying wave profiles with the highest and lowest correlation to the average profile, when the wave crest is 5 m from the wave paddle in a laboratory wave tank. The figure shows a strong correlation ($p_{x\eta}>0.99$) between the average wave profile and all ten instantaneous wave profiles, further suggesting that the physical plunging solitary wave is highly repeatable offshore in the laboratory wave tank.

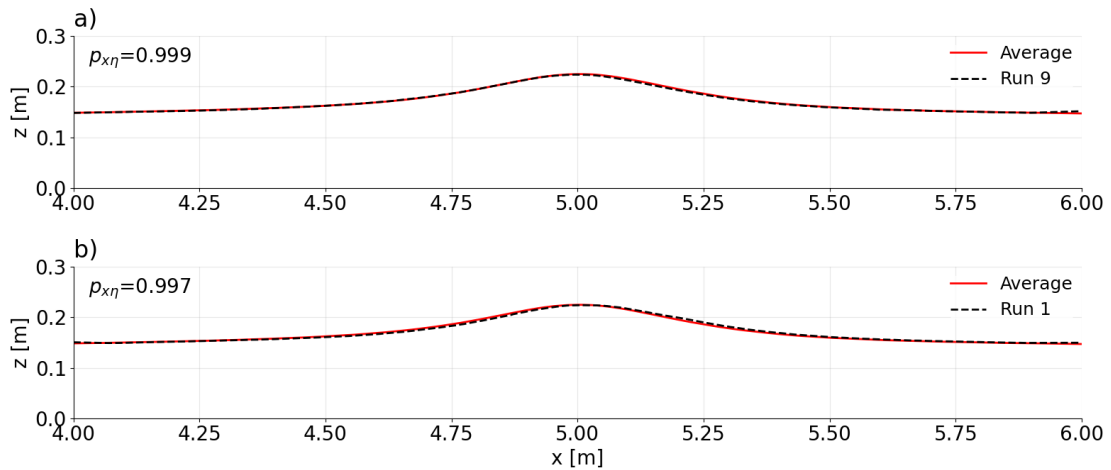


Figure 5-3: The average spatially varying wave profile of a plunging solitary wave ($S_0=0.118$) compared to the instantaneous spatially varying wave profiles with the a) highest and b) lowest correlation to the average when the wave crest is 5 m from the wave paddle in a laboratory wave tank. The x-axis is the horizontal distance from the wave paddle.

5.2.2 Phase two: shoaling wave profile

Figure 5-4 shows the spatially varying wave profile of a plunging solitary wave ($S_0=0.118$) at 0.16 s before wave impingement on a plane beach slope in a laboratory wave tank. Figure 5-4(a) shows an example of one of ten instantaneous waves recorded in a laboratory wave tank with the digitised wave profile overlaid. Figure 5-4(b) shows the digitised wave profile of ten instantaneous waves recorded in a laboratory wave tank. Figure 5-4(c) shows the average wave profile of ten waves recorded in a laboratory wave tank with the standard deviation. The shape and position of the wave front slightly vary among the ten instantaneous wave profiles (Figure 5-4b). Hence, the average wave profile (Figure 5-4c) are different from the instantaneous wave profiles (Figure 5-4b) and do not preserve the actual shape of the physical wave. Although, the shape and position are still qualitatively comparable among the ten instantaneous wave profiles (Figure 5-4b). This suggests that the ten instantaneous waves generated in the laboratory wave tank are repeatable during wave shoaling but were recorded slightly out of phase. The observed margin of error is related to the 24 fps frame rate used to capture the waves and minor errors in post-processing the images of the physical wave.

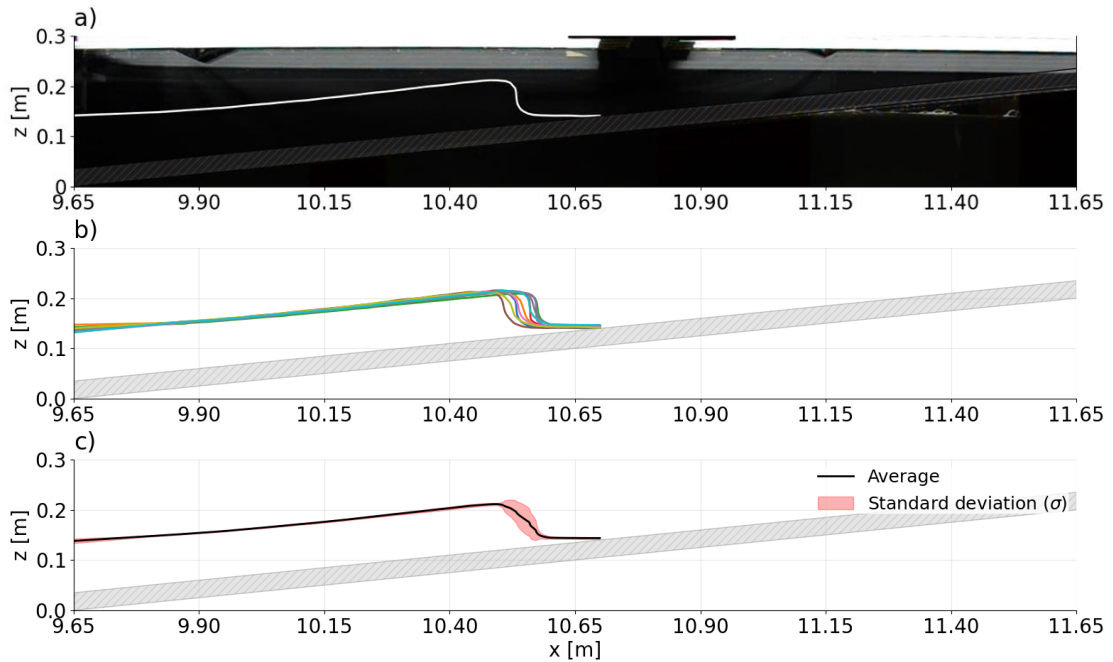


Figure 5-4: The spatially varying wave profile of a plunging solitary wave ($S_0=0.118$) at 0.16 s before wave impingement on a plane beach slope in a laboratory wave tank. The image shows a) one of ten instantaneous waves recorded in the laboratory wave tank with the digitised wave profile overlaid, b) the digitised wave profile of ten instantaneous waves recorded in a laboratory wave tank, and c) the average wave profile of ten instantaneous waves recorded in a laboratory wave tank with the standard deviation. The x-axis is the horizontal distance from the wave paddle.

Figure 5-5 shows the average spatially varying wave profile of a plunging solitary wave ($S_0=0.118$) compared to the instantaneous spatially varying wave profiles with the highest and lowest correlation to the average profile, at 0.16 s before wave impingement on a plane beach slope in a laboratory wave tank. The figure shows a strong correlation ($p_{x\eta}>0.9$) between the average and all ten instantaneous wave profiles, further suggesting that the physical plunging solitary wave is highly repeatable during wave shoaling in the laboratory wave tank.

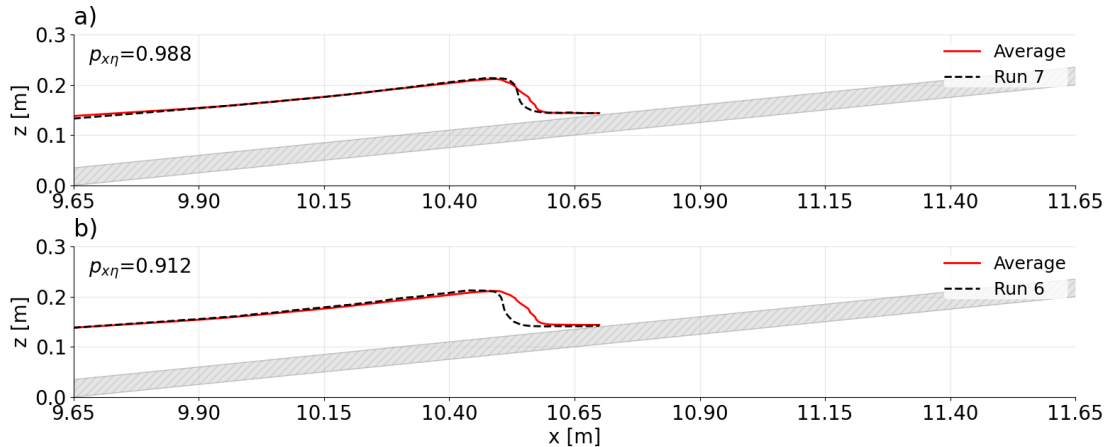


Figure 5-5: The average spatially varying wave profile of a plunging solitary wave ($S_0=0.118$) compared to the instantaneous spatially varying wave profiles with the a) highest and b) lowest correlation to the average profile, at 0.16 s before wave impingement on a beach slope in a laboratory wave tank. The x-axis is the horizontal distance from the wave paddle.

5.2.3 Phase three: breaking wave profile

Figure 5-6 shows the spatially varying wave profile of a plunging solitary wave ($S_0=0.118$) at 0.08 s before wave impingement on a plane beach slope in a laboratory wave tank. Figure 5-6(a) shows an example of one of ten instantaneous waves recorded in a laboratory wave tank with the digitised wave profile overlaid. Figure 5-6(b) shows the digitised wave profile of ten instantaneous waves recorded in a laboratory wave tank. Figure 5-6(c) shows the average wave profile of ten waves recorded in a laboratory wave tank with the standard deviation. Again, the shape and position of the wave front slightly vary among the ten instantaneous wave profiles (Figure 5-6b). Hence, the average wave profile (Figure 5-6c) are different from the instantaneous wave profiles (Figure 5-6b) and do not preserve the actual shape of the physical wave. Although, the shape and position are still qualitatively comparable among the ten instantaneous wave profiles (Figure 5-6b). This suggests that the ten instantaneous waves generated in the laboratory wave tank are repeatable during wave breaking but were recorded slightly out of phase. The observed margin of error is again related to the 24 fps frame rate used to capture the waves and minor errors in post-processing the images of the physical wave.

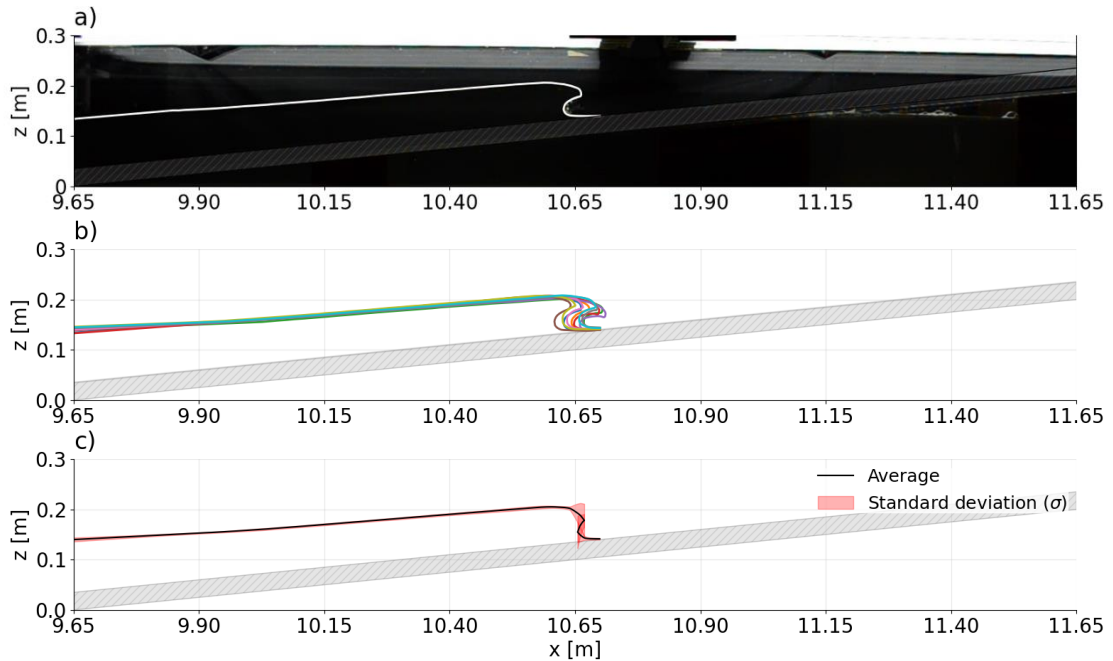


Figure 5-6: The spatially varying wave profile of a plunging solitary wave ($S_0=0.118$) at 0.08 s before wave impingement on a plane beach slope in a laboratory wave tank. The image shows a) one of ten instantaneous waves recorded in the laboratory wave tank with the digitised wave profile overlaid, b) the digitised wave profile of ten instantaneous waves recorded in a laboratory wave tank, and c) the average wave profile of ten instantaneous waves recorded in a laboratory wave tank with the standard deviation. The x-axis is the horizontal distance from the wave paddle.

Figure 5-7 shows the average spatially varying wave profile of a plunging solitary wave ($S_0=0.118$) compared to the instantaneous spatially varying wave profiles with the highest and lowest correlation to the average profile, at 0.08 s before wave impingement on a plane beach slope in a laboratory wave tank. The figure shows a strong correlation ($p_{x\eta}>0.9$) between the average and individual physical spatially varying wave profiles, further suggesting that the physical plunging solitary wave is highly repeatable during wave breaking in the laboratory wave tank. However, only the monotonically increasing section of the wave profiles was cross-correlated. Therefore, the correlation coefficient is not a completely accurate measurement of the similarity between the wave profiles during wave breaking.

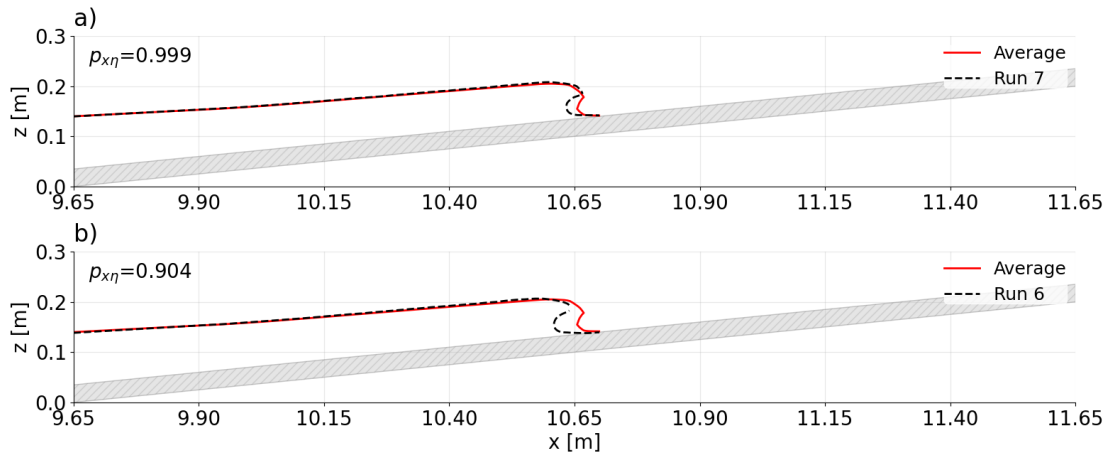


Figure 5-7: The average spatially varying wave profile of a plunging solitary wave ($S_0=0.118$) compared to the instantaneous spatially varying wave profiles with the a) highest and b) lowest correlation to the average profile, at 0.08 s before wave impingement on a beach slope in a laboratory wave tank. The x-axis is the horizontal distance from the wave paddle.

5.2.4 Phase four: breaking wave profile

Figure 5-8 shows the spatially varying wave profile of a plunging solitary wave ($S_0=0.118$) at 0.04 s before wave impingement on a plane beach slope in a laboratory wave tank. Figure 5-8(a) shows an example of one of ten instantaneous waves recorded in a laboratory wave tank with the digitised wave profile overlaid. Figure 5-8(b) shows the digitised wave profile of ten instantaneous waves recorded in a laboratory wave tank. Figure 5-8(c) shows the average wave profile of ten waves recorded in a laboratory wave tank with the standard deviation. Again, the shape and position of the wave front slightly vary among the ten instantaneous wave profiles (Figure 5-8b). Hence, the average wave profile (Figure 5-8c) are different from the instantaneous wave profiles (Figure 5-8b) and do not preserve the actual shape of the physical wave. Although, the shape and position are still qualitatively comparable among the ten instantaneous wave profiles (Figure 5-8b). This suggests that the ten instantaneous waves generated in the laboratory wave tank are repeatable before wave impingement on the beach slope but were recorded slightly out of phase. The observed margin of error is again related to the 24 fps frame rate used to capture the waves and minor errors in post-processing the images of the physical wave.

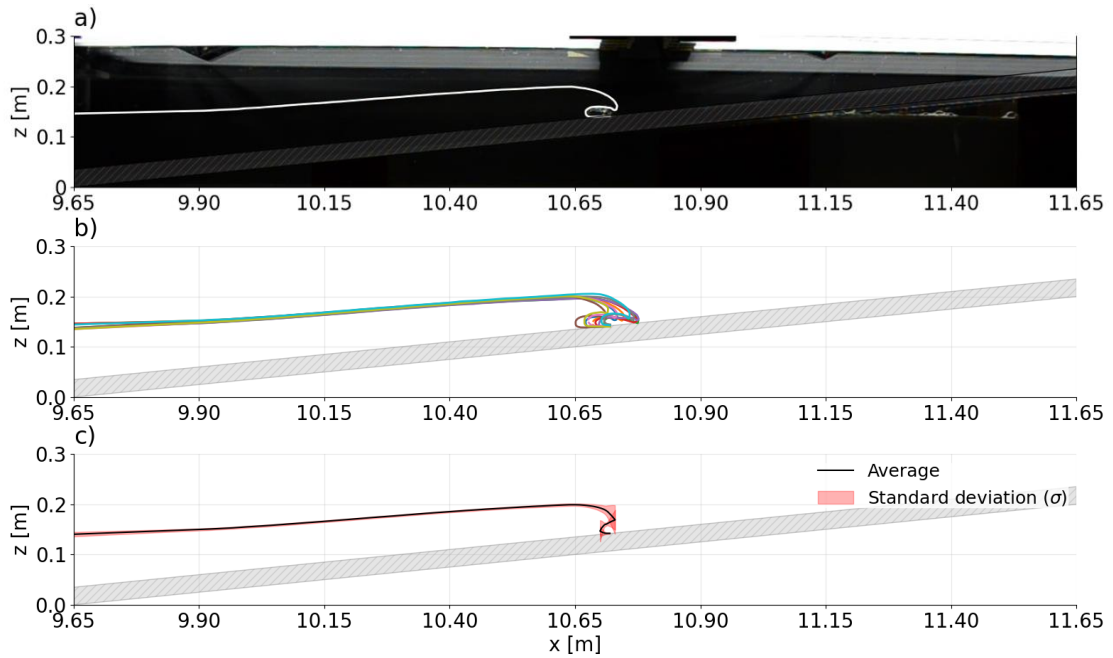


Figure 5-8: The spatially varying wave profile of a plunging solitary wave ($S_0=0.118$) at 0.04 s before wave impingement on a plane beach slope in a laboratory wave tank. The image shows a) one of ten instantaneous waves recorded in the laboratory wave tank with the digitised wave profile overlaid, b) the digitised wave profile of ten instantaneous waves recorded in a laboratory wave tank, and c) the average wave profile of ten instantaneous waves recorded in a laboratory wave tank with the standard deviation. The x-axis is the horizontal distance from the wave paddle.

Figure 5-9 shows the average spatially varying wave profile of a plunging solitary wave ($S_0=0.118$) compared to the instantaneous spatially varying wave profiles with the highest and lowest correlation to the average wave profile, at 0.04 s before wave impingement on a plane beach slope in a laboratory wave tank. The figure shows a strong correlation ($p_{x\eta}>0.9$) between the average and individual physical spatially varying wave profiles, which further suggests that the physical plunging solitary wave is highly repeatable just before wave impingement on the beach slope in the laboratory wave tank. Again, however, only the monotonically increasing section of the wave profiles was cross-correlated. Therefore, the correlation coefficient is not a completely accurate measurement of the similarity between the wave profiles during wave breaking.

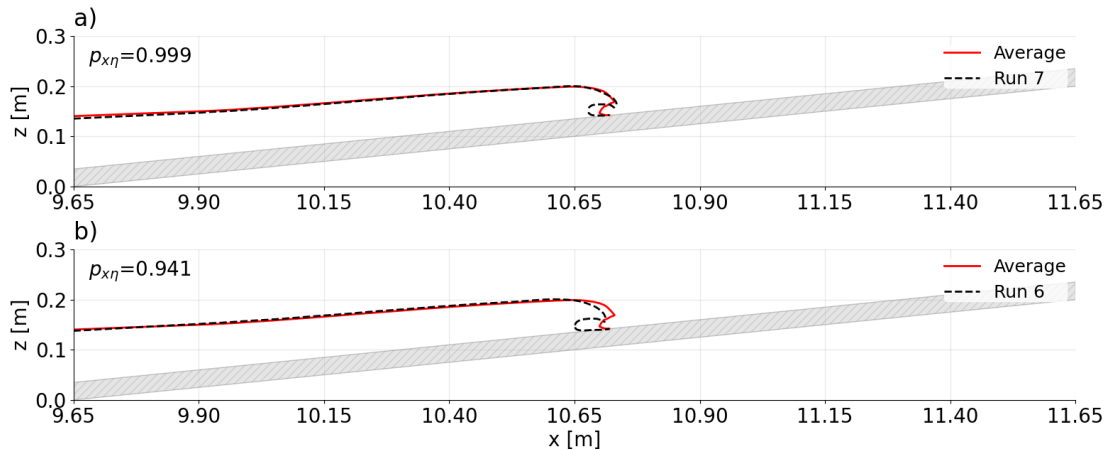


Figure 5-9: The average spatially varying wave profile of a plunging solitary wave ($S_0=0.118$) compared to the instantaneous spatially varying wave profiles with the a) highest and b) lowest correlation to the average profile, at 0.04 s before wave impingement on a beach slope in a laboratory wave tank. The x-axis is the horizontal distance from the wave paddle.

5.2.5 Final wave profiles

Figure 5-10 shows the spatially varying wave profile, representing a plunging solitary wave ($S_0=0.118$), at four phases of evolution in a laboratory wave tank. Figure 5-10(a) shows the average wave profile of ten waves recorded in a laboratory wave tank when the solitary wave crest is 5 m from the wave paddle. Figure 5-10(b-c) show the instantaneous wave profile of the seventh wave recorded in a laboratory wave tank at 0.16 s, 0.08 s, and 0.04 s before wave impingement on the beach slope, respectively. The instantaneous profile of the seventh wave was used instead of the average profile because the physical wave was captured slightly (0.04 s) out of phase on the beach slope. Hence, the average wave profile did not preserve the actual shape of the shoaling and breaking physical wave. The instantaneous spatially varying wave profile of the seventh wave preserved the actual shape of the physical wave during shoaling and breaking and had the highest correlation to the average wave profile among ten instantaneous wave profiles. Figure 5-10 qualitatively shows that the physically modelled wave exhibits the characteristics of a plunging solitary wave. As the wave travels onshore, the wave profile loses its symmetry and becomes increasingly pitched forward with a steep front face and a gentle rear face (Ruessink et al., 2012). The wave profile breaks due to a steepening wave front, and the wave front overturns, forming a plunging jet (Figure 5-10c-d) that impinges onto the beach slope (not shown).

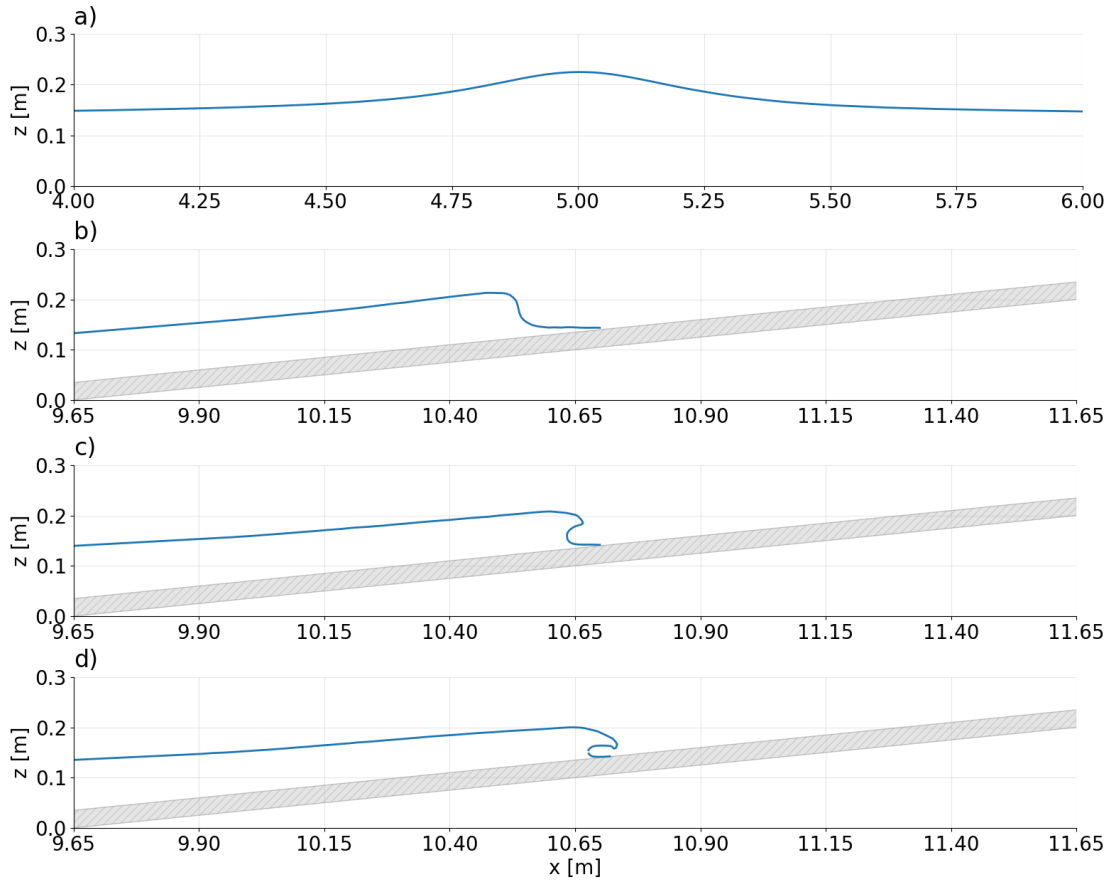


Figure 5-10: The spatially varying wave profile of a plunging solitary wave ($S_0=0.118$) in a laboratory wave tank at a) the instant the wave crest is 5 m from the wave paddle, b) 0.16 s before wave impingement on the beach slope, c) 0.08 s before wave impingement on the beach slope, and d) 0.04 s before wave impingement on the beach slope. The x-axis is the horizontal distance from the wave paddle.

Table 5-1 shows the peak wave elevation (η_{peak}) of a plunging solitary wave ($S_0=0.118$) above the still water depth (h_0) and the location of this peak value (x_{peak}) at the four phases of evolution in a laboratory wave tank shown in Figure 5-10 (a-d).

Table 5-1: The peak wave elevation (η_{peak}) of a plunging solitary wave above the still water depth (h_0) and the location of this peak value (x_{peak}) at the four phases of evolution in a laboratory wave tank shown in Figure 5-10 (a-d).

Phase	η_{peak} [m]	x_{peak} [m]
1	0.075	5.002
2	0.063	10.486
3	0.058	10.601
4	0.050	10.664

5.3 Temporal evolution of the wave surface

Figure 5-11 shows the time varying wave elevation (η) profile of a plunging solitary wave ($S_0=0.118$) at 1.238 m from the toe of the beach slope in a laboratory wave tank. Figure 5-11(a) shows the digitised wave profile of ten instantaneous waves recorded in a laboratory wave tank during the interval 7.16 s and 8.84 s after wave generation. Figure 5-6(b) shows the average wave profile of ten instantaneous waves recorded in a laboratory wave tank with the standard deviation during the interval 7.16 s and 8.84 s after wave generation. The figure shows that the shape slightly varies among the ten instantaneous wave profiles (Figure 5-6a), and the standard deviation of the average wave profile increases when the physical wave reaches the measuring location (Figure 5-6b). However, the shape is still qualitatively comparable among the ten instantaneous wave profiles (Figure 5-6a) and the average wave profile preserves the shape of the instantaneous physical wave. This further indicates that the ten instantaneous waves generated in the laboratory wave tank are repeatable before breaking on the beach slope but were recorded slightly out of phase. The observed margin of error is again related to the 24 fps frame rate used to capture the waves and minor errors in post-processing the images of the physical wave. The figure shows that the shoaling/steepening wave front reaches the measuring location at approximately $t=7.92$ s after wave generation and the peak wave elevation (η_{peak}) above the still water depth (h_0) reaches the measuring location at approximately $t=8.04$ s after wave generation. Thereafter, the tail end of the wave passes the measuring location, and a gentle reduction in the wave elevation occurs due to the asymmetrical spatially varying shape of the plunging solitary wave on the beach slope.

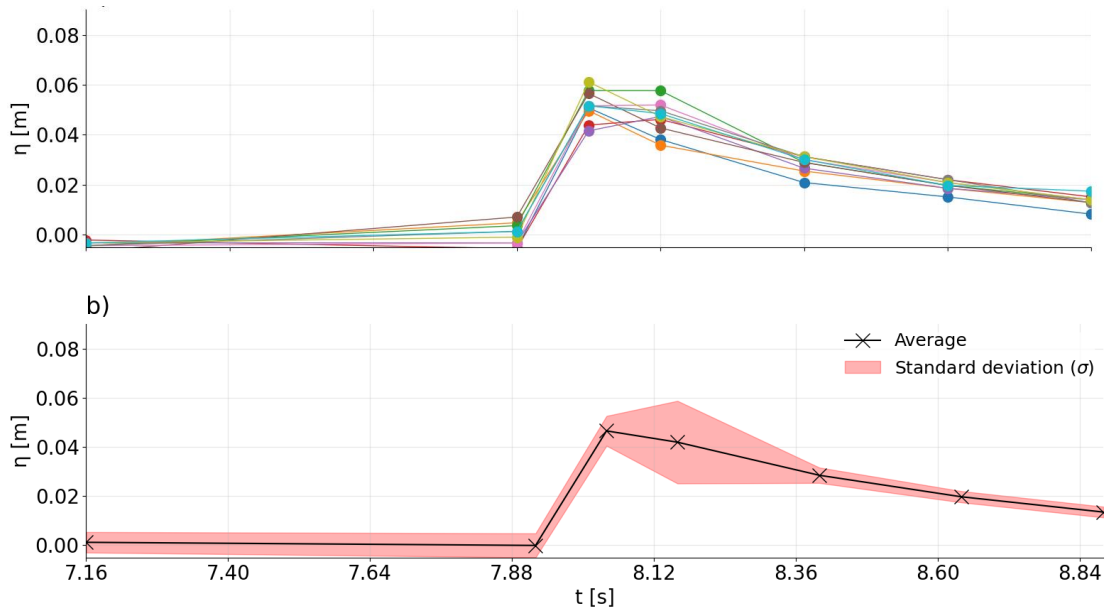


Figure 5-11: The time varying wave elevation (η) profile of a plunging solitary wave ($S_0=0.118$), at 1.238 m from the toe of the beach slope in a laboratory wave tank. The image shows a) the digitised wave profile of ten instantaneous waves recorded in a laboratory wave tank and b) the average wave profile of ten instantaneous waves recorded in a laboratory wave tank with the standard deviation., The x-axis is the time since the paddle motion stops, and the wave leaves the paddle.

Figure 5-12 shows the average time varying wave profile of a plunging solitary wave ($S_0=0.118$) compared to the instantaneous time varying wave profiles with the highest and lowest correlation to the average wave profile, at 1.238 m from the toe of the beach slope in a laboratory wave tank. The figure shows a moderately high correlation ($0.36 > p_{x,\eta} > 0.67$) between the average and instantaneous physical time varying wave profile with the lowest correlation to the average wave profile. This suggests that the physical plunging solitary wave is repeatable on the beach slope in the laboratory wave tank. Although, it is expected that the correlation coefficient would be higher without the errors relating to the 24 fps frame rate used to capture the waves and in post-processing the images of the physical wave.

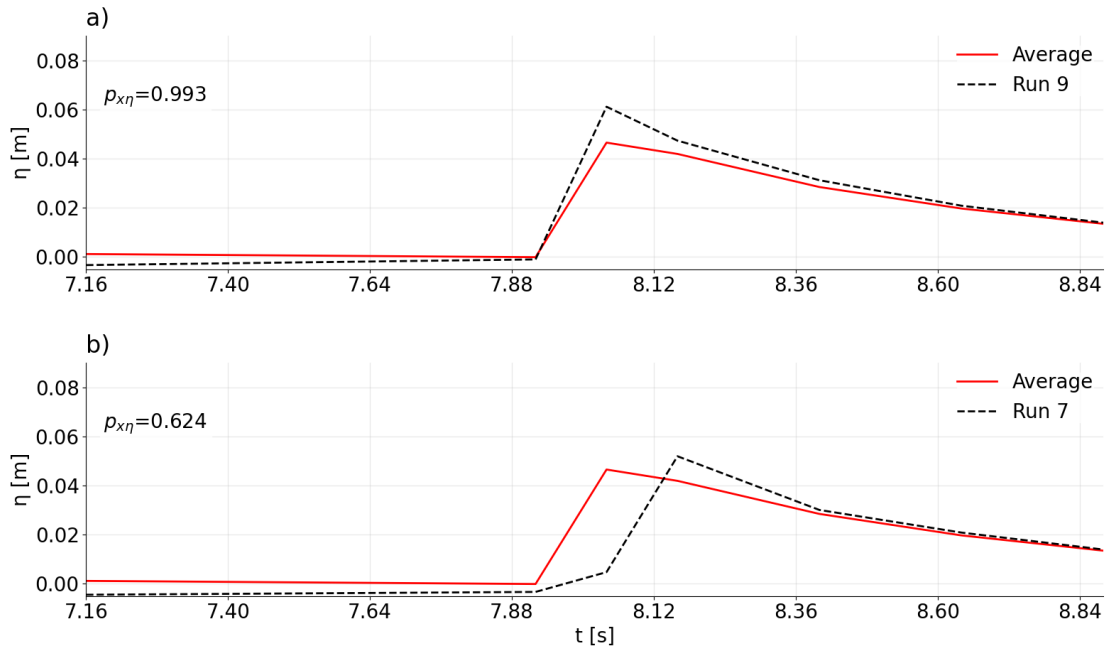


Figure 5-12: The average time varying wave profile of a plunging solitary wave ($S_0=0.118$) compared to the instantaneous time varying wave profiles with the a) highest and b) lowest correlation to the average wave profile, at 1.238 m from the toe of the beach slope in a laboratory wave tank. The x-axis is the time since the paddle motion stops, and the wave leaves the paddle.

CHAPTER 6

SPH WAVE MODEL: RESULTS AND DISCUSSION

This chapter presents the results of a two-dimensional smoothed particle hydrodynamics (SPH) model used to simulate the flow field beneath breaking waves. The first section presents the SPH model calibration and sensitivity analysis for various model parameters. Section 6.2 assesses the SPH model performance and capability based on the simulated flow field beneath breaking plunging and spilling waves.

The correlation coefficient ($\rho_{x\eta}$) was used throughout this chapter to measure the similarity between the simulated and physical wave profiles. Furthermore, the wave energy dissipation was expressed as,

$$D = 1 - \frac{E_x}{E_p} \quad (6-1)$$

where D is the wave energy dissipation [%], E_x is the total wave energy [J] above the still water depth at some horizontal distance [m] from the wave paddle, and E_p is the total wave energy [J] above the still water depth at 1 m from the wave paddle. The term x/h_0 was used to denote a non-dimensional distance from the wave paddle where x is the horizontal distance from the wave paddle [m], and h_0 is the still water depth [m]. However, the non-dimensional distance on the beach slope was defined as,

$$X = \frac{x - x_0}{h_0} \quad (6-2)$$

where X is the non-dimensional distance coordinate from the toe of the beach slope ($X=0$), and x_0 is the horizontal distance [m] from the wave paddle to the toe of the beach slope. Furthermore, the non-dimensional time was defined as,

$$T = (t - t_0) \left(\frac{g}{h_0} \right)^{1/2} \quad (6-3)$$

where T is the nondimensional time coordinate from the instant the solitary wave crest is directly above the toe of the beach slope ($T=0$), t is the total time [s] after the paddle motion stops and the wave leaves the wave paddle, and t_0 is the instant [s] the solitary wave crest is directly above the toe of the slope since leaving the wave paddle.

6.1 Model calibration and sensitivity analysis

A two-dimensional SPH model was systematically calibrated using the results of a laboratory experiment (refer to section 4.2.1). The calibrated parameters were the artificial viscosity coefficient (α), dimensionless smoothing length ratio (h_{SPH}/dp), and particle resolution (H/dp) (refer to section 3.8). The case dependency of the calibrated α , h_{SPH}/dp , and H/dp was investigated based on the viscosity treatment method (artificial viscosity scheme or laminar viscosity and sub-particle scale (SPS) turbulence scheme) and type of wave breaking type (spilling or plunging). Furthermore, the influence of α , h_{SPH}/dp , and H/dp individually on the numerical wave energy dissipation and simulated wave profile was analysed.

6.1.1 Calibrated model parameters

Table 6-1 shows the combinations of α , h_{SPH}/dp , and H/dp , from 48 trialled combinations, that yielded a numerical wave energy dissipation within 5% of the measured value ($D \approx 44\%$) of a plunging solitary wave ($S_0=0.118$) at $x/h_0=60$ from the wave paddle.

Table 6-1: Trialled combinations of α , h_{SPH}/dp , and H/dp that yielded a numerical wave energy dissipation (D) within 5% of the measured value ($D \approx 44\%$) of a plunging solitary wave ($S_0=0.118$) at $x/h_0=60$ from the wave paddle.

Combination	α	h_{SPH}/dp	H/dp	D [%]
2.2.1	0.01	2	10	39.96
2.2.2	0.01	2	15	39.58
2.3.1	0.01	3	10	49.24
2.3.2	0.01	3	15	43.72
3.2.4	0.1	2	90	45.22
3.3.4	0.1	3	90	47.70

Figure 6-1 shows the numerical wave energy dissipation (D) of a plunging solitary wave ($S_0=0.118$), using the combinations of α , h_{SPH}/dp , and H/dp in Table 6-1, in comparison to measured data. The figure compares the numerical and measured wave energy dissipation over the horizontal wave tank section. Based on the results, all combinations of α , h_{SPH}/dp , and H/dp in Table 6-1 appear suitable for use in the SPH model. However, combination 2.3.2 in Table 6-1 appears most suitable based on the numerical wave energy dissipation ($D \approx 43.72\%$) at $x/h_0=60$ from the wave paddle.

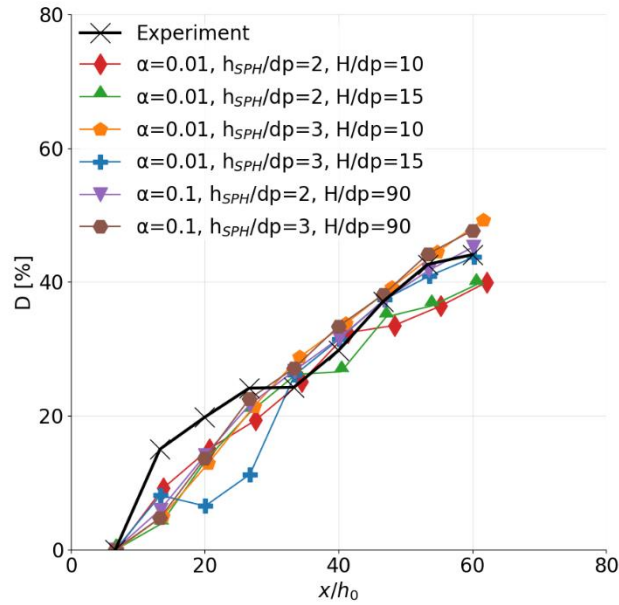


Figure 6-1: The numerical wave energy dissipation (D) of a plunging solitary wave ($S_0=0.118$), using the combinations of α , h_{SPH}/dp , and H/dp in Table 6-1, in comparison to measured data, over the horizontal wave tank section.

Table 6-2 shows the combinations of α , h_{SPH}/dp , and H/dp , from 48 trialled combinations, that yielded a simulated time varying wave elevation profile similar ($p_{x\eta} \geq 0.98$) to measured data of a plunging solitary wave ($S_0=0.118$), at $X=8.25$ on the beach slope.

Table 6-2: Trialled combinations of α , h_{SPH}/dp , and H/dp that yielded a simulated time varying wave elevation (η/h_0) profile similar ($p_{x\eta} \geq 0.98$) to measured data of a plunging solitary wave ($S_0=0.118$), at $X=8.25$ on the beach slope.

Combination	α	h_{SPH}/dp	H/dp	$p_{x\eta}$
1.1.3	0	1	30	0.98
1.2.1	0	2	10	0.98
2.1.3	0.01	1	30	0.98
2.2.1	0.01	2	10	0.98
2.2.2	0.01	2	15	0.99
2.2.3	0.01	2	30	0.98
2.3.1	0.01	3	10	0.98
2.3.2	0.01	3	15	0.98
2.3.3	0.01	3	30	0.98
3.2.4	0.1	2	90	0.99
3.3.4	0.1	3	90	0.99

Figure 6-2 shows the simulated time varying wave elevation (η/h_0) profile of a plunging solitary wave ($S_0=0.118$), using the combinations of α , h_{SPH}/dp , and H/dp in Table 6-2, in comparison to measured data. The figure compares the simulated and measured wave elevation profiles at $X=8.25$ on the beach slope during $T=0$ to $T=14$. Based on the results, all combinations of α , h_{SPH}/dp , and H/dp in Table 6-2 appear suitable for use in the SPH model. However, combination 1.1.3 in Table 6-2 appears to be most suitable qualitatively based on the shape of the simulated time varying wave elevation profile.

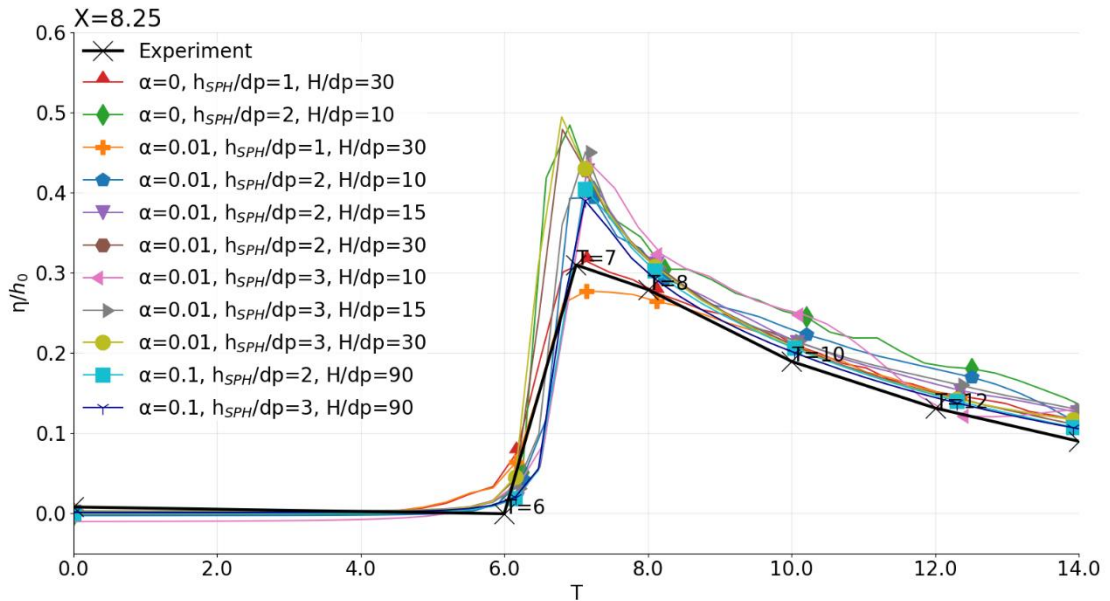


Figure 6-2: The simulated time varying wave surface elevation (η/h_0) profile of a plunging solitary wave ($S_0=0.118$), using the combinations of α , h_{SPH}/dp , and H/dp in Table 6-2, compared to measured data, at $X=8.25$ on the beach slope. The measured profile is annotated at times $T=6$, $T=7$, $T=8$, $T=10$, and $T=12$.

Table 6-3 shows the combinations of α , h_{SPH}/dp , and H/dp , from 48 trialed combinations, that yielded a simulated spatially varying wave profile similar ($p_{x\eta} \geq 0.98$) to measured data of a plunging solitary wave ($S_0=0.118$) at four defined phases of evolution in the wave tank. The first phase was when the wave crest was at $x/h_0=33.3$ from the wave paddle. The second, third, and fourth phases occurred at four timesteps, two timesteps and one timestep before wave impingement on the beach slope, respectively. The time step corresponded to the camera frame rate used to record the physical plunging solitary wave in a laboratory wave tank. In Table 6-3, the correlation coefficient is between the simulated and measured wave profiles at the fourth defined phase of evolution.

Table 6-3: Trialed combinations of α , h_{SPH}/dp , and H/dp that yielded a simulated spatially varying wave profile similar ($p_{x\eta} \geq 0.98$) to measured data of a plunging solitary wave ($S_0=0.118$), at four phases of evolution in the wave tank. The correlation coefficient ($p_{x\eta}$) denotes the similarity between the simulated and measured wave profiles at the fourth phase of evolution, one model time step before wave impingement on the beach slope.

Combination	α	h_{SPH}/dp	H/dp	$p_{x\eta}$
1.1.1	0	1	10	0.98
1.1.2	0	1	15	0.99
1.1.3	0	1	30	0.99
1.1.4	0	1	90	0.99
1.2.1	0	2	10	0.99
1.2.2	0	2	15	0.99
1.2.3	0	2	30	0.98
1.2.4	0	2	90	0.98
1.3.1	0	3	10	0.98
1.3.3	0	3	30	0.98
1.3.4	0	3	90	0.98
2.1.2	0.01	1	15	0.99
2.1.3	0.01	1	30	0.99
2.1.4	0.01	1	90	0.99
2.2.1	0.01	2	10	0.98
2.2.2	0.01	2	15	0.98
2.2.3	0.01	2	30	0.99
2.2.4	0.01	2	90	0.98
2.3.3	0.01	3	30	0.98
2.3.4	0.01	3	90	0.98
3.1.3	0.1	1	30	0.98
3.1.4	0.1	1	90	0.99
3.2.3	0.1	2	30	0.98
3.2.4	0.1	2	90	0.99
3.3.3	0.1	3	30	0.98
3.3.4	0.1	3	90	0.99

Figure 6-3 shows the simulated spatially varying wave (z/h_0) profile of a plunging solitary wave ($S_0=0.118$), using the combinations of α , h_{SPH}/dp , and H/dp in Table 6-3 in comparison to measured data. The figure compares the simulated and measured spatially varying wave profiles at the fourth defined phase of evolution, one timestep before wave impingement on the beach slope. Based on the results, nearly all combinations of α , h_{SPH}/dp , and H/dp in Table 6-3 are not suitable for use in the SPH

model, despite a high correlation coefficient ($p_{x\eta}$) between the simulated and measured wave profiles. Only the monotonically increasing section of the breaking wave profiles was cross-correlated, which explains why the wave front is poorly simulated using most combinations of α , h_{SPH}/dp , and H/dp in Table 6-3 when the correlation coefficient is high ($p_{x\eta} \geq 0.98$). Combinations 3.2.4 and 3.3.4 in Table 6-3 appear to be most suitable qualitatively based on the shape of the simulated spatially varying wave profile.

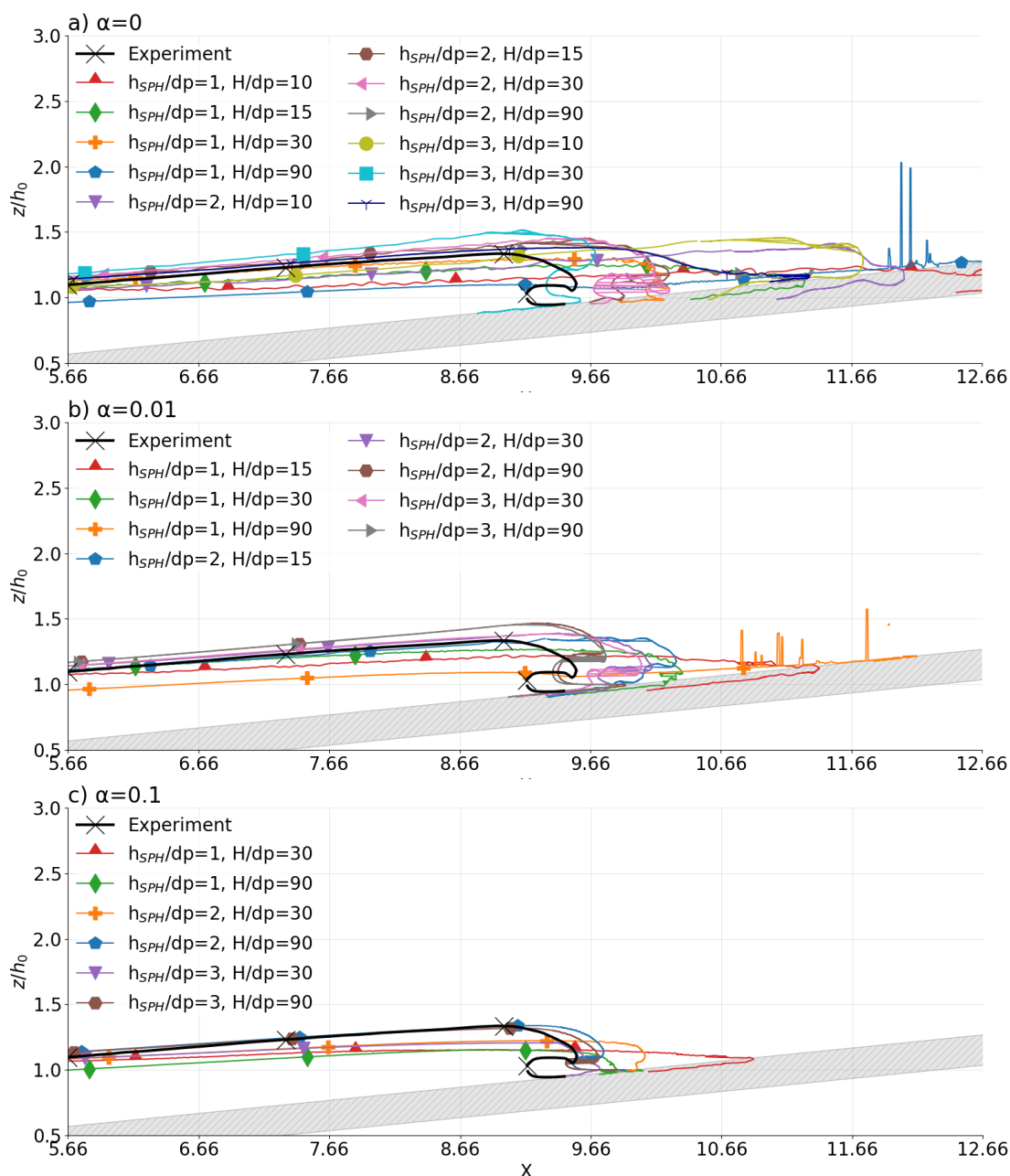


Figure 6-3 The simulated spatially varying wave (z/h_0) profile of a plunging solitary wave ($S_0=0.118$), using the combinations of α , h_{SPH}/dp , and H/dp in Table 6-3, compared to measured data, at the fourth defined phase of evolution, one timestep before wave impingement on the beach slope.

From 48 trialled combinations of α , h_{SPH}/dp , and H/dp , suitable calibrated parameters for the SPH model were chosen as $\alpha=0.1$, $h_{\text{SPH}}/dp=3$, and $H/dp=90$. This choice was based on the numerical wave energy dissipation and simulated wave profile of a plunging solitary wave ($S_0=0.118$) relative to measured data. An $\alpha=0.1$ is comparable to an $\alpha=0.085$ used by De Padova et al. (2014) to simulate a breaking plunging wave. De Padova et al. (2014) chose an $\alpha=0.085$ after defining the best value of h_{SPH}/dp to be 1.4 and the best value of H/dp to be 3. Although $h_{\text{SPH}}/dp=3$ is higher than $h_{\text{SPH}}/dp=1.4$ used by De Padova et al. (2014), the results presented here have shown that computation results are similar when $1 < h_{\text{SPH}}/dp \leq 3$. Furthermore, $H/dp=90$ is a significantly higher particle resolution than $H/dp=3$ used by De Padova et al. (2014) because this study used the Wendland quintic smoothing function (refer to section 3.1.1) for all SPH computations. In contrast, De Padova et al. (2014) applied the cubic spline smoothing function (refer to section 3.1.1), which yields a higher resolution when defined on a sphere of diameter $2h_{\text{SPH}}$ using the same number of particles (De Padova et al., 2014). However, the cubic spline smoothing function is less accurate and less effective than the quintic kernel in interpolating the second-order derivatives and can also be less stable, according to Liu and Liu (2010).

6.1.2 Case dependency of calibrated parameters

The calibrated SPH parameters $h_{\text{SPH}}/dp=3$ and $H/dp=90$ were used with an alternative viscosity scheme to simulate a plunging solitary wave ($S_0=0.118$) to test their case dependency based on the viscosity treatment method. Thereafter, the calibrated SPH parameters $\alpha=0.1$, $h_{\text{SPH}}/dp=3$, and $H/dp=90$ were used to simulate breaking plunging and spilling waves to test their case dependency based on the type of wave breaking. The relative wave height (H/h_0) and beach slope ($\tan(\beta)$) in the SPH model were varied, respectively, to simulate solitary waves with varying slope parameters (S_0).

6.1.2.1 Viscosity treatment method

Figure 6-4 and Figure 6-5 show the simulated spatially varying wave (z) profile of a plunging solitary wave ($S_0=0.118$), using the standard artificial viscosity approach (refer to section 3.2.1) and the alternative SPS approach (refer to section 3.2.2), respectively, compared to measured data, at four defined phases of evolution in a wave tank. The first phase (Figure 6-4a and Figure 6-5a) was when the wave crest was at $x/h_0=33.3$ from the wave paddle. The second (Figure 6-4b and Figure 6-5b), third (Figure 6-4c and Figure 6-5c), and fourth (Figure 6-4d and Figure 6-5d) phases occurred at four timesteps, two timesteps, and one timestep, before wave impingement on the beach slope, respectively. The timestep, as stated earlier, was the model timestep and corresponded to the frame rate used to capture the measured wave profile in a laboratory wave tank. The figures show that both viscosity treatment methods yield a simulated spatially varying wave

profile that is similar ($p_{x\eta} > 0.98$) to measured data. Although, the simulated waves break at a position slightly ahead of the measured wave. These differences are similar to the errors in capturing the measured wave profile in the laboratory wave tank using a 0.04 s camera frame rate and minor errors in post-processing the images of the measured wave profile. It is also observed that the size of the simulated plunging wave jet increases upon changing the viscosity scheme in the SPH model to the laminar viscosity and SPS turbulence scheme (Figure 6-5).

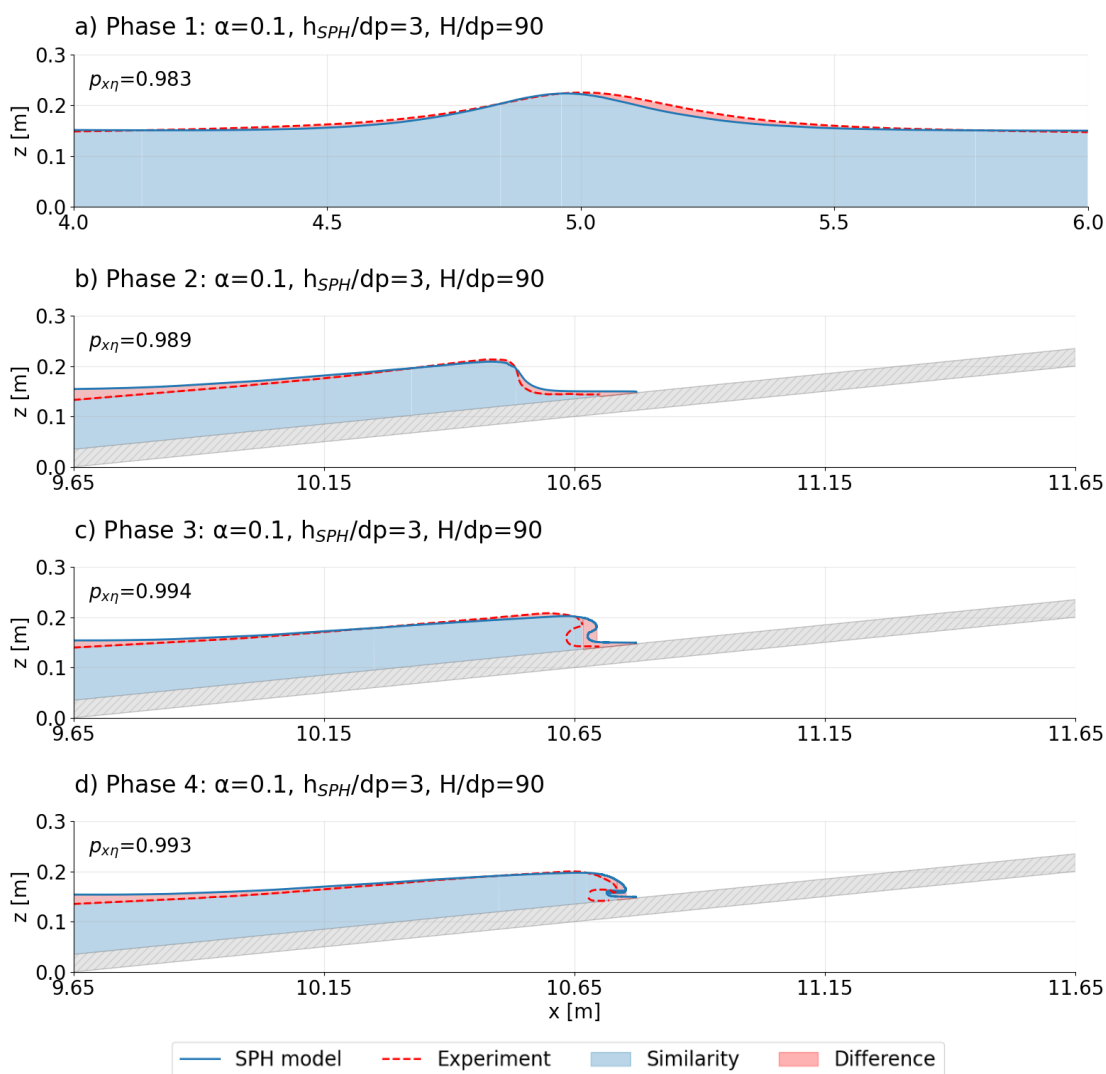


Figure 6-4: The simulated spatially varying wave (z) profile of a plunging solitary wave ($S_0=0.118$), using the standard artificial viscosity approach, compared to measured data, at four phases of wave evolution in a wave tank.

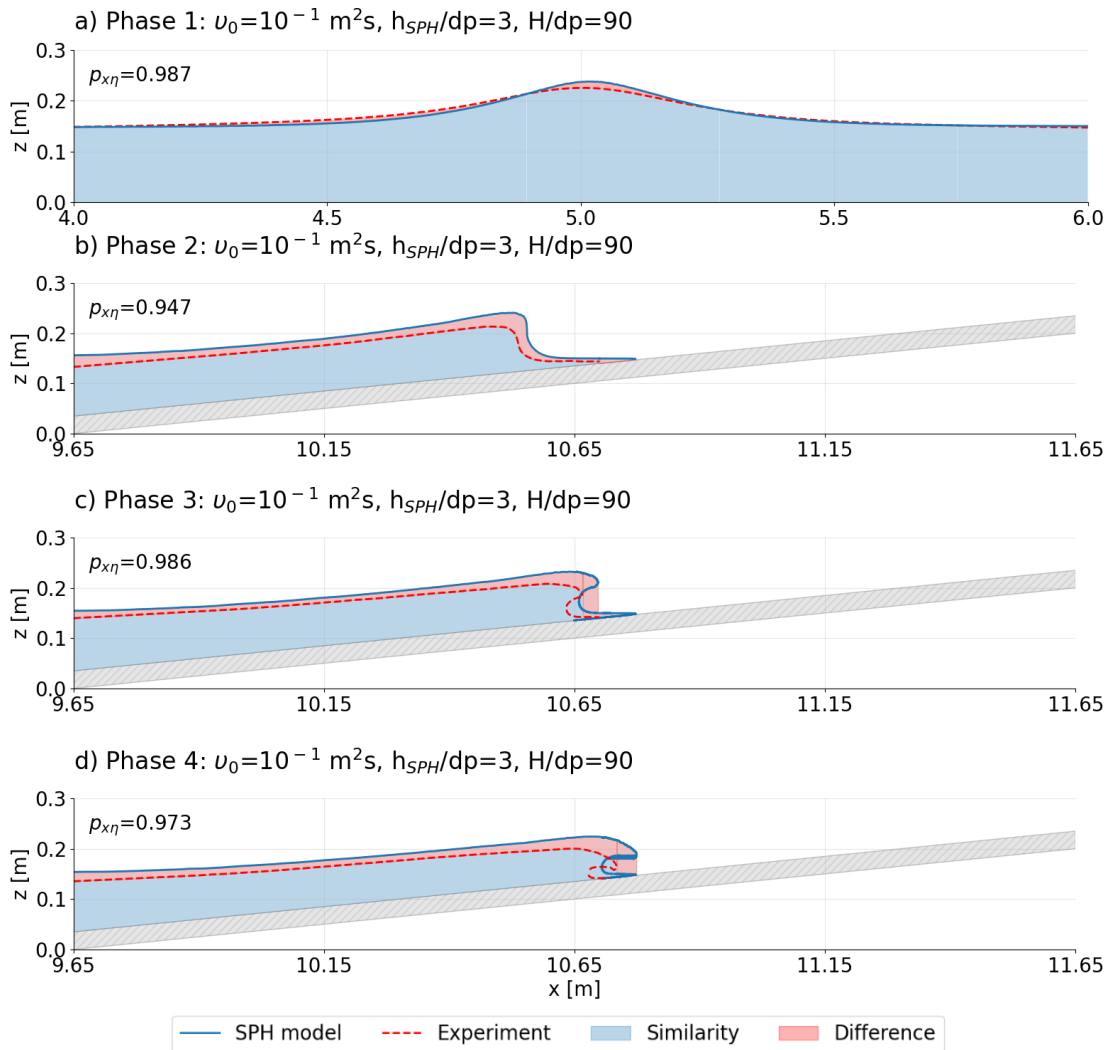


Figure 6-5 The simulated spatially varying wave (z) profile of a plunging solitary wave ($S_0=0.118$), using the laminar viscosity and sub particle turbulence (SPS) scheme, compared to measured data, at four defined phases of evolution in a wave tank.

Table 6-4 shows a quantitative comparison between the simulated and measured spatially varying plunging wave profiles in Figure 6-4(d) and Figure 6-5(d). The criteria used for the comparison included the correlation coefficient ($\rho_{x\eta}$) between the simulated and measured spatially varying wave profiles, the peak wave elevation (η_{peak}) above the still water depth (h_0), and the location of the peak wave elevation (x_{peak}) in the wave tank.

Table 6-4: A quantitative comparison between the simulated and measured spatially varying plunging wave profiles in Figure 6-4(d) and Figure 6-5(d). The correlation coefficient ($p_{x\eta}$) between the simulated and measured spatially varying wave profiles, the peak wave elevation (η_{peak}) above the still water depth (h_0), and the location of the peak wave elevation in the wave tank (x_{peak}) are shown.

Criteria	Experiment	Artificial viscosity approach	SPS approach
$p_{x\eta}$	-	0.99	0.97
η_{peak} [m]	0.05	0.05	0.07
x_{peak} [m]	10.64	10.66	10.68

Figure 6-6 standard artificial viscosity approach (refer to section 3.2.1) and the alternative SPS approach (refer to section 3.2.2), compared to measured data, at $X=8.25$ on the beach slope. Qualitatively, the calibrated artificial viscosity scheme yields better results than the SPS viscosity scheme based on the simulated time varying wave elevation profile. Furthermore, there is a poor correlation ($p_{x\eta}=0.18$) between the simulated and measured time varying wave elevation profiles when using the SPS viscosity approach.

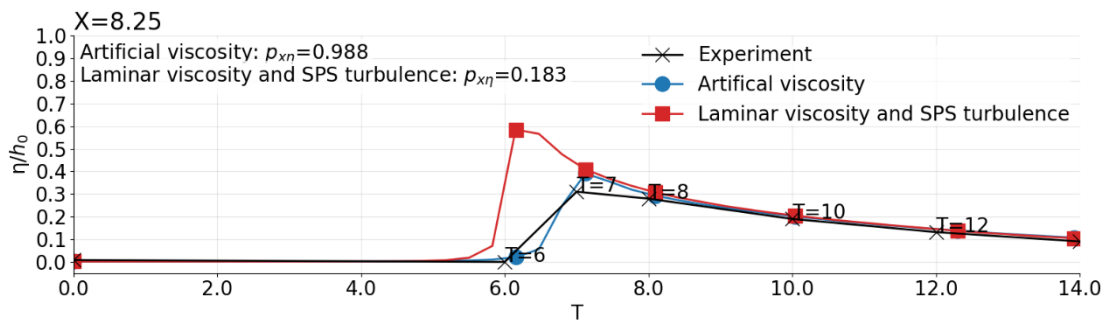


Figure 6-6: The simulated time varying wave elevation (η/h_0) profile, using the standard artificial viscosity scheme and the laminar viscosity and SPS turbulence scheme, compared to measured data, at $X=8.25$ on the beach slope. The measured wave profile is annotated at $T=6$, $T=7$, $T=8$, $T=10$, and $T=12$.

The results suggest that for the same h_{SPH}/dp and H/dp , the laminar viscosity and SPS turbulence scheme (refer to section 3.2.2) yields a lower numerical wave energy dissipation than a calibrated artificial viscosity scheme. Hence the simulated wave is even larger and more slightly out of phase when compared to the measured wave. However, the two-dimensional SPH model negates the effect of the tank walls during wave propagation in the wave tank, which may explain why the wave energy dissipation is under-predicted even though the laminar viscosity and SPS turbulence scheme is a more realistic approach for describing the viscosity. Therefore, to implement the proper

dissipation in the SPH model using the SPS approach, either a three-dimensional SPH model can be utilised, or the interparticle spacing (dp) can be reduced. The DualSPHysics model uses a set Smagorinsky constant (C_s) of 0.12, which cannot be tuned. Hence, the artificial viscosity scheme seems more advantageous for two-dimensional simulations because the artificial viscosity coefficient (α) can be tuned for a set H/dp , allowing the SPH user to implement the proper numerical wave energy dissipation without compromising on the particle resolution (H/dp) of the model. Additionally, the artificial viscosity scheme also dampens the numerical instabilities and spurious oscillations in the SPH model (refer to section 3.2.1). Although, Khayyer et al. (2007) suggest that the influence of SPS turbulence becomes significant, and turbulence modelling should be considered for more realistic simulation results in cases where low particle resolutions (H/dp) are implemented due to computational limitations. Such cases generally involve large numerical domains, especially when considering realistic three-dimensional simulations, which require at least 20 particles to be placed in the transverse direction to eliminate boundary influences (Shao and Ji, 2006).

A comparison of the simulated flow field beneath a breaking wave using the artificial viscosity approach compared to the SPS viscosity approach was not in the scope of the present study. However, for two-dimensional simulations utilising a high particle resolution, the macroscopic behaviours of the flow are expected to be similar using both viscosity treatment methods, especially since a two-dimensional SPS turbulence model cannot accurately treat three-dimensional turbulence in breaking waves (Gotoh et al., 2005; Shao and Ji, 2006). Furthermore, Shao and Ji (2006) showed that more turbulence could be directly resolved using a refined spatial resolution and that the contributions from the SPS turbulence become less critical at smaller particle spacings (dp).

6.1.2.2 Breaker type

Table 6-5 shows the relative wave height (H/h_0), beach slope ($\tan(\beta)$), slope parameter (S_0), and associated breaker type (plunging/spilling) for the simulated solitary waves, including the original plunging solitary wave ($S_0=0.118$), used to calibrate the SPH model parameters. The table also shows the computation runtime for a 15 s simulation and the number of simulated water particles (N) in the numerical domain for the simulated solitary waves. The table shows that varying S_0 can significantly impact the number of simulated water particles in the numerical domain and hence the computation time of the SPH model. If S_0 is reduced by decreasing H/h_0 , a smaller interparticle spacing (dp) is required to obtain the same particle resolution $H/dp=90$. Hence more water particles are simulated in the numerical domain, and the computation time increases. However, if S_0 is increased by decreasing H/h_0 , a larger interparticle spacing (dp) is used to obtain the same particle

resolution $H/dp=90$. Hence fewer water particles are simulated in the same numerical domain and the computation time decreases. Furthermore, if S_0 is reduced by decreasing $\tan(\beta)$, the numerical domain is extended to accommodate the more gradual wave breaking on a gentler slope. Hence more water particles are simulated in the numerical domain, and the computation time increases. On the contrary, if S_0 is increased by decreasing $\tan(\beta)$, the size of the numerical domain becomes smaller. Hence fewer water particles are simulated in the numerical domain and the computation time decreases.

Table 6-5: The relative wave height (H/h_0), beach slope ($\tan(\beta)$), slope parameter (S_0), and associated breaker type, for various simulated solitary waves, including the original plunging solitary wave ($S_0=0.118$), used to calibrate the SPH model parameters. The number of simulated water particles (N) in the numerical domain, and computation runtime for a 15 s simulation, are also shown for each case.

Case	H/h_0	$\tan(\beta)$	S_0	Breaker type	N	Runtime [hours]
Original	0.6	1/10	0.118	Plunging	1 536 789	3.97
Test 1	0.8	1/10	0.136	Plunging	911 817	2.07
Test 2	0.4	1/10	0.078	Plunging	3 113 689	10.88
Test 3	0.6	1/5	0.192	Plunging	1 476 972	3.75
Test 4	0.6	1/20	0.048	Plunging	1 656 503	4.18
Test 5	0.6	1/40	0.024	Spilling	1 895 938	4.66
Test 6	0.6	1/50	0.019	Spilling	2 015 649	4.92

Figure 6-7 shows the simulated wave profile of a solitary wave with a relative wave height (H/h_0) of 0.8 and slope parameter (S_0) of 0.136, propagating over a 1/10 beach slope (test 1 in Table 6-5) in space and time. The slope parameter $S_0=0.136$ is within the range ($0.025 < S_0 < 0.3$) associated with plunging breakers, and the simulated solitary wave profile in Figure 6-7 exhibits the wave characteristics of a plunging breaker (refer to section 2.4.2.1). Hence, $\alpha=0.1$, $h_{SPH}/dp=3$, and $H/dp=90$ yield the correct simulated wave profile when increasing S_0 to 0.136 by increasing the relative wave height (H/h_0) of the simulated solitary wave.

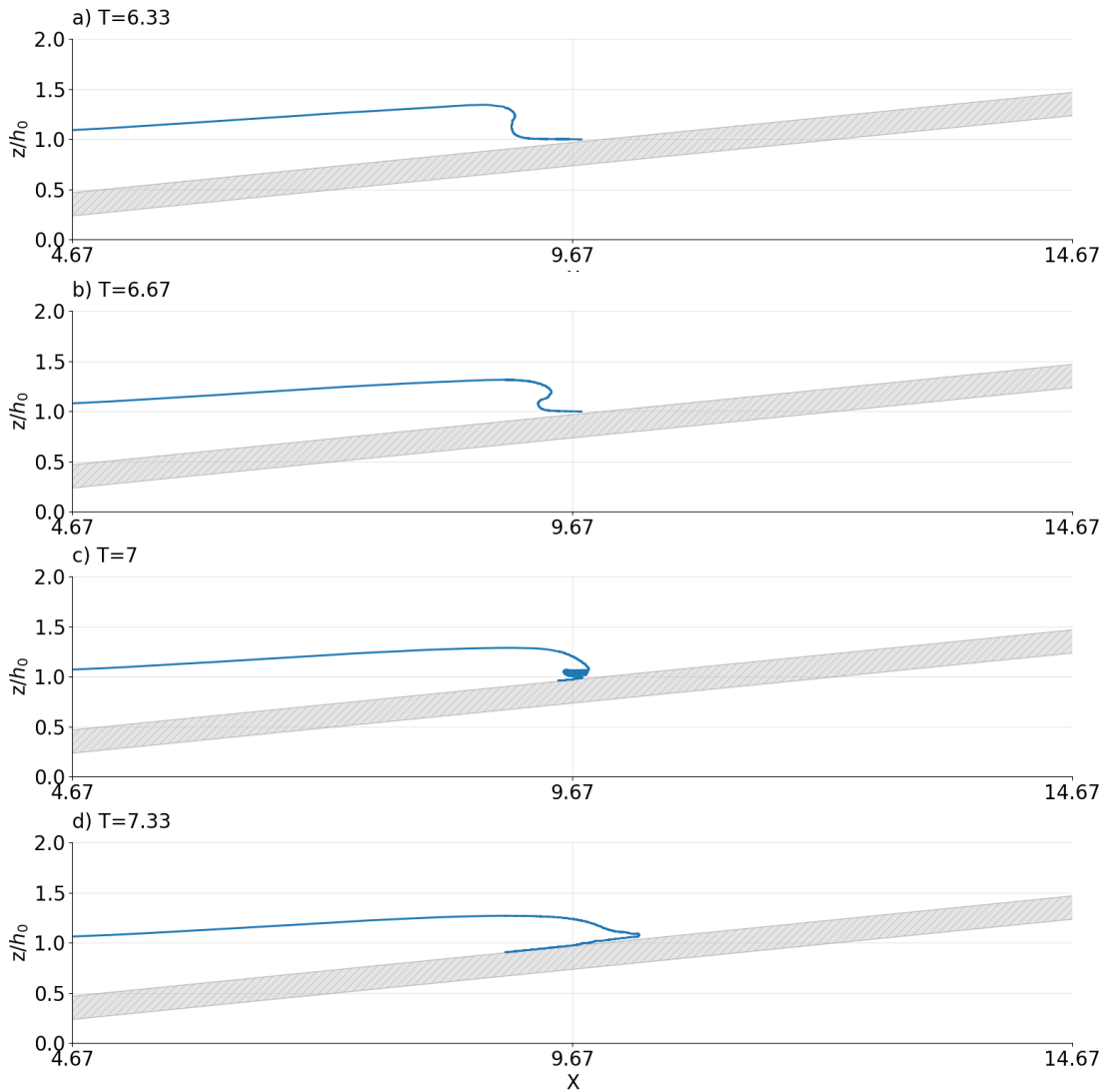


Figure 6-7: The simulated wave profile of a solitary wave with a relative wave height (H/h_0) of 0.8 and slope parameter (S_0) of 0.136, propagating over a 1/10 beach slope (test 1 in Table 6-5) in space and time.

Figure 6-8 shows the simulated wave profile of a solitary wave with a relative wave height (H/h_0) of 0.4 and slope parameter (S_0) of 0.078, propagating over a 1/10 beach slope (test 2 in Table 6-5) in space and time. The slope parameter $S_0=0.078$ is within the range ($0.025 < S_0 < 0.3$) associated with plunging breakers, and the simulated solitary wave profile in Figure 6-8 exhibits the wave characteristics of a plunging breaker (refer to section 2.4.2.1). Hence, $\alpha=0.1$, $h_{SPH}/dp=3$, and $H/dp=90$ yield the correct simulated wave profile when reducing S_0 to 0.078 by decreasing the relative wave height (H/h_0) of the simulated solitary wave.

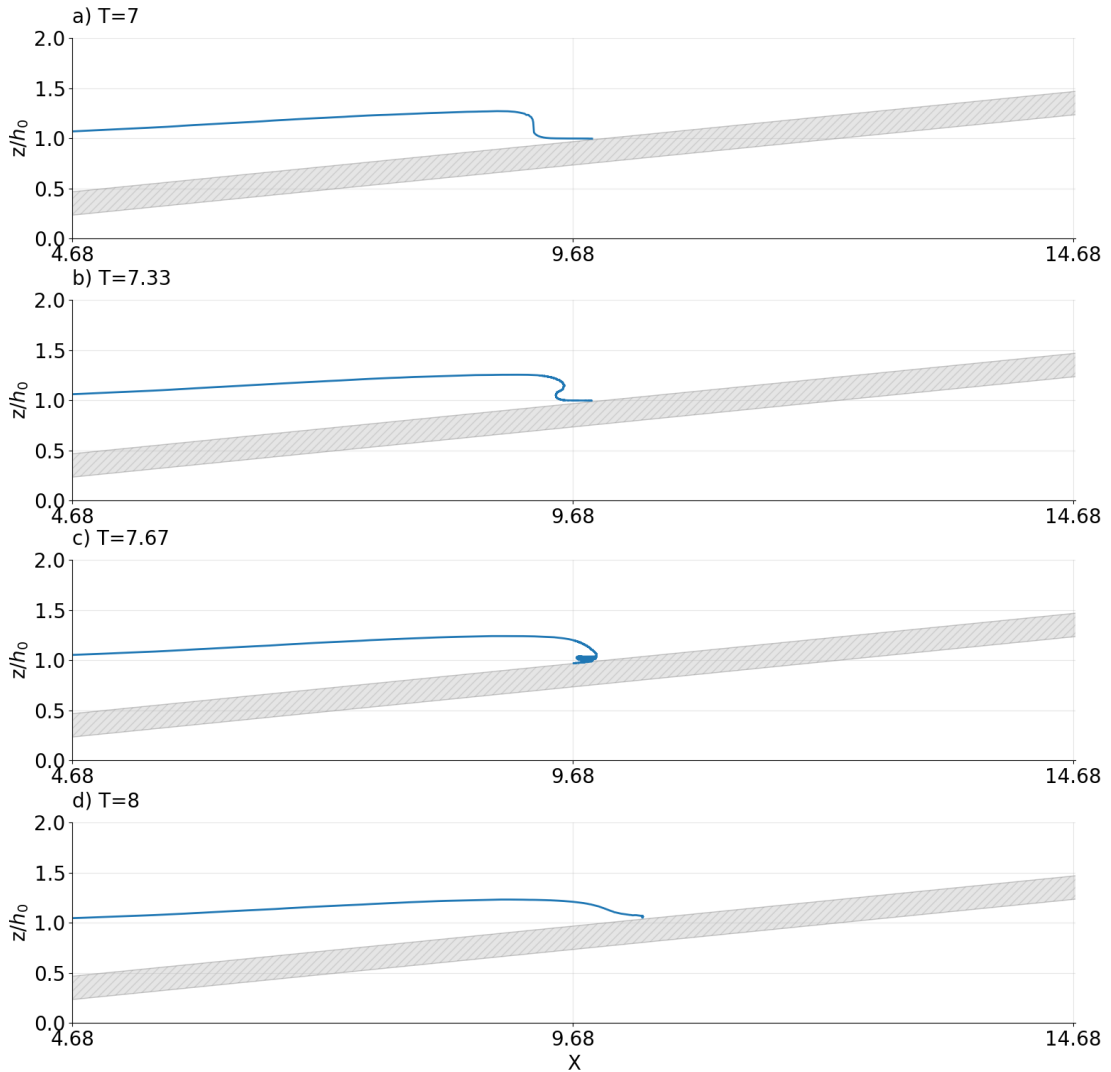


Figure 6-8: The simulated wave profile of a solitary wave with a relative wave height (H/h_0) of 0.4 and slope parameter (S_0) of 0.078, propagating over a 1/10 beach slope (test 2 in Table 6-5) in space and time.

Figure 6-9 shows the simulated wave profile of a solitary wave with a relative wave height (H/h_0) of 0.6 and slope parameter (S_0) of 0.192, propagating over a 1/5 beach slope (test 3 in Table 6-5) in space and time. The slope parameter $S_0=0.192$ is within the range ($0.025 < S_0 < 0.3$) associated with plunging breakers. However, the simulated solitary wave profile in Figure 6-9 does not exhibit the wave characteristics of a plunging breaker and instead resembles a collapsing breaker (refer to section 2.4.2.1). Hence, $\alpha=0.1$, $h_{SPH}/dp=3$, and $H/dp=90$ fail in yielding the correct simulated wave profile when increasing S_0 to 0.192 by increasing the beach slope ($\tan(\beta)$).

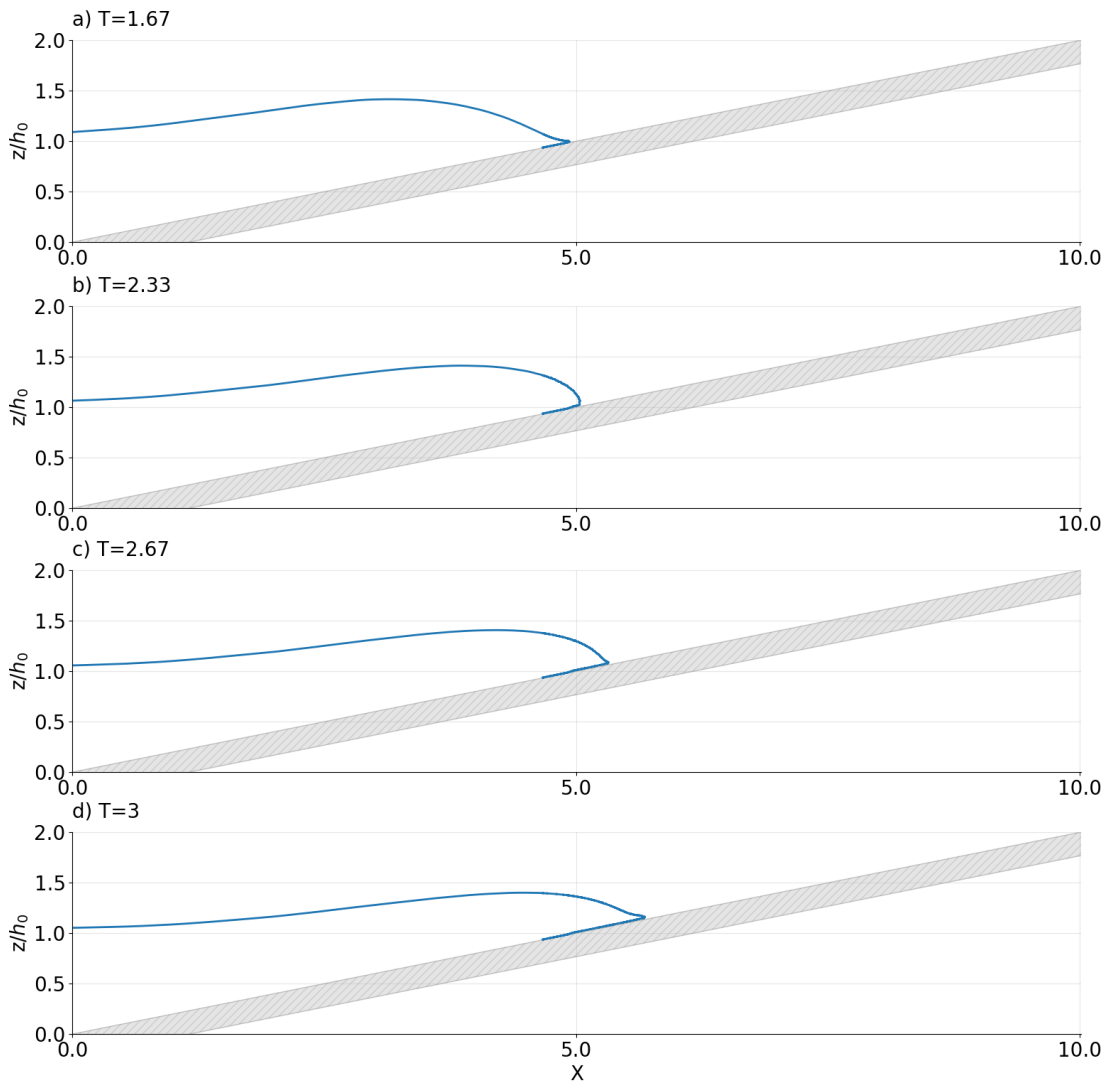


Figure 6-9: The simulated wave profile of a solitary wave with a relative wave height (H/h_0) of 0.6 and slope parameter (S_0) of 0.192, propagating over a 1/5 beach slope (test 3 in Table 6-5) in space and time.

Figure 6-10 shows the simulated wave profile of a solitary wave with a relative wave height (H/h_0) of 0.6 and slope parameter (S_0) of 0.048, propagating over a 1/20 beach slope (test 4 in Table 6-5) in space and time. The slope parameter $S_0=0.048$ is within the range ($0.025 < S_0 < 0.3$) associated with plunging breakers, and the simulated solitary wave profile in Figure 6-10 exhibits the wave characteristics of a plunging breaker (refer to section 2.4.2.1). Hence, $\alpha=0.1$, $h_{SPH}/dp=3$, and $H/dp=90$ yield the correct simulated wave profile when reducing S_0 to 0.048 by decreasing the beach slope ($\tan(\beta)$).

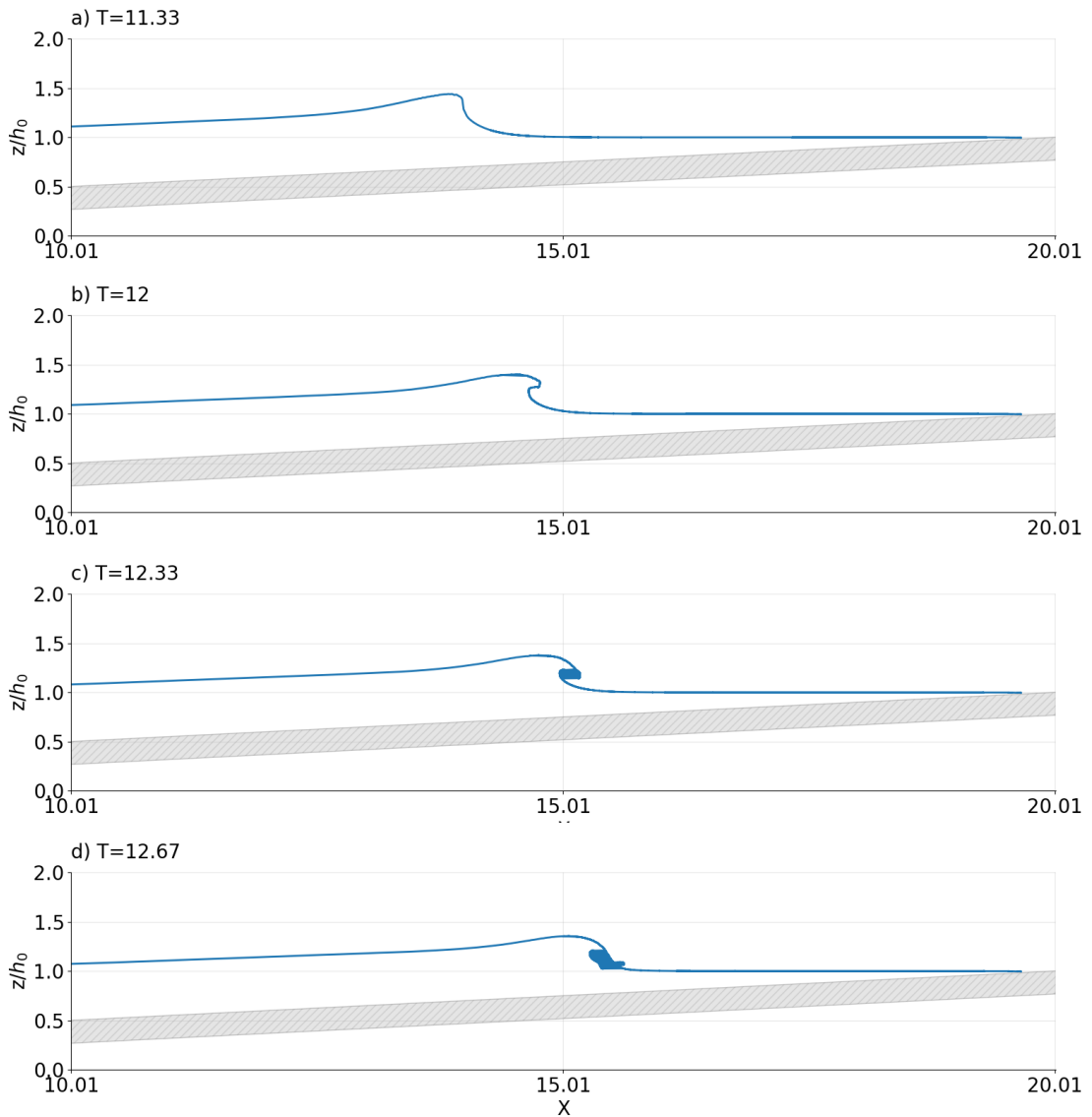


Figure 6-10: The simulated wave profile of a solitary wave with a relative wave height (H/h_0) of 0.6 and slope parameter (S_0) of 0.048, propagating over a 1/20 beach slope (test 4 in Table 6-5) in space and time.

Figure 6-11 shows the simulated wave profile of a solitary wave with a relative wave height (H/h_0) of 0.6 and slope parameter (S_0) of 0.024, propagating over a 1/40 beach slope (test 5 in Table 6-5) in space and time. The slope parameter $S_0=0.024$ is just within the range ($S_0<0.025$) associated with spilling breakers, and the simulated solitary wave profile in Figure 6-11 shows the transition from a plunging to a spilling breaker, exhibiting the wave characteristics of a spilling breaker (refer to section 2.4.2.1). Hence, $\alpha=0.1$, $h_{SPH}/dp=3$, and $H/dp=90$ yield the correct simulated wave profile when reducing S_0 to 0.024 by decreasing the beach slope ($\tan(\beta)$).

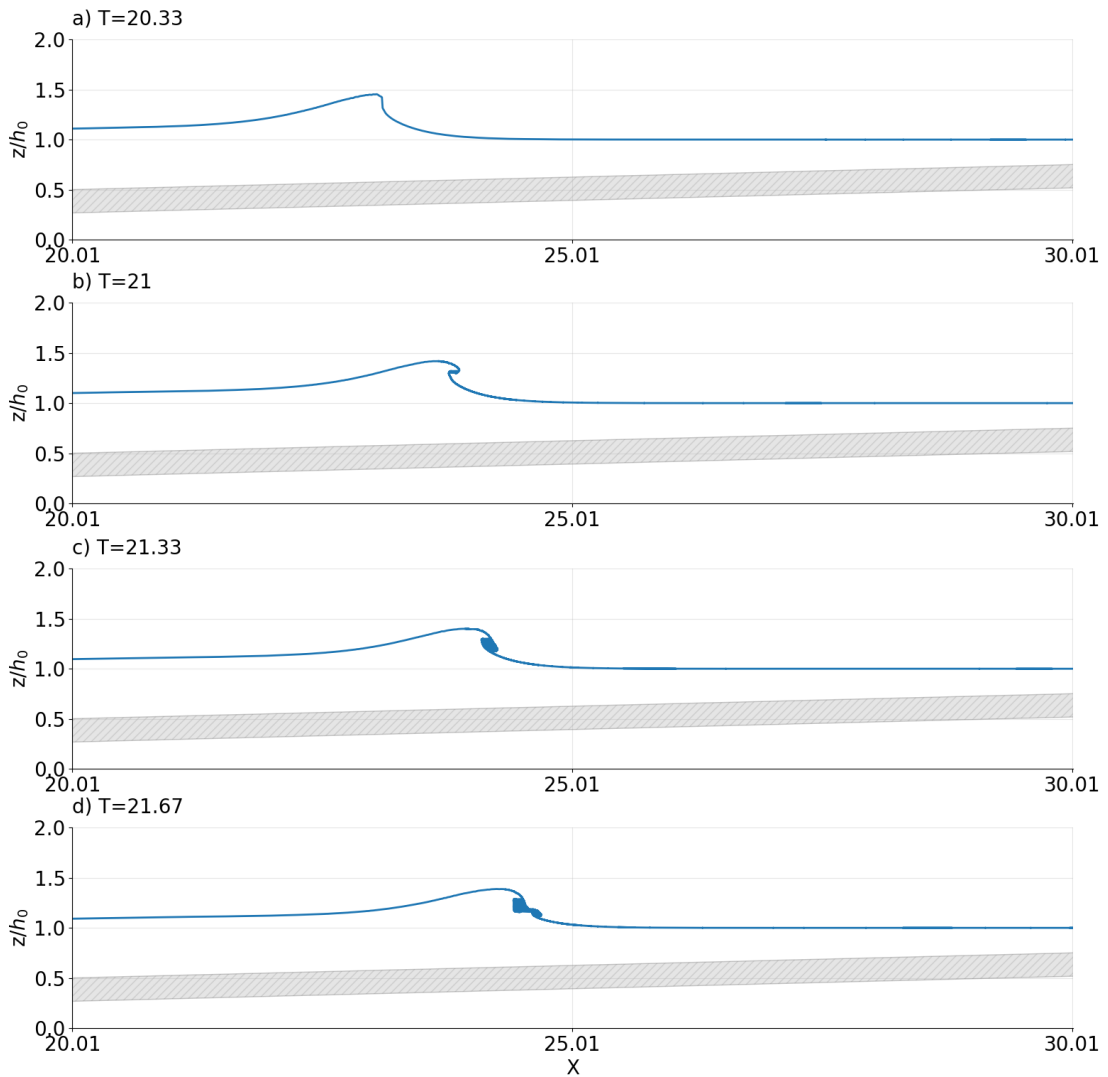


Figure 6-11: The simulated wave profile of a solitary wave with a relative wave height (H/h_0) of 0.6 and slope parameter (S_0) of 0.024, propagating over a 1/40 beach slope (test 5 in Table 6-5) in space and time.

Figure 6-12 shows the simulated wave profile of a solitary wave with a relative wave height (H/h_0) of 0.6 and slope parameter (S_0) of 0.019, propagating over a 1/50 beach slope (test 6 in Table 6-5) in space and time. The slope parameter $S_0=0.019$ is within the range ($S_0 < 0.025$) associated with spilling breakers, and the simulated solitary wave profile in Figure 6-12 exhibits the wave characteristics of a spilling breaker (refer to section 2.4.2.1). Hence, $\alpha=0.1$, $h_{SPH}/dp=3$, and $H/dp=90$ yield the correct simulated wave profile when reducing S_0 to 0.019 by decreasing the beach slope ($\tan(\beta)$).

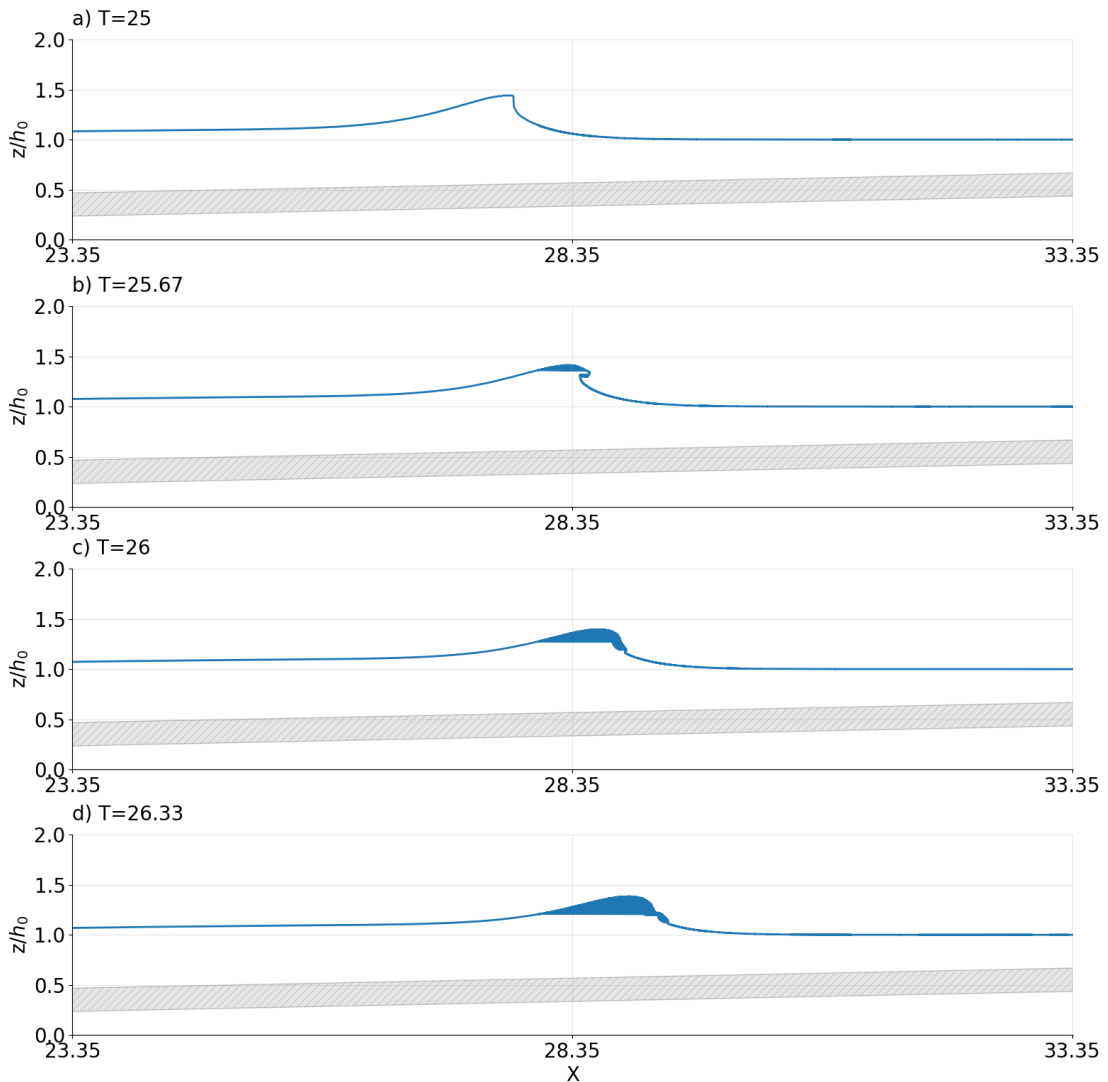


Figure 6-12: The simulated wave profile of a solitary wave with a relative wave height (H/h_0) of 0.6 and slope parameter (S_0) of 0.019, propagating over a 1/50 beach slope (test 6 in Table 6-5) in space and time.

The results presented suggest that $\alpha=0.1$, $h_{SPH}/dp=3$, $H/dp=90$, are still suitable parameters for the SPH model when reducing the slope parameter (S_0) from the original plunging wave case ($S_0=0.118$) by reducing the relative wave height (H/h_0) of the simulated wave or reducing the beach slope ($\tan(\beta)$). The results also suggest that $\alpha=0.1$, $h_{SPH}/dp=3$, $H/dp=90$, are suitable parameters for the SPH model when increasing the slope parameter (S_0) from the original plunging wave case ($S_0=0.118$) by increasing the relative wave height (H/h_0) of the simulated wave. However, $\alpha=0.1$, $h_{SPH}/dp=3$, $H/dp=90$, are not suitable parameters for the SPH model when increasing the slope parameter (S_0) from the original plunging wave case ($S_0=0.118$) by increasing beach slope ($\tan(\beta)$). Therefore, the best choice of α , h_{SPH}/dp , and H/dp depends on S_0 and hence the type of wave breaking (plunging/spilling), particularly when increasing S_0 by increasing the beach slope ($\tan(\beta)$). This may be due to the beach slope ($\tan(\beta)$) being more significant than the relative wave height (H/h_0) for determining the shape of breaking waves. Waves

break at smaller water depths on steep beach slopes than gentle beach slopes, which significantly increases the size of plunging jets for spilling and plunging breakers (Grilli et al., 1997; Arntsen et al. 2000). De Padova et al. (2014) showed that only α requires tuning according to the type of wave breaking when the best values of h_{SPH}/dp and H/dp have been defined. De Padova et al. (2014) established a relationship between α and the type of wave breaking, which shows that the best value of α can be regarded as a linear function of the Iribarren number (ζ) when the best values of h_{SPH}/dp and H/dp have been defined (refer to Equation (3-20)). Thus, a similar linear relationship is predicted between the best value of α and the slope parameter (S_0) of a solitary wave.

The results also suggest that using the particle resolution $H/dp=90$ becomes computationally more expensive when reducing S_0 because the number of simulated water particles in the numerical domain significantly increases. When reducing the slope parameter (S_0) from the original plunging wave case ($S_0=0.118$) by reducing the relative wave height (H/h_0), a smaller interparticle spacing (dp) is required to obtain the exact resolution ($H/dp=90$). Furthermore, when reducing the slope parameter (S_0) from the original plunging wave case ($S_0=0.118$) by reducing the beach slope ($\tan(\beta)$), the numerical domain is extended to accommodate a more gradually breaking wave on a gentler slope. If the relative wave height (H/h_0) or beach slope ($\tan(\beta)$) is significantly reduced, then the particle resolution $H/dp=90$ may become computationally infeasible. Hence, $\alpha=0.1$, $h_{SPH}/dp=3$, and $H/dp=90$ may need to be adjusted. Therefore, it is important to analyse the influence of α , h_{SPH}/dp , and H/dp on the SPH computation.

6.1.3 Influence of the artificial viscosity coefficient (α)

Figure 6-13 shows the numerical wave energy dissipation and simulated wave profile of a plunging solitary wave ($S_0=0.118$), using various α , compared to measured data. Figure 6-13(a) compares the numerical and measured wave energy dissipation (D) over the horizontal wave tank section. Figure 6-13(b) compares the simulated and measured spatially varying wave (z/h_0) profiles at a defined phase of evolution (one timestep before wave impingement on the beach slope). Figure 6-13(c) compares the simulated and measured time varying wave elevation (η/h_0) profiles at $X=8.25$ on the beach slope. In the figure, $h_{SPH}/dp=3$ and $H/dp=90$ are constant. The results show that an $\alpha < 0.1$ decreases the wave energy dissipation when $h_{SPH}/dp=3$ and $H/dp=90$ and the wave height is over-predicted at breaking. However, an $\alpha=1$ increases the wave energy dissipation when $h_{SPH}/dp=3$ and $H/dp=90$ and the wave height is under-predicted at breaking. An $\alpha=0.1$ yields an appropriate level of wave energy dissipation when $h_{SPH}/dp=3$ and $H/dp=90$, and the simulated wave height is comparable to measured data at breaking.

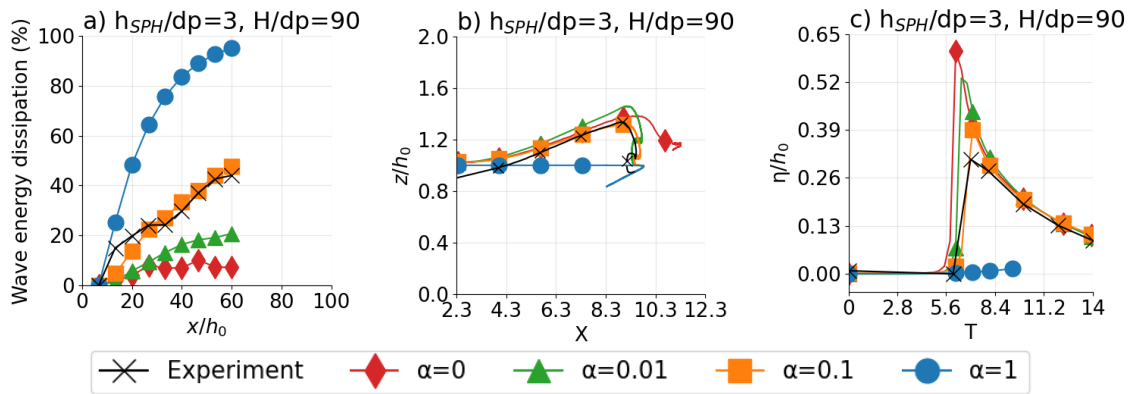


Figure 6-13: Simulated results of a plunging solitary wave ($S_0=0.118$), using various α , compared to measured data. The image compares the (a) numerical and measured wave energy dissipation (D) over the horizontal wave tank section, the (b) simulated and measured spatially varying wave (z/h_0) profiles, at a defined phase of evolution, one timestep before wave impingement on the beach slope, and the (c) simulated and measured time varying wave elevation (η/h_0) profiles, at $X=8.25$ on the beach slope.

Figure 6-14 shows the simulated wave surface of a plunging solitary wave ($S_0=0.118$), using various α , compared to measured data in space and time, as well as the simulated water particles in the numerical domain, using various α . Figure 6-14(a-d) compares the simulated and measured spatially varying wave (z) profile offshore at $T=-22$. Figure 6-14(e-h), Figure 6-14(i-l), and Figure 6-14(m-p) compare the simulated and measured spatially varying wave (z) profile onshore at $T=5.52$, $T=6.49$, and $T=6.81$, respectively. In the figure, $h_{SPH}/dp=3$ and $H/dp=90$ are constant. The results also show an $\alpha < 0.1$ decreases the wave energy dissipation when $h_{SPH}/dp=3$, and $H/dp=90$ and the simulated wave surface and speed are over-predicted and hence out of phase compared to measured data. On the contrary, an $\alpha=1$ increases the wave energy dissipation when $h_{SPH}/dp=3$, and $H/dp=90$ and the simulated wave surface and speed are under-predicted onshore and offshore in the wave tank. An $\alpha=0.1$ yields an appropriate wave energy dissipation when $h_{SPH}/dp=3$, and $H/dp=90$ and the simulated wave surface and speed is comparable to measured data in space and time. De Padova et al. (2014) similarly showed that α can drastically influence the SPH computation and that the SPH model becomes overly diffusive when α is too high and far from the optimal value, which results in wave height under-prediction at breaking.

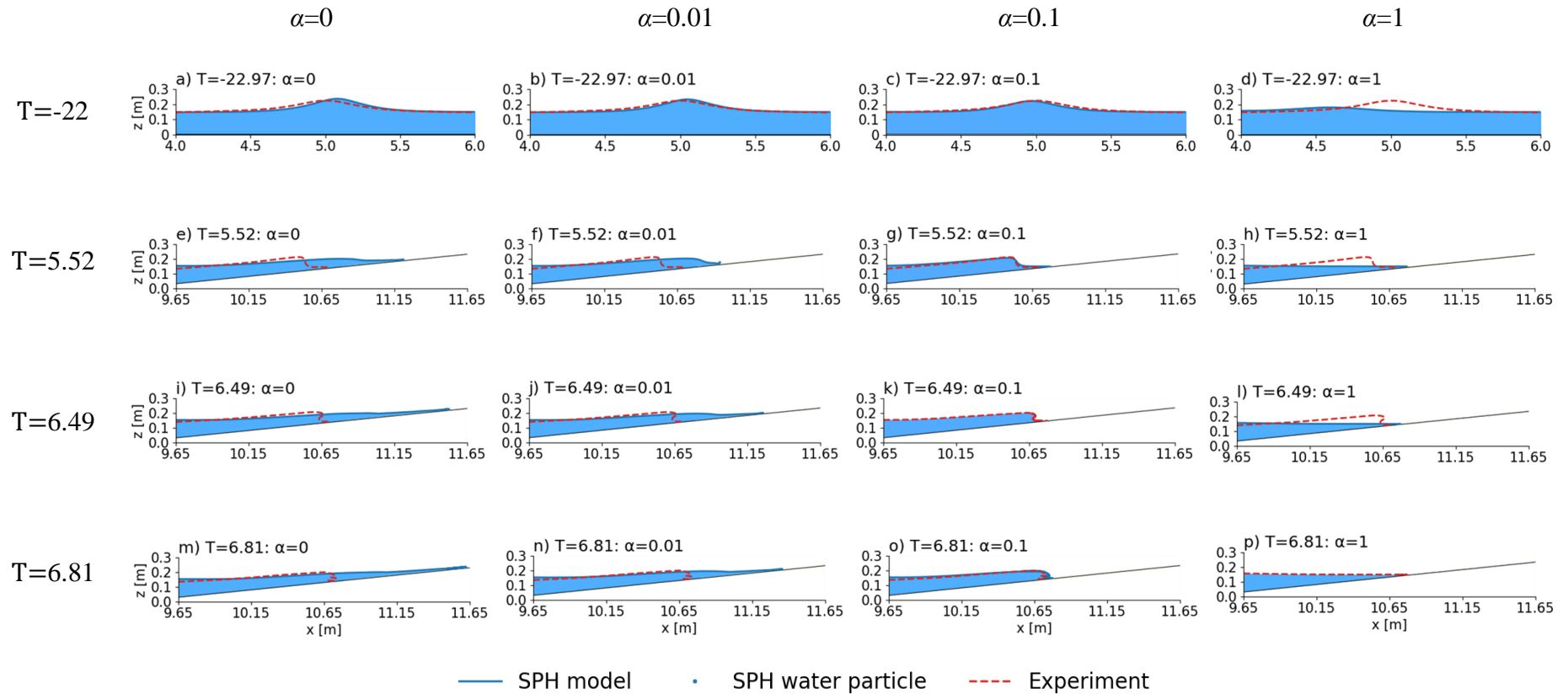


Figure 6-14: The simulated wave surface (z) of a plunging solitary wave ($S_0=0.118$) using various α , compared to measured data in space and time, as well as the simulated water particles in the numerical domain, using various α . The parameters $h_{SPH}/dp=3$ and $H/dp=90$ are constant.

Figure 6-15 shows the influence of various α (in combination with a range of h_{SPH}/dp and H/dp) on the correlation coefficient ($p_{x\eta}$) between the simulated and measured time varying wave elevation (η/h_0) profiles, at $X=8.25$ on the beach slope. The figure shows no clear relationship between h_{SPH}/dp , H/dp and $p_{x\eta}$ for a constant α . However, $\alpha=0$, $\alpha=0.01$ and $\alpha=0.1$ generally yield a higher correlation ($p_{x\eta}>0.5$) between the simulated and measured wave profiles for various h_{SPH}/dp and H/dp compared to $\alpha=1$, which yields a low correlation ($p_{x\eta}<0.5$) for all combinations of h_{SPH}/dp and H/dp .

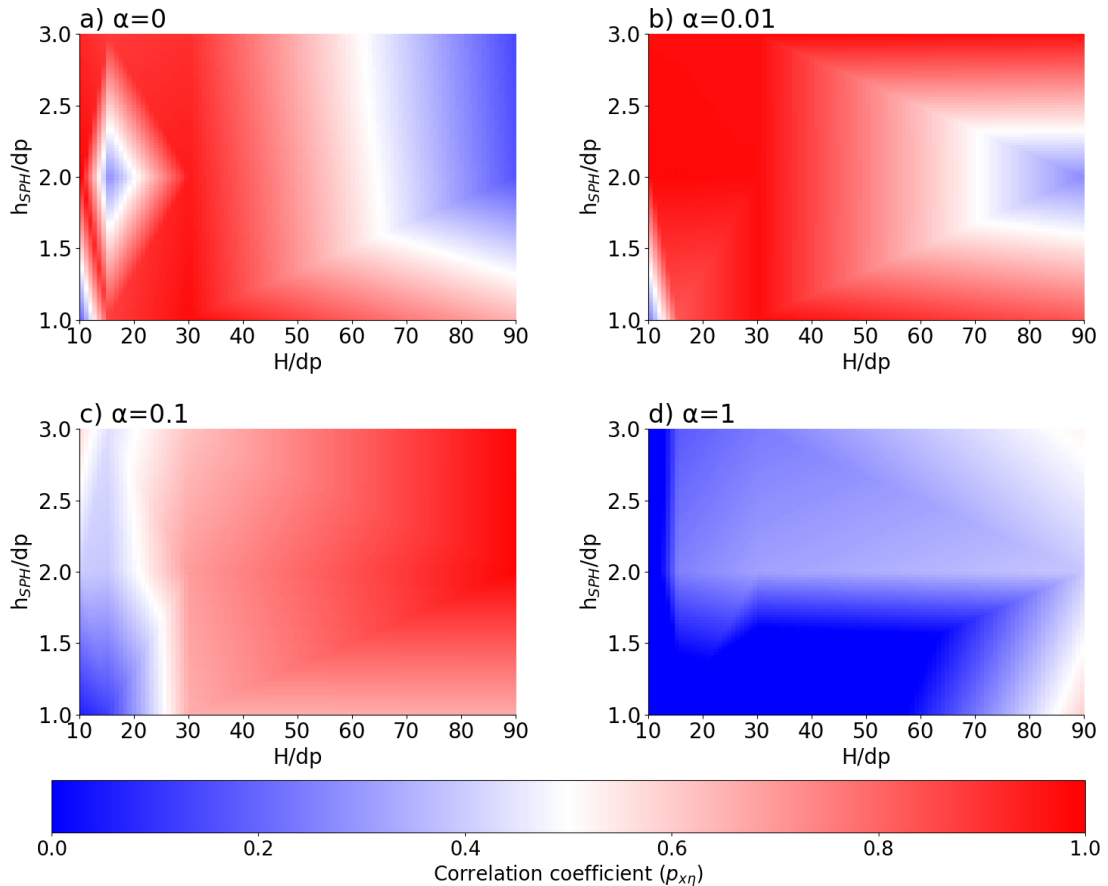


Figure 6-15: The influence of various α (in combination with a range of h_{SPH}/dp and H/dp) on the correlation coefficient ($p_{x\eta}$) between the simulated and measured time varying wave elevation (η/h_0) profiles, at $X=8.25$ on the beach slope.

6.1.4 Influence of the dimensionless smoothing length ratio (h_{SPH}/dp)

Figure 6-16 shows the numerical wave energy dissipation and simulated wave profile of a plunging solitary wave ($S_0=0.118$), using various h_{SPH}/dp , compared to measured data. Figure 6-16(a) compares the numerical and measured wave energy dissipation (D) over the horizontal wave tank section. Figure 6-16(b) compares the simulated and measured spatially varying wave (z/h_0) profiles at a defined phase of evolution (one timestep before wave impingement on the beach slope). Figure 6-16(c) compares the simulated and measured time varying wave elevation (η/h_0) profiles at $X=8.25$ on the beach slope. In

the figure, $\alpha=0.1$ and $H/dp=90$ are constant. The results show that an $h_{SPH}/dp=1$ increases the wave energy dissipation when $\alpha=0.1$ and $H/dp=90$ and the wave height is under-predicted at breaking. The results also show that decreasing h_{SPH}/dp for a fixed dp decreases the smoothing length (h_{SPH}), which reduces the size of the area around a particle in which the SPH smoothing function considers neighbouring particles (refer to section 3.1.1). Thus, the accuracy of the SPH computation is reduced because the number of neighbouring particles used to compute the fluid properties is reduced. An $h_{SPH}/dp=2$ or $h_{SPH}/dp=3$ yields an appropriate wave energy dissipation when $\alpha=0.1$ and $H/dp=90$ and the simulated wave height is comparable to measured data at breaking.

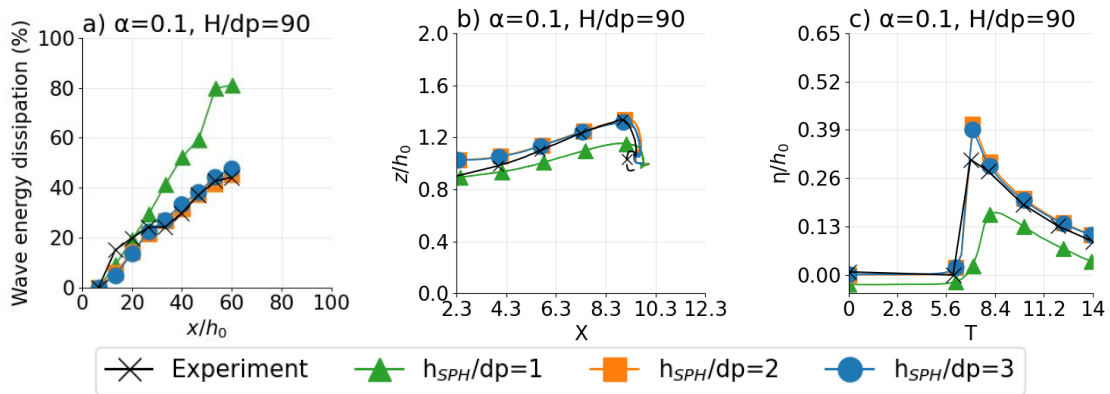


Figure 6-16: Simulated results of a plunging solitary wave ($S_0=0.118$), using various h_{SPH}/dp , compared to measured data. The image compares the (a) numerical and measured wave energy dissipation (D) over the horizontal wave tank section, the (b) simulated and measured spatially varying wave (z/h_0) profiles, at a defined phase of evolution, one timestep before wave impingement on the beach slope, and the (c) simulated and measured time varying wave elevation (η/h_0) profiles, at $X=8.25$ on the beach slope.

Figure 6-17 shows the simulated wave surface of a plunging solitary wave ($S_0=0.118$), using various h_{SPH}/dp , compared to measured data in space and time, as well as the simulated water particles in the numerical domain, using various h_{SPH}/dp . Figure 6-17(a-c) compares the simulated and measured spatially varying wave (z) profile offshore at $T=-22$. Figure 6-17(d-f), Figure 6-17(g-i), and Figure 6-17(j-l) compare the simulated and measured spatially varying wave (z) profile onshore at $T=5.52$, $T=6.49$, and $T=6.81$, respectively. In the figure, $\alpha=0.1$ and $H/dp=90$ are constant. The results also show that an $h_{SPH}/dp=1$ increases the wave energy dissipation when $\alpha=0.1$ and $H/dp=90$ and the simulated wave height and speed are under-predicted, particularly at breaking. An $h_{SPH}/dp=2$ or $h_{SPH}/dp=3$ yields an appropriate wave energy dissipation when $\alpha=0.1$ and $H/dp=90$ and the simulated wave surface and speed is comparable to measured data in space and time. De Padova et al. (2014) obtained similar results and suggested that the value of h_{SPH}/dp should be ≥ 1.4 for cases of regular wave breaking on a plane slope.

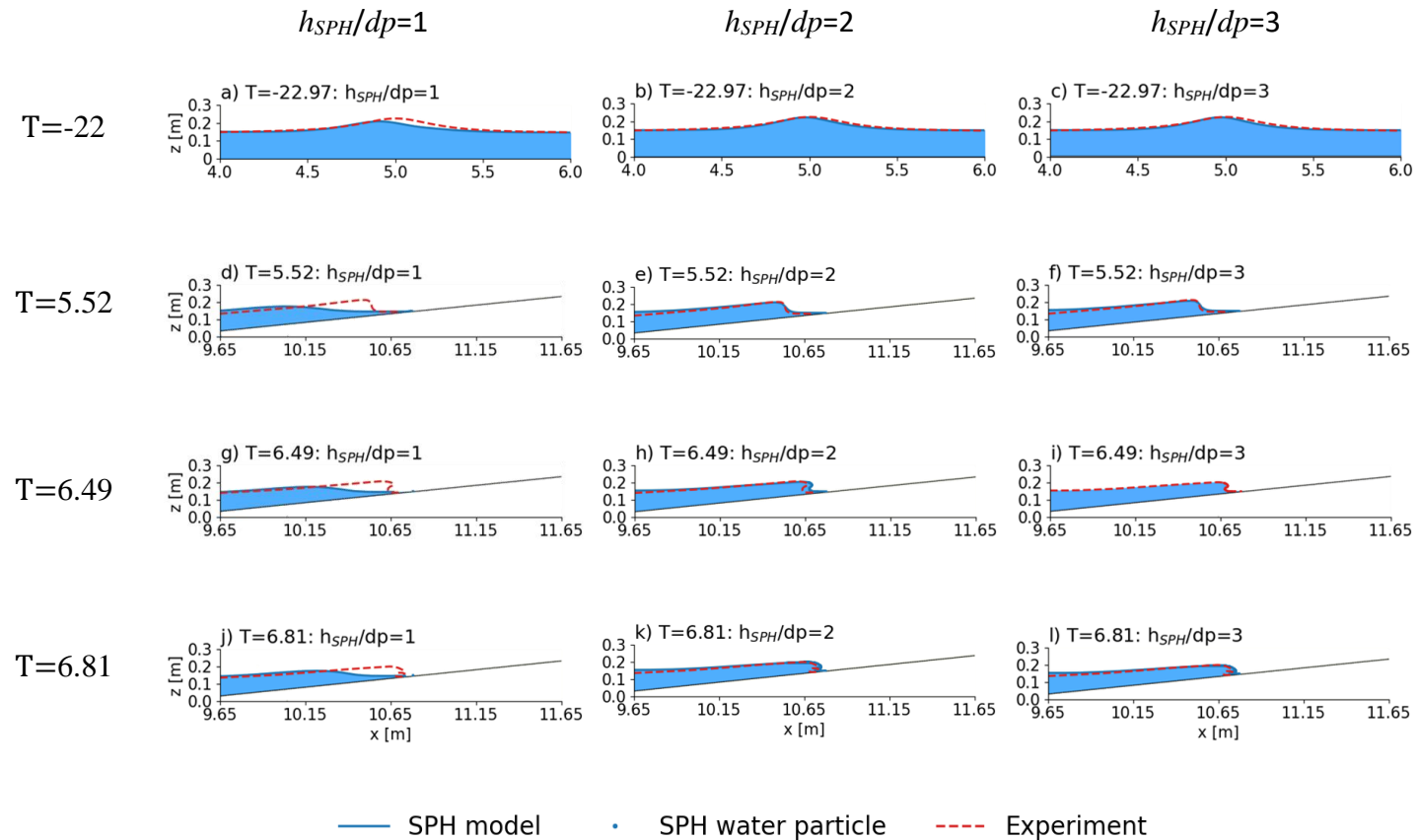


Figure 6-17: The simulated wave surface (z) of a plunging solitary wave ($S_0=0.118$) using various h_{SPH}/dp , compared to measured data in space and time, as well as the simulated water particles in the numerical domain, using various h_{SPH}/dp . The parameters $\alpha=0.1$ and $H/dp=90$ are constant.

Figure 6-18 shows the influence of various h_{SPH}/dp (in combination with a range of α and H/dp) on the correlation coefficient ($p_{x\eta}$) between the simulated and measured time varying wave elevation (η/h_0) profiles, at $X=8.25$ on the beach slope. The figure shows no clear relationship between α , H/dp and $p_{x\eta}$ for a constant h_{SPH}/dp . However, the relationship between α , H/dp and $p_{x\eta}$ is similar for $h_{SPH}/dp=2$ and $h_{SPH}/dp=3$. Furthermore, $h_{SPH}/dp=2$ and $h_{SPH}/dp=3$ generally yield a higher correlation ($p_{x\eta}>0.5$) between the simulated and measured wave profiles for various h_{SPH}/dp and H/dp compared to $h_{SPH}/dp=1$, which generally yields a low correlation ($p_{x\eta}<0.5$) for various h_{SPH}/dp and H/dp .

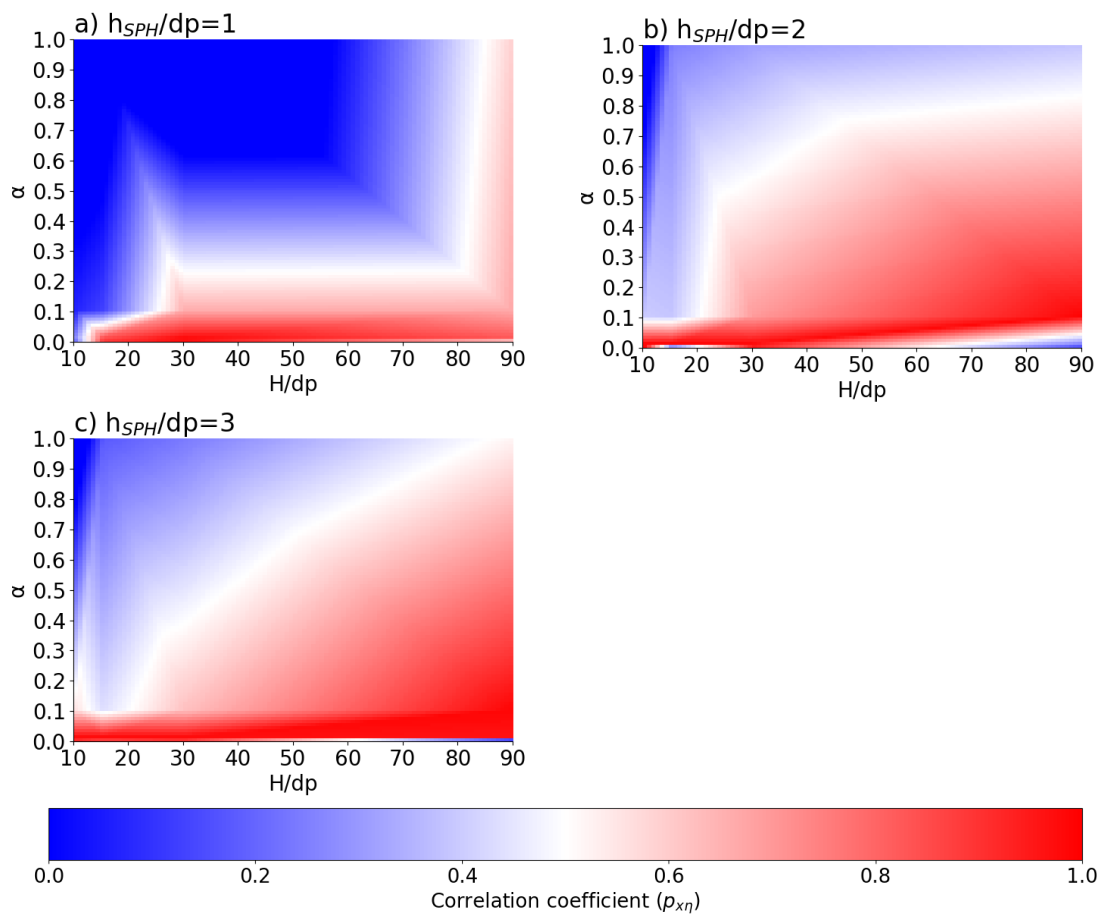


Figure 6-18: The influence of various h_{SPH}/dp (in combination with a range of α and H/dp) on the correlation coefficient ($p_{x\eta}$) between the simulated and measured time varying wave elevation (η/h_0) profiles, at $X=8.25$ on the beach slope.

6.1.5 Influence of the particle resolution (H/dp)

Figure 6-19 shows the numerical wave energy dissipation and simulated wave profile of a plunging solitary wave ($S_0=0.118$), using various H/dp , compared to measured data. Figure 6-19(a) compares the numerical and measured wave energy dissipation (D) over the horizontal wave tank section. Figure 6-19(b) compares the simulated and measured spatially varying wave (z/h_0) profiles at a defined phase of evolution (one timestep before

wave impingement on the beach slope). Figure 6-19(c) compares the simulated and measured time varying wave elevation (η/h_0) profiles at $X=8.25$ on the beach slope. In the figure, $\alpha=0.1$ and $h_{SPH}/dp=3$ are constant. The results show that an $H/dp < 90$ increases the wave energy dissipation when $\alpha=0.1$ and $h_{SPH}/dp=3$ and the wave height is under-predicted at breaking. The results also show that decreasing H/dp decreases the interparticle spacing (dp), which reduces the number of simulated water particles in the numerical domain. Therefore, the accuracy of the SPH computation is reduced because the number of neighbouring particles used to compute the fluid properties is reduced. An $H/dp=90$ yields an appropriate wave energy dissipation when $\alpha=0.1$ and $h_{SPH}/dp=3$ and the simulated wave height is comparable to measured data at breaking.

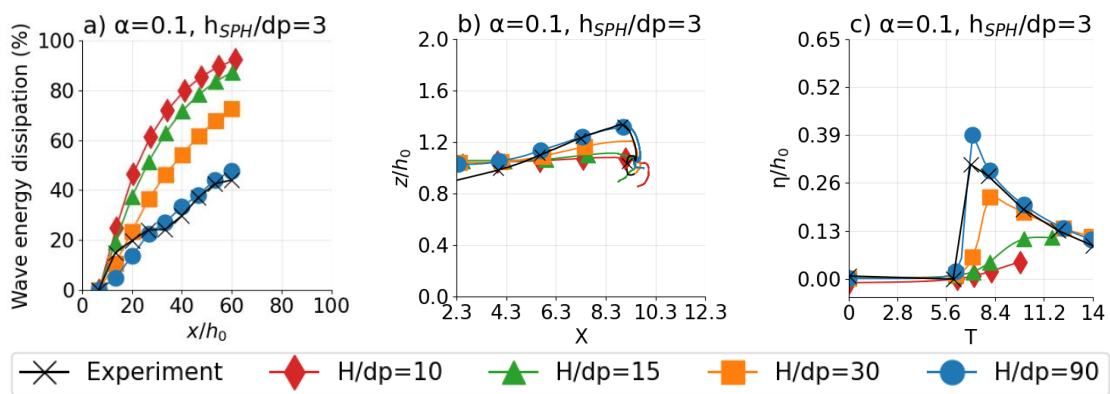


Figure 6-19: Simulated results of a plunging solitary wave ($S_0=0.118$), using various H/dp , compared to measured data. The image compares the (a) numerical and measured wave energy dissipation (D) over the horizontal wave tank section, the (b) simulated and measured spatially varying wave (z/h_0) profiles, at a defined phase of evolution, one timestep before wave impingement on the beach slope, and the (c) simulated and measured time varying wave elevation (η/h_0) profiles, at $X=8.25$ on the beach slope.

Figure 6-20 shows the simulated wave surface of a plunging solitary wave ($S_0=0.118$), using various H/dp , compared to measured data in space and time, as well as the simulated water particles in the numerical domain, using various H/dp . Figure 6-20(a-d) compares the simulated and measured spatially varying wave (z) profile offshore at $T=-22$. Figure 6-20(e-h), Figure 6-20(i-l), and Figure 6-20(m-p) compare the simulated and measured spatially varying wave (z) profile onshore at $T=5.52$, $T=6.49$, and $T=6.81$, respectively. In the figure, $\alpha=0.1$ and $h_{SPH}/dp=3$ are constant. The results also show that an $H/dp < 90$ increases the wave energy dissipation when $\alpha=0.1$ and $h_{SPH}/dp=3$. Hence, the simulated wave height and speed are under-predicted and poorly simulated onshore and offshore in the wave tank. The decreasing number of simulated water particles in the numerical domain with a decreasing H/dp is also evident in Figure 6-20. An H/dp of 90 yields an appropriate wave energy dissipation when $\alpha=0.1$ and $h_{SPH}/dp=3$ and the simulated wave surface and speed is comparable to measured data in space and time.

De Padova et al. (2014) similarly showed that the dissipative effects in the SPH model became smaller and smaller as the spatial resolution increased.

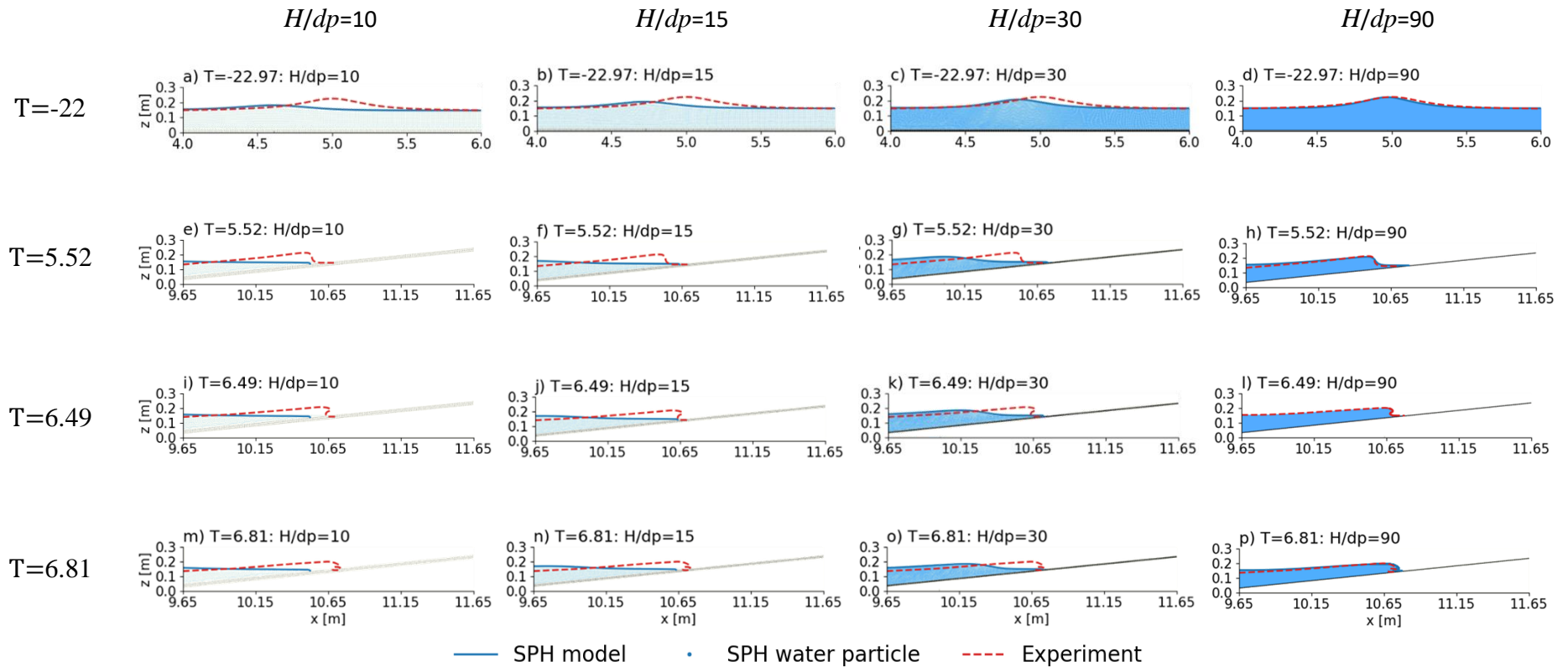


Figure 6-20: The simulated wave surface (z) of a plunging solitary wave ($S_0=0.118$) using various H/dp , compared to measured data in space and time, as well as the simulated water particles in the numerical domain, using various H/dp . The parameters $\alpha=0.1$ and $h_{SPH}/dp=3$ are constant.

Figure 6-21 shows the influence of various H/dp (in combination with a range of α and h_{SPH}/dp) on the correlation coefficient ($p_{x\eta}$) between the simulated and measured time varying wave elevation (η/h_0) profiles, at $X=8.25$ on the beach slope. The figure shows no clear relationship between α and h_{SPH}/dp and $p_{x\eta}$ for a constant H/dp . However, the relationship between α and h_{SPH}/dp and $p_{x\eta}$ is similar for $H/dp=10$ and $H/dp=15$. Furthermore, $H/dp=30$ and $H/dp=90$ generally yield a higher correlation ($p_{x\eta}>0.5$) between the simulated and measured wave profiles for various α and h_{SPH}/dp compared to $H/dp=10$, and $H/dp=15$ which generally yields a low correlation ($p_{x\eta}<0.5$) for various α , and h_{SPH}/dp .

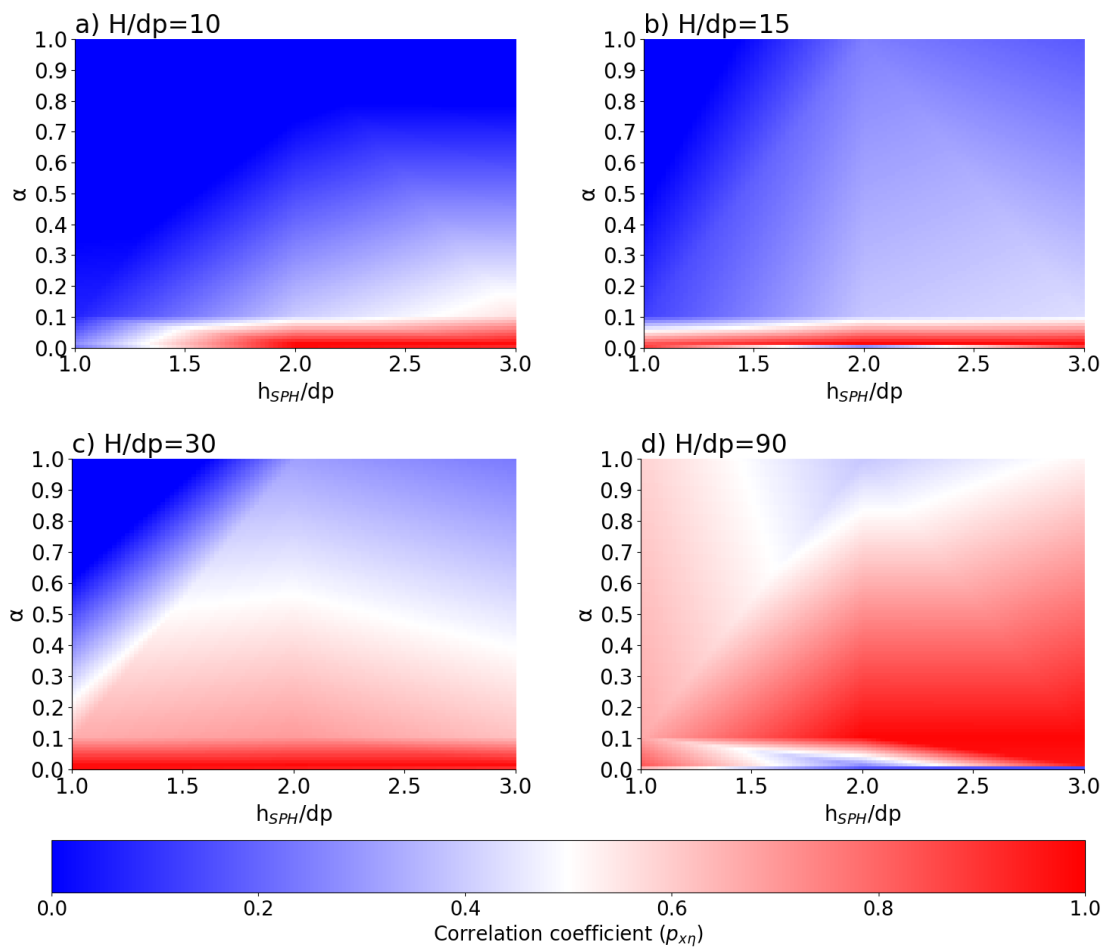


Figure 6-21: The influence of various H/dp (in combination with a range of α and h_{SPH}/dp) on the correlation coefficient ($p_{x\eta}$) between the simulated and measured time varying wave elevation (η/h_0) profiles, at $X=8.25$ on the beach slope.

6.2 Model performance

The performance of a two-dimensional SPH model was analysed and based on the simulated flow field beneath breaking waves. The velocity, vorticity and bed shear stress was evaluated and analysed in the surf zone for three cases of breaking waves. The first case was a plunging solitary wave with a relative wave height (H/h_0) of 0.6 and slope parameter (S_0) of 0.118. The second case was a plunging solitary wave with a relative wave height (H/h_0) of 0.262 and slope parameter (S_0) of 0.078. The last case was a spilling solitary wave with a relative wave height (H/h_0) of 0.6 and slope parameter (S_0) of 0.019.

6.2.1 Case one: plunging solitary wave ($S_0=0.118$)

A plunging solitary wave, with a relative wave height (H/z_0) of 0.6 and slope parameter (S_0) of 0.118, was simulated using the calibrated parameters $\alpha=0.1$, $h_{SPH}/dp=3$ and $H/dp=90$. Due to experimental limitations, the simulated flow field beneath the breaking wave could not be validated using laboratory measurements for the same wave characteristics. Instead, the simulated results were compared to previous studies that measured plunging waves (e.g., Sumer et al., 2013; Ting, 2013; Lin. et al., 2015; LeClaire and Ting, 2017).

6.2.1.1 Wave shoaling and wave breaking

Figure 6-22 and Figure 6-23 show the simulated spatially varying velocity magnitude and vorticity beneath a plunging solitary wave ($S_0=0.118$), respectively, during the interval $T=5.67$ and $T=6.33$. The figures show that the velocity accelerates shorewards as the plunging solitary wave shoals and begins to break. The bottom friction increases with the increasing velocity on the beach slope. Hence, the clockwise (positive) vorticity near the bottom increases. Furthermore, the clockwise (positive) and anticlockwise (negative) vorticity increases in the wave crest as the wave begins to break and overturn. Hence, the flow in the overturning wave crest begins to transition from laminar to rotational. The point of wave breaking, defined as the instant the wave front becomes vertical (Iverson, 1952; Seyama and Kimura, 1988; Bonmarin, 1989; Smith and Kraus, 1991; Grilli, 1997; Blenkinsopp and Chaplin, 2008), occurs during the interval $T=6$ and $T=6.33$ and between $X=8.5$ and $X=9$ on the beach slope (Figure 6-22c-d and Figure 6-23c-d). The water particle velocities directly prior to wave breaking exceed the wave celerity (C) of 1.53 m/s and is a distinct characteristic for breaking plunging solitary waves, according to Peregrine et al. (1980).

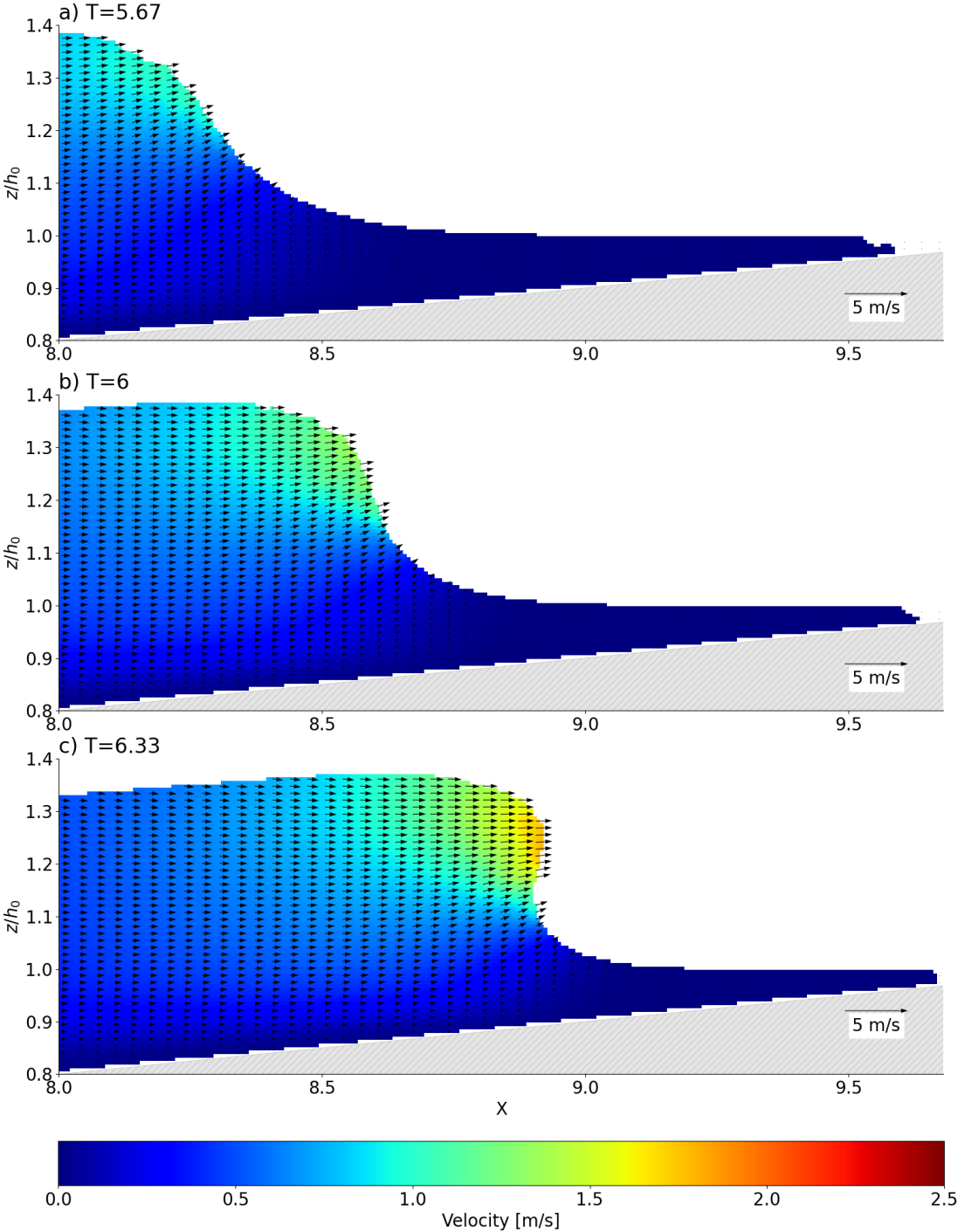


Figure 6-22: The simulated spatially varying velocity magnitude beneath a plunging solitary wave ($S_0=0.118$), propagating over a 1/10 beach slope, during the interval $T=5.67$ to $T=6.33$. The velocity vectors are overlaid as a quiver plot.

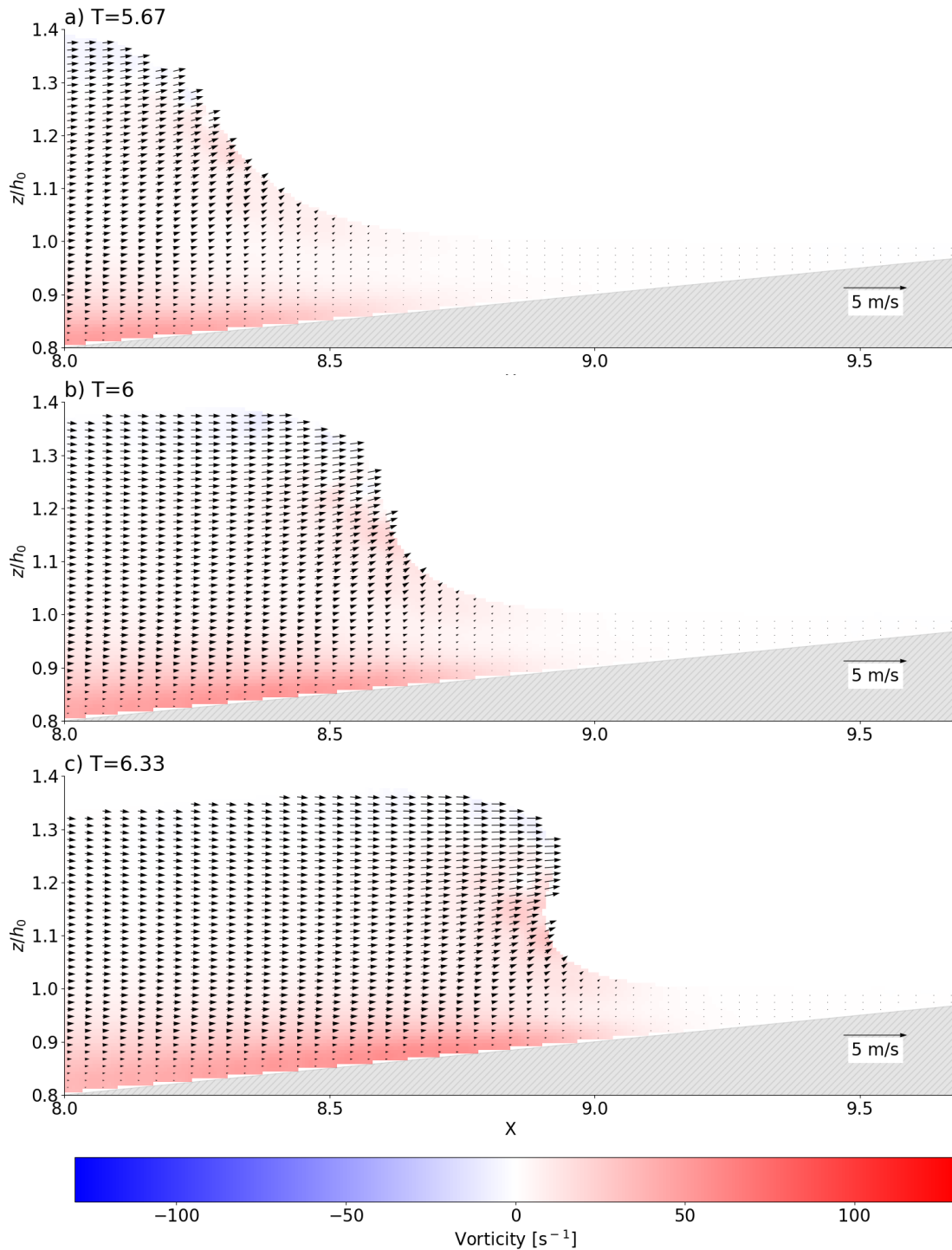


Figure 6-23: The simulated spatially varying vorticity beneath a plunging solitary wave ($S_0=0.118$), propagating over a $1/10$ beach slope, during the interval $T=5.67$ to $T=6.33$. The velocity vectors are overlaid as a quiver plot.

Figure 6-24 and Figure 6-25 show the simulated spatially varying velocity magnitude and vorticity beneath a plunging solitary wave ($S_0=0.118$), respectively, during the interval $T=6.67$ and $T=7.67$. The figures show that the velocity continues accelerating shorewards as the plunging solitary wave overturns, forms a plunging jet, and impinges onto the beach slope. Similar to observations by Battjes (1988), a cavity forms during wave

impingement which results in the initially simply connected fluid domain becoming doubly connected and a nonzero, topologically induced circulation forms around the cavity. Thereafter, the cavity collapses, and mixing occurs between the entrapped air and water. The bottom friction further increases with the increasing velocity on the beach slope. Hence, the clockwise (positive) vorticity near the bottom further increases. The clockwise (positive) and anticlockwise (negative) vorticity also further increases in the wave crest during the overturning wave motion and wave impingement on the beach slope. The flow in the overturning and impingement wave crest is rotational, and the clockwise (positive) vorticity ranges from 50.21 s^{-1} to 129.43 s^{-1} . The vorticity outside the wave crest (above the boundary layer) is small compared to the vorticity in the region of the overturning wave front. Fedder and Trowbridge (2005) similarly showed that the clockwise (positive) vorticity near the front face of a breaking plunging wave is in the order of 80 s^{-1} , while the vorticity in the rest of the wave is negligible.

The plunging solitary wave jet impacts the beach slope at approximately $T=7.33$ and between $X=9.3$ and $X=10.3$ on the beach slope (Figure 6-24c and Figure 6-25c). Prior to the impact, the maximum water particle velocity at the tip of the plunging jet is 2.49 m/s (Figure 6-24b) which equates to 1.63 times the wave celerity (c) and is similar to measured results obtained by Chang and Liu (1998;1999). Chang and Liu (1998; 1999) found the breaking jet of a plunging wave to have a velocity of $1.68c$ and $1.5c$, respectively.

The simulated clockwise (positive) and anticlockwise (negative) vorticity in the region of the plunging jet increases and reaches a maximum near the bed at the same instant the wave-induced onshore horizontal velocity reaches a maximum (Figure 6-24c and Figure 6-25c). The simulated vorticity agrees with measured results by Ting (2013) showing a plunger vortex generated at incipient breaking reaches the bed at approximately the instant of maximum positive wave-induced velocity. Additionally, the asymmetrical velocity pattern observed is an indication of impinging counter-rotating eddies with intense downward velocity fluctuations (Ting, 2013). According to Battjes (1988) a vortical motion and a high concentration of air bubbles occurs due to the mixing of entrapped air with water. However, this process was not modelled and cannot be observed in the results presented here.

Following wave impingement, the broken plunging solitary wave enters the run-up phase on the beach slope, and the onshore motion is again in the laminar flow regime (Figure 6-24d and Figure 6-25d). A small gap appears between the simulated fluid and boundary particles in the region where the plunging solitary wave impinges onto the beach slope

and enters the run-up phase due to a boundary effect. The dynamic boundary condition (DBC) (refer to section 3.7) was applied in the SPH model results in forces exerted by the boundary particles that create a small gap between them and fluid particles, which is of the order of the smoothing length ($1.5h_{\text{SPH}}$).

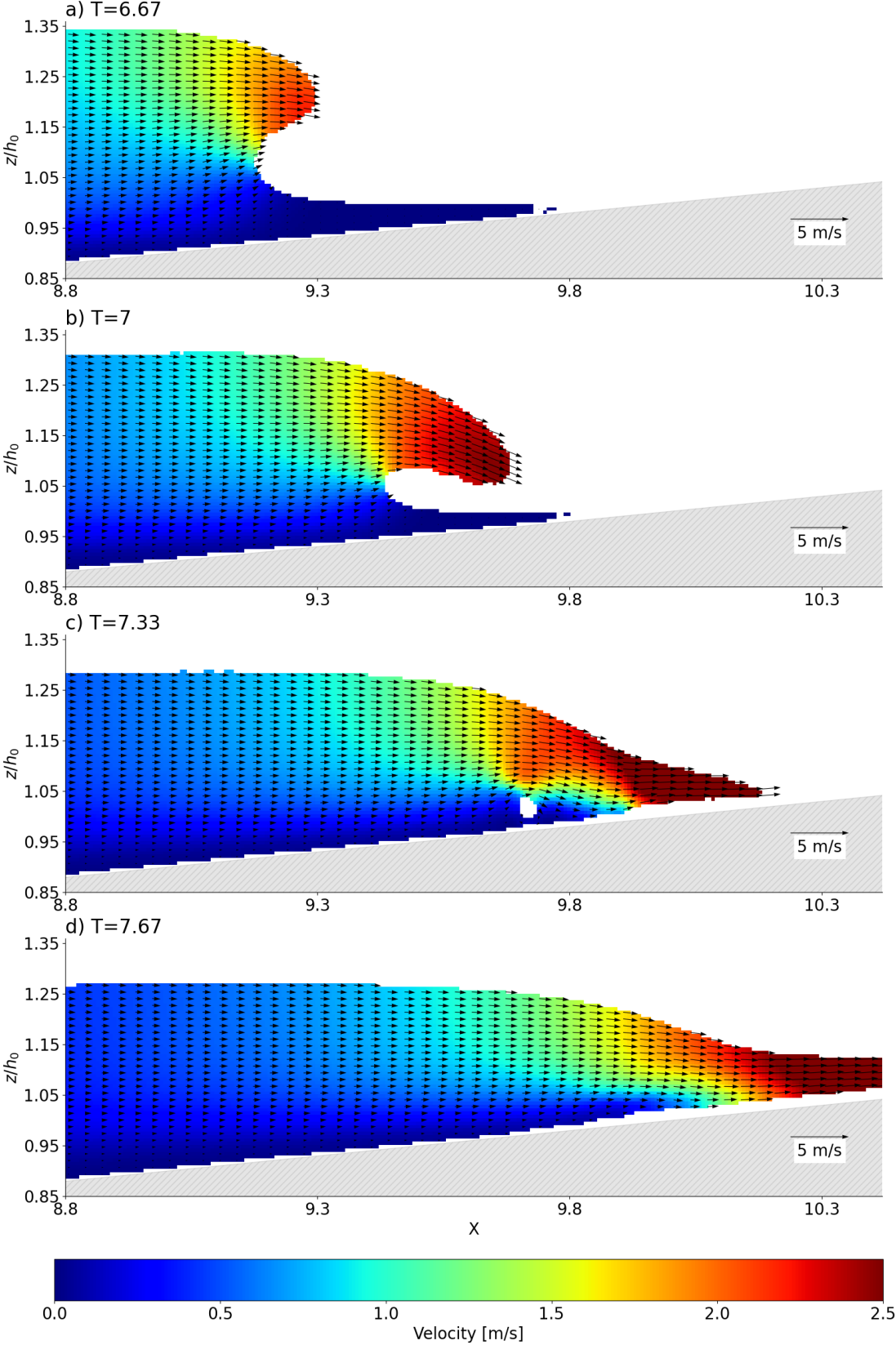


Figure 6-24: The simulated spatially varying velocity magnitude beneath a plunging solitary wave ($S_0=0.118$), propagating over a $1/10$ beach slope, during the interval $T=6.33$ to $T=7.33$. The velocity vectors are overlaid as a quiver plot.

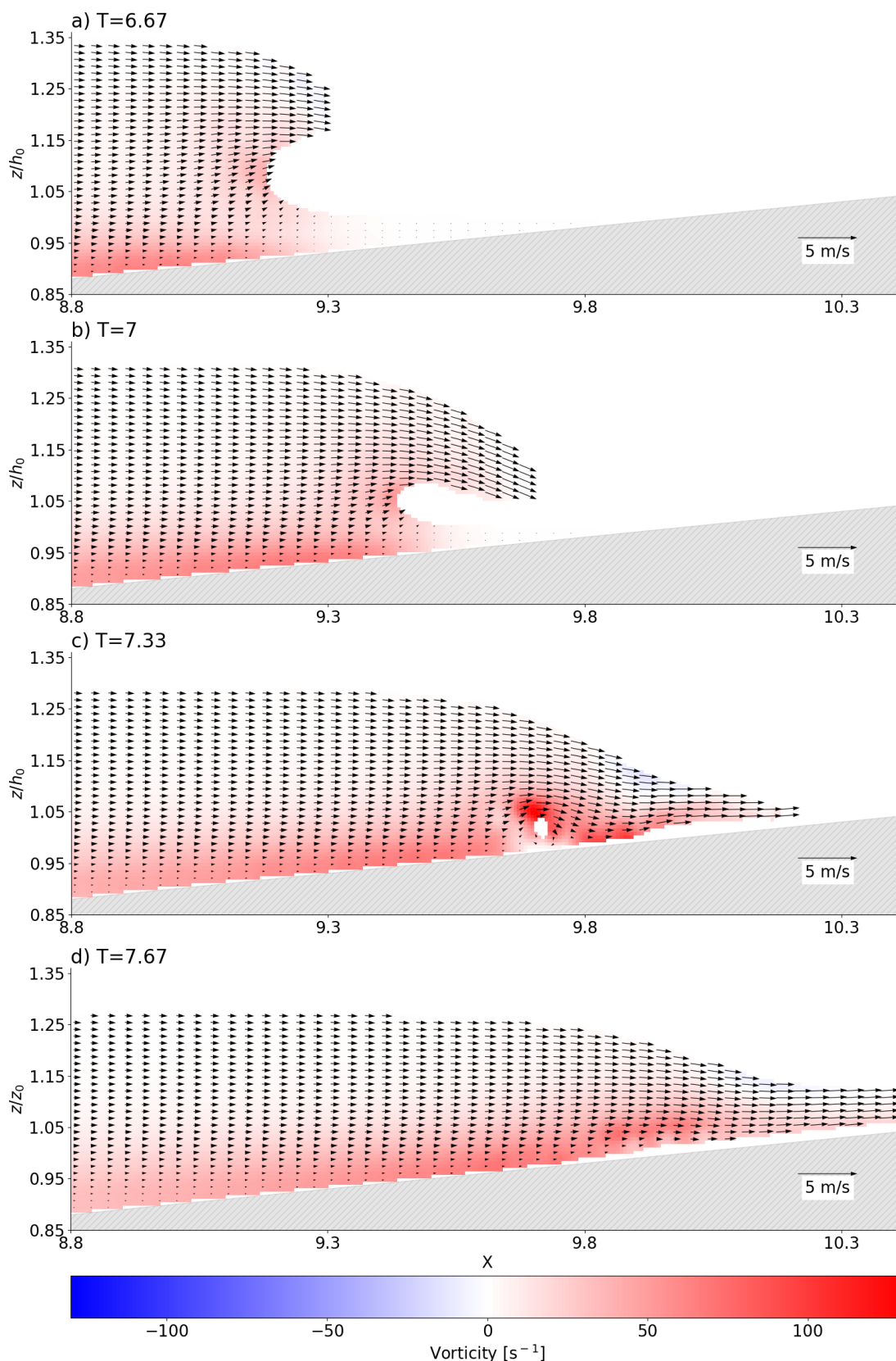


Figure 6-25: The simulated spatially varying vorticity beneath a plunging solitary wave ($S_0=0.118$), propagating over a $1/10$ beach slope, during the interval $T=6.33$ to $T=7.33$. The velocity vectors are overlaid as a quiver plot.

Table 6-6 shows the maximum simulated velocity and vorticity beneath a plunging solitary wave ($S_0=0.118$) at different times, during the interval $T=5.67$ to $T=7.67$. The maximum values occurred in the plunging jet region as the wave impinges onto the beach slope, during the interval $T=7.33$ to $T=7.67$ (Figure 6-24c-d and Figure 6-25c-d). The maximum velocity magnitude was 3.92 m/s, the maximum onshore horizontal velocity was 1.98 m/s, and the maximum offshore horizontal velocity was 0.35 m/s. Furthermore, the maximum clockwise (positive) and anticlockwise (negative) vorticity was 129.43 s^{-1} and 12.98 s^{-1} , respectively.

Table 6-6: The maximum simulated velocity and vorticity beneath a plunging solitary wave ($S_0=0.118$), propagating over a 1/10 beach slope, during the interval $T=5.33$ to $T=7.33$.

T	Velocity magnitude [m/s]	Onshore horizontal velocity [m/s]	Offshore horizontal velocity [m/s]	Clockwise vorticity [s^{-1}]	Anti-clockwise vorticity [s^{-1}]
5.67	1.06	1.00	0.08	50.21	7.73
6	1.34	1.15	0.08	54.82	9.54
6.33	1.79	1.33	0.08	58.19	7.45
6.67	2.20	1.46	0.09	63.50	7.26
7	2.49	1.48	0.09	67.94	7.07
7.33	3.91	1.97	0.35	129.43	12.98
7.67	3.92	1.98	0.09	71.64	8.07

Figure 6-26 shows the simulated spatially varying velocity vectors and vorticity, near the bed, beneath a plunging solitary wave ($S_0=0.118$), during the interval $T=6$ to $T=12$. The sequence and structure of the simulated velocity vectors are similar to measured data by Lin et al. (2015), shown in Figure B-1 (refer to Appendix B). However, the simulated velocity is greater and slightly out of phase compared to the measured data. A possible explanation for these differences is that the simulated wave characteristics were different to the experimental wave characteristics. The relative wave height (H/h_0) and slope parameter (S_0) of the simulated plunging solitary wave were 0.6 and 0.118, respectively. The relative wave height (H/h_0) and slope parameter (S_0) of the experimental plunging solitary wave were 0.262 and 0.078, respectively.

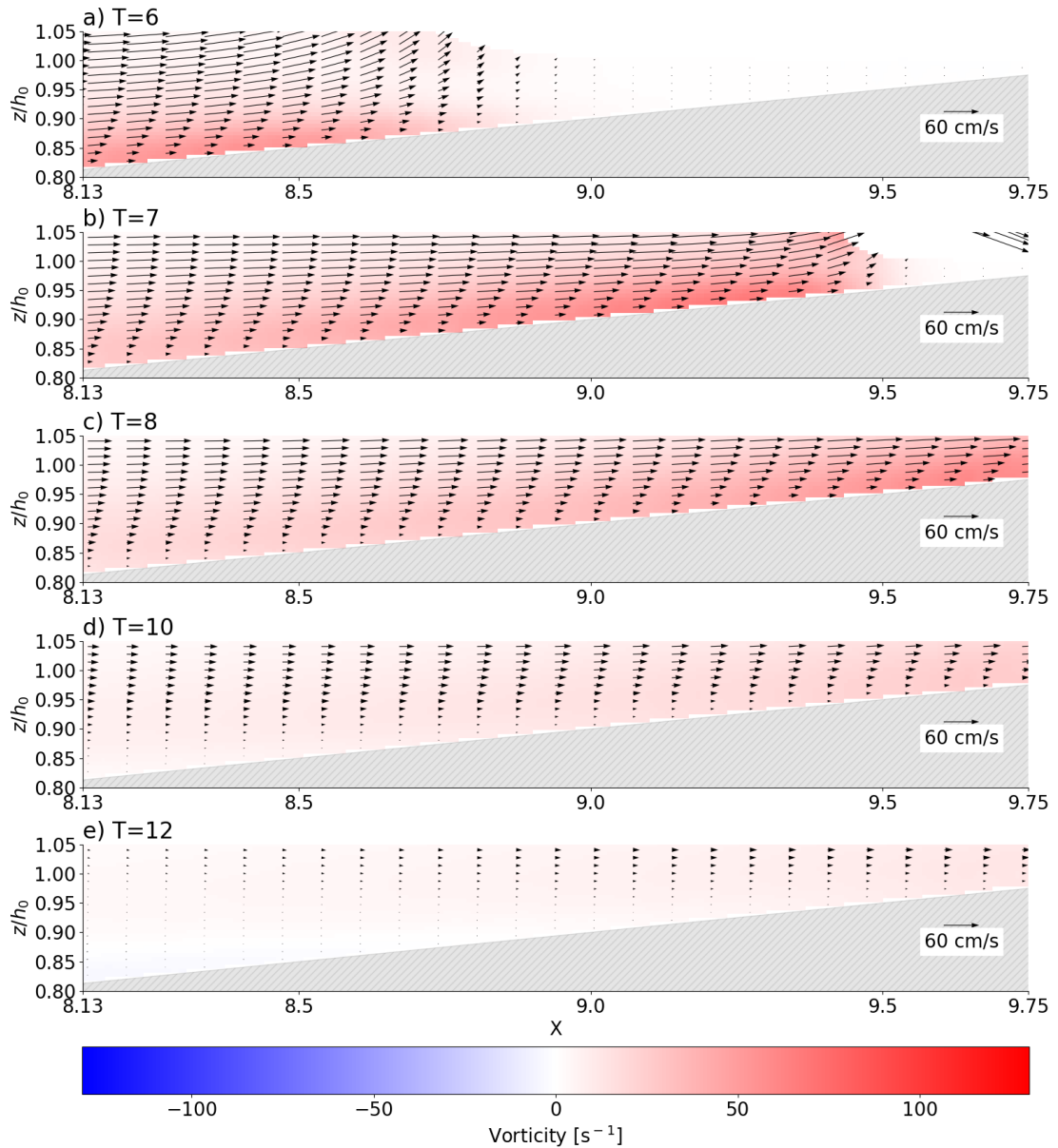


Figure 6-26: The simulated spatially varying velocity vectors and vorticity, near the bed, beneath a plunging solitary wave ($S_0=0.118$), propagating over a $1/10$ beach slope, during the interval $T=6$ to $T=12$.

6.2.1.2 Wave run-up and flow reversal

Figure 6-27 and Figure 6-28 show the simulated spatially varying velocity magnitude and vorticity beneath a plunging solitary wave ($S_0=0.118$), respectively, during the interval $T=15$ and $T=20$. The figures show that the velocity decelerates as the broken plunging solitary runs up the beach slope due to bottom friction. The velocity and vorticity gradually decrease to zero, and the maximum wave run-up is approximately $X=14.67$ on the beach slope. Thereafter, the onshore wave motion completely transitions into an offshore flow of water during the interval $T=16$ to $T=20$ and wave run-down commences (Figure 6-27c-e and Figure 6-28c-e). As wave run-down commences, the velocity

accelerates in the offshore direction and the bottom friction increases. Hence, the anti-clockwise (negative) vorticity near the bottom increases.

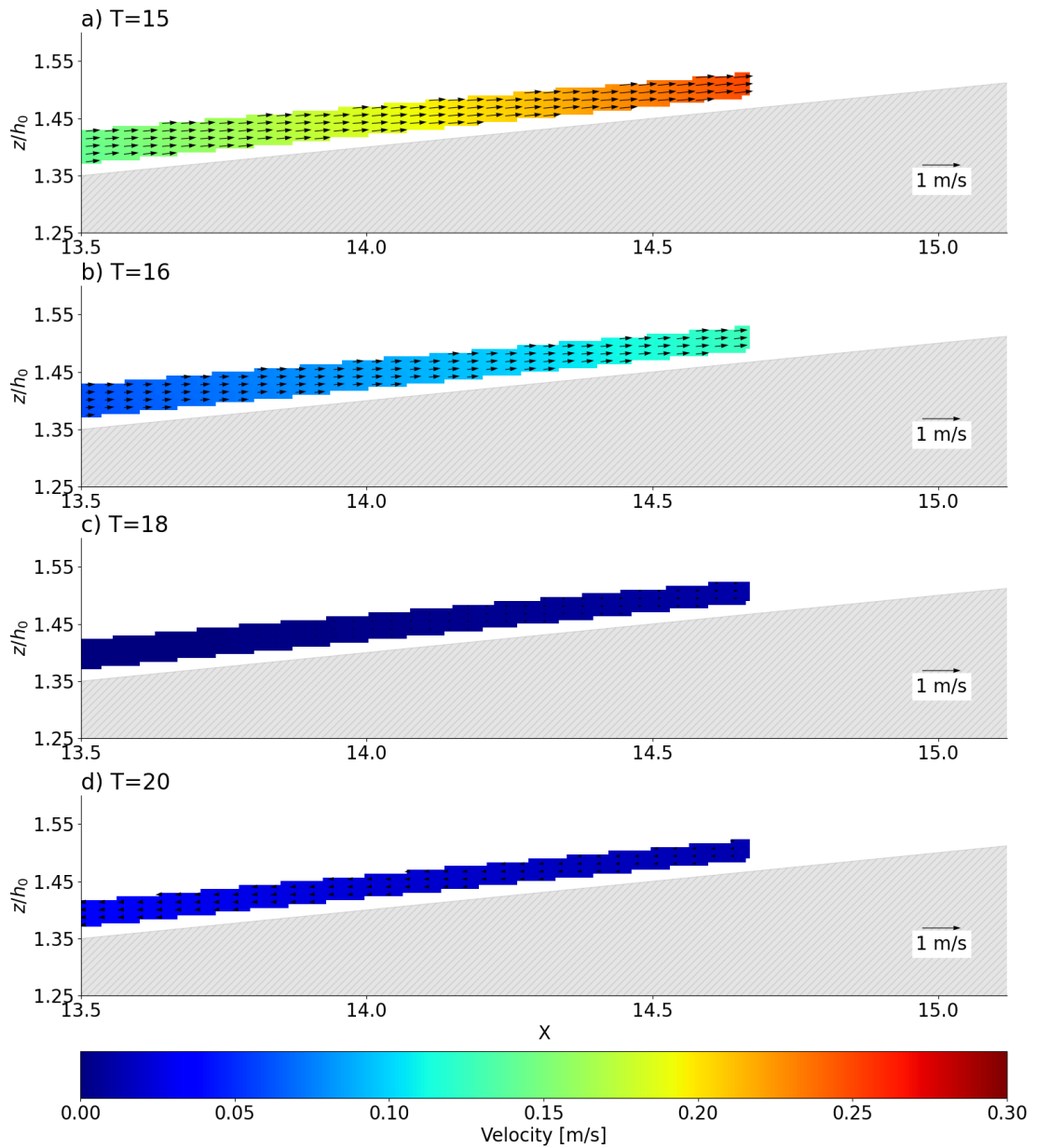


Figure 6-27: The simulated spatially varying velocity magnitude beneath a plunging solitary wave ($S_0=0.118$), propagating over a $1/10$ beach slope, during the interval $T=14$ to $T=20$. The velocity vectors are overlaid as a quiver plot.

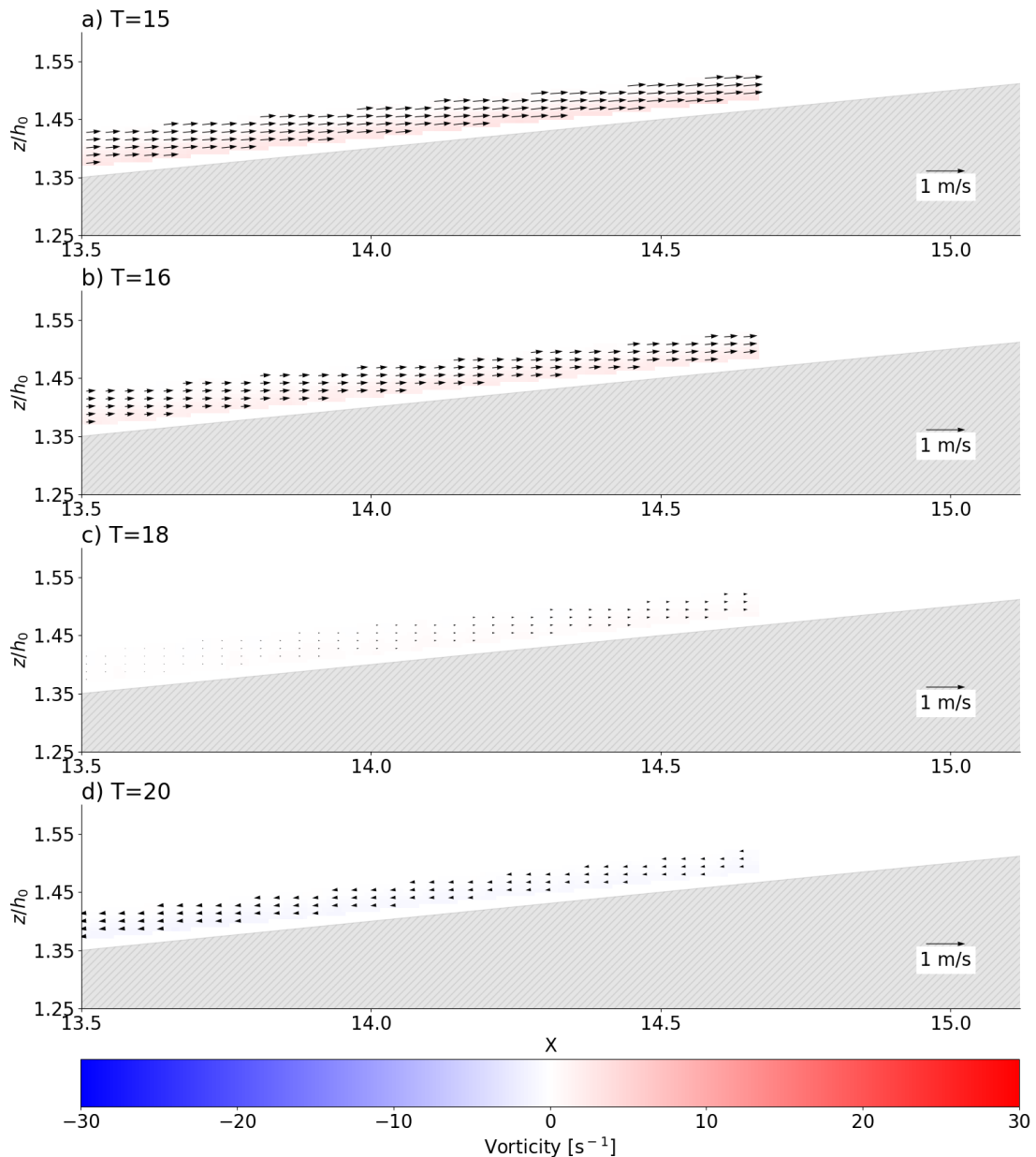


Figure 6-28: The simulated spatially varying vorticity beneath a plunging solitary wave ($S_0=0.118$), propagating over a $1/10$ beach slope, during the interval $T=14$ to $T=20$. The velocity vectors are overlaid as a quiver plot.

Table 6-7 shows the maximum simulated velocity and vorticity beneath a plunging solitary wave ($S_0=0.118$) at different times, during the interval $T=15$ to $T=20$. The maximum velocity magnitude was 0.25 m/s, and the maximum onshore horizontal velocity was 0.5 m/s. The maximum velocity magnitude and onshore horizontal velocity both occurred at $T=15$ (Figure 6-27) before the onshore motion of the broken plunging solitary wave transitioned into an offshore motion on the beach slope. The maximum offshore horizontal velocity was 0.37 m/s, the maximum clockwise (positive) vorticity was $8.86 s^{-1}$, and the maximum anticlockwise (negative) was $27.78 s^{-1}$. These values occurred at $T=20$

(Figure 6-27d and Figure 6-28d) as the broken plunging solitary wave entered the run-down phase on the beach slope.

Table 6-7: The maximum simulated velocity and vorticity beneath a plunging solitary wave ($S_0=0.118$), propagating over a 1/10 beach slope, during the interval $T=15$ to $T=20$.

T	Velocity magnitude [m/s]	Onshore horizontal velocity [m/s]	Offshore horizontal velocity [m/s]	Clockwise vorticity [s^{-1}]	Anti-clockwise vorticity [s^{-1}]
15	0.25	0.50	0.14	3.39	10.18
16	0.13	0.36	0.16	2.45	10.77
17	0.05	0.23	0.18	1.43	12.5
18	0.04	0.11	0.21	1.75	16.98
19	0.06	0	0.25	3.69	20.98
20	0.10	0	0.32	7.16	24.86

Figure 6-29 shows the simulated spatially varying velocity vectors and vorticity near the bed, beneath a plunging solitary wave ($S_0=0.118$), during the interval $T=14$ to $T=20$. The sequence and structure of the simulated velocity vectors are similar to measured data by Lin et al. (2015), shown in Figure B-2 (refer to Appendix B). However, the simulated velocity is greater and slightly out of phase compared to the measured data. Additionally, the negative velocity profiles in Figure 6-29(b–d) do not appear with overshooting near the sloping bed, as shown in Figure B-2(b–d). Again, a possible explanation for these differences is that the simulated wave characteristics differed from the experimental wave characteristics. The relative wave height (H/h_0) and slope parameter (S_0) of the simulated plunging solitary wave were 0.6 and 0.118, respectively. The relative wave height (H/h_0) and slope parameter (S_0) of the experimental plunging solitary wave were 0.262 and 0.078, respectively.

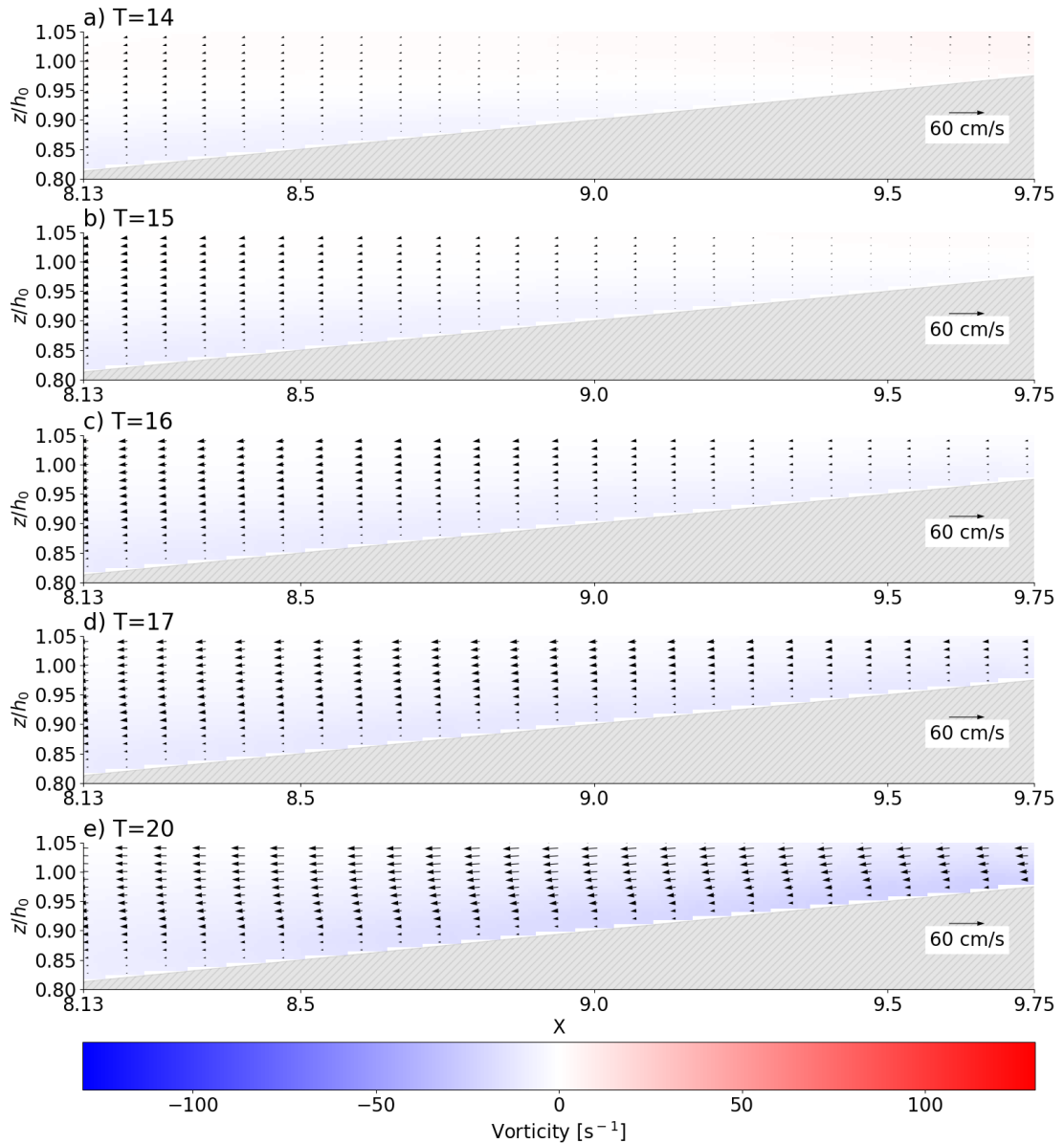


Figure 6-29: The simulated spatially varying velocity vectors and vorticity, near the bed, beneath a plunging solitary wave ($S_0=0.118$), propagating over a $1/10$ beach slope, during the interval $T=14$ to $T=20$.

6.2.1.3 Wave run-down

Figure 6-30 and Figure 6-31 show the simulated spatially varying velocity magnitude and vorticity beneath a plunging solitary wave ($S_0=0.118$), respectively, during the interval $T=30$ and $T=34$. The figures show that the velocity accelerates offshore as the broken plunging solitary runs down the beach slope. The bottom friction increases with the increasing offshore velocity. This leads to a hydraulic jump and a secondary plunging wave forming on the beach slope. The secondary plunging wave overturns, forms a plunging jet, and impinges onto the accelerating flow running down the beach slope with splash up during the interval $T=32$ and $T=34$, and between $X=8.5$ and $X=9.5$ on the beach slope (Figure 6-30d-e and Figure 6-31d-e). Strong clockwise (positive) and anticlockwise

(negative) vorticity is observed in the downflow and secondary plunging wave jet. The flow separates on the beach slope around $T=33$ and between $X=9.5$ and $X=10$ on the beach slope.

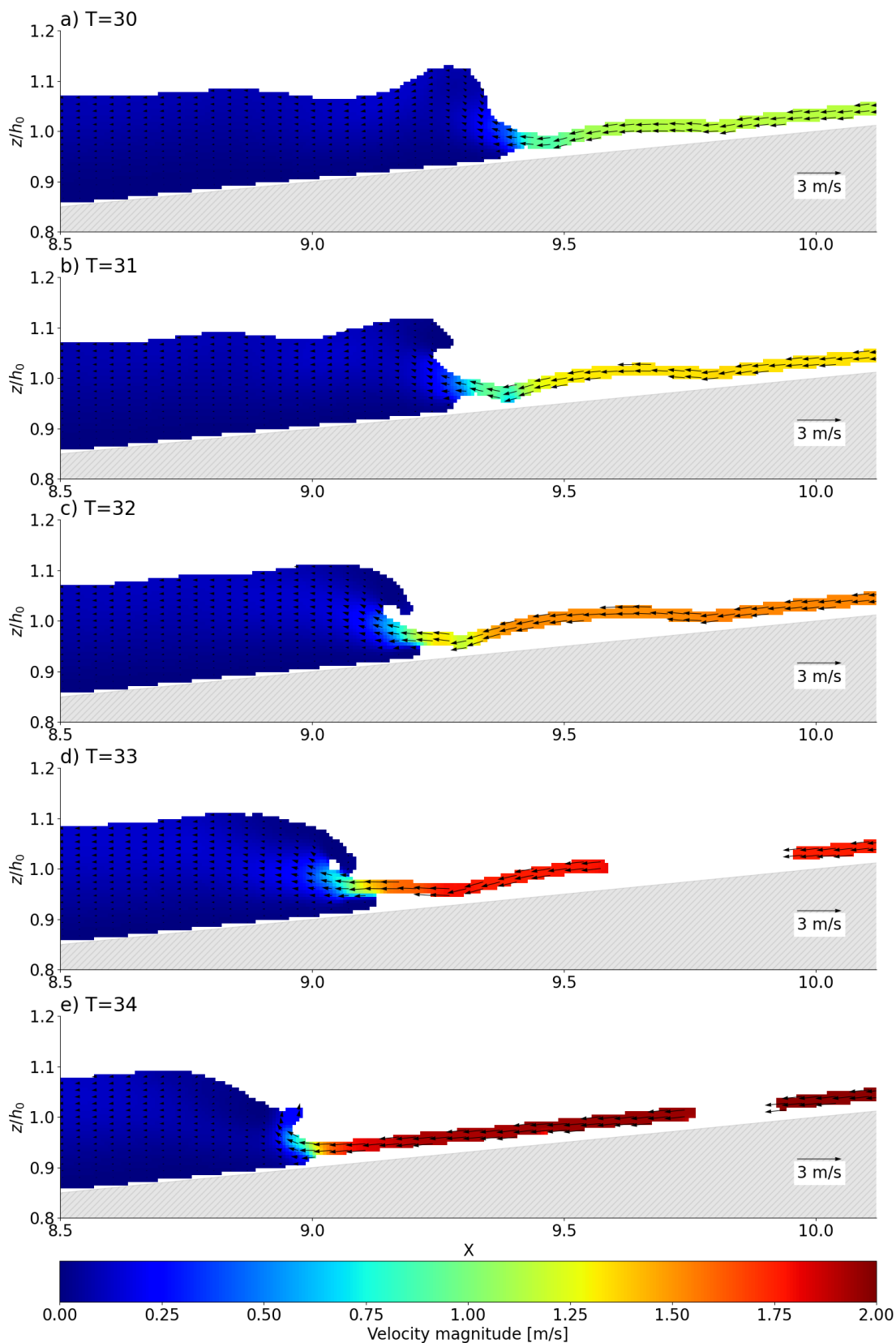


Figure 6-30: The simulated spatially varying velocity magnitude beneath a plunging solitary wave ($S_0=0.118$), propagating over a 1/10 beach slope, during the interval $T=30$ to $T=34$. The velocity vectors are overlaid as a quiver plot.

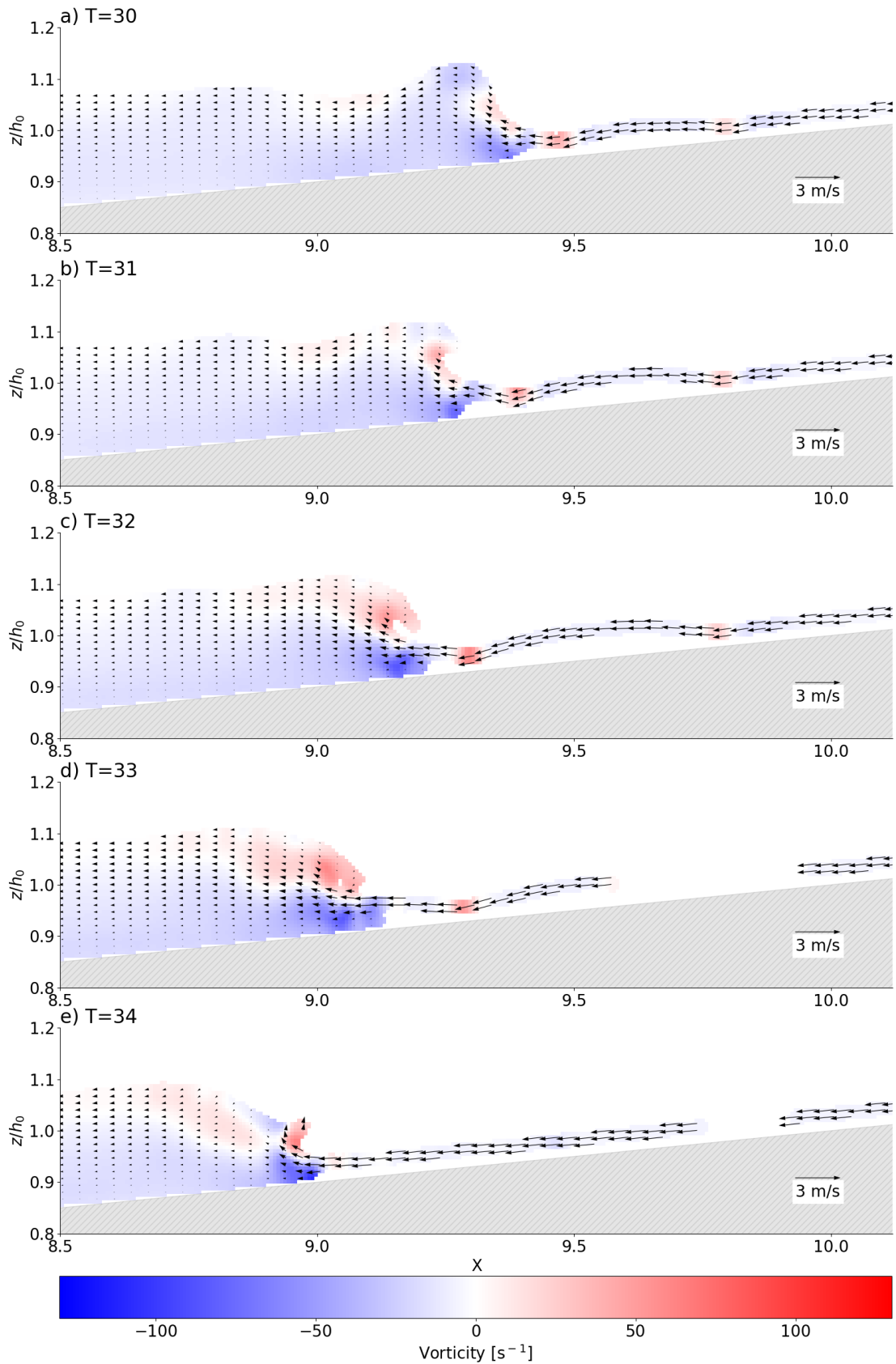


Figure 6-31: The simulated spatially varying vorticity beneath a plunging solitary wave ($S_0=0.118$), propagating over a $1/10$ beach slope, during the interval $T=30$ to $T=34$. The velocity vectors are overlaid as a quiver plot.

Table 6-8 shows the maximum simulated velocity and vorticity beneath a plunging solitary wave ($S_0=0.118$) at different times, during the interval $T=30$ and $T=34$. The maximum values occurred in the secondary plunging solitary wave region, at $T=34$, as the secondary wave impinges onto the accelerating downflow with splash-up. The maximum velocity magnitude was 1.98 m/s, the maximum onshore horizontal velocity was 0.12 m/s, and the maximum offshore horizontal velocity was 1.40 m/s. Furthermore, the maximum clockwise (positive) and anticlockwise (negative) vorticity was 63.38 s^{-1} and 108.61 s^{-1} , respectively.

Table 6-8: The maximum simulated velocity and vorticity beneath a plunging solitary wave ($S_0=0.118$), propagating over a 1/10 beach slope, during the interval $T=30$ to $T=34$.

T	Velocity magnitude [m/s]	Onshore horizontal velocity [m/s]	Offshore horizontal velocity [m/s]	Clockwise vorticity [s^{-1}]	Anti-clockwise vorticity [s^{-1}]
30	1.16	0	1.08	43.55	66.54
31	1.36	0.02	1.16	54.15	76.38
32	1.55	0	1.24	59.79	85.51
33	1.80	0	1.34	60.35	83.3
34	1.98	0.12	1.40	63.38	108.61

Figure 6-32 shows the simulated spatially varying velocity vectors and vorticity, near the bed, beneath a plunging solitary wave ($S_0=0.118$), during the intervals $T=24$ to $T=28$ and $T=38$ to $T=40$. The sequence, structure, magnitude and phase of the simulated velocity vectors vary in comparison to measured data by Lin et al. (2015), shown in Figure B-3 (refer to Appendix B). In addition to the simulated wave characteristics being different to the measured wave characteristics, a possible explanation for these differences is that the simulated flow field was computed using a two-dimensional SPH model. The near-bed velocity fields beneath plunging waves are highly three-dimensional (Ting, 2013). Hence, the two-dimensional SPH model cannot capture the three-dimensional nature of the downflow with complete accuracy. However, according to Lin. et al. (2015), at $T=36$ (not shown), the offshore horizontal velocity of the downflow decreases to zero after the hydraulic jump and thereafter (after $T=40$), the velocity should accelerate shoreward, producing a secondary run-up flow. This can be observed in Figure 6-32(c-e) for the simulated plunging solitary wave.

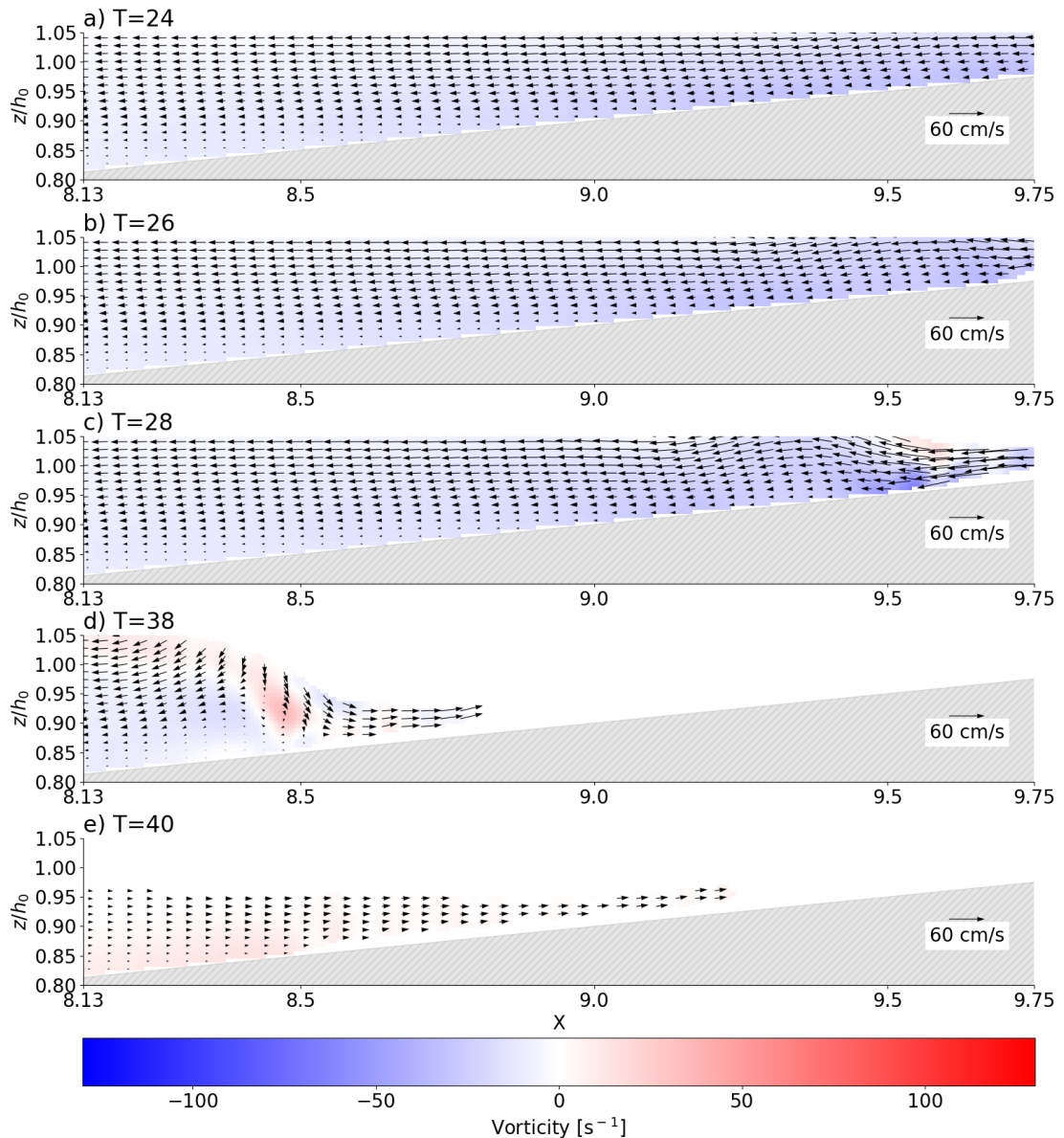


Figure 6-32 The simulated spatially varying velocity vectors and vorticity, near the bed, beneath a plunging solitary wave ($S_0=0.118$), propagating over a $1/10$ beach slope, during the interval $T=24$ to $T=28$ and $T=38$ to $T=40$.

6.2.1.4 The bed shear stress

Figure 6-33 shows the evolution of the bed shear stress beneath a plunging solitary wave ($S_0=0.118$) at $z/h_0=0.03$ above the beach slope in the surf zone. Figure 6-33(a) shows the spatially varying peak bed shear stress ($\tau_{b(peak)}$) during the interval $T=0$ to $T=40$. Figure 6-33(b) shows the time varying bed shear stress (τ_b) at $X=10.1$ on the beach slope. The figure shows that the peak bed shear stress ($\tau_{b(peak)}$) is generally higher in the offshore direction compared to the onshore direction, except in the region $X=10$ and $X=10.5$ on the beach slope (Figure 6-33a) wherein the breaking plunging wave first impinges onto the beach slope (refer to section 6.2.1.1).

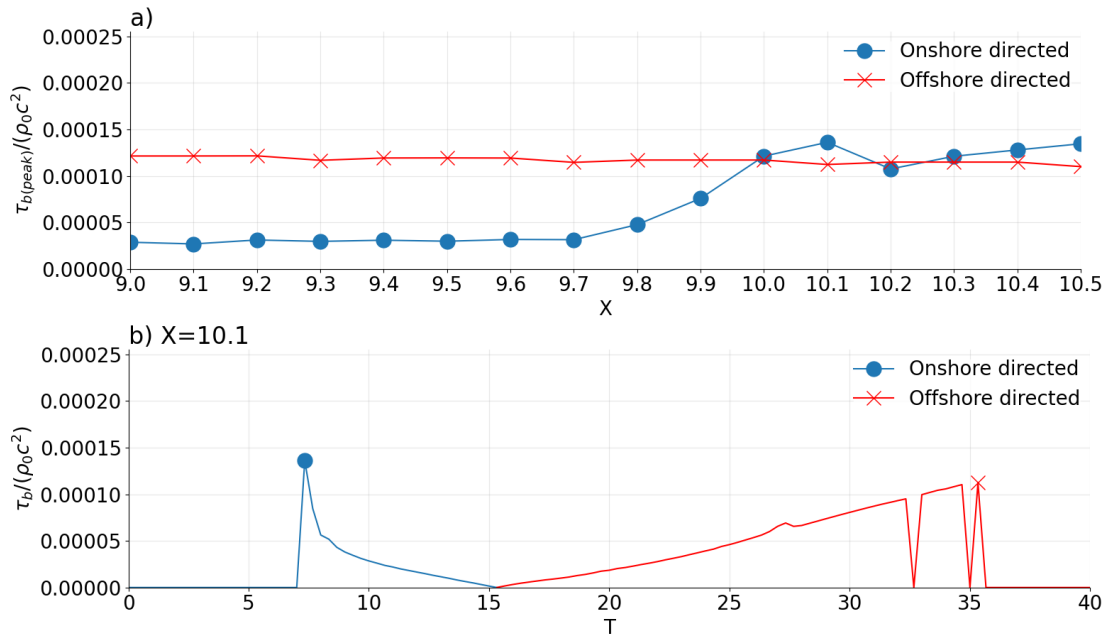


Figure 6-33: The a) spatially varying peak bed shear stress ($\tau_{b(\text{peak})}$), and the b) time varying bed shear stress (τ_b) at $X=10.1$ on the beach slope, as a plunging solitary wave ($S_0=0.118$), propagates over a 1/10 beach slope, during the interval $T=0$ to $T=40$.

Table 6-9 shows the maximum bed shear stress ($\tau_{b(\text{max})}$) and shear velocity ($u_{*(\text{max})}$) in the onshore and offshore direction beneath a plunging solitary wave ($S_0=0.118$) during the interval $T=0$ to $T=40$. The table also shows when these maximum values occurred and where these maximum values occurred on the beach slope. The maximum onshore directed bed shear stress and shear velocity were 0.32 N/m² and 1.79 cm/s, respectively, and occurred at $X=10.1$ on the beach slope and $T=7.33$ during wave impingement on the beach slope (refer to section 6.2.1.1). The maximum offshore directed bed shear stress and shear velocity was 0.29 N/m² and 1.69 cm/s, respectively, and occurred at $X=9.2$ on the beach slope and $T=37$, towards the end of wave-run down (refer to section 6.2.1.3).

Table 6-9: The maximum onshore and offshore directed bed shear stresses ($\tau_{b(\text{max})}$) and shear velocities ($u_{*(\text{max})}$), the time they occur, and their position on the beach slope, as a plunging solitary wave ($S_0=0.118$), propagates over a 1/10 beach slope, during the interval $T=0$ to $T=40$.

Direction	$\tau_{b\text{max}}$ [N/m ²]	$u_{*\text{max}}$ [cm/s]	T	X
Onshore	0.32	1.79	7.33	10.1
Offshore	0.29	1.69	37	9.2

The results suggest that the wave-induced bed shear stress beneath a plunging solitary wave ($S_0=0.118$) enhances onshore sediment transport during wave impingement on the beach slope and offshore sediment transport during wave run down on the wave the

beach slope. However, sediment mobilisation depends on the grain density and size. For sand with a density of 2.65 g/cm^3 , the maximum wave-induced bed shear stresses beneath a plunging solitary wave ($S_0=0.118$) would mobilise particles smaller than 0.1 cm in diameter (refer to Figure B-4 and in Appendix B). The results also suggest that the net sediment transport beneath a plunging solitary wave ($S_0=0.118$) is offshore directed. The results agree with previous studies on plunging breakers (e.g., Sato et al., 1990; Aagaard and Hughes, 2010; Sumer et al., 20130; Ting, 2013; and LeClaire and Ting, 2017, Yang et al., 2017).

6.2.2 Case two: plunging solitary wave ($S_0=0.078$)

A plunging solitary wave, with a relative wave height (H/h_0) of 0.262 and slope parameter (S_0) of 0.078 , was simulated using the adjusted parameters $\alpha=0$, $h_{SPH}/dp=3$ and $H/dp=50$. The wave characteristics follow a laboratory experiment by Lin et al. (2015). The parameters were adjusted to maintain a feasible computation time for the small relative wave height (H/h_0) (refer to section 6.1.2). Using the adjusted SPH parameters $\alpha=0$, $h_{SPH}/dp=3$, $H/dp=50$, the number of simulated water particles in the numerical domain was $4\,323\,021$, and the computation time for a 15 s simulation was 41.28 hours. Figure 6-34 shows the simulated spatially varying wave (z) profile of the plunging solitary wave ($S_0=0.078$) before breaking, using the adjusted SPH parameters $\alpha=0$, $h_{SPH}/dp=3$, $H/dp=50$. The simulated wave profile is comparable to the measured data by Lin et al. (2015) shown in Figure C-1 (refer to Appendix C).

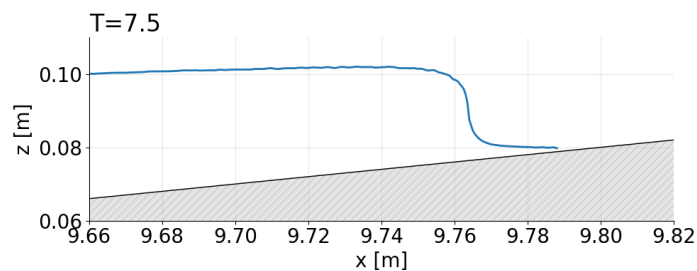


Figure 6-34: The simulated spatially varying wave (z) profile of a plunging solitary wave ($S_0=0.078$), propagating over a $1/10$ beach slope, at $T=7.5$, using $\alpha=0$, $h_{SPH}/dp=3$ and $H/dp=50$.

Figure 6-35 shows the simulated time varying wave elevation (η/h_0) profile of the plunging solitary wave ($S_0=0.078$) at $X=8.25$ on the beach slope, using the adjusted SPH parameters $\alpha=0$, $h_{SPH}/dp=3$, $H/dp=50$. The simulated wave profile is slightly out of phase but comparable to the measured data by Lin et al. (2015) shown in Figure C-2 (refer to Appendix C). during the interval $T=0$ to $T=26$. After $T=26$, the solitary wave is in the run-down phase on the beach slope (refer to Figure C-3 in Appendix C), and the shape of the time varying wave elevation profile is poorly simulated.

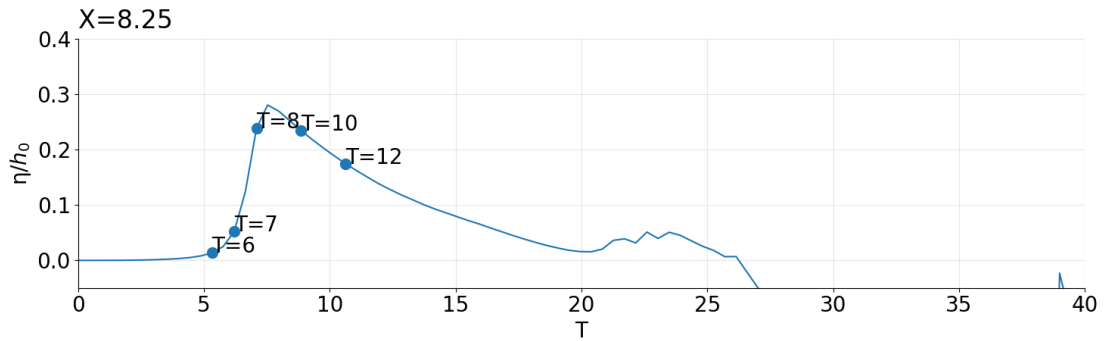


Figure 6-35: The simulated time varying wave elevation (η/h_0) profile of a plunging solitary wave ($S_0=0.078$), propagating over a $1/10$ beach slope, using $\alpha=0$, $h_{SPH}/dp=3$, and $H/dp=50$.

6.2.2.1 Wave shoaling and wave breaking

Figure 6-36 and Figure 6-37 show the simulated spatially varying velocity magnitude and vorticity beneath a plunging solitary wave ($S_0=0.078$), respectively, during the interval $T=7.5$ and $T=9$. The figures show that the shoaling and breaking sequence of the wave is similar to the plunging solitary wave ($S_0=0.118$) analysed in section 6.2.1.1. However, the effects of using a lower particle resolution ($H/dp=50$) combined with a lower artificial viscosity coefficient ($\alpha=0$) are noticeable at the edges around the simulated flow field, which are less smooth. Furthermore, wave breaking commences during the interval $T=7.5$ and $T=8$ and between $X=9.8$ and $X=10.8$ on the beach slope (Figure 6-36a-b and Figure 6-37a-b) for the case presented here. Moreover, the plunging jet impacts the beach slope at approximately $T=8.5$ and between $X=9.8$ and $X=10.8$ on the beach slope (Figure 6-36c and Figure 6-37c). According to Ting (2013), differences in the plunging jet impact angle and water depth account for the differences in the flow field beneath breaking plunging waves.

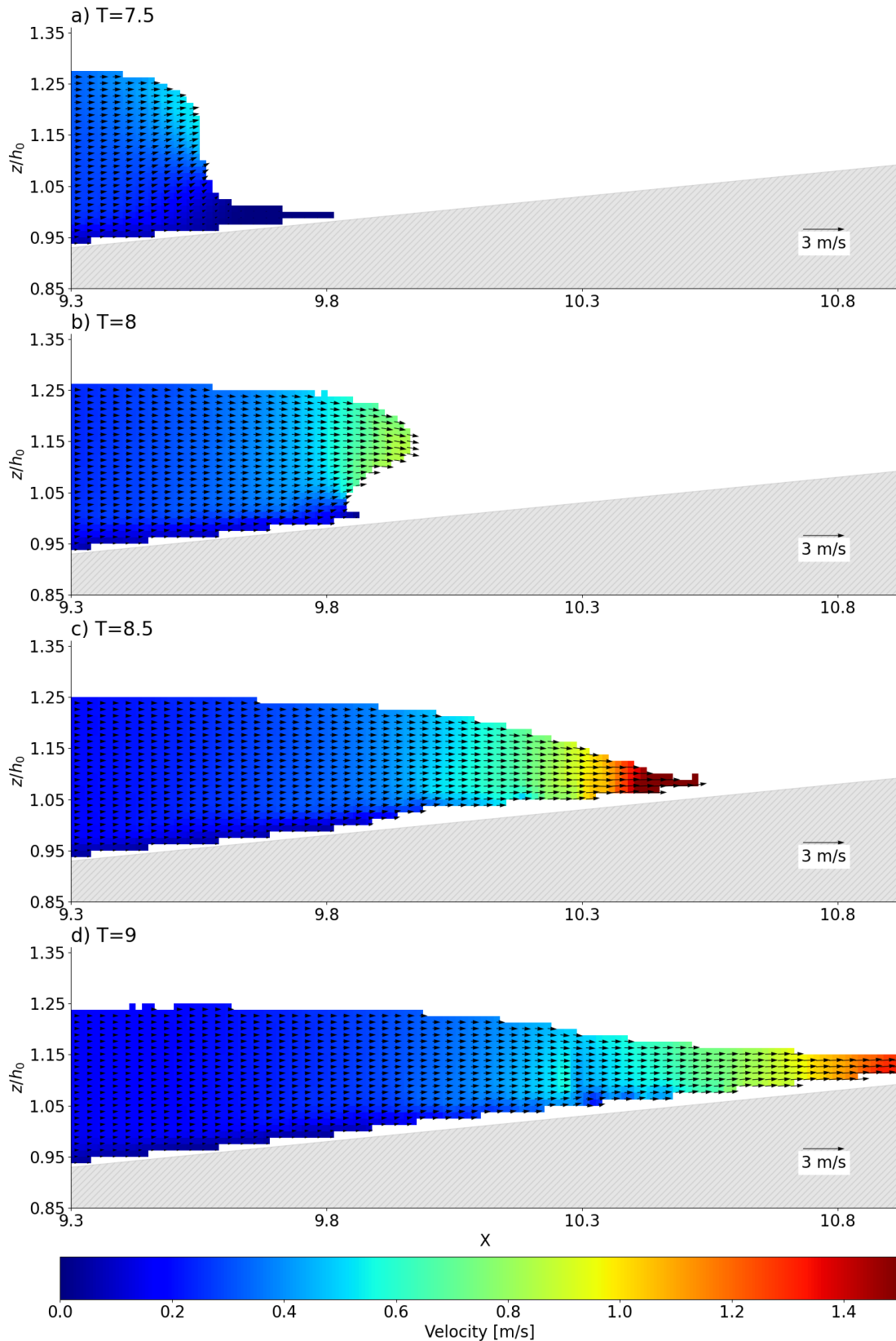


Figure 6-36: The simulated spatially varying velocity magnitude beneath a plunging solitary ($S_0=0.078$), propagating over a $1/10$ beach slope, during the interval $T=7.5$ to $T=9$. The velocity vectors are overlaid as a quiver plot.

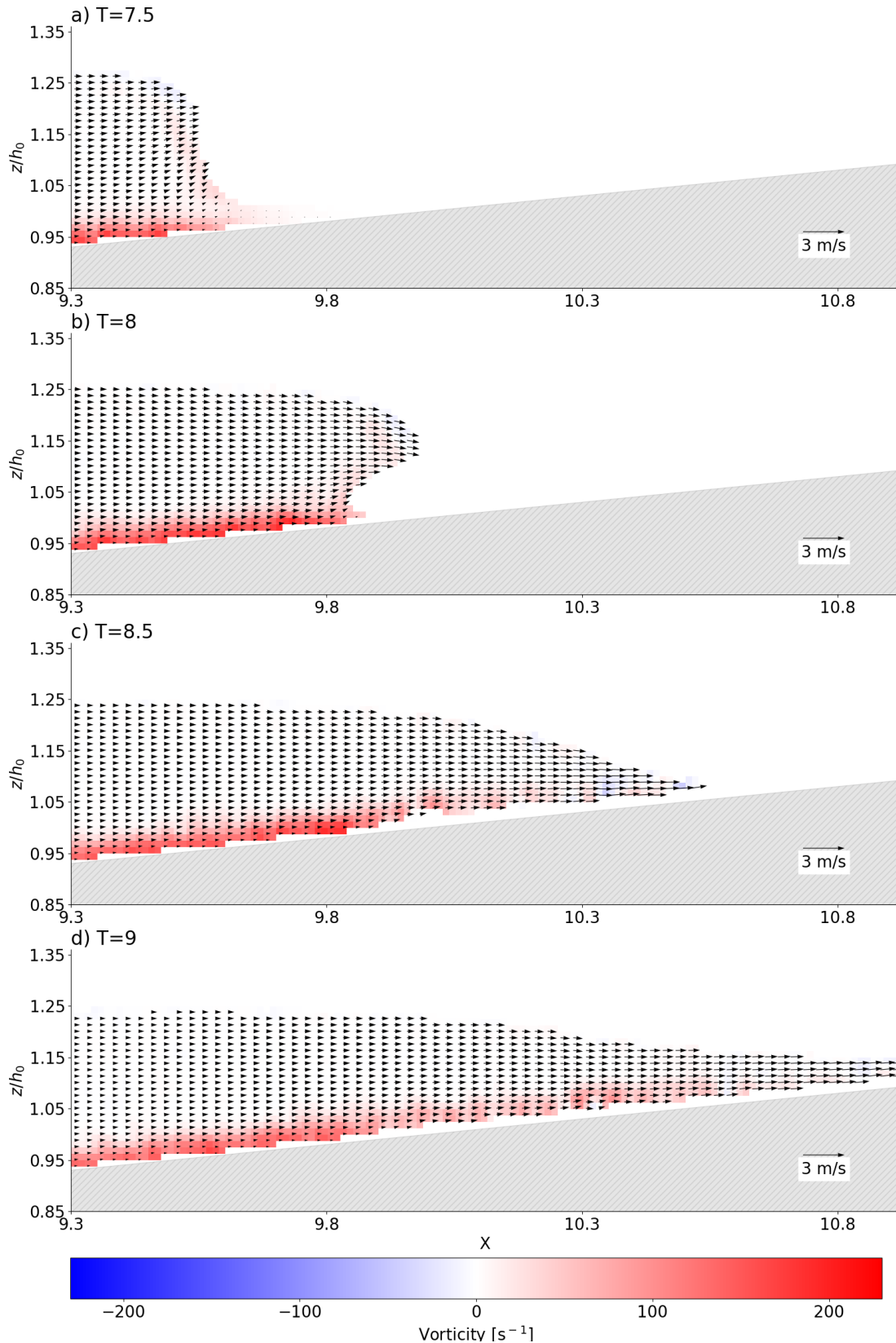


Figure 6-37: The simulated spatially varying vorticity beneath a plunging solitary wave ($S_0=0.078$), propagating over a $1/10$ beach slope, during the interval $T=7.5$ to $T=9$. The velocity vectors are overlaid as a quiver plot.

Table 6-10 shows the maximum simulated velocity and vorticity beneath a plunging solitary wave ($S_0=0.078$) at different times, during the interval $T=7.5$ to $T=9$. The maximum values occur in the plunging jet region, at $T=8.5$, as the wave impinges onto the beach slope. The maximum velocity magnitude was 1.95 m/s, the maximum onshore horizontal velocity was 1.384 m/s, and the maximum offshore horizontal velocity was 0.06 m/s. Furthermore, the maximum clockwise (positive) and anticlockwise (negative) vorticity was 188.72 s^{-1} and 46.11 s^{-1} , respectively.

Table 6-10: The maximum simulated velocity and vorticity beneath a plunging solitary wave ($S_0=0.078$), propagating over a 1/10 beach slope, during the interval $T=7.5$ to $T=9$.

T	Velocity magnitude [m/s]	Onshore horizontal velocity [m/s]	Offshore horizontal velocity [m/s]	Clockwise vorticity [s^{-1}]	Anti-clockwise vorticity [s^{-1}]
7.5	0.54	0.72	0.056	178.279	25.849
8	0.855	0.911	0.059	194	28.02
8.5	1.948	1.384	0.062	188.715	46.111
9	1.805	1.337	0.062	165.575	30.98

Figure 6-38 shows the simulated spatially varying vorticity and velocity vectors, near the bed, beneath a plunging solitary wave ($S_0=0.078$), during the interval $T=6$ to $T=12$. The sequence and structure of the simulated velocity vectors are similar to measured data by Lin et al. (2015), shown in Figure B-1 (refer to Appendix B). However, the simulated velocity is slightly out of phase compared to the measured velocity. The simulated and experimental wave characteristics were the same. Hence, the results suggest that the SPH model, using the adjusted parameters $\alpha=0$, $h_{SPH}/dp=3$, $H/dp=50$, slightly over predicts the numerical wave energy dissipation.

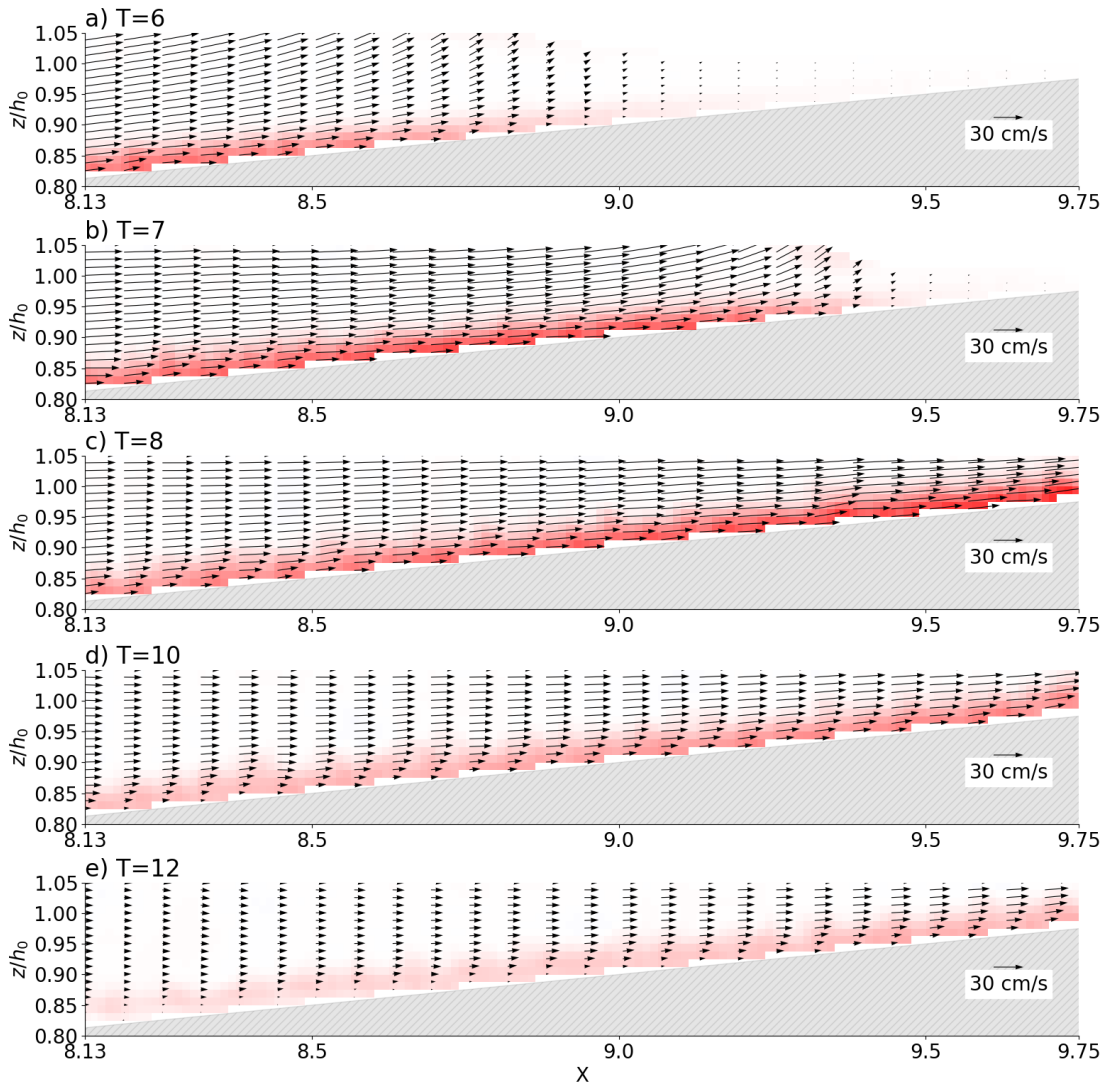


Figure 6-38: The simulated spatially varying vorticity and velocity vectors, near the bed, beneath a plunging solitary wave ($S_0=0.078$), propagating over a 1/10 beach slope, during the interval $T=6$ to $T=12$.

6.2.2.2 Wave run-up and flow reversal

Figure 6-39 and Figure 6-40 show examples of the simulated spatially varying velocity magnitude and vorticity beneath a plunging solitary wave ($S_0=0.078$), respectively, at $T=15$. The figures show that the run-up motion of the broken plunging solitary wave on the beach slope is poorly simulated. During wave run-up, the simulated water particles are scattered and vary considerably compared to the plunging solitary wave ($S_0=0.118$) analysed in section 6.2.1.2. Hence, the particle resolution $H/dp=50$ is too low for the SPH model to accurately capture the thin and aerated run-up flow in the swash zone.

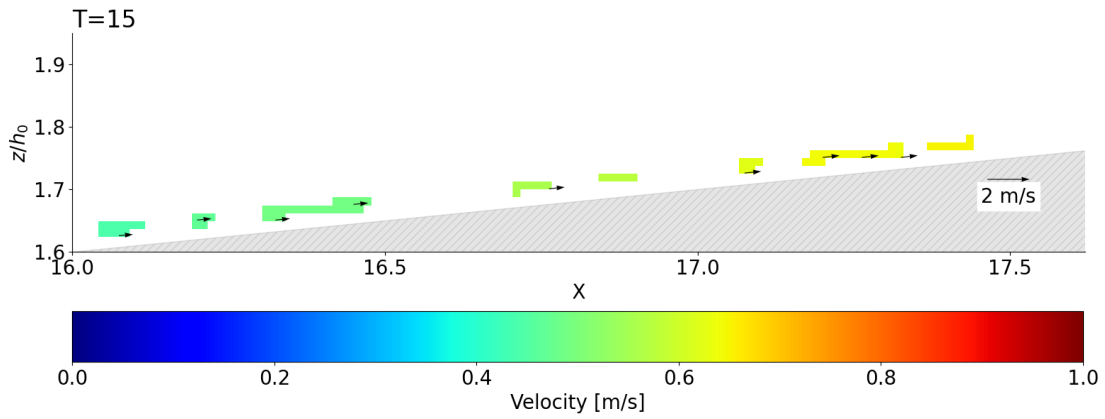


Figure 6-39: The simulated spatially varying velocity magnitude of a plunging solitary ($S_0=0.078$), propagating over a 1/10 beach slope, at $T=15$. The velocity vectors are overlaid as a quiver plot.

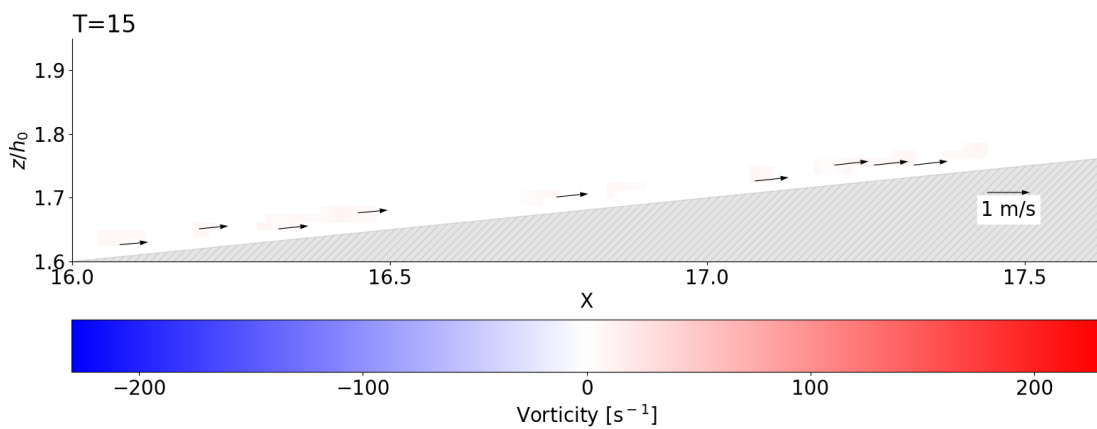


Figure 6-40: The simulated spatially varying vorticity of a plunging solitary ($S_0=0.078$), propagating over a 1/10 beach slope, at $T=15$. The velocity vectors are overlaid as a quiver plot.

Figure 6-41 shows the simulated spatially varying velocity vectors and vorticity near the bed, beneath a plunging solitary wave ($S_0=0.078$), during the interval $T=14$ to $T=20$. The sequence, structure, and magnitude of the simulated velocity vectors are similar to measured data by Lin et al. (2015), shown in Figure B-2 (refer to Appendix B). The negative velocity profiles in Figure 6-41 (b–d) similarly appear with overshooting near the sloping bed, as shown in the measured data. However, the simulated velocity is slightly out of phase compared to the measured data. The simulated and experimental wave characteristics were the same. Hence, the results further suggest that the SPH model, using the adjusted parameters $\alpha=0$, $h_{SPH}/dp=3$, $H/dp=50$, slightly over predicts the numerical wave energy dissipation. The results also show that the SPH model, using $\alpha=0$, $h_{SPH}/dp=3$, $H/dp=50$, simulates the velocity vectors in the outer surf zone fairly accurately during the wave run-up phase, likely because the flow occurs in a greater water depth compared to the thin and aerated flow that runs up the beach slope in the swash zone.

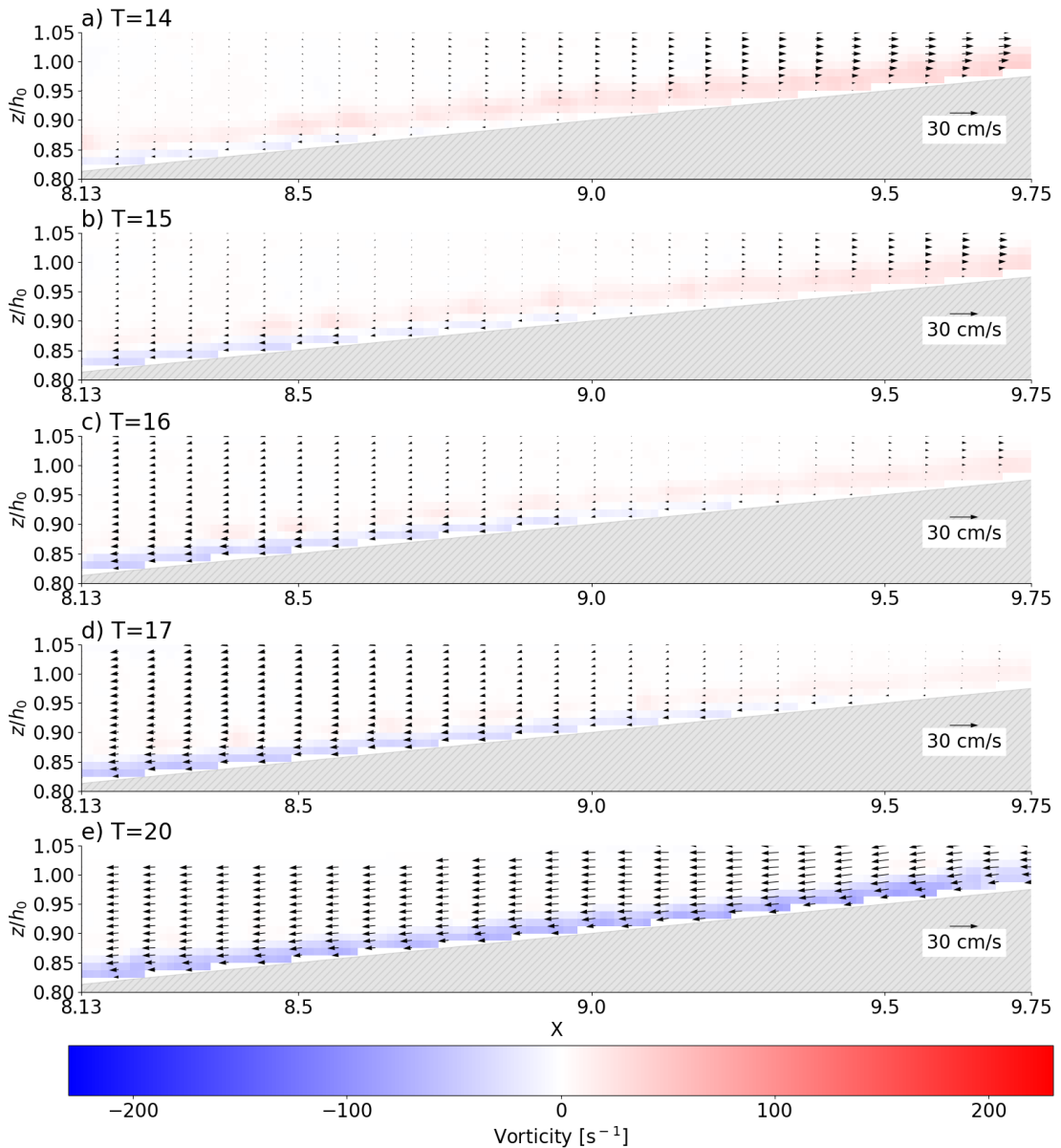


Figure 6-41 The simulated spatially varying vorticity and velocity vectors, near the bed, beneath a plunging solitary wave ($S_0=0.078$), propagating over a 1/10 beach slope, during the interval $T=14$ to $T=20$.

6.2.2.3 Wave run down

Figure 6-42 and Figure 6-43 show examples of the simulated spatially varying velocity magnitude and vorticity beneath a plunging solitary wave ($S_0=0.078$), at $T=33$. The figures show that the run-down motion of the broken plunging solitary wave on the beach slope and the formation of a secondary plunging jet is poorly simulated. During wave run-down, the simulated water particles are again scattered and vary considerably compared to the plunging solitary wave ($S_0=0.118$) analysed in section 6.2.1.3. Hence, the particle resolution $H/d_p=50$ is too low for the SPH model to capture the run downflow on the beach slope accurately.

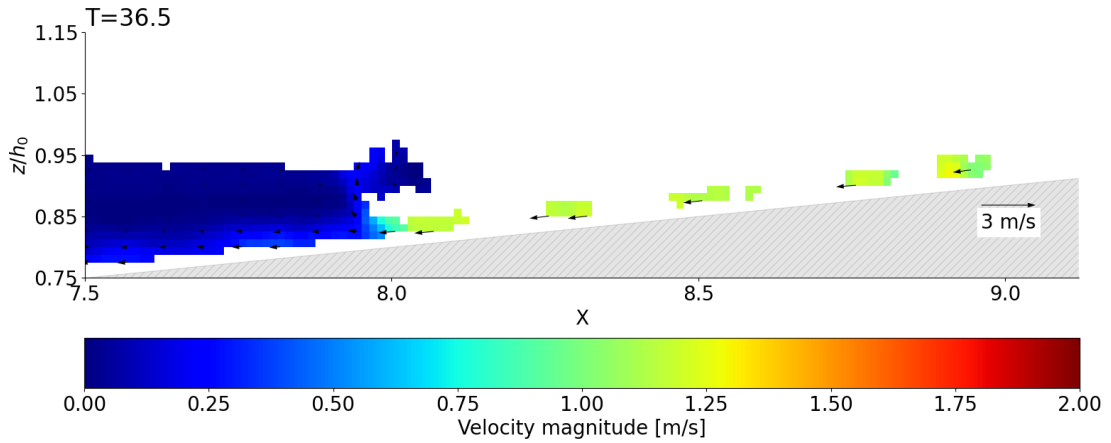


Figure 6-42: The simulated spatially varying velocity magnitude beneath a plunging solitary ($S_0=0.078$), propagating over a $1/10$ beach slope, at $T=38$. The velocity vectors are overlaid as a quiver plot.

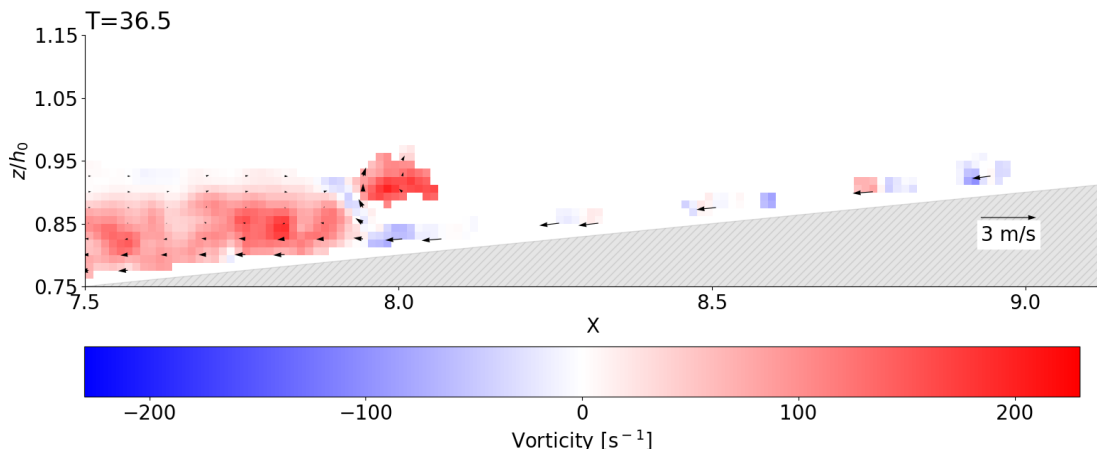


Figure 6-43: The simulated spatially varying vorticity beneath a plunging solitary ($S_0=0.078$), propagating over a $1/10$ beach slope, at $T=38$. The velocity vectors are overlaid as a quiver plot.

Figure 6-44 shows the simulated spatially varying velocity vectors and vorticity, near the bed, beneath a plunging solitary wave ($S_0=0.078$), during the intervals $T=24$ to $T=28$ and $T=38$ to $T=40$. The sequence, structure and magnitude of the simulated velocity vectors varies considerably compared to measured data by Lin et al. (2015), shown in Figure B-3 (refer to Appendix B). Hence, the SPH model, using $\alpha=0$, $h_{SPH}/dp=3$, $H/dp=50$, fails in accurately simulating the velocity vectors during wave run-down and commencement of a secondary run-up flow on the beach sope. However, it was discussed (refer to section 6.2.1.3) that even for a higher particle resolution ($H/dp=90$), a two-dimensional SPH model cannot capture the three-dimensional nature of the downflow with complete accuracy.

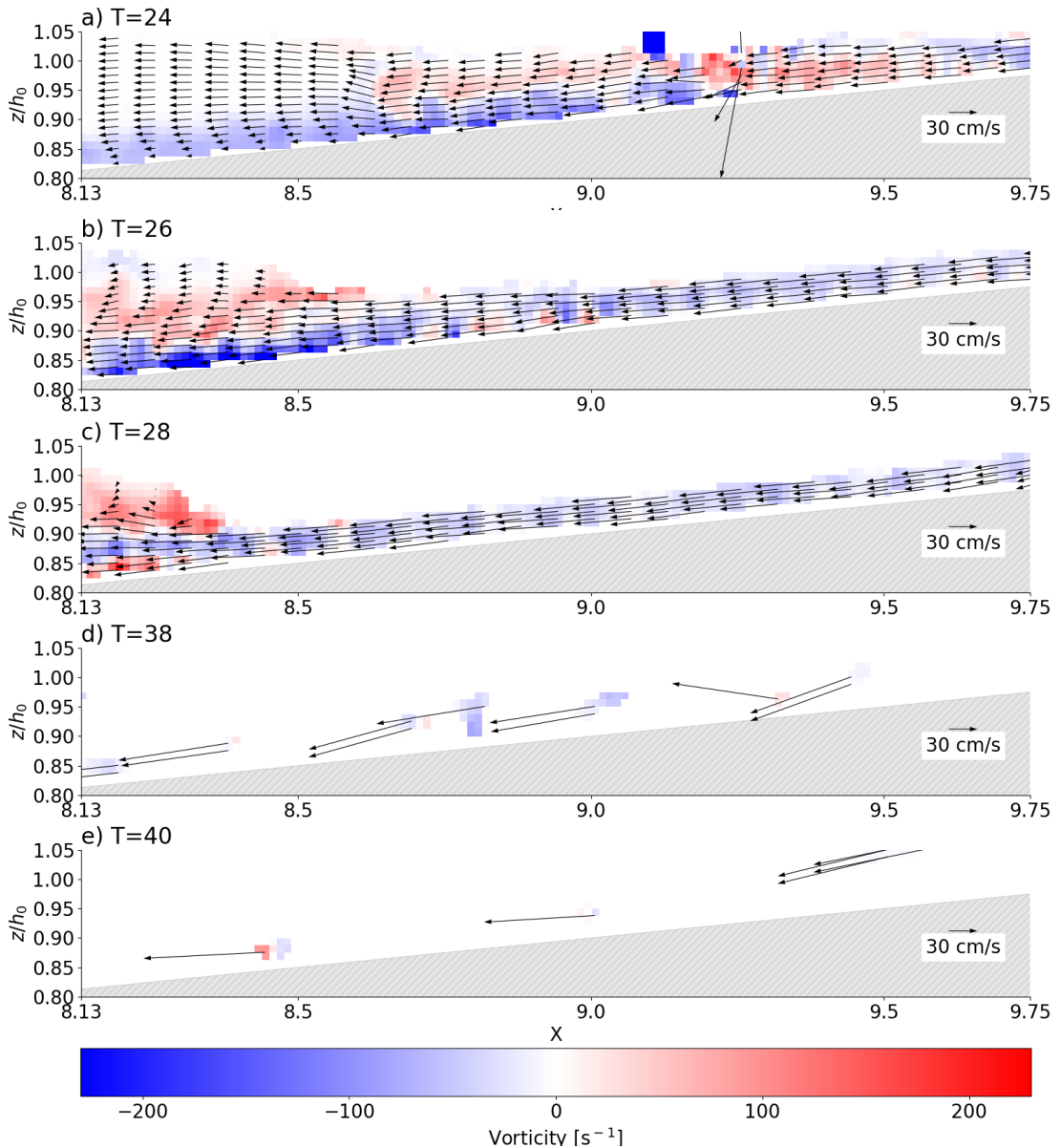


Figure 6-44 The simulated spatially varying vorticity and velocity vectors, near the bed, beneath a plunging solitary wave ($S_0=0.078$), propagating over a 1/10 beach slope during the intervals $T=24$ to $T=28$ and $T=38$ to $T=40$.

6.2.2.4 The bed shear stress

Figure 6-45 shows the evolution of the bed shear stress beneath a plunging solitary wave ($S_0=0.078$) at $z/h_0=0.03$ above the beach slope in the surf zone. Figure 6-45(a) shows the spatially varying peak bed shear stress ($\tau_{b(peak)}$) during the interval, during the interval $T=0$ to $T=40$. Figure 6-45(b) shows the time varying bed shear stress (τ_b) at $X=10.5$ on the beach slope. The figure shows that the peak bed shear stress ($\tau_{b(peak)}$) is generally higher in the offshore direction compared to the onshore direction, except in the region $X=10.4$ and $X=10.55$ on the beach slope (Figure 6-45a) wherein the breaking plunging wave first impinges onto the beach slope (refer to section 6.2.2.1). Furthermore, it is noted that the

shear stress is indeterminate for $30 < T < 35$ (Figure 6-45a) due to an insufficient particle resolution.

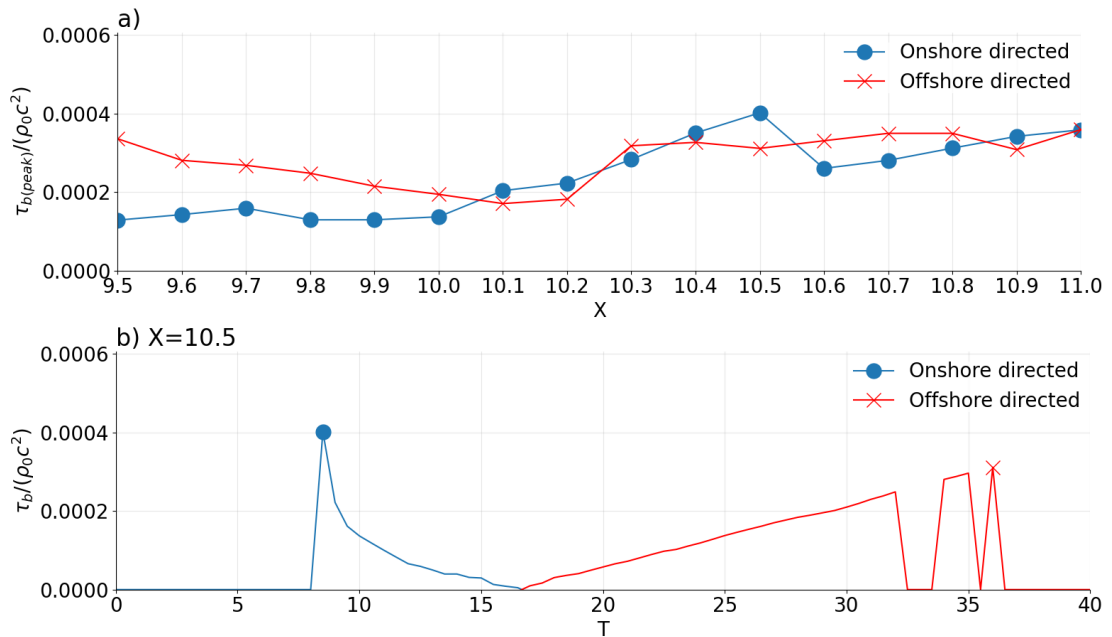


Figure 6-45: The a) spatially varying peak bed shear stress ($\tau_{b(peak)}$) and the b) time varying bed shear stress (τ_b) at $X=10.5$ on the beach slope, as a plunging solitary wave ($S_0=0.078$), propagates over a 1/10 beach slope, during the interval $T=0$ to $T=40$.

Table 6-11 shows the maximum bed shear stress ($\tau_{b(max)}$) and shear velocity ($u^*_{(max)}$) in the onshore and offshore direction beneath a plunging solitary wave ($S_0=0.118$) during the interval $T=0$ to $T=40$. The table also shows when these maximum values occurred and where these maximum values occurred on the beach slope. The maximum onshore directed bed shear stress and shear velocity were 0.40 N/m^2 and 1.99 cm/s , respectively, and occurred at $X=10.4$ on the beach slope and $T=8.5$ during wave impingement on the beach slope (refer to section 6.2.2.1). The maximum offshore directed bed shear stress was 0.36 N/m^2 and 1.99 cm/s , respectively, and occurred at $X=11$ on the beach slope and $T=37$, towards the end of wave-run down on the beach slope (refer to section 6.2.2.2).

Table 6-11: The maximum onshore and offshore directed bed shear stresses ($\tau_{b(max)}$) and shear velocities ($u^*_{(max)}$), the time they occur, and their position on the beach slope, as a plunging solitary wave ($S_0=0.078$), propagates over a 1/10 beach slope, during the interval $T=0$ to $T=40$.

Direction	τ_{bmax} [N/m ²]	u^*_{max} [cm/s]	T	X
Onshore	0.40	1.99	8.5	10.4
Offshore	0.36	1.99	40	11

The results are comparable to the plunging solitary wave ($S_0=0.118$) analysed in section 6.2.1.4 and suggest that the wave-induced bed shear stress beneath a plunging solitary wave ($S_0=0.078$) enhances onshore sediment transport during wave impingement on the beach slope and offshore sediment transport during wave run down on the wave the beach slope. Similarly, for sand with a density of 2.65 g/cm^3 , the maximum wave-induced bed shear stresses beneath a plunging solitary wave ($S_0=0.078$) would mobilise particles smaller than 0.1 cm in diameter (refer to Figure B-4 and in Appendix B). The results also suggest that the net sediment transport beneath a plunging solitary wave ($S_0=0.078$) is offshore directed. Hence, the results agree with previous studies on plunging breakers (e.g., Sato et al., 1990; Aagaard and Hughes, 2010; Ting, 2013; and LeClaire and Ting, 2017, Yang et al., 2017). However, the simulated velocity was shown to be poorly represented during the wave run-up and run-down phases. Hence, the offshore directed instantaneous bed shear stress values are likely inaccurate.

6.2.3 Case three: spilling solitary wave ($S_0=0.019$)

A spilling solitary wave, with a relative wave height (H/h_0) of 0.6 and slope parameter (S_0) of 0.019, was simulated using the calibrated parameters $\alpha=0.1$, $h_{SPH}/dp=3$ and $H/dp=90$. Due to experimental limitations, the simulated flow field beneath the breaking wave could not be validated using laboratory measurements for the same wave characteristics. Instead, the simulated results were compared to previously measured spilling waves (e.g., Sato et al., 1990; Dabiri and Gharib, 1997; Aagaard and Jensen, 2013; LeClaire and Ting, 2017).

6.2.3.1 Wave shoaling and wave breaking

Figure 6-46 and Figure 6-47 show the simulated spatially varying velocity magnitude and vorticity beneath a spilling solitary wave ($S_0=0.019$), respectively, during the interval $T=24.33$ to $T=28$. The figures show that the velocity in a small region of the wave crest accelerates shorewards as the wave shoals and breaks. Wave breaking commences during the interval $T=24.33$ and $T=25$ and between $X=27$ and $X=28$ on the beach slope (Figure 6-46a-c and Figure 6-47a-c). Subsequently, the water near the surface spills down over the face of the wave front and is preceded by the projection of a small jet. The clockwise (positive) and anticlockwise (negative) vorticity increases in the wave crest as the water near the surface spills down and the flow becomes rotational. The spilling water over the face of the wave front impinges onto the depth of water ahead at approximately $T=26$ and between $X=28.5$ and $X=29.5$ on the beach slope. The wave-induced velocity does not reach the bed during wave impingement. Hence, the velocity near the bed and bottom friction remain constant. While the shoaling and breaking sequence of the spilling solitary wave is similar to a plunging solitary wave (refer to

section 6.2.1.1 and 6.2.2.1), for the spilling case, wave breaking occurs more gradually and in a larger water depth. Furthermore, the free-surface jet preceding the spilling breaker is thin with low vorticity (Figure 6-47c). Dabiri and Gharib (1997) obtained similar results in their study on the vorticity generation within a spilling wave.

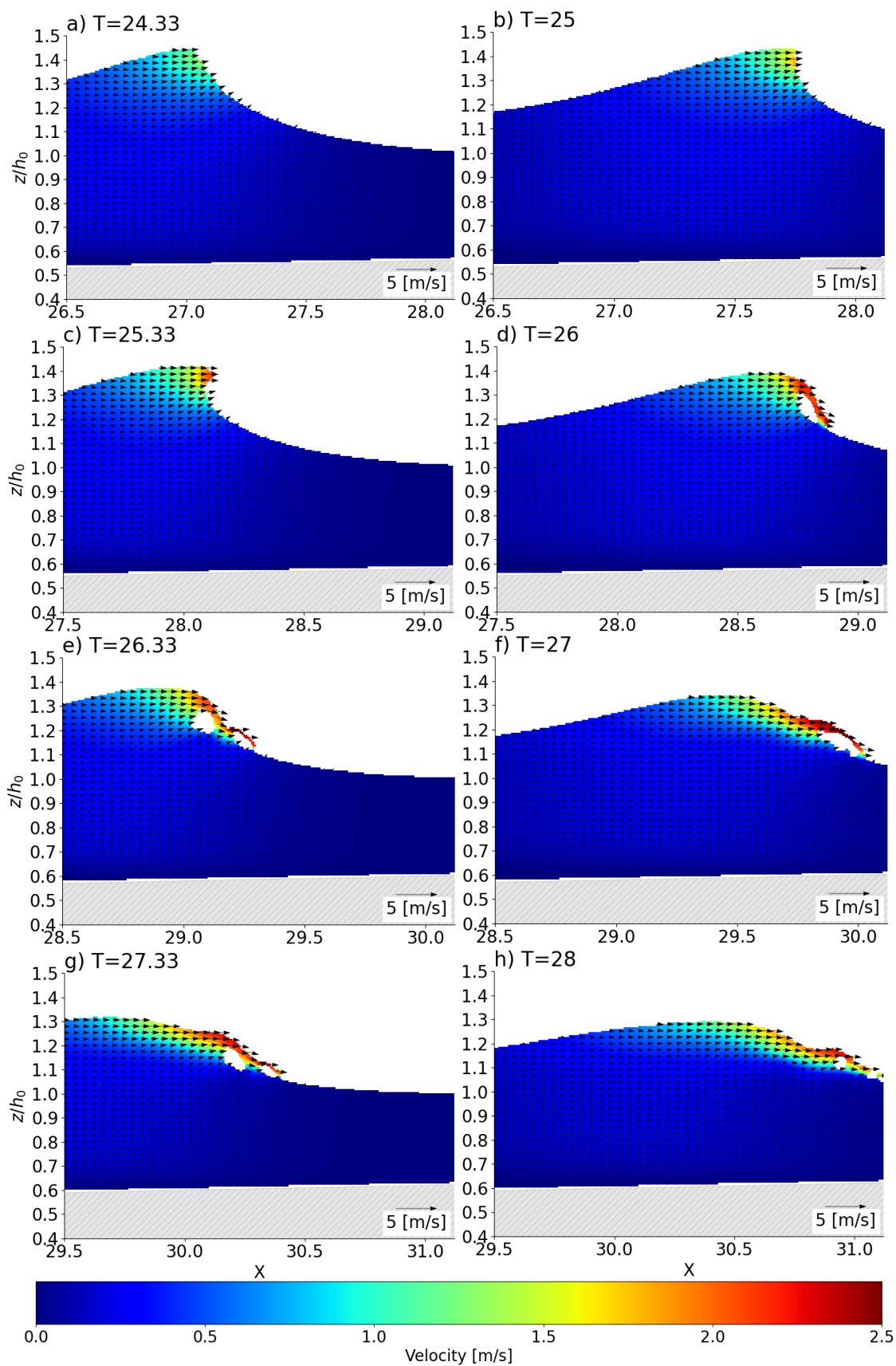


Figure 6-46 The simulated spatially varying velocity magnitude beneath a spilling solitary wave ($S_0=0.019$), propagating over a 1/50 beach slope, during the interval $T=24.33$ to $T=28$. The velocity vectors are overlaid as a quiver plot.

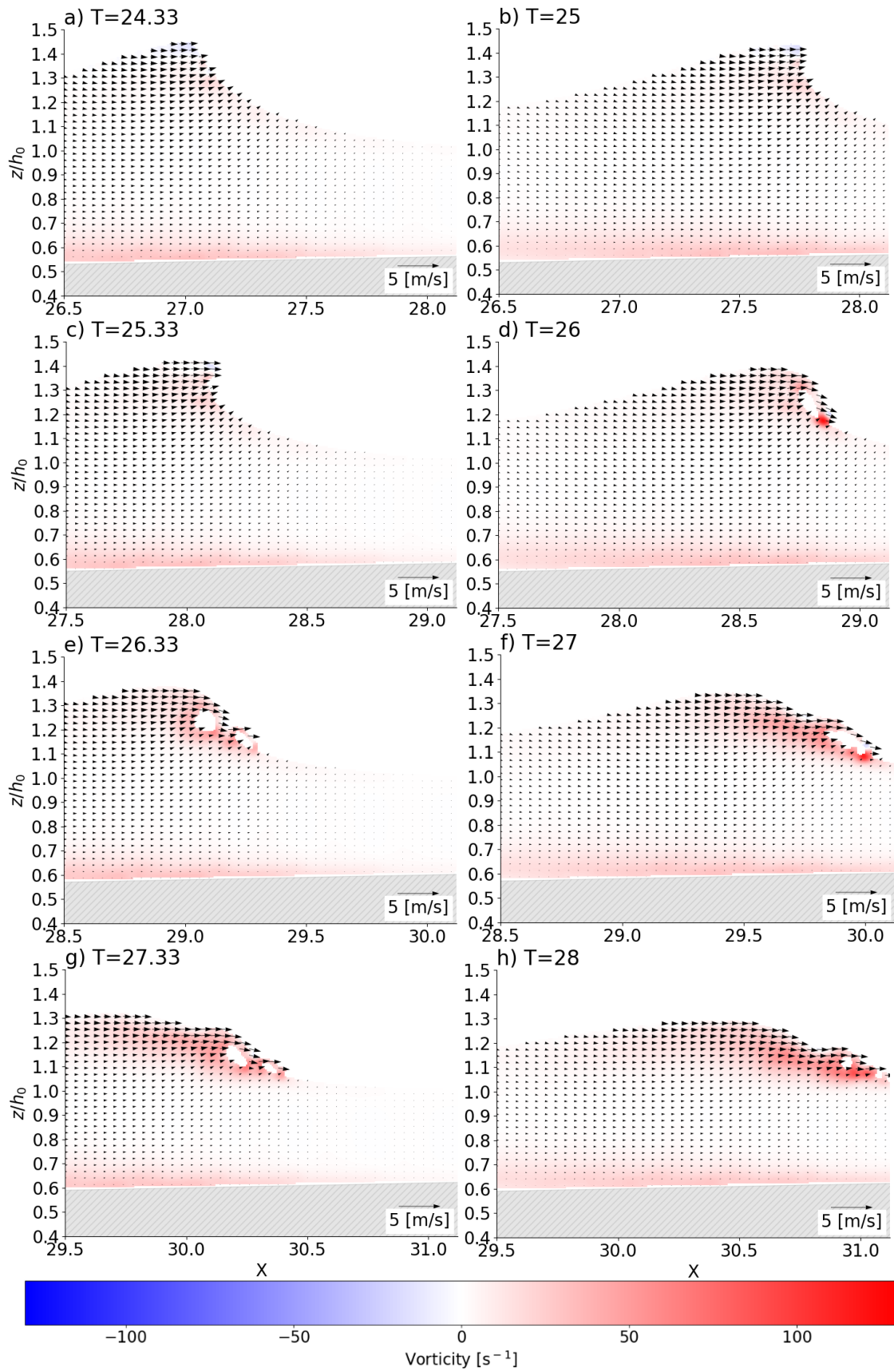


Figure 6-47 The simulated spatially varying vorticity beneath a spilling solitary wave ($S_0=0.019$), propagating over a $1/50$ beach slope, during the interval $T=24.33$ to $T=28$. The velocity vectors are overlaid as a quiver plot.

Table 6-12 shows the maximum simulated velocity and vorticity beneath a spilling solitary wave ($S_0=0.019$) at different times, during the interval $T=24.33$ to $T=28$. The maximum values occurred in the wave crest, during the interval $T=26$ to $T=26.33$, as the water near the surface spilt down over the face of the wave front. The maximum velocity magnitude was 2.68 m/s, the maximum onshore horizontal velocity was 1.63 m/s, and the maximum offshore horizontal velocity was 0.03 m/s. Furthermore, the maximum clockwise (positive) and anticlockwise (negative) vorticity was 124.124 s^{-1} and 23.739 s^{-1} , respectively.

Table 6-12: The maximum velocity and vorticity beneath a spilling solitary wave ($S_0=0.019$), propagating over a 1/50 beach slope, during the interval $T=24.33$ to $T=28$.

T	Velocity magnitude [m/s]	Onshore horizontal velocity [m/s]	Offshore horizontal velocity [m/s]	Clockwise vorticity [s^{-1}]	Anti-clockwise vorticity [s^{-1}]
24.33	1.35	1.14	0.03	32.00	13.47
25	1.83	1.35	0.03	32.36	16.55
25.33	2.11	1.45	0.03	32.28	14.92
26	2.56	1.53	0.03	124.12	23.74
26.33	2.68	1.63	0.03	59.57	9.95
27	2.50	1.55	0.03	114.71	20.76
27.33	2.44	1.56	0.03	68.93	11.15
28	2.26	1.50	0.03	88.98	4.95

6.2.3.2 The bed shear stress

Figure 6-48 shows the evolution of the bed shear stress beneath a spilling solitary wave ($S_0=0.019$) at $z/h_0=0.03$ above the beach slope in the surf zone. Figure 6-48(a) shows the spatially varying peak bed shear stress ($\tau_{b(peak)}$) during the interval $T=0$ to $T=40$. Figure 6-48(b) shows the time varying bed shear stress (τ_b) at $X=28.9$ on the beach slope. The figure shows that the peak bed shear stress ($\tau_{b(peak)}$) is generally higher in the onshore direction compared to the offshore direction.

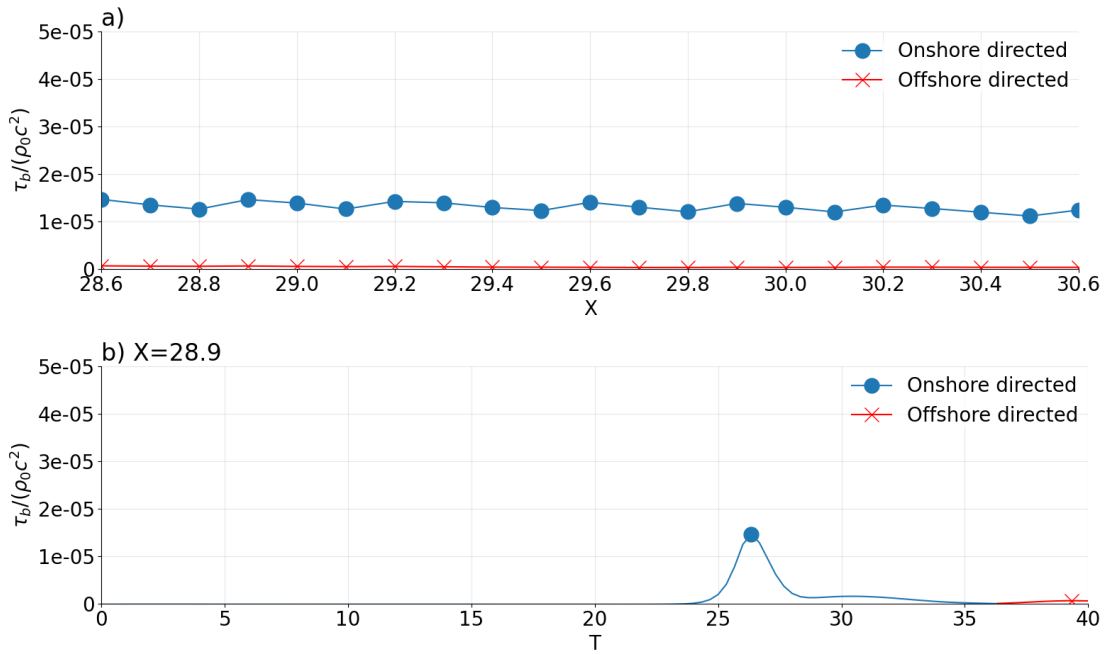


Figure 6-48: The a) spatially varying peak bed shear stress ($\tau_{b(\text{peak})}$), and the b) time varying bed shear stress (τ_b) at $X=28.9$ on the beach slope, as a spilling solitary wave ($S_0=0.019$), propagates over a 1/50 beach slope, during the interval $T=0$ to $T=40$ (where $\tau_b=0$ no fluid particles were present).

Table 6-13 shows the maximum bed shear stress ($\tau_{b(\text{max})}$) and shear velocity ($u_{*(\text{max})}$) in the onshore and offshore direction beneath a spilling solitary wave ($S_0=0.019$) during the interval $T=0$ to $T=40$. The table also shows when these maximum values occurred and where these maximum values occurred on the beach slope. The maximum onshore directed bed shear stress and shear velocity were 0.03 N/m^2 and 0.59 cm/s , respectively, and occurred at $X=28.9$ on the beach slope and $T=26.33$ as the water near the surface spills down over the face of the wave front. (refer to section 6.2.3.1). The maximum offshore directed bed shear stress was 0.001 N/m^2 and 0.12 cm/s , respectively, and was constant between $X=28.6$ and $X=30.6$ on the beach slope and during $T=38.33$ and $T=40$ (not shown).

Table 6-13: The maximum onshore and offshore directed bed shear stresses ($\tau_{b(\text{max})}$) and shear velocities ($u_{*(\text{max})}$), the time they occur, and their position on the beach slope, as a spilling solitary wave ($S_0=0.019$), propagates over a 1/50 beach slope, during the interval $T=0$ to $T=60$.

Direction	$\tau_{b\text{max}}$ [N/m ²]	$u_{*\text{max}}$ [cm/s]	T	X
Onshore	0.03	0.59	26.33	28.9
Offshore	0.001	0.12	38.33 - 40	28.6 - 30.6

The results suggest that the wave-induced bed shear stress beneath a spilling solitary wave ($S_0=0.118$) enhances onshore sediment transport during wave impingement on the beach slope and, contrary to a plunging solitary wave (refer to section 6.2.1.4 and 6.2.2.4), the net sediment transport beneath a spilling solitary wave ($S_0=0.019$) is onshore directed. However, for sand with a density of 2.65 g/cm^3 , the maximum wave-induced bed shear stresses beneath a spilling solitary wave ($S_0=0.019$) would only mobilise particles smaller than 0.001 cm in diameter (refer to Figure B-4 and in Appendix B). This is significantly smaller than the maximum sediment size of 0.1 cm that a plunging solitary wave would mobilise during wave breaking and wave run down. This is likely because wave shoaling and breaking occur in a larger water depth for the spilling solitary wave. Hence, the wave-induced velocities and shear stresses do not impinge onto the bed as they do in plunging solitary waves. The results agree with previous studies emphasising the magnitude of sediment in suspension is influenced by the breaker type and position in the surf zone and that more sediment is suspended during wave breaking as the wave steepness increases and the as the water depth decreases (e.g., Kana, 1977, 1978, 1979; Inman et al., 1980; Shibayama and Horikawa, 1982; Sato et al., 1990; Beach and Sternberg, 1996; Aagaard and Hughes, 2010; LeClaire and Ting, 2017; Yang et al., 2017).

CHAPTER 7

CONCLUSION

The purpose of this study was to show the capability of the mesh-free, Lagrangian smoothed particle hydrodynamics (SPH) method for simulating the free surface of nearshore breaking waves and accurately predicting the flow beneath nearshore breaking waves. The results show that a calibrated two-dimensional SPH model can replicate the free surface of nearshore breaking waves. The results also suggest that a calibrated SPH model can accurately predict parameters (local velocities, vorticities, and shear stresses) of the nearshore breaking wave field that are useful for predicting coastal phenomena, namely sediment transport in the surf zone. However, SPH applications must choose between accuracy and computational efficiency. Furthermore, a systematic model calibration and sensitivity analysis showed that a suitable choice of values for the model parameters depends on the viscosity treatment method and the type of breaking simulated. The results of this study serve as a physically based framework for using a weakly compressible two-dimensional SPH model to accurately predict the water surface and flow field during wave breaking.

7.1 Suitable model parameters

After conducting a literature survey, key SPH calibration parameters for simulating nearshore breaking waves were identified. These SPH parameters were the artificial viscosity coefficient (α), the dimensionless smoothing length ratio (h_{SPH}/dp), and the particle resolution (H/dp). The standard SPH viscous formulation, the artificial viscosity scheme (Monaghan 1992), was used to calibrate the SPH model to simulate a plunging solitary wave ($S_0=0.118$). Extensive comparative analysis was performed between simulated results and measured data to obtain suitable values for the model parameters. A suitable choice of $\alpha=0.1$, $h_{SPH}/dp=3$, and $H/dp=90$ were selected based on the results. The case dependency of the calibrated parameters was also explored based on the viscosity treatment method (artificial/sub-particle scale viscosity approach) and the type of wave breaking simulated (plunging/spilling), respectively. Furthermore, the individual role of α , h_{SPH}/dp , and H/dp in simulating a plunging solitary wave was analysed to reveal their importance regarding wave breaking applications.

7.1.1 Case dependency of calibrated parameters

The calibrated SPH parameters $h_{SPH}/dp=3$ and $H/dp=90$ were used with an alternative viscosity scheme to simulate a plunging solitary wave ($S_0=0.118$) to test their case dependency based on the viscosity treatment method. Moreover, the calibrated SPH parameters $\alpha=0.1$, $h_{SPH}/dp=3$, and $H/dp=90$ were used to simulate breaking plunging and spilling waves to test their case dependency based on the type of wave breaking.

7.1.1.1 The viscosity treatment method

In addition to the artificial viscosity approach, DualSPHysics (Crespo et al., 2015) offers an alternative viscosity treatment method, the laminar viscosity (Lo and Shao, 2002) and sub-particle scale (SPS) turbulence scheme (Dalrymple and Rogers, 2006). The concept is similar to the large eddy simulation (LES) used to represent the effects of turbulence at sub-grid scales in Eulerian models and is a more realistic way of treating the fluid viscosity (Shao and Ji, 2006, Gomez-Gesteira et al., 2010). However, in the SPS approach, the Smagorinsky constant (C_s) is set as 0.12 and could not be tuned.

The SPS viscosity approach was used to simulate a plunging solitary wave ($S_0=0.118$) with the same dimensionless smoothing length ratio $h_{SPH}/dp=3$ and particle resolution $H/dp=90$ used with a calibrated artificial viscosity formulation. The results suggested that a suitable h_{SPH}/dp and H/dp depends on the viscosity treatment method. For the same ideal values of h_{SPH}/dp and H/dp , a lower numerical wave energy dissipation was implemented in the SPH model when using the SPS approach than a calibrated artificial viscosity approach. Hence, the numerical wave energy dissipation and wave surface were slightly under-predicted compared to measured data despite the SPS approach being a more realistic approach for describing the viscosity. A possible reason for this was that a two-dimensional simulation negates the effect of the tank walls on the propagating wave. To implement the proper dissipation in the two-dimensional SPH model, the interparticle spacing (dp) would need to be reduced. However, this reduces H/dp and affects the model resolution.

The advantage of using an artificial viscosity scheme is that the artificial viscosity coefficient (α) can be tuned for a set H/dp , allowing the user to implement the proper dissipation without compromising the particle resolution (H/dp) of the model. Additionally, the artificial viscosity scheme dampens any numerical instabilities or spurious oscillations at the free surface (Dalrymple and Rogers, 2006).

The effect of the laminar viscosity (Lo and Shao, 2002) and SPS turbulence scheme (Dalrymple and Rogers, 2006) on the simulated flow field beneath nearshore breaking waves was not in the scope of this study. However, research suggests that the effect of

SPS turbulent motions is insignificant if the SPH model is used with a high particle resolution, especially in the case of two-dimensional SPH models (Gotoh et al., 2005; Shao and Ji, 2006).

7.1.1.2 Breaker type

The relative wave height (H/h_0) and beach slope ($\tan(\beta)$) in the SPH model were varied, respectively, to simulate solitary waves with varying slope parameters (S_0) and hence different breaker types. The results suggested that a suitable α , h_{SPH}/dp , and H/dp depends on S_0 and hence the type of wave breaking, specifically when S_0 is increased by increasing the beach slope ($\tan(\beta)$) in the model. A possible reason for this was due to the effect of the slope ($\tan(\beta)$) being more significant than the relative wave height (H/h_0). The size of plunging jets for spilling and plunging breakers increases significantly with the beach slope due to shallower water depths in front of the breakers (Grilli et al., 1997; Arntsen et al. 2000).

The results suggested a relationship between the best value of α and the slope parameter (S_0) of a solitary wave. The relationship should be similar to the linear relationship established by De Padova et al. (2014) between α and the Iribarren number (ξ) of a wave when the best values of h_{SPH}/dp and H/dp are defined. However, the relationship between α and S_0 was not quantified here.

The results also showed that varying S_0 could significantly impact the number of simulated water particles in the numerical domain and hence the computation time of the SPH model. The particle resolution $H/dp=90$ becomes computationally expensive when reducing S_0 . When S_0 is reduced by decreasing the relative wave height (H/h_0) of the simulated wave, a smaller interparticle spacing (dp) is required to obtain the same particle resolution $H/dp=90$. Hence more water particles are simulated in the same numerical domain and the computation time increases. Additionally, when S_0 is reduced by decreasing the beach slope ($\tan(\beta)$) in the model, the numerical domain must be extended to accommodate a more gradually breaking wave on a gentler slope. Hence more water particles are simulated, and the computation time increases. Thus, if the relative wave height or beach slope is significantly lower than $H/h_0 < 0.6$ and $\tan(\beta) = 1/10$, then $H/dp=90$ may become computationally infeasible. The results showed that changing the relative wave height (H/h_0) of the simulated wave more significantly influences the computation time compared to changing the slope ($\tan(\beta)$) in the model.

7.1.2 Influence of the artificial viscosity coefficient (α)

The artificial viscosity coefficient (α) applies when using the standard SPH artificial viscosity formulation. In agreement with De Padova et al. (2014), this study shows that the choice of α significantly influences the simulated results and is a crucial decision in applying the SPH method. When α is above or below the ideal value of 0.1 for a given h_{SPH}/dp and H/dp , the numerical wave energy dissipation is over-predicted or under-predicted, respectively. Hence, the wave height at breaking is under-predicted or over-predicted, respectively. This study shows that an $\alpha=0.1$ is suitable for simulating breaking waves on beach slopes milder than 1/10. However, it is also clear from the results that a suitable α is related to the choice of H/dp as previously emphasised in literature (DePadova et al., 2014; Crespo et al., 2015a; Roselli et al., 2018). The choice of α depends more on the chosen H/dp than the chosen h/dp , and a reduced α becomes more appropriate for a lower H/dp .

7.1.3 Influence of the dimensionless smoothing length ratio (h_{SPH}/dp)

The dimensionless smoothing length ratio (h_{SPH}/dp) affects the smoothing length (h_{SPH}) for a fixed particle spacing (dp). In agreement with De Padova et al. (2014) and Roselli et al. (2018), this study shows that an h_{SPH}/dp of 2 or 3 is suitable for simulating breaking waves. However, contrary to Roselli et al. (2018), who suggested that h_{SPH} might be more significant than the diffusive schemes for reliable wave propagation, this study showed that the choice of h_{SPH} is less significant than the choice of α in terms of the model performance. When h_{SPH}/dp was less than 1, for any given α and H/dp , the numerical wave energy dissipation was under-predicted, and the wave height at breaking was under predicted. However, an h_{SPH}/dp of 2 or 3 yielded similar results for any given α and H/dp . This study did not analyse the influence of an $h_{SPH}/dp > 3$.

7.1.4 Influence of the particle resolution (H/dp)

The particle resolution (H/dp) influences the number of simulated particles in the numerical domain and, therefore, significantly influences the accuracy and computation time of the SPH model. Thus, the choice of H/dp is of principal importance and influences the choice of the other model parameters. When H/dp is below the ideal value of 90, for any given α and h_{SPH}/dp , the numerical wave energy dissipation is over-predicted. Hence, the wave height at breaking is under-predicted. Additionally, the breaking wave shape is poorly simulated, even if the correct numerical wave energy dissipation is implemented in the SPH model. This study shows that $H/dp=90$ is suitable for simulating the complete evolution of breaking waves on a beach slope. However, $H/dp=90$ becomes computationally expensive when simulating breaking waves in large numerical domains

or with relative wave heights significantly less than 0.6. Hence, the available computing power limits the choice of H/dp .

7.2 Model performance

The performance of a two-dimensional SPH model was assessed by analysing the simulated flow field beneath several breaking waves. The local velocities, vorticities, and bed shear stresses were evaluated beneath two plunging solitary waves and a spilling solitary wave. The simulated results were compared to previous results for plunging breakers (e.g., Peregrine et al., 1980; Chang and Liu, 1998;1999; Ting, 2013; Lin. et al., 2015; LeClaire and Ting, 2017) and spilling breakers (e.g., Sato et al., 1990; Dabiri and Gharib 1997; Aagaard and Jensen, 2013; LeClaire and Ting, 2017). The simulated results showed varying accuracy depending on the position of the breaking wave in the surf zone. Generally, the characteristics of the simulated flow field were fairly accurate during wave shoaling and wave breaking, less accurate during wave run-up, and inaccurate during wave run-down. The results also hinted at obliquely descending eddies beneath the breaking plunging waves. However, this could not be verified, nor the eddy structure analysed using the limited two-dimensional model setup. The results also showed that using the SPH dynamic boundary condition (DBC) leads to a boundary effect that is observable during wave impingement, wave run-up and wave run-down on the beach slope. The forces exerted by the boundary particles created a small gap between them and fluid particles in order of the smoothing length.

7.2.1 Case one: a plunging solitary wave

The flow field beneath a plunging solitary wave, with a relative wave height (H/h_0) of 0.6 and slope parameter (S_0) of 0.095, was simulated using the calibrated SPH parameters $\alpha=0.1$, $h_{SPH}/dp=3$ and $H/dp=90$. The results suggested that the computed wave field parameters (local velocities, vorticities, and bed shear stresses) were accurate during wave shoaling, wave breaking, and wave run-up and less accurate during wave run-down. The variations in the magnitude of the simulated flow field parameters compared to measured values in literature were mainly attributed to the simulated wave characteristics being different from the experimental wave characteristics. However, the increased variations in the magnitude of the simulated velocity compared to measured values during wave run-down were primarily due to a two-dimensional model's inability to capture the highly three-dimensional nature of the downflow with complete accuracy (Ting, 2013). Due to experimental limitations, the simulated flow field could not be validated using laboratory measurements for the same wave characteristics.

7.2.2 Case two: a plunging solitary wave

The flow field beneath a plunging solitary wave, with a relative wave height (H/h_0) of 0.262 and slope parameter (S_0) of 0.078, was simulated using adjusted SPH parameters $\alpha=0$, $h_{SPH}/dp=3$ and $H/dp=50$. The values of α and H/dp were adjusted because it was computationally expensive to use the initially calibrated particle resolution $H/dp=90$ to simulate a relative wave height (H/h_0) of 0.262. The simulated wave characteristics followed a laboratory experiment by Lin et al. (2015), and the results were comparable to the measured results during wave shoaling and wave breaking. The simulated flow field was also comparable to the measured results during wave run-up but only in the outer region of the surf zone. In addition to the highly three-dimensional nature of the downflow (Ting, 2013), the thin layer of water running up and down the beach slope in the inner surf and swash zones was poorly simulated due to a reduced particle resolution $H/dp=50$. Hence, the particle resolution $H/dp=90$ should be maintained for wave breaking problems concerning wave run-up and wave run-down at the expense of a long computation time.

7.2.3 Case three: a spilling solitary wave

The flow field beneath a spilling solitary wave, with a relative wave height (H/h_0) of 0.6 and slope parameter (S_0) of 0.019, propagating over a 1/50 beach slope, was simulated using the calibrated SPH parameters $\alpha=0.1$, $h_{SPH}/dp=3$ and $H/dp=90$. The simulated flow field beneath the spilling solitary wave was only analysed during wave shoaling and wave breaking on the beach slope. The results suggested that the computed wave field parameters (local velocities, vorticities, and bed shear stresses) were accurate during wave shoaling and wave breaking. However, the simulated flow field could not be validated using laboratory measurements for the same wave characteristics due to experimental limitations.

7.3 Engineering implications

An essential component of coastal modelling and coastal management planning is the prediction of sediment transport. In order to predict sediment transport, it is necessary to analyse the velocity of the fluid and the near-bottom shear stress in the surf zone, which drives the onshore or offshore transport beneath the breakings waves (Cox and Kobayashi 1997; Trowbridge and Elgar 2001; Vittori and Blondeaux, 2009; LeClaire and Ting, 2017). This study shows that the mesh-free Lagrangian SPH method is a powerful tool to accurately describe the wave field (local velocities, vorticities, and shear stresses).

This enables the use of SPH to predict sediment transport due to wave breaking in nearshore, wave-driven environments.

This study focused on evaluating the flow field beneath breaking solitary waves and predicting the overall response of suspended sediment due to wave breaking in the surf zone. A calibrated two-dimensional SPH evaluated the flow field beneath breaking plunging and spilling solitary waves. The results were similar to several previous studies regarding sediment transport beneath breaking plunging and spilling waves (e.g., Kana, 1977; 1978; 1979; Inman et al., 1980; Sato et al., 1990, Beach and Sternberg, 1996; Aagaard and Hughes, 2010; Sumer et al., 2013; Ting, 2013; LeClaire and Ting, 2017; Yang et al. 2017). Regarding sediment transport in the surf zone, the results implied the following,

- The wave-induced bed shear stresses beneath plunging breakers would exceed the critical shear stress required to mobilise sediment particles smaller than 0.1 cm in diameter.
- An asymmetrical flow pattern produces a stronger deflecting flow during wave impingement that enhances onshore sediment transport than a more symmetrical flow pattern.
- The sediment transport in the onshore or offshore direction depends on the wave velocity phase. Onshore sediment transport occurs during wave impingement when the instantaneous horizontal velocities are shoreward. Offshore sediment transport occurs during wave run-down when the instantaneous horizontal velocities are seaward.
- The sediment transport is predominantly offshore beneath plunging breakers. Hence, offshore sediment transport is the net effect of the breaking wave-induced flow beneath plunging breakers.
- Impinging or strong deflecting flows on the bed are necessary to lift sediment particles in suspension in the surf zone. Hence, less sediment is suspended during wave breaking as the water depth increases and the wave steepness decreases. Therefore, less sediment suspension occurs beneath a spilling breaker than a plunging breaker with the same wave height.

While the flow field beneath breaking plunging and spilling waves were successfully simulated, a two-dimensional simulation could not account for all three-dimensional flow characteristics beneath breaking waves. Furthermore, excessively long computational times arise if a high particle resolution ($H/d_p=90$) is applied to simulate breaking waves

in a large numerical domain or to simulate breaking waves with a low relative wave height ($H/h_0 < 0.3$). Therefore, hardware acceleration and parallel computing will make SPH more viable and versatile to real engineering problems (Crespo et al., 2015b). Furthermore, research is still ongoing to achieve a computationally efficient and robust formulation to accurately treat the viscosity in SPH simulations (Gomez-Gesteira et al., 2010).

7.4 Recommendations for further research

An extension of this study should examine the distributions of turbulent flow properties around sediment particles suspended and transported due to wave breaking. Breaking waves generate three-dimensional turbulence and vortex structures within the flow field, which is expected to mobilise a lot of sediment (Vittori, 2003; Vittori and Blondeaux, 2009; Werf et al., 2012). Therefore a calibrated three-dimensional SPH model can lead to a more complete understanding of the underlying physical processes beneath breaking waves, including the generation of large-scale eddies, and thus the driving mechanisms of sediment transport in the surf zone (Werf et al., 2012; Ting, 2013). However, the calibrated SPH parameters $\alpha=0.1$, $h_{SPH}/dp=3$ and $H/dp=90$ used in this study are likely unfeasible for a three-dimensional SPH computation (Shao and Ji, 2006). Depending on available computing power, a more suitable particle resolution may need to be used. Furthermore, Khayyer et al. (2007) suggest using the SPS viscosity approach for more realistic simulation results due to low particle resolutions for three-dimensional SPH computations. Hence, the proposed calibration framework in this study is not suited to three-dimensional SPH modelling of nearshore breaking waves, and a similar framework should be developed for such cases. While three-dimensional SPH studies have been carried out previously (e.g., Dalrymple and Rogers, 2006; Farahani et al., 2014), research is limited.

An extension of this study can also analyse and predict the overall response of suspended sediment due to a range of periodic wave conditions breaking over a beach slope. A suspended sand transport module could also be coupled with the hydrodynamic model to improve model predictions of sediment transport rate and direction due to the breaking waves.

Finally, this study also encourages using the proposed SPH model calibration framework to solve other coastal engineering problems concerning wave-structure interactions and wave run-up on beaches on different scales and for a wide range of wave conditions.

REFERENCES

- AAGAARD, T. & HUGHES, M. G. 2010. Breaker turbulence and sediment suspension in the surf zone. *Marine Geology*, 271, 250-259.
- AIRY, G. B. 1845. *Tides and waves*, B. Fellowes.
- ALONSO, J. M. D., CRESPO, A. J. C., GESTEIRA, M. G., ROGERS, B. D., FOURTAKAS, G., STANSBY, P., VACONDIO, R., ALTOMARE, C., TAFUNI, A., FEAL, O. G. & ESTEVEZ, I. M. 2020. Available: <https://dual.sphysics.org/> [Accessed].
- ALTOMARE, C., CRESPO, A. J., DOMÍNGUEZ, J. M., GÓMEZ-GESTEIRA, M., SUZUKI, T. & VERWAEST, T. 2015. Applicability of Smoothed Particle Hydrodynamics for estimation of sea wave impact on coastal structures. *Coastal Engineering*, 96, 1-12.
- ALTOMARE, C., DOMÍNGUEZ, J. M., CRESPO, A., GONZÁLEZ-CAO, J., SUZUKI, T., GÓMEZ-GESTEIRA, M. & TROCH, P. 2017. Long-crested wave generation and absorption for SPH-based DualSPHysics model. *Coastal Engineering*, 127, 37-54.
- BALDOCK, T. E., MANOONVORAVONG, P. & PHAM, K. S. 2010. Sediment transport and beach morphodynamics induced by free long waves, bound long waves and wave groups. *Coastal Engineering*, 57, 898-916.
- BATCHELOR, G. K. 1974. *An introduction to fluid dynamics*, Cambridge university press.
- BATTJES, J. A. 1974. SURF SIMILARITY. *Coastal Engineering Proceedings*, 1.
- BATTJES, J. A. 1988. Surf-Zone Dynamics. *Annual Review of Fluid Mechanics*, 20, 257-291.
- BEACH, R. A. & STERNBERG, R. W. 1996. Suspended-sediment transport in the surf zone: response to breaking waves. *Continental Shelf Research*, 16, 1989-2003.
- BIESEL, F. S. F. 1954. *Laboratory wave generating apparatus*, (Grenoble, La Houille Blanche).
- BLENKINSOPP, C. & CHAPLIN, J. 2008. The effect of relative crest submergence on wave breaking over submerged slopes. *Coastal Engineering*, 55, 967-974.
- BONMARIN, P. 1989. GEOMETRIC PROPERTIES OF DEEP-WATER BREAKING WAVES. *Journal of Fluid Mechanics*, 209, 405-433.
- BOSBOOM, J. & STIVE, M. J. 2012. *Coastal dynamics I: lectures notes CIE4305*.
- BOUSSINESQ, J. 1871. Théorie de l'intumescence liquide appelée onde solitaire ou de translation se propageant dans un canal rectangulaire. *CR Acad. Sci. Paris*, 72, 1871.
- BRENNINKMEYER, B. M. 1974. Mode and Period of Sand Transport in the Surf Zone. *Coastal Engineering* 1974.
- BRENNINKMEYER, S. J. 1976. In situ measurements of rapidly fluctuating, high sediment concentrations. *Marine Geology*, 20, 117-128.
- CHANG, K.-A. & LIU, P. L.-F. 1998. Velocity, acceleration and vorticity under a breaking wave. *Physics of Fluids*, 10, 327-329.
- CHANG, K.-A. & LIU, P. L.-F. 1999. Experimental investigation of turbulence generated by breaking waves in water of intermediate depth. *Physics of Fluids*, 11, 3390-3400.
- CHEN, G., KHARIF, C., ZALESKI, S. & LI, J. 1999. Two-dimensional Navier–Stokes simulation of breaking waves. *Physics of fluids*, 11, 121-133.
- COLAGROSSI, A. & LANDRINI, M. 2003. Numerical simulation of interfacial flows by smoothed particle hydrodynamics. *Journal of Computational Physics*, 191, 448-475.
- CONLEY, D. C. & INMAN, D. L. 1992. Field observations of the fluid-granular boundary layer under near-breaking waves. *Journal of Geophysical Research: Oceans*,

- 97, 9631-9643.
- COX, D. T. & ANDERSON, S. L. 2001. Statistics of intermittent surf zone turbulence and observations of large eddies using PIV. *Coastal Engineering Journal*, 43, 121-131.
- COX, D. T. & KOBAYASHI, N. 2000. Identification of intense, intermittent coherent motions under shoaling and breaking waves. *Journal of Geophysical Research: Oceans*, 105, 14223-14236.
- CRESPO, A., ALTOMARE, C., DOMÍNGUEZ, J. M., SUZUKI, T., VERWAEST, T. & GÓMEZ-GESTEIRA, M. 2015. *SPH MODELLING IN COASTAL ENGINEERING*.
- CRESPO, A., GÓMEZ-GESTEIRA, M. & DALRYMPLE, R. A. 2008. Modeling dam break behavior over a wet bed by a SPH technique. *Journal of waterway, port, coastal, and ocean engineering*, 134, 313-320.
- CRESPO, A. J., GÓMEZ-GESTEIRA, M. & DALRYMPLE, R. A. 2007. Boundary conditions generated by dynamic particles in SPH methods. *Computers, materials and continua*, 5, 173-184.
- CRESPO, A. J. C., DOMÍNGUEZ, J. M., ROGERS, B. D., GÓMEZ-GESTEIRA, M., LONGSHAW, S., CANELAS, R., VACONDIO, R., BARREIRO, A. & GARCÍA-FEAL, O. 2015. DualSPHysics: Open-source parallel CFD solver based on Smoothed Particle Hydrodynamics (SPH). *Computer Physics Communications*, 187, 204-216.
- CUMMINS, S. J. & RUDMAN, M. 1999. An SPH projection method. *Journal of computational physics*, 152, 584-607.
- DALLY, W. R., DEAN, R. G. & DALRYMPLE, R. A. 1984. Modeling Wave Transformation in the Surf Zone. COASTAL ENGINEERING RESEARCH CENTER VICKSBURG MS.
- DALRYMPLE, R. A. & KNIO, O. SPH modelling of water waves. *Coastal dynamics' 01*, 2001. 779-787.
- DALRYMPLE, R. A. & ROGERS, B. 2006. Numerical modeling of water waves with the SPH method. *Coastal engineering*, 53, 141-147.
- DAY, M. A. 1990. The no-slip condition of fluid dynamics. *Erkenntnis*, 33, 285-296.
- DE PADOVA, D., DALRYMPLE, R., MOSSA, M. & PETRILLO, A. 2009. SPH simulations of regular and irregular waves and their comparison with experimental data. *arXiv preprint arXiv:0911.1872*.
- DE PADOVA, D., DALRYMPLE, R. A. & MOSSA, M. 2014. Analysis of the artificial viscosity in the smoothed particle hydrodynamics modelling of regular waves. *Journal of Hydraulic Research*, 52, 836-848.
- DE PADOVA, D., MOSSA, M., SIBILLA, S. & TORTI, E. 2013. 3D SPH modelling of hydraulic jump in a very large channel. *Journal of Hydraulic Research*, 51, 158-173.
- DE SERIO, F. & MOSSA, M. 2006. Experimental study on the hydrodynamics of regular breaking waves. *Coastal Engineering*, 53, 99-113.
- DEAN, R. 1973. Heuristic Models of Sand Transport in the Surf Zone. *In: First Australian Conference on Coastal Engineering, 1973: Engineering Dynamics of the Coastal Zone. Sydney, N.S.W.: Institution of Engineers, Australia, 1973: [215]-[221]*.
- DEAN, R. G. D., ROBERT A. 1984. *Water wave mechanics for engineers and scientists / Robert G. Dean, Robert A. Dalrymple*, Englewood Cliffs, N.J, Prentice-Hall.
- DEHNEN, W. & ALY, H. 2012. Improving convergence in smoothed particle hydrodynamics simulations without pairing instability. *Monthly Notices of the Royal Astronomical Society*, 425, 1068-1082.
- DI LISIO, R., GRENIER, E. & PULVIRENTI, M. 1998. The convergence of the SPH method. *Computers & Mathematics with Applications*, 35, 95-102.
- DOERING, J. C. & BOWEN, A. J. 1995. Parametrization of orbital velocity asymmetries

- of shoaling and breaking waves using bispectral analysis. *Coastal Engineering*, 26, 15-33.
- DOMÍNGUEZ, J., CRESPO, A., FOURTAKAS, G., ROGERS, B., CERCOS-PITA, J. & VACONDIO, R. 2015. *Evaluation of reliability and efficiency of different boundary conditions in an SPH code*.
- DONG, C.-M. & HUANG, C.-J. 2004. Generation and propagation of water waves in a two-dimensional numerical viscous wave flume. *Journal of waterway, port, coastal, and ocean engineering*, 130, 143-153.
- DRAKE, T. & CALANTONI, J. 2001. Discrete particle model for sheet flow sediment transport. *Journal of Geophysical Research*, 106.
- ELLERO, M. & HESS, S. 2002. Viscoelastic flows studied by smoothed particle dynamics. *Journal of Non-Newtonian Fluid Mechanics*, 105, 35-51.
- FARAHANI, R. J., DALRYMPLE, R. A., HÉRAULT, A. & BILOTTA, G. 2014. Three-dimensional SPH modeling of a bar/rip channel system. *Journal of waterway, port, coastal, and ocean engineering*, 140, 82-99.
- FENTON, J. 1972. A ninth-order solution for the solitary wave. *Journal of fluid mechanics*, 53, 257-271.
- FOURTAKAS, G., DOMINGUEZ, J. M., VACONDIO, R. & ROGERS, B. D. 2019. Local uniform stencil (LUST) boundary condition for arbitrary 3-D boundaries in parallel smoothed particle hydrodynamics (SPH) models. *Computers & Fluids*, 190, 346-361.
- FULK, D. A. & QUINN, D. W. 1995. Hybrid formulations of smoothed particle hydrodynamics. *International journal of impact engineering*, 17, 329-340.
- GALVIN, C. 1972. Wave breaking in shallow water. *Waves on beaches and resulting sediment transport*, 413-456.
- GALVIN JR., C. J. 1968. Breaker type classification on three laboratory beaches. *Journal of Geophysical Research (1896-1977)*, 73, 3651-3659.
- GEORGE, R., FLICK, R. E. & GUZA, R. 1994. Observations of turbulence in the surf zone. *Journal of Geophysical Research: Oceans*, 99, 801-810.
- GINGOLD, R. A. & MONAGHAN, J. J. 1977. Smoothed particle hydrodynamics: theory and application to non-spherical stars. *Monthly Notices of the Royal Astronomical Society*, 181, 375.
- GODA, Y. 1967. The fourth order approximation to the pressure of standing waves. *Coastal Engineering in Japan*, 10, 1-11.
- GÓMEZ-GESTEIRA, M., CERQUEIRO, D., CRESPO, C. & DALRYMPLE, R. 2005. Green water overtopping analyzed with a SPH model. *Ocean Engineering*, 32, 223-238.
- GÓMEZ-GESTEIRA, M. & DALRYMPLE, R. A. 2004. Using a three-dimensional smoothed particle hydrodynamics method for wave impact on a tall structure. *Journal of waterway, port, coastal, and ocean engineering*, 130, 63-69.
- GOMEZ-GESTEIRA, M., ROGERS, B. D., DALRYMPLE, R. A. & CRESPO, A. J. C. 2010. State-of-the-art of classical SPH for free-surface flows. *Journal of Hydraulic Research*, 48, 6-27.
- GONZALEZ-RODRIGUEZ, D. & MADSEN, O. S. 2007. Seabed shear stress and bedload transport due to asymmetric and skewed waves. *Coastal Engineering*, 54, 914-929.
- GORING, D. G. 1978. Tsunamis--the propagation of long waves onto a shelf.
- GOTOH, H., IKARI, H., MEMITA, T. & SAKAI, T. 2005. Lagrangian Particle Method for Simulation of Wave Overtopping on a Vertical Seawall. *Coastal Engineering Journal*, 47.
- GRASSO, F., CASTELLE, B. & RUESSINK, B. 2012. Turbulence dissipation under breaking waves and bores in a natural surf zone. *Continental Shelf Research*, 43, 133-141.
- GRILLI, S. T., SVENDSEN, I. A. & SUBRAMANYA, R. 1997. Breaking Criterion and Characteristics for Solitary Waves on Slopes. *Journal of Waterway, Port,*

- Coastal, and Ocean Engineering*, 123, 102-112.
- HATTORI, M. & AONO, T. 1985. Experimental study on turbulence structures under breaking waves. *Coastal Engineering in Japan*, 28, 97-116.
- HENRIQUEZ, M., RENIERS, A., RUESSINK, B., STIVE, M., STANTON, T. & FOSTER, D. On the scaling of sediment transport in the nearshore. Coastlab 2008 Conference, 2008. 193-204.
- HOEFEL, F. & ELGAR, S. 2003. Wave-Induced Sediment Transport and Sandbar Migration. *Science (New York, N.Y.)*, 299, 1885-7.
- HUANG, Z.-C., HWUNG, H.-H., HSIAO, S.-C. & CHANG, K.-A. 2010. Laboratory observation of boundary layer flow under spilling breakers in surf zone using particle image velocimetry. *Coastal Engineering*, 57, 343-357.
- HUGHES, S. A. 1993. *Physical models and laboratory techniques in coastal engineering*, Singapore, World Scientific.
- INMAN, D. L., ZAMPOL, J. A., WHITE, T. E., HANES, D. M., WALDORF, W. B. & KASTENS, K. A. 1980. Field Measurements of Sand Motion in the Surf Zone. *Coastal Engineering 1980*.
- IRIBARREN, C. & NOGALES, C. 1949. Protection des ports. PIANC. <http://resolver.tudelft.nl/uuid:7ab718ff-a74d-4141-8c3f-413044c751c4>
- ISOBE, M. & HORIKAWA, K. 1982. Study on water particle velocities of shoaling and breaking waves. *Coastal Engineering in Japan*, 25, 109-123.
- IVERSEN, H. 1952. Waves and breakers in shoaling water. *Coastal Engineering Proceedings*, 1-1.
- JAFFE, B. & SALLENGER JR, A. 1993. The contribution of suspension events to sediment transport in the surf zone. *Coastal Engineering 1992*.
- JANSEN, P. C. M. 1986. Laboratory observations of the kinematics in the aerated region of breaking waves. *Coastal Engineering*, 9, 453-477.
- JANSSEN, P. A. 2008. Progress in ocean wave forecasting. *Journal of Computational Physics*, 227, 3572-3594.
- JOHNSON, C. M. 2009. *The effect of artificial reef configuration on wave breaking intensity relating to recreational surfing conditions*. Stellenbosch: University of Stellenbosch.
- JOHNSON, E. D. & COWEN, E. A. 2017. Estimating bed shear stress from remotely measured surface turbulent dissipation fields in open channel flows. *Water Resources Research*, 53, 1982-1996.
- KANA, T. 1977. Suspended Sediment Transport at Price Inlet, South Carolina. [No source information available], 18.
- KANA, T. 1978. Surf zone Measurements of Suspended Sediment. *Coastal Engineering Proceedings*, 1, 104.
- KANA, T. W. 1979. *Suspended sediment in breaking waves*. University of South Carolina.
- KHAYYER, A. & GOTOH, H. 2010. On particle-based simulation of a dam break over a wet bed. *Journal of Hydraulic Research*, 48, 238-249.
- KIMMOUN, O. & BRANGER, H. 2007. A particle image velocimetry investigation on laboratory surf-zone breaking waves over a sloping beach. *Journal of Fluid Mechanics*, 588, 353.
- KOBAYASHI, N. & TEGA, Y. 2002. Sand suspension and transport on equilibrium beach. *Journal of waterway, port, coastal, and ocean engineering*, 128, 238-248.
- KOMAR, P. D. 1998. *Beach Processes and Sedimentation*, Prentice Hall.
- KRAUS, N. C. & LARSON, M. 1988. Beach profile change measured in the tank for large waves 1956-1957 and 1962. COASTAL ENGINEERING RESEARCH CENTER VICKSBURG MS.
- LE MÉHAUTÉ, B. 1976. An introduction to water waves. *An Introduction to Hydrodynamics and Water Waves*. Springer.
- LE MÉHAUTÉ, B. 2013. *An introduction to hydrodynamics and water waves*, Springer

- Science & Business Media.
- LECLAIRE, P. & TING, F. 2017. Measurements of suspended sediment transport and turbulent coherent structures induced by breaking waves using two-phase volumetric three-component velocimetry. *Coastal Engineering*, 121, 56-76.
- LEIMKUHLER, B. & MATTHEWS, C. 2016. *Molecular Dynamics*, Springer.
- LIN, C., HSIEH, S., YU, S., RAIKAR, R., RAHMAN, M. & BREBBIA, C. 2010. Characteristics of boundary layer flow induced by a solitary wave. *Advances in Fluid Mechanics*, 8, 267.
- LIN, C., WONG, W.-Y., KAO, M.-J., TSAI, C.-P., HWUNG, H.-H., WU, Y.-T. & RAIKAR, R. V. 2018. Evolution of Velocity Field and Vortex Structure during Run-Down of Solitary Wave over Very Steep Beach. *Water*, 10, 1713.
- LIN, C., YEH, P.-H., KAO, M.-J., YU, M.-H., HSIEH, S.-C., CHANG, S.-C., WU, T.-R. & TSAI, C.-P. 2015. Velocity Fields in near-bottom and boundary layer Flows in prebreaking zone of a solitary wave propagating over a 1: 10 slope. *Journal of Waterway, Port, Coastal, and Ocean Engineering*, 141, 04014038.
- LIN, P. 2008. *Numerical Modeling of Water Waves*.
- LIU, M. & LIU, G. 2010. Smoothed particle hydrodynamics (SPH): an overview and recent developments. *Archives of computational methods in engineering*, 17, 25-76.
- LO, E. Y. & SHAO, S. 2002. Simulation of near-shore solitary wave mechanics by an incompressible SPH method. *Applied Ocean Research*, 24, 275-286.
- LUCY, L. B. 1977. A numerical approach to the testing of the fission hypothesis. *The Astronomical Journal*, 82, 1013.
- MALARKEY, J. & DAVIES, A. G. 2012. Free-stream velocity descriptions under waves with skewness and asymmetry. *Coastal Engineering*, 68, 78-95.
- MCCOWAN, J. 1894. XXXIX. On the highest wave of permanent type. *The London, Edinburgh, and Dublin Philosophical Magazine and Journal of Science*, 38, 351-358.
- MELVILLE, W. K., VERON, F. & WHITE, C. J. 2002. The velocity field under breaking waves: coherent structures and turbulence. *Journal of Fluid Mechanics*, 454, 203.
- MENEVEAU, C. & KATZ, J. 2000. Scale-Invariance and Turbulence Models for Large-Eddy Simulation. *Annual Review of Fluid Mechanics*, 32, 1-32.
- MICHE, M. 1944. Mouvements ondulatoires de la mer en profondeur constante ou décroissante. *Annales de Ponts et Chaussées*, 1944, pp (1) 26-78,(2) 270-292,(3) 369-406.
- MILES, J. W. 1980. Solitary waves. *Annual review of fluid mechanics*, 12, 11-43.
- MILLER, M. C. & KOMAR, P. D. 1977. The development of sediment threshold curves for unusual environments (Mars) and for inadequately studied materials (foram sands). *Sedimentology*, 24, 709-721.
- MILLER, R. L. 1976. Role of Vortices in Surf Zone Prediction: Sedimentation and Wave Forces. In: DAVIS, R. A., JR. & ETHINGTON, R. L. (eds.) *Beach and Nearshore Sedimentation*. SEPM Society for Sedimentary Geology.
- MOLTENI, D. & COLAGROSSI, A. 2009. A simple procedure to improve the pressure evaluation in hydrodynamic context using the SPH. *Computer Physics Communications*, 180, 861-872.
- MONAGHAN, J. & KOS, A. 1999. Solitary Waves on a Cretan Beach. *Journal of Waterway Port Coastal and Ocean Engineering-asce - J WATERW PORT COAST OC-ASCE*, 125.
- MONAGHAN, J. J. 1992. Smoothed particle hydrodynamics. *Annual review of astronomy and astrophysics*, 30, 543-574.
- MONAGHAN, J. J. 1994. Simulating Free Surface Flows with SPH. *Journal of Computational Physics*, 110, 399-406.
- MONAGHAN, J. J. & LATTANZIO, J. C. 1985. A refined particle method for astrophysical problems. *Astronomy and astrophysics*, 149, 135-143.

- MUKARO, R., GOVENDER, K., GLEDHILL, I. M. A. & KOKWE, N. L. Velocity flow field and water level measurements in shoaling and breaking water waves. 2010-01 2010.
- MUNK, W. 2006. The solitary wave theory and its application to surf problems. *Annals of the New York Academy of Sciences*, 51, 376-424.
- NADAOKA, K. A Fundamental Study on Shoaling and Velocity Field Structure of Water Waves in the Nearshore Zone. 1986.
- NADAOKA, K., HINO, M. & KOYANO, Y. 1989. Structure of the turbulent flow field under breaking waves in the surf zone. *Journal of Fluid Mechanics*, 204, 359-387.
- NADAOKA, K. & KONDOH, T. 1982. Laboratory measurements of velocity field structure in the surf zone by LDV. *Coastal Engineering in Japan*, 25, 125-145.
- NADAOKA, K., UENO, S. & IGARASHI, T. 1988. Field observation of three-dimensional large-scale eddies and sediment suspension in the surf zone. *Coastal Engineering in Japan*, 31, 277-287.
- NIELSEN, P. 1984. On the motion of suspended sand particles. *Journal of Geophysical Research: Oceans*, 89, 616-626.
- NIELSEN, P. 2002. Shear stress and sediment transport calculations for swash zone modelling. *Coastal Engineering*, 45, 53-60.
- OGSTON, A. S. & STERNBERG, R. W. 1995. On the importance of nearbed sediment flux measurements for estimating sediment transport in the surf zone. *Continental Shelf Research*, 15, 1515-1524.
- OKAYASU, A., UNO, Y., KOBAYASHI, T. & SHIMAYA, M. 2004. LABORATORY MEASUREMENT OF SUSPENDED SEDIMENT CONCENTRATION IN SURF ZONE WITH CT CONCENTRATION METER. *Coastal Engineering Journal*, 46, 203-218.
- PEDERSEN, G. K., LINDSTRØM, E., BERTELSEN, A. F., JENSEN, A., LASKOVSKI, D. & SÆLEVIK, G. 2013. Runup and boundary layers on sloping beaches. *Physics of Fluids*, 25, 012102-012102-23.
- PEDROZO-ACUÑA, A., SIMMONDS, D. J. & REEVE, D. E. 2008. Wave-impact characteristics of plunging breakers acting on gravel beaches. *Marine Geology*, 253, 26-35.
- PEREGRINE, D. H. 1983. Breaking waves on beaches. *Annual review of fluid mechanics*, 15, 149-178.
- PETTI, M. & LONGO, S. 2001. Turbulence experiments in the swash zone. *Coastal Engineering*, 43, 1-24.
- QUINLAN, N., BASA, M. & LASTIWKA, M. An analysis of accuracy in one-dimensional smoothed particle hydrodynamics. 17th AIAA Computational Fluid Dynamics Conference, 2005. 4622.
- ROBERTSON, B., HALL, K., ZYTNER, R. & NISTOR, I. 2013. Breaking Waves: Review of Characteristic Relationships. *Coastal Engineering Journal*, 55.
- ROCHA, M. V. L., MICHALLET, H., SILVA, P. A. & CIENFUEGOS, R. 2014. Nonlinearities of waves propagating over a mild-slope beach: laboratory and numerical results.
- ROTA ROSELLI, R. A., VERNENGO, G., ALTOMARE, C., BRIZZOLARA, S., BONFIGLIO, L. & GUERCIO, R. 2018. Ensuring numerical stability of wave propagation by tuning model parameters using genetic algorithms and response surface methods. *Environmental Modelling & Software*, 103, 62-73.
- RUSSINK, G., BERG, T. J. J. & RIJN, L. C. 2009. Modeling sediment transport beneath skewed-asymmetric waves above a plane bed. *J. Geophys. Res.*, 114.
- RUSSINK, G., RAMAEKERS, G. & RIJN, L. C. 2012. On the parameterization of the free-stream non-linear wave orbital motion in nearshore morphodynamic models. *Coastal Engineering*, 65, 56-63.
- SANA, A. & TANAKA, H. 2007. Full-range equation for wave boundary layer thickness. *Coastal Engineering*, 54, 639-642.

- SATO, S., HOMMA, K. & SHIBAYAMA, T. 1990. Laboratory study on sand suspension due to breaking waves. *Coastal Engineering in Japan*, 33, 219-231.
- SCOTT, N. V., HSU, T.-J. & COX, D. 2009. Steep wave, turbulence, and sediment concentration statistics beneath a breaking wave field and their implications for sediment transport. *Continental Shelf Research*, 29, 2303-2317.
- SEYAMA, A. & KIMURA, A. 1989. The measured properties of irregular wave breaking and wave height change after breaking on the slope. *Coastal Engineering 1988*.
- SHAO, S. & JI, C. 2006. SPH computation of plunging waves using a 2-D sub-particle scale (SPS) turbulence model. *International Journal for numerical methods in fluids*, 51, 913-936.
- SHAO, S., JI, C., GRAHAM, D. I., REEVE, D. E., JAMES, P. W. & CHADWICK, A. J. 2006. Simulation of wave overtopping by an incompressible SPH model. *Coastal engineering*, 53, 723-735.
- SHIBAYAMA, T. & HORIKAWA, K. 1982. Sediment transport and beach transformation. *Coastal Engineering 1982*.
- SHUTO, N. 1977. Transformation of nonlinear long waves. *Coastal Engineering 1976*.
- SILVA, P. A., ABREU, T., VAN DER A, D. A., SANCHO, F., RUESSINK, B. G., VAN DER WERF, J. & RIBBERINK, J. S. 2011. Sediment transport in nonlinear skewed oscillatory flows: Transkew experiments. *Journal of Hydraulic Research*, 49, 72-80.
- SMITH, E. R. & KRAUS, N. C. 1991. Laboratory Study of Wave-Breaking Over Bars and Artificial Reefs. *Journal of Waterway Port Coastal and Ocean Engineering- asce*, 117, 307-325.
- SOU, I., COWEN, E. A. & LIU, P. L.-F. 2010. Evolution of the turbulence structure in the surf and swash zones. *Journal of Fluid Mechanics*, 644, 193.
- SOU, I. M. & YE, H. 2011. Laboratory study of the cross-shore flow structure in the surf and swash zones. *Journal of Geophysical Research: Oceans*, 116.
- STANSBY, P. K. & FENG, T. 2005. Kinematics and depth-integrated terms in surf zone waves from laboratory measurement. *Journal of Fluid Mechanics*, 529, 279.
- STIVE, M. 1980. Velocity and pressure field of spilling breakers. *Coastal Engineering 1980*.
- STOKES, G. G. 1847. On the Theory of Oscillatory Waves, volume 1 of Cambridge Library Collection-Mathematics. Cambridge University Press.
- SUMER, B., ARI GUNER, H., HANSEN, N., FUHRMAN, D. & FREDSOE, J. 2013. Laboratory observations of flow and sediment transport induced by plunging regular waves. *Journal of Geophysical Research: Oceans*, 118.
- SVENDSEN, I. 1985. Wave attenuation and set-up on a beach. *Coastal Engineering 1984*.
- SVENDSEN, I. A. 1987. Analysis of surf zone turbulence. *Journal of Geophysical Research: Oceans*, 92, 5115-5124.
- TANAKA, M., DOLD, J., LEWY, M. & PEREGRINE, D. 1987. Instability and breaking of a solitary wave. *Journal of Fluid Mechanics*, 185, 235-248.
- TING, F. C. 2002. Laboratory study of wave and turbulence characteristics in narrow-band irregular breaking waves. *Coastal Engineering*, 46, 291-313.
- TING, F. C. 2006. Large-scale turbulence under a solitary wave. *Coastal Engineering*, 53, 441-462.
- TING, F. C. 2008. Large-scale turbulence under a solitary wave: Part 2: Forms and evolution of coherent structures. *Coastal Engineering*, 55, 522-536.
- TING, F. C. & KIRBY, J. T. 1994. Observation of undertow and turbulence in a laboratory surf zone. *Coastal Engineering*, 24, 51-80.
- TING, F. C. & KIRBY, J. T. 1995. Dynamics of surf-zone turbulence in a strong plunging breaker. *Coastal Engineering*, 24, 177-204.
- TING, F. C. & KIRBY, J. T. 1996. Dynamics of surf-zone turbulence in a spilling breaker. *Coastal Engineering*, 27, 131-160.
- TING, F. C. & NELSON, J. R. 2011. Laboratory measurements of large-scale near-bed

- turbulent flow structures under spilling regular waves. *Coastal Engineering*, 58, 151-172.
- TING, F. C. K. 2013. Laboratory measurements of large-scale near-bed turbulent flow structures under plunging regular waves. *Coastal Engineering*, 77, 120-139.
- TROWBRIDGE, J. & ELGAR, S. 2001. Turbulence measurements in the surf zone. *Journal of Physical Oceanography*, 31, 2403-2417.
- URSELL, F. The long-wave paradox in the theory of gravity waves. *Mathematical Proceedings of the Cambridge Philosophical Society*, 1953. Cambridge University Press, 685-694.
- VAN DER WERF, J. J., DOUCETTE, J., O'DONOGHUE, T. & RIBBERINK, J. S. 2007. Detailed measurements of velocities and suspended sand concentrations over full-scale ripples in regular oscillatory flow. *Journal of Geophysical Research: Earth Surface*, 112.
- VAN RIJN, L. C. 1989. *Handbook sediment transport by currents and waves*, Delft Hydraulics Laboratory.
- VAN RIJN, L. C., TONNON, P. K. & WALSTRA, D. J. R. 2011. Numerical modelling of erosion and accretion of plane sloping beaches at different scales. *Coastal Engineering*, 58, 637-655.
- VERLET, L. 1967. Computer" experiments" on classical fluids. I. Thermodynamical properties of Lennard-Jones molecules. *Physical review*, 159, 98.
- VILA, J. 1999. On particle weighted methods and smooth particle hydrodynamics. *Mathematical models and methods in applied sciences*, 9, 161-209.
- VITTORI, G. & BLONDEAUX, P. 2009. BOUNDARY LAYER FLOW AND BED SHEAR STRESS UNDER A SOLITARY WAVE. *Coastal Engineering 2008: (In 5 Volumes)*. World Scientific.
- VOULGARIS, G. & COLLINS, M. B. 2000. Sediment resuspension on beaches: response to breaking waves. *Marine Geology*, 167, 167-187.
- WANG, Z.-B., CHEN, R., WANG, H., LIAO, Q., ZHU, X. & LI, S.-Z. 2016. An overview of smoothed particle hydrodynamics for simulating multiphase flow. *Applied Mathematical Modelling*, 40, 9625-9655.
- WENDLAND, H. 1995. Piecewise polynomial, positive definite and compactly supported radial functions of minimal degree. *Advances in computational Mathematics*, 4, 389-396.
- YANG, Z., LU, X., GUO, X., LIU, Y. & SHEN, L. 2017. Numerical Simulation of Sediment Suspension and Transport under Plunging Breaking Waves. *Computers & Fluids*, 158.
- YOON, H.-D. & COX, D. T. 2012. Cross-shore variation of intermittent sediment suspension and turbulence induced by depth-limited wave breaking. *Continental Shelf Research*, 47, 93-106.
- YOUNG, I. R. 2017. A review of parametric descriptions of tropical cyclone wind-wave generation. *Atmosphere*, 8, 194.
- ZHANG, D. & SUNAMURA, T. 1990. Conditions for the occurrence of vortices induced by breaking waves. *Coastal Engineering in Japan*, 33, 145-155.
- ZHANG, D. P. & SUNAMURA, T. 1995. Multiple Bar Formation by Breaker-Induced Vortices: A Laboratory Approach. *Coastal Engineering 1994*.
- ZHU, Q., HERNQUIST, L. & LI, Y. 2015. Numerical convergence in smoothed particle hydrodynamics. *The Astrophysical Journal*, 800, 6.

APPENDIX A

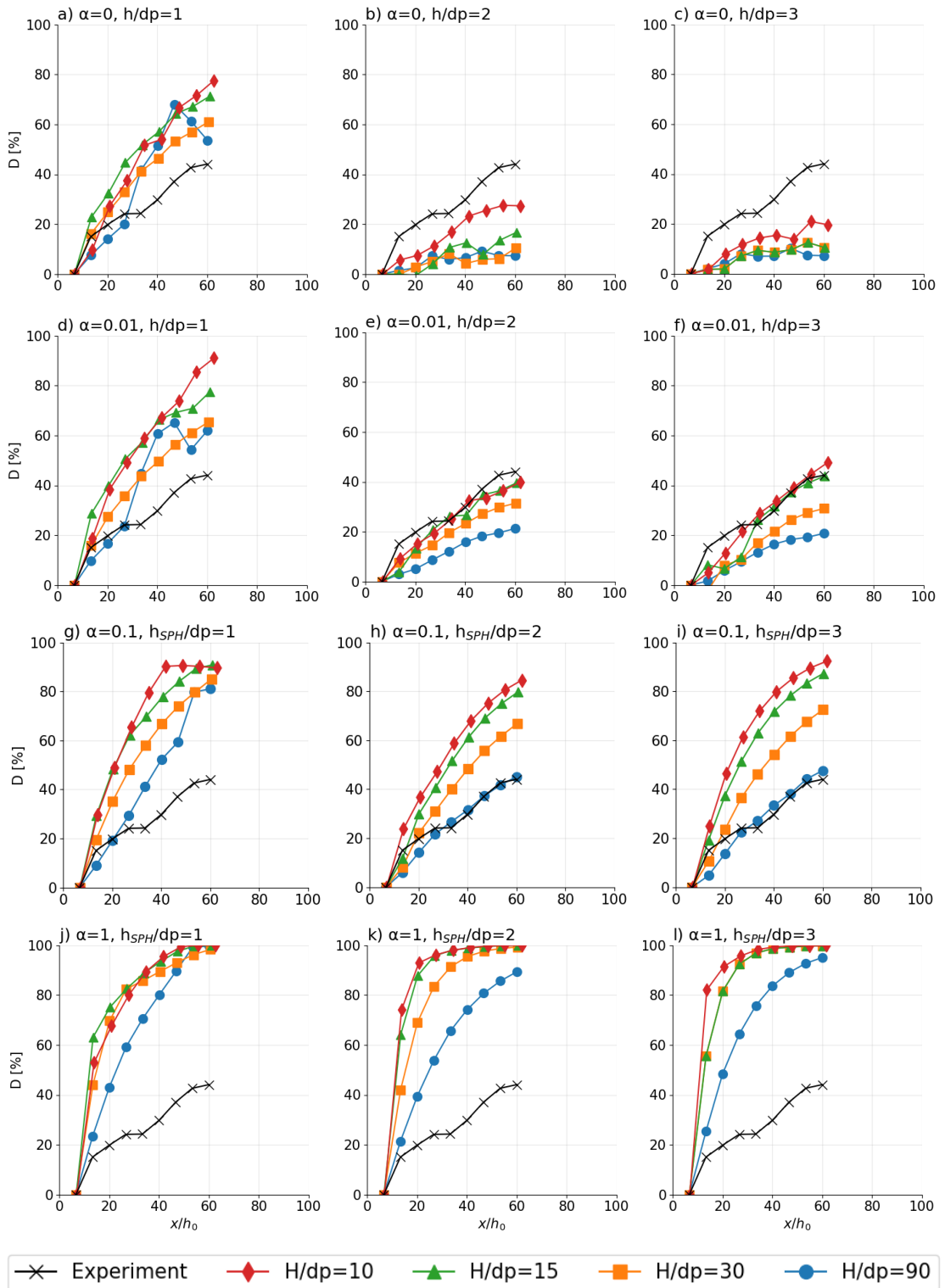


Figure A-1: The numerical wave energy dissipation (D) of a plunging solitary wave ($S_0=0.118$), using various combinations of α , h_{SPH}/dp , and H/dp , compared to measured data, over the horizontal wave tank section.

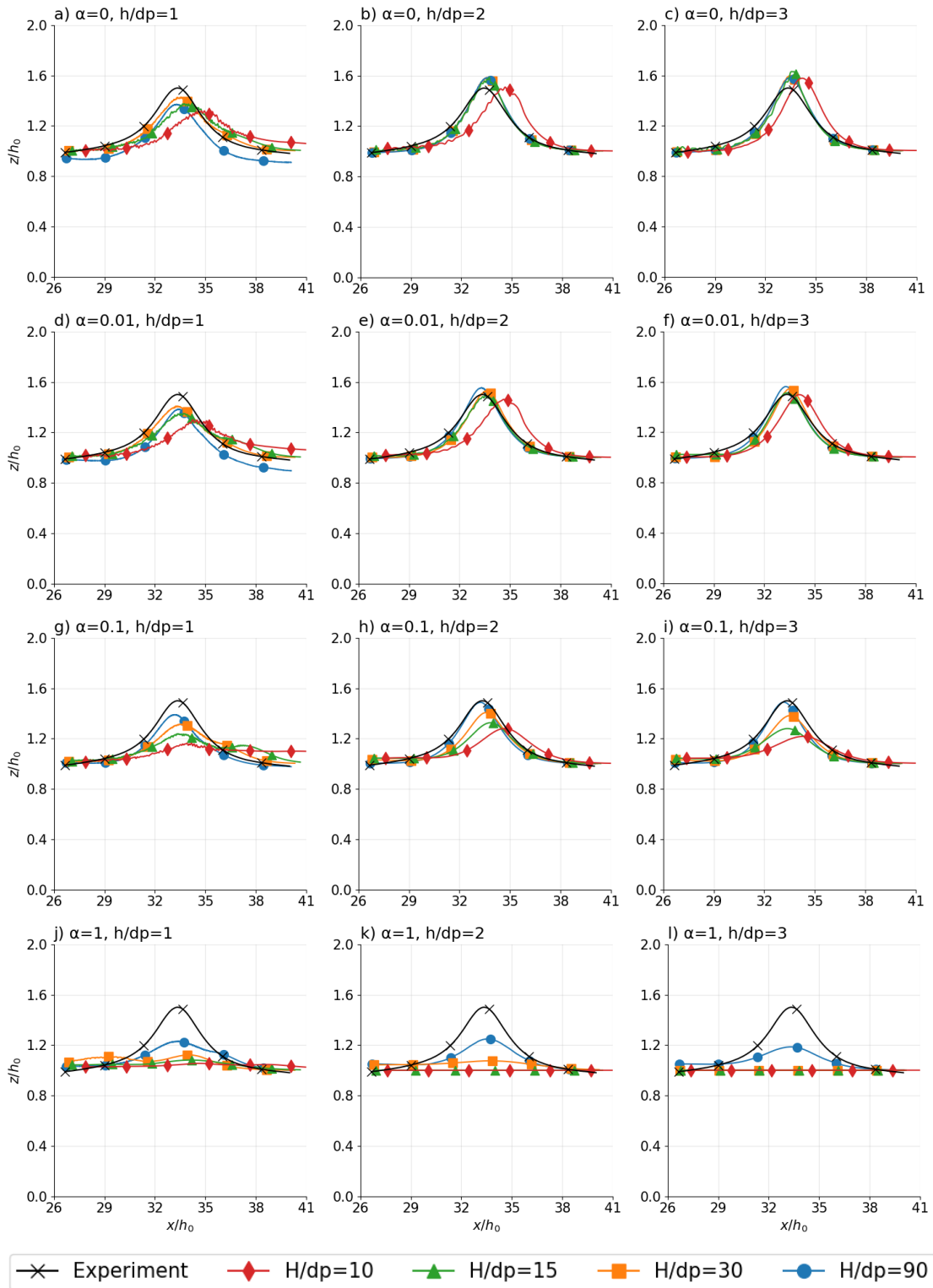


Figure A-2 The simulated spatially varying wave (z/h_0) profile of a plunging solitary wave ($S_0=0.118$), using various combinations of α , h_{SPH}/dp , and H/dp , compared to measured data, at the first defined phase of evolution, when the solitary wave crest is at $x/h_0=33.3$ from the wave paddle.

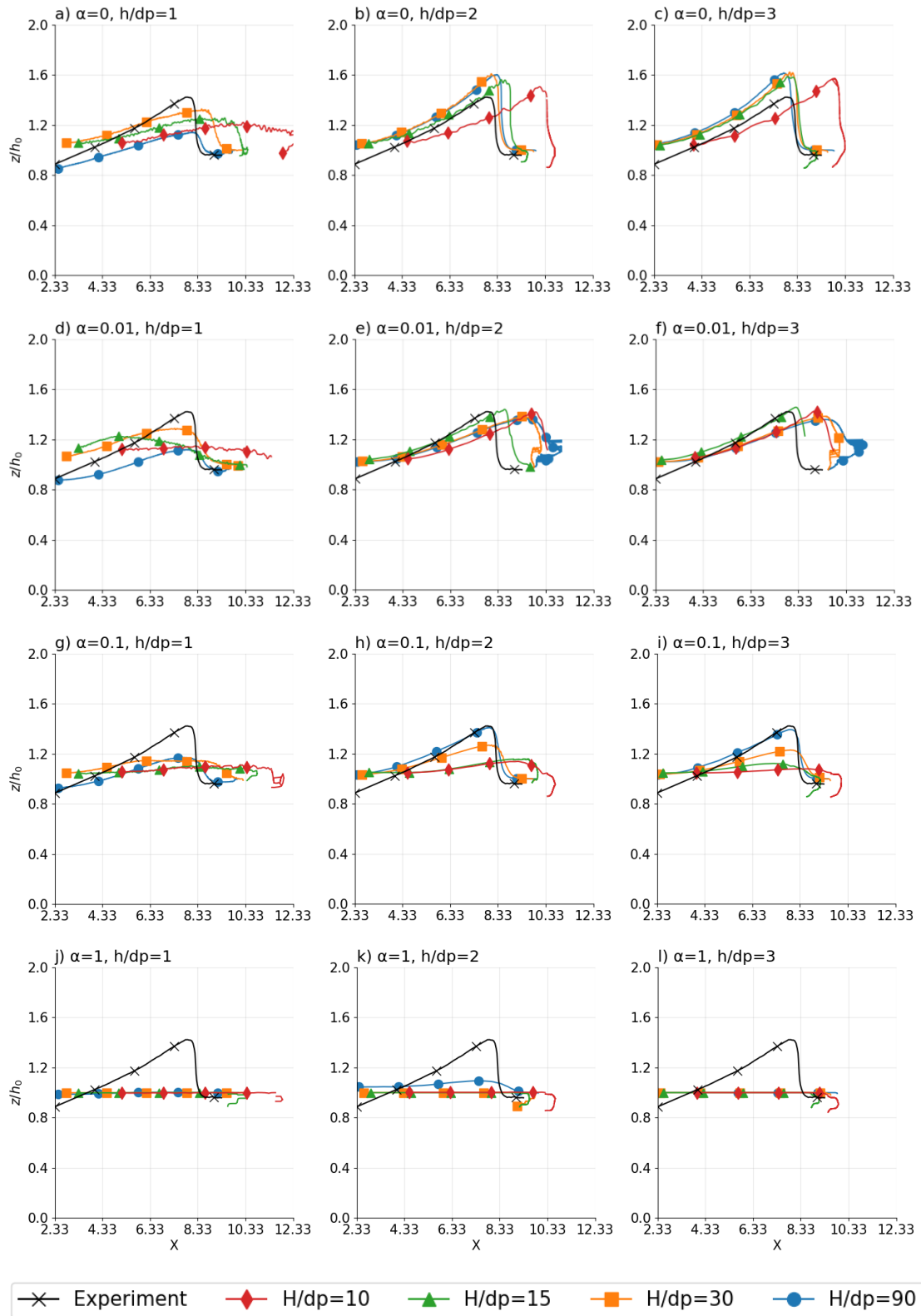


Figure A-3: The simulated spatially varying wave (z/h_0) profile of a plunging solitary wave ($S_0=0.118$), using various combinations of α , h_{SPH}/dp , and H/dp , compared to measured data, at the third defined phase of evolution, four timesteps before wave impingement on the beach slope.

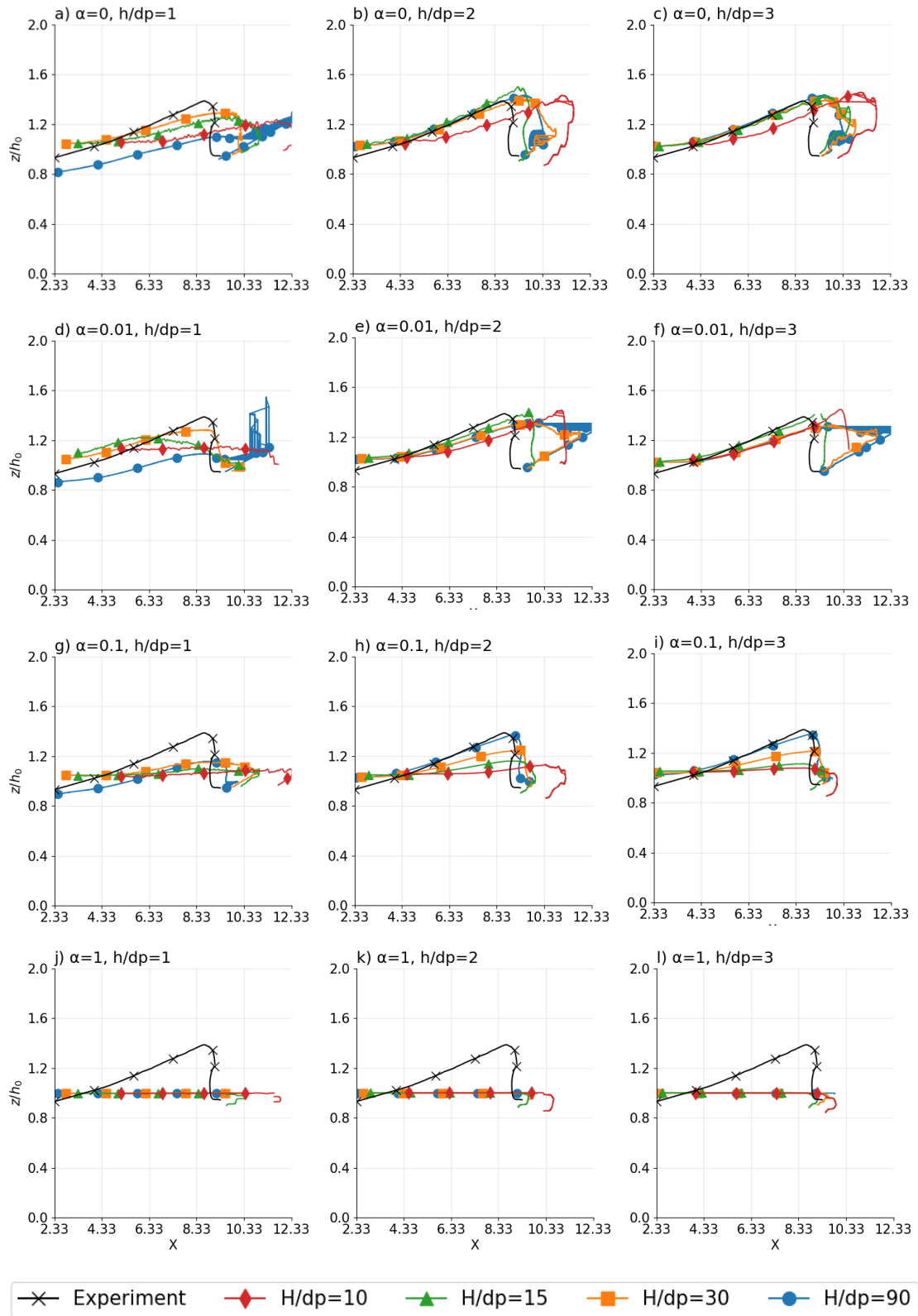


Figure A-4: The simulated spatially varying wave (z/h_0) profile of a plunging solitary wave ($S_0=0.118$), using various combinations of α , h_{SPH}/dp , and H/dp , compared to measured data, at the third defined phase of evolution, two timesteps before wave impingement on the beach slope.

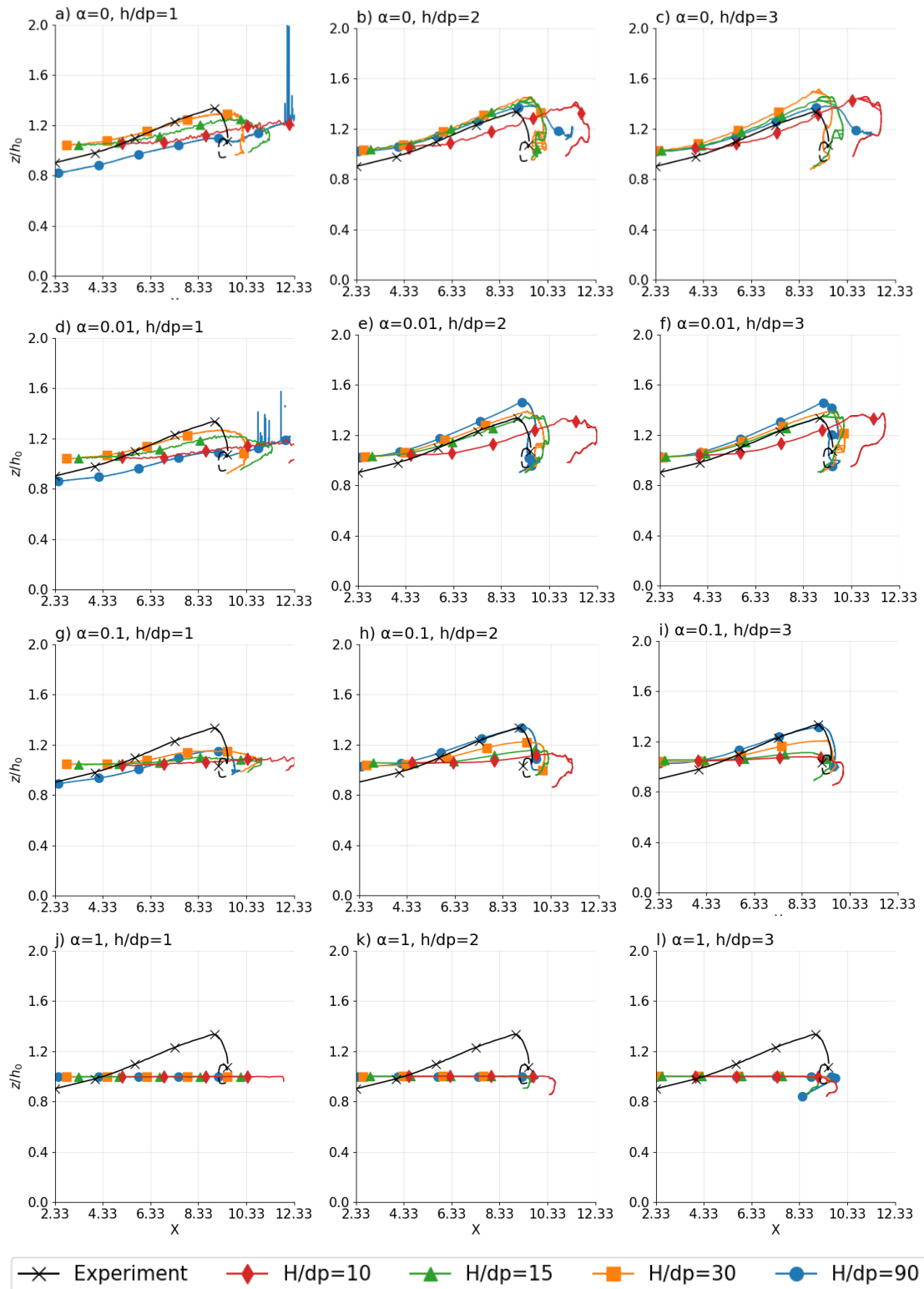


Figure A-5: The simulated spatially varying wave (z/h_0) profile of a plunging solitary wave ($S_0=0.118$), using various combinations of α , h_{SPH}/dp , and H/dp , compared to measured data, at the fourth defined phase of evolution, one timestep before wave impingement on the beach slope.

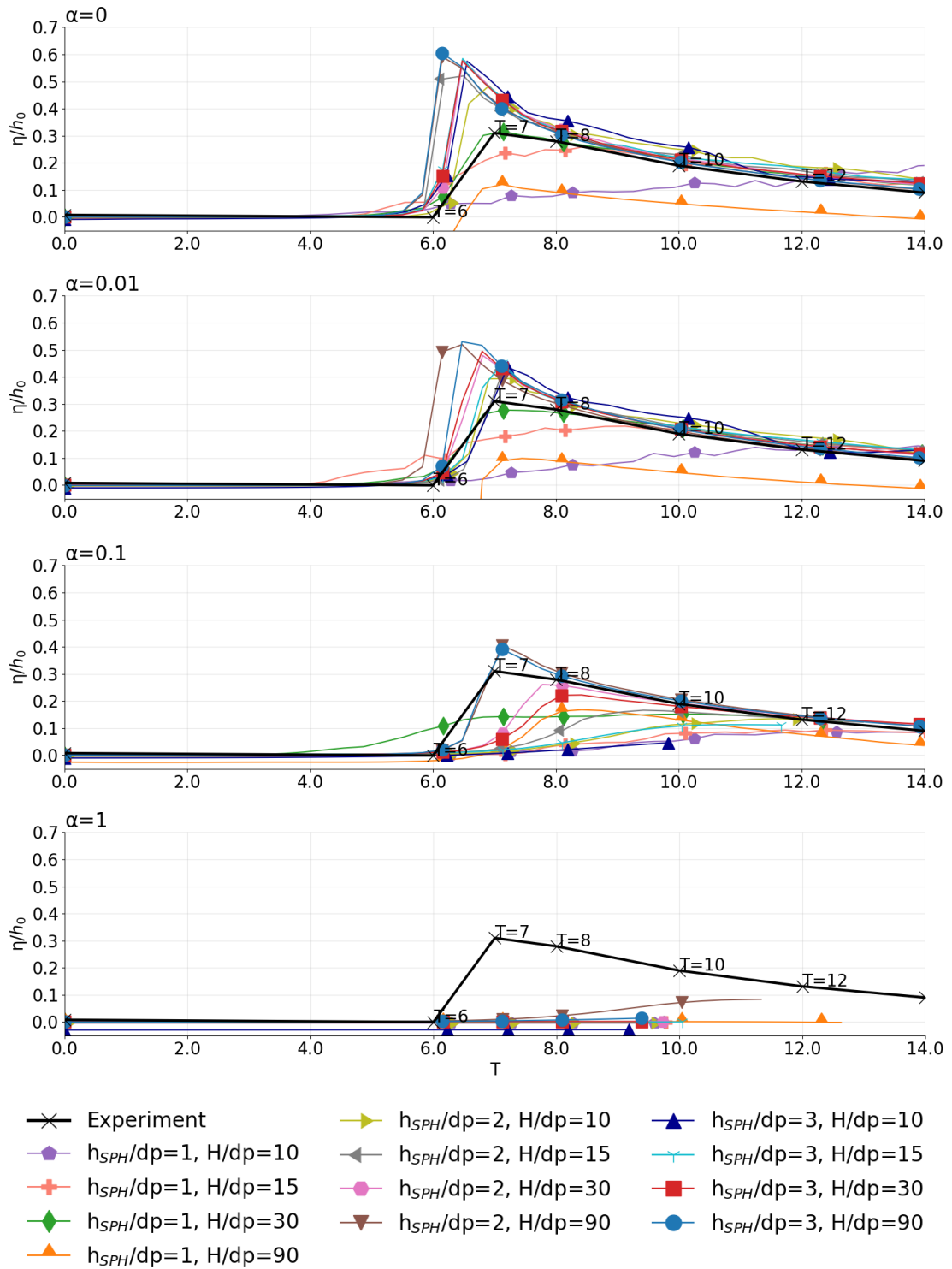


Figure A-6: The simulated time varying wave surface elevation (η/h_0) profile of a plunging solitary wave ($S_0=0.118$), using various combinations of h_{SPH}/dp and H/dp , compared to measured data, at $X=8.25$ on the beach slope. The measured profile is annotated at times $T=6, T=7, T=8, T=10$, and $T=12$.

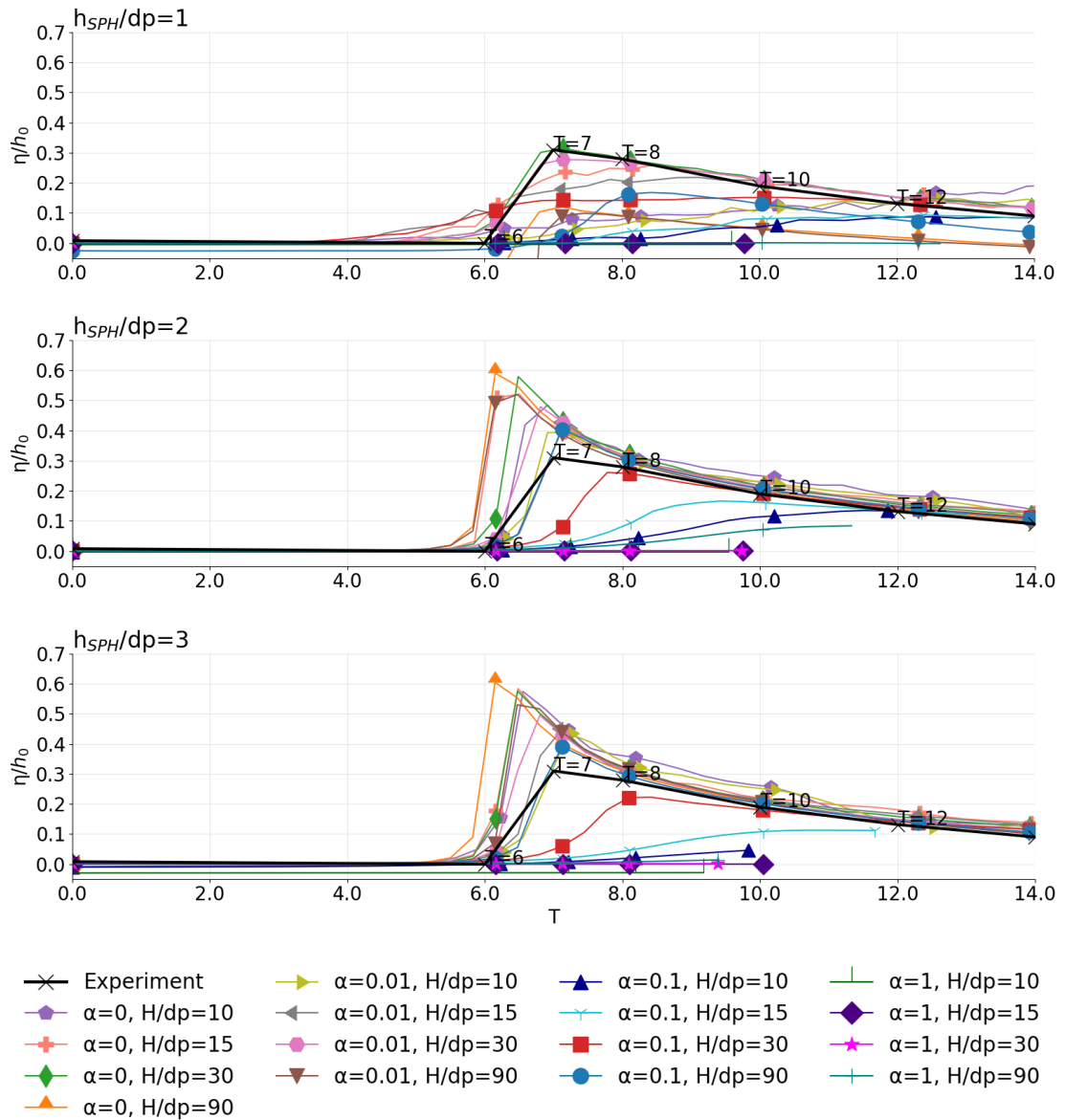


Figure A-7: The simulated time varying wave surface elevation (η/h_0) profile of a plunging solitary wave ($S_0=0.118$), using various combinations of α and H/dp , compared to measured data, at $X=8.25$ on the beach slope. The measured profile is annotated at times $T=6, T=7, T=8, T=10$, and $T=12$.

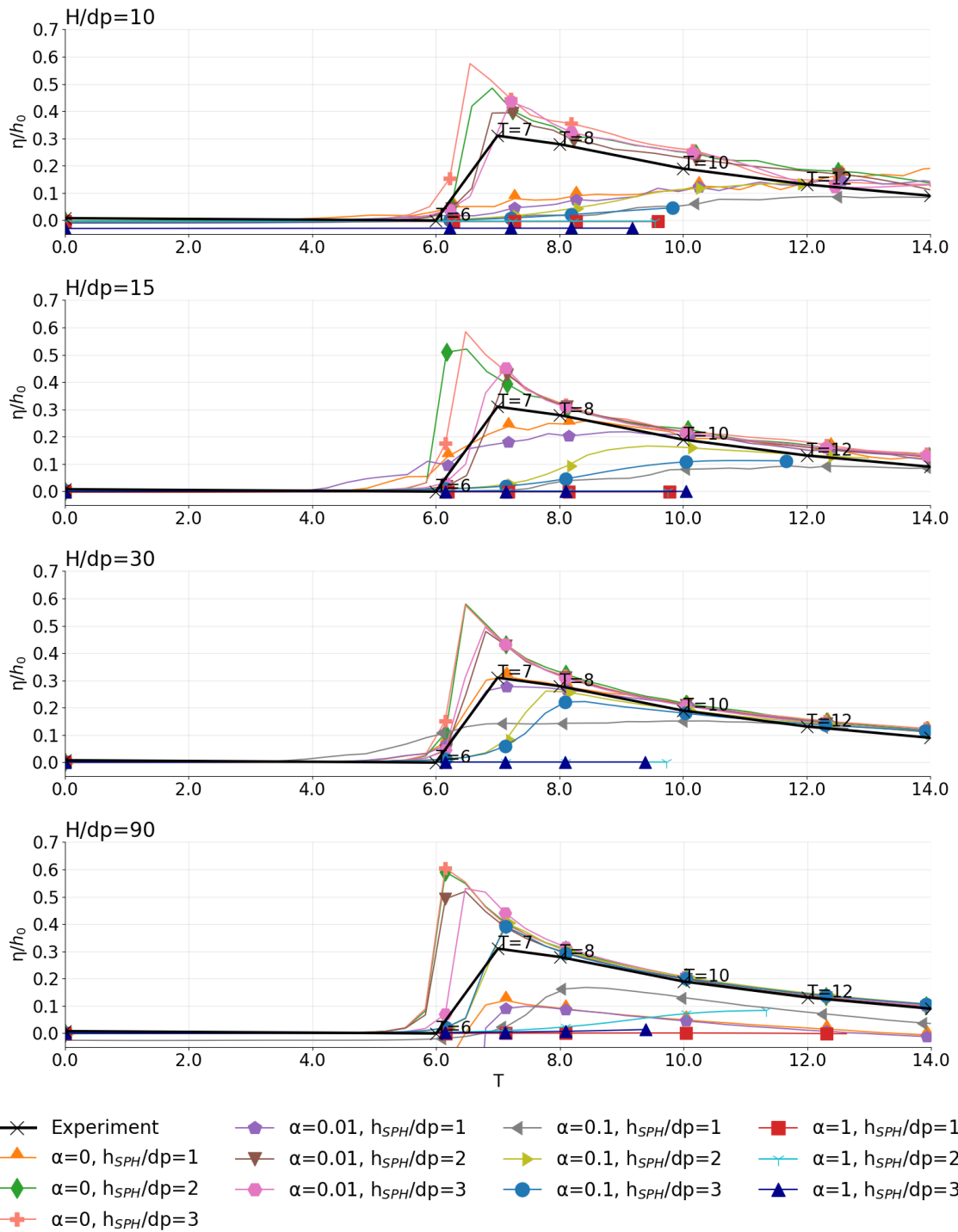


Figure A-8: The simulated time varying wave surface elevation (η/h_0) profile of a plunging solitary wave ($S_0=0.118$), using various combinations of α and h_{SPH}/d_p , compared to measured data, at $X=8.25$ on the beach slope. The measured profile is annotated at times $T=6, T=7, T=8, T=10, T=12$.

APPENDIX B

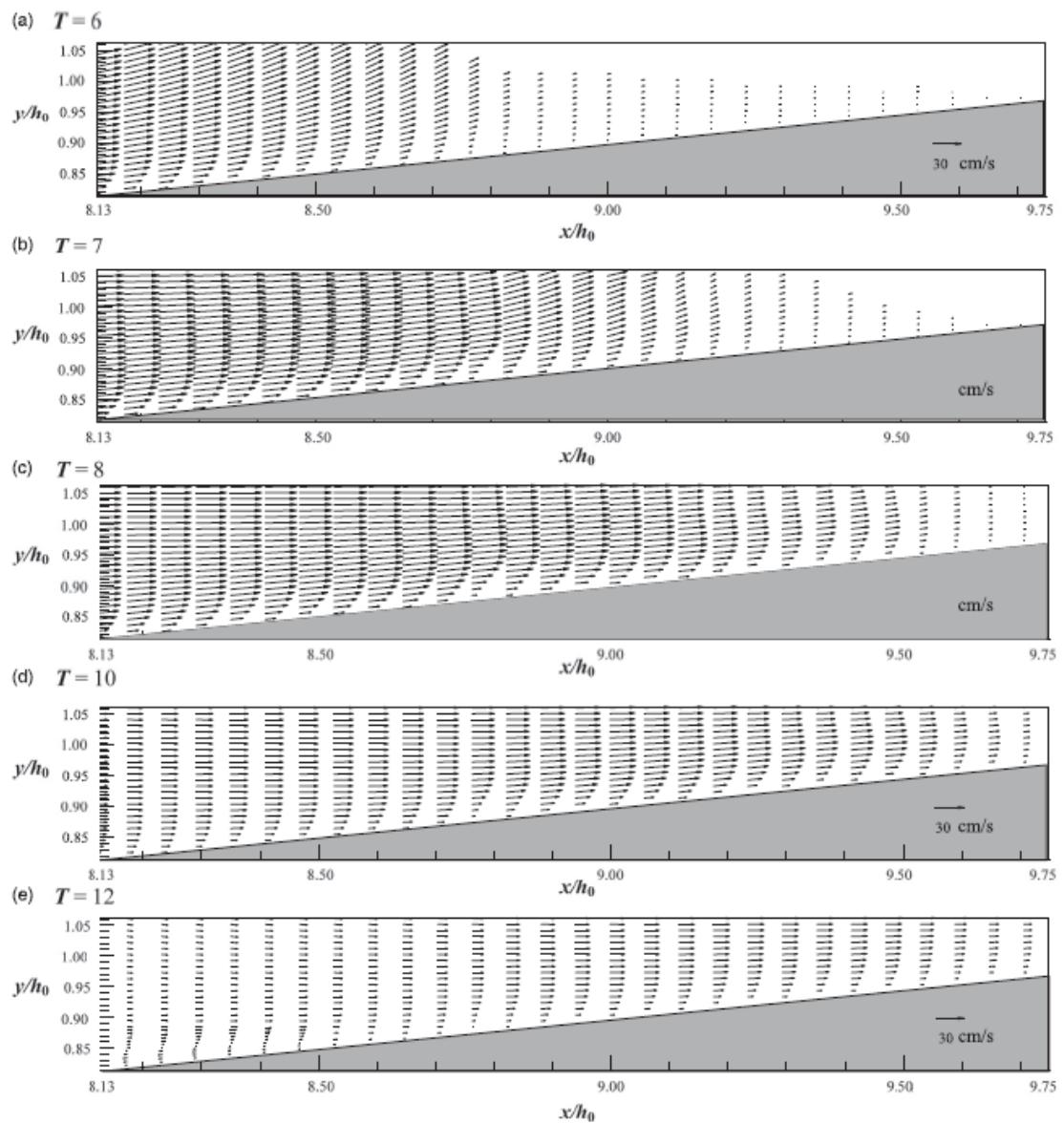


Figure B-1: The measured spatially varying velocity vectors, near the bed, under a plunging solitary wave ($S_0=0.078$), propagating over a 1/10 beach slope, during the interval $T=6$ to $T=12$ (after Lin et al., 2015).

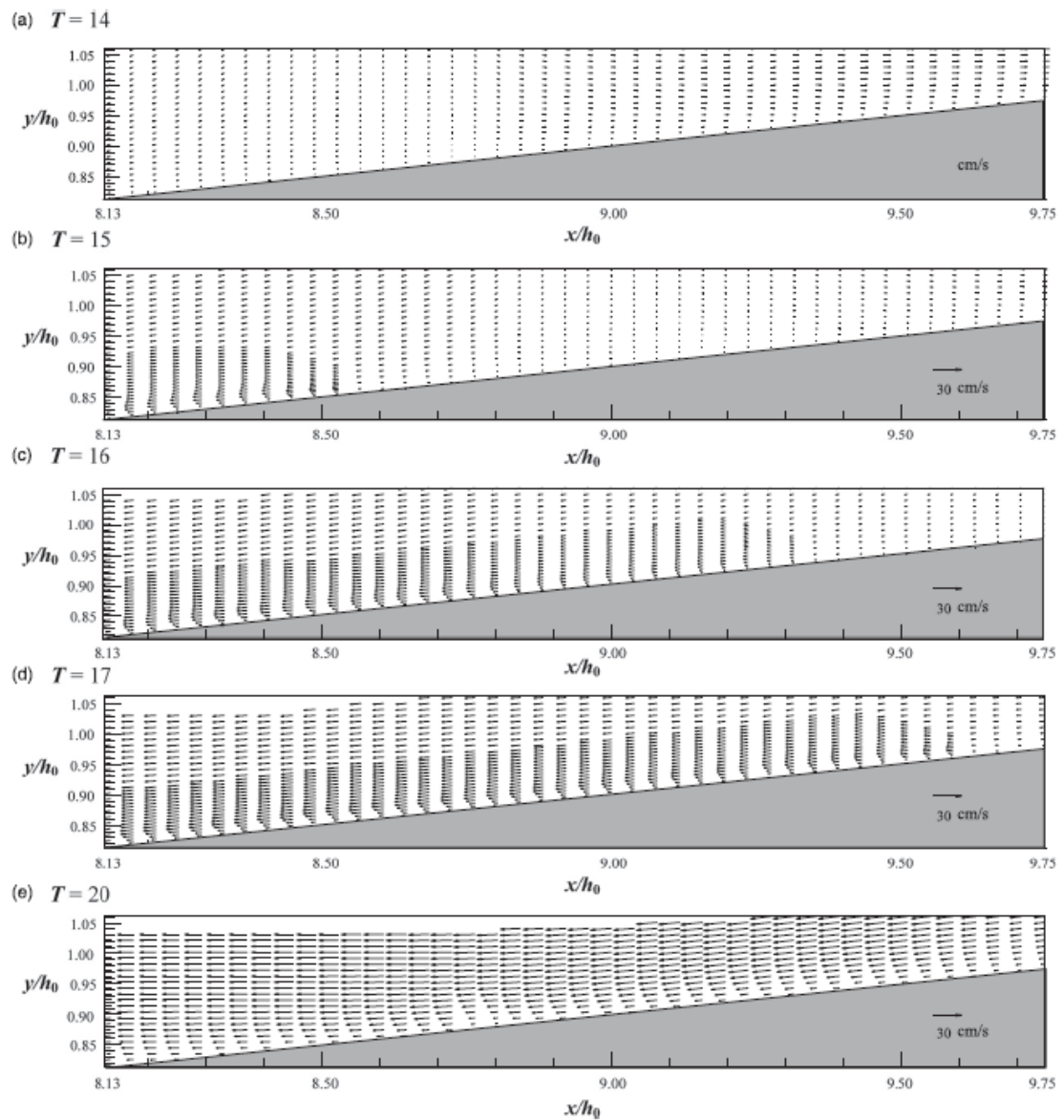


Figure B-2: The measured spatially varying velocity vectors near the bed, under a plunging solitary wave ($S_0=0.078$), propagating over a $1/10$ beach slope, during the interval $T=14$ to $T=20$. (after Lin et al., 2015).

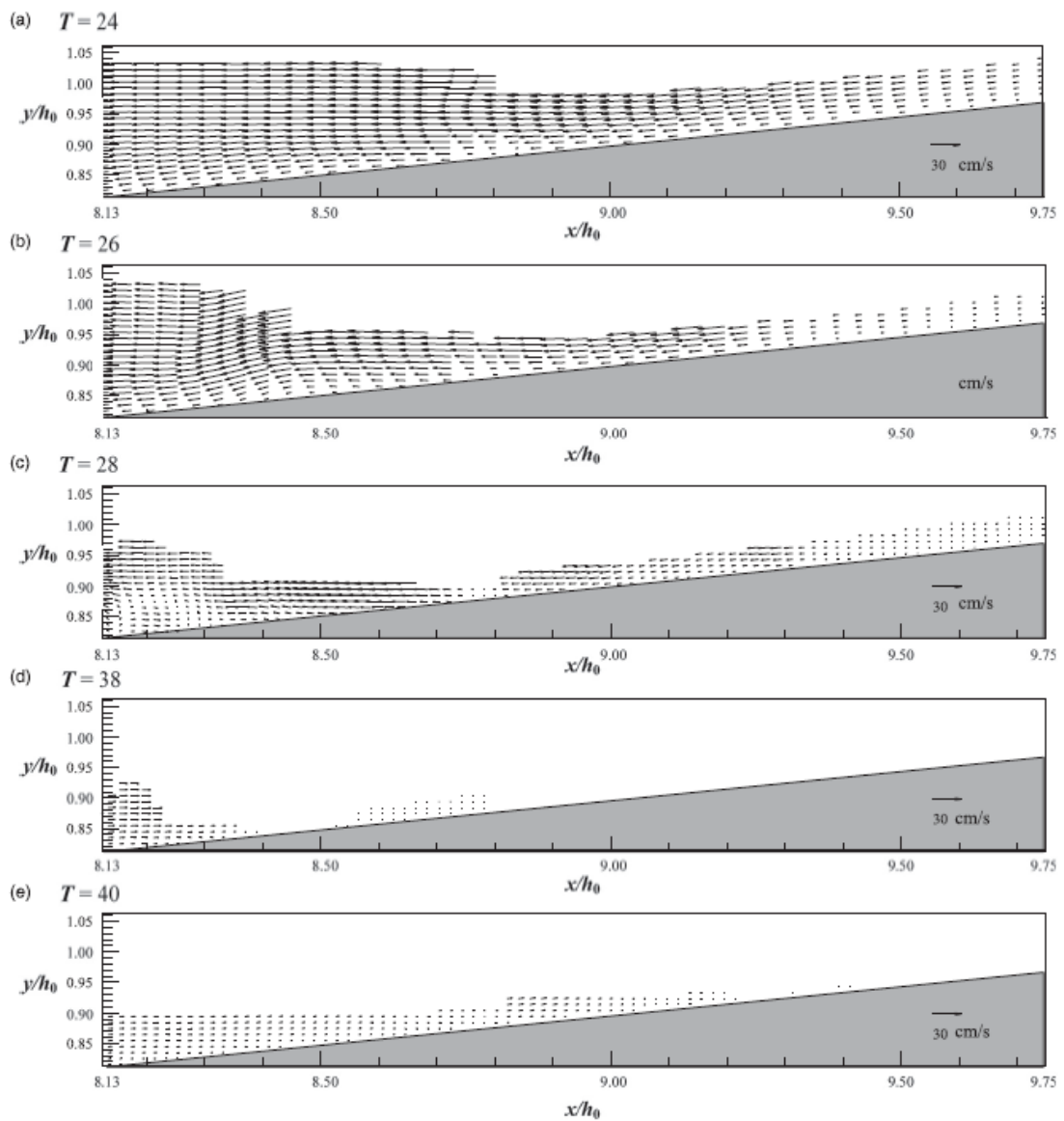


Figure B-3: The measured spatially varying velocity vectors near the bed, under a plunging solitary wave ($S_0=0.078$), propagating over a 1/10 beach slope during the intervals $T=24$ to $T=28$ and $T=38$ to $T=40$ (after Lin et al., 2015).

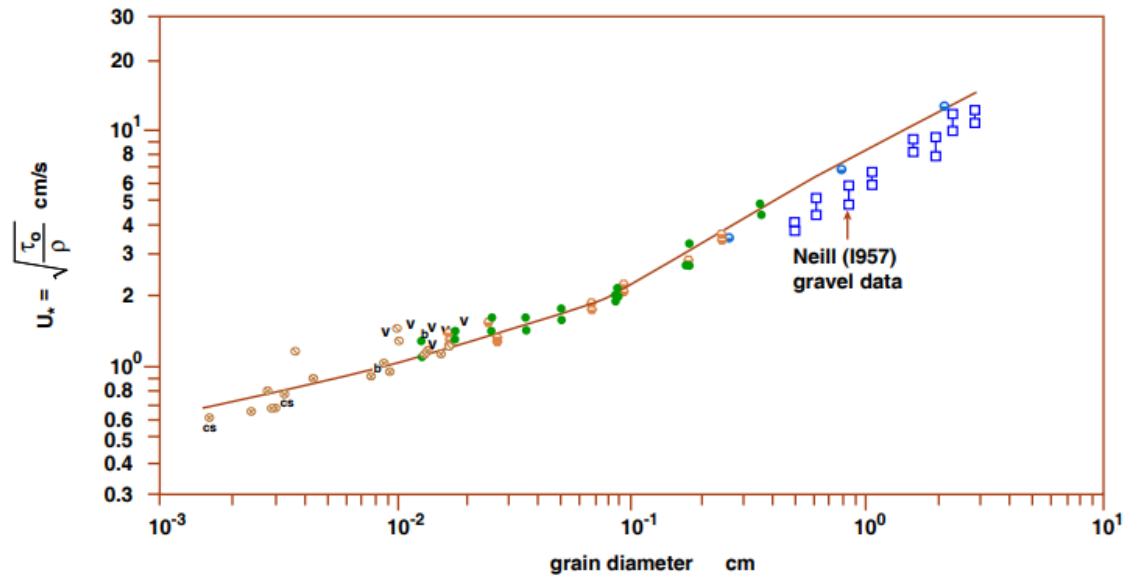


Figure B-4: A version of Shields diagram showing the grain diameter versus the shear velocity (u_*) required to initiate the movement of quartz density material ($\rho_s=2.65$ g/cm³) in water at 20° C (adapted Miller and Komar, 1977).

APPENDIX C

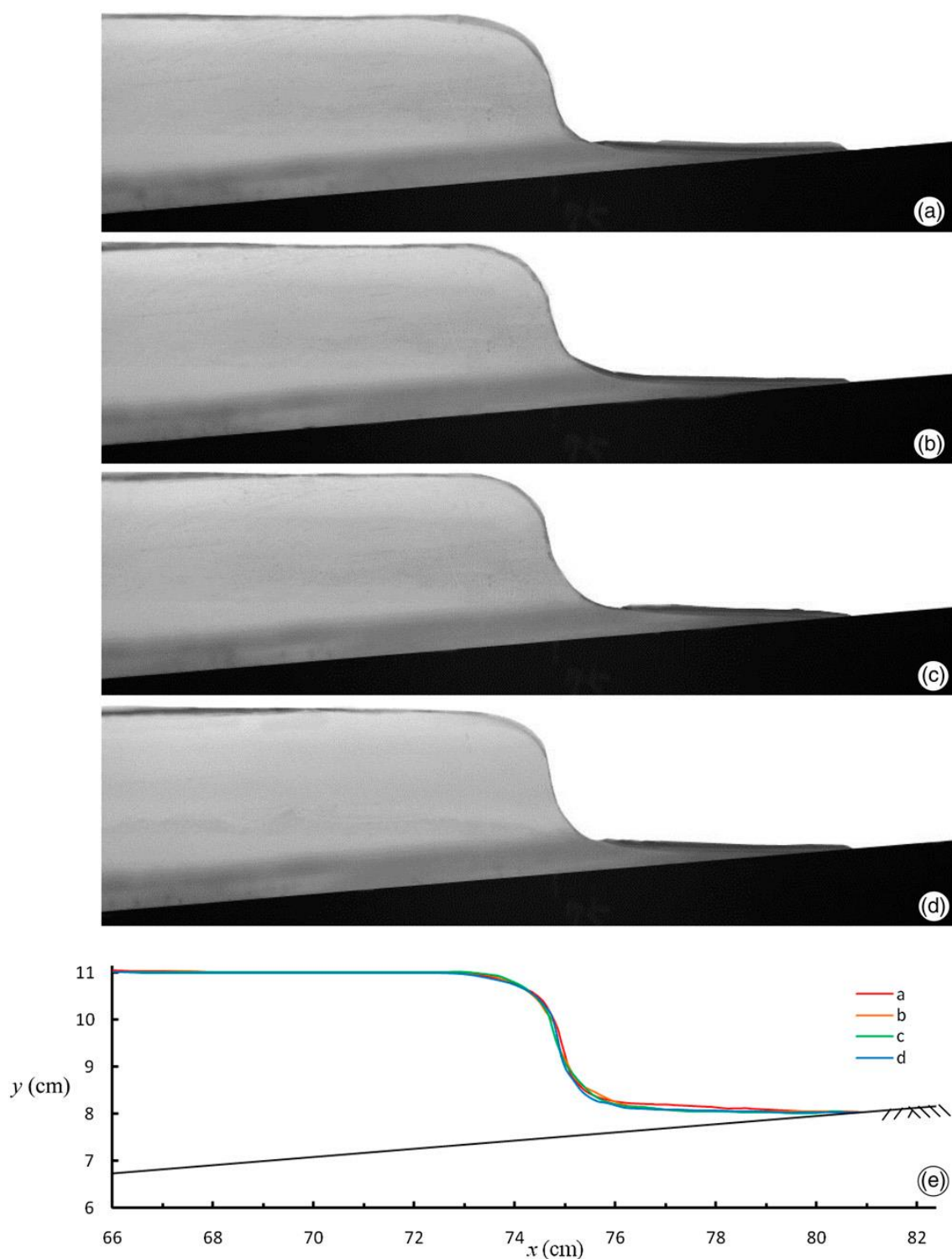


Figure C-1 The measured spatially varying wave (z) profile of a plunging solitary wave ($S_0=0.078$), propagating over a 1/10 beach slope (after Lin et al., 2015). Images (a–d) show four runs for the spatial evolution of free surface elevation before breaking, and (e) compares the free surface elevations among the four runs.

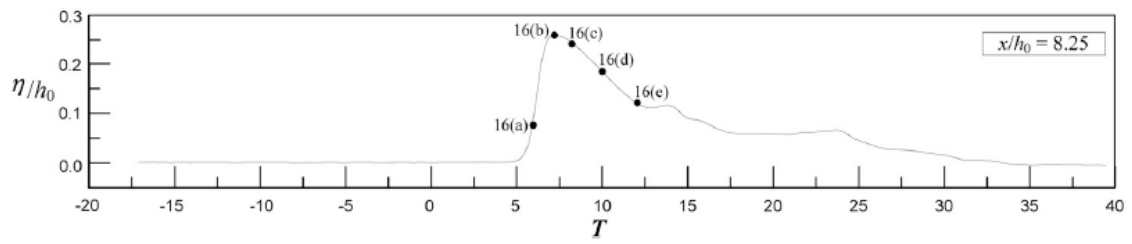


Figure C-2: The measured time varying wave elevation (η/h_0) profile of a plunging solitary wave ($S_0=0.078$), propagating over a 1/10 beach slope, at $X=8.25$ (after Lin et al., 2015).

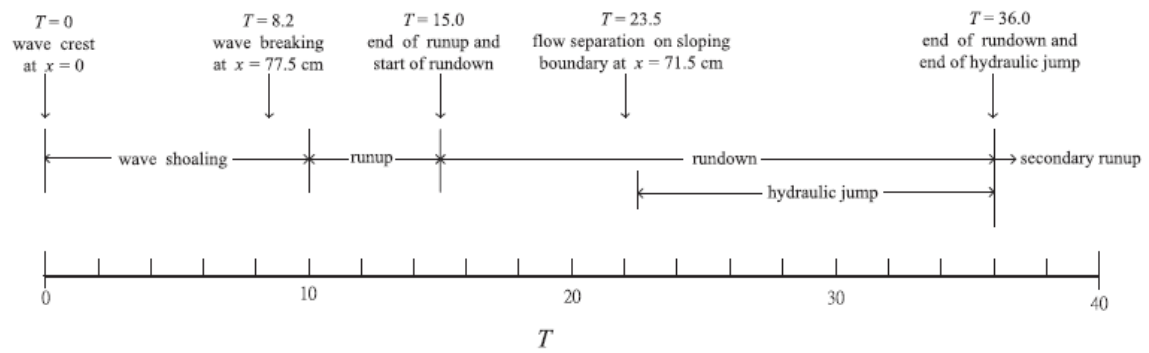


Figure C-3: A non-dimensional timeline showing the complete evolution of a plunging solitary wave ($S_0=0.078$), propagating over a 1/10 beach slope (after Lin et al., 2015).